Understanding fundamental migration processes during battery cycling and material synthesis using advanced transmission electron microscopy methods

TECHNISCHE UNIVERSITÄT DARMSTADT

Dissertation approved by
the Department of Materials- and Geosciences,
Technical University of Darmstadt
in fulfilment of the requirements for the degree of
Doctor rerum naturalium
(Dr. rer. nat.)

by
Kai Wang
M.E. in Chemical Engineering
Born on April 15, 1991 at Hengshui, Hebei, China

Referee: Prof. Dr. rer. nat. Christian Kübel
Co-referee: Prof. Dr. rer. nat Helmut Ehrenberg
Date of submission: 21.03.2022
Date of oral exam: 02.06.2022

Darmstadt 2022

Erklärung zur Dissertation

Hiermit versichere ich, dass ich meine Dissertation selbständig und nur mit den angegebenen Quellen und Hilfsmitteln angefertigt habe. Die Arbeit wurde bisher keiner anderen Prüfungsbehörde vorgelegt und noch nicht veröffentlicht.

Karlsruhe, 19.03.2022
Kai Wang

Abstract

To satisfy the increasing need for efficient energy storage systems resulting from the worldwide rapid development of renewable energy sources, rechargeable ion batteries are getting unprecedented attention. Anode materials, as essential components of rechargeable ion batteries, have been widely investigated to meet the increasing demands for higher energy density. Metal oxides (MOs) and transition-metal dichalcogenides (TMDs) are regarded as promising future anode materials with their potential to provide high capacity, cycling stability and volumetric energy density. However, these materials undergo complex reaction processes and generate large amounts of amorphous products, making their characterization difficult. Nevertheless, understanding the reaction mechanisms during synthesis and during electrochemical cycling is essential to guide the design of novel electrode materials.

Transmission electron microscopy (TEM) is commonly considered to be a powerful technique for morphological characterization, structure determination, elemental mapping and valence state analysis, both for amorphous and crystalline materials. In this work, conventional TEM methods and a number of advanced TEM-characterization techniques, such as *in-situ* heating in defined gas environment, pair distribution function (PDF) analysis and 4D-STEM, have been carried out to understand the fundamental aspects of elemental migration, the local chemical environment and the structural evolution during material synthesis and battery cycling. Moreover, additional characterization techniques including X-ray diffraction (XRD), X-ray absorption spectroscopy (XAS), and electrochemical testing have been applied to obtain complementary bulk information about the battery systems.

Due to their outstanding electrochemical performance high entropy oxides (HEOs) have attracted intensive attention for application in the area of energy storage. However, the fundamental understanding of the elemental processes during material synthesis and of the reactions during electrochemical cycling is still limited. This knowledge is essential to design and optimize materials, particularly for advanced materials based on the high entropy concept. First, the processes during HEO $(Co_{0.2}Cu_{0.2}Mg_{0.2}Ni_{0.2}Zn_{0.2})O$ synthesis by calcination of the corresponding oxides have been studied, mainly by *in-situ* heating XRD and TEM techniques. The results of this work reveal the structural evolution and morphological from the separated raw metal oxides with increasing temperature to the final HEO. The interpretation of elemental diffusion parameters indicates that some intermediate oxide phases are formed prior to the HEO generation, thus implying that the formation of the HEO proceeds in multiple steps. The results further demonstrate that Co_3O_4 is an alternative to CoO as Co source for the HEO $(Co_{0.2}Cu_{0.2}Mg_{0.2}Ni_{0.2}Zn_{0.2})O$ synthesis.

Furthermore, the de/lithiation mechanism of the HEO $(Co_{0.2}Cu_{0.2}Mg_{0.2}Ni_{0.2}Zn_{0.2})O$ was studied by correlative TEM and XAS measurements at various battery states. The results indicate that during the 1st

discharge, Ni, Cu, Co and Zn are reduced. Ni, Cu and partially Co do not further participate in the electrochemical reactions in the following cycles as they form an inert alloy at grain boundaries and fine dispersed inside the grain. In the entire particle, the alloy builds up a 3D network that enables the fast electron transfer during the following electrochemical cycles. Zn, and partially Co provide the capacity of HEO through conversion and alloying reactions. As Mg cannot be reduced by Li during battery cycling it remains in a 2^+ oxidation state during all cycling stages and forms a continuous oxide network that provides a 3D network for lithium ion transfer. In addition, MgO also stabilizes the overall structure of the material inducing an epitaxial relationship with the phases generated during battery cycling. Thus, this study revealed the synergy of the constituent cations critical for the excellent electrochemical performance of this HEO. These findings can be used in the quest of obtaining high performance anode materials.

Molybdenum disulfide (MoS_2) as another promising anode material for both, lithium ion batteries (LIBs) and sodium ion batteries (SIBs), has a high theoretical capacity based on a multi-electron conversion reaction. Although various novel sample designs have improved its electrochemical performance significantly, the reaction mechanism of MoS_2 in sodium ion batteries is still equivocal due to the strongly reduced crystallinity upon deep sodiation. Using advanced TEM techniques effective for analyzing amorphous materials, in the present work the de-/sodiation reaction mechanism of MoS_2-based materials was revisited. The results from the electron based PDF analysis and X-ray absorption spectroscopy show that the initially long range ordered MoS_2 is breaking apart into Mo-S_x clusters during sodiation, rather than the originally expected fully conversion into metallic Mo and Na_2S. It was further found that, although MoS_2/carbon composites show a significant enhancement of the electrochemical performance compared to bare MoS_2, the carbon in the MoS_2/carbon composite does not directly influence the electrochemical reaction of MoS_2. S(TEM) images and 4D-STEM analysis demonstrated that the carbon matrix prevents leaching of Mo-S_x clusters into electrolyte and is therefore beneficial during battery cycling. This work adds a new perspective to the understanding of the MoS_2 reaction mechanism in SIBs.

Contents

List of Figures

List of abbreviations

EV	Electric vehicle
LIBs	Lithium ion batteries
SIBs	Sodium ion batteries
PIBs	Potassium ion batteries
AIBs	Aluminum ion batteries
MIBs	Magnesium ion batteries
NMC	Nickel cobalt manganese
TMDs	Transition-metal dichalcogenides
SEI	Solid electrolyte interface
TEM	Transmission electron microscopy
STEM	Scanning transmission electron microscopy
BF	Bright field
DF	Dark field
BF-TEM	Bright field TEM
DF-TEM	Dark field TEM
HRTEM	High-resolution transmission electron microscopy
SAED	Selected area electron diffraction
PDF	Pair distribution function
ePDF	Electron diffraction based pair distribution function
ADF	Annular dark field
HAADF	High-angle annular dark-field
CCD	Charged coupled device
CMOS	Complementary metal-oxide semiconductor
EDX	Energy-dispersive X-ray spectroscopy
EELS	Electron energy-loss spectroscopy
EFTEM	Energy filtered TEM
XAS	X-ray absorption spectroscopy
XANES	X-ray absorption near edge structure

EXAFS	Extended X-Ray Absorption Fine Structure
FT	Fourier transform
FEG	Field emission gun
FFT	Fast Fourier transform
XRD	X-ray diffraction
XPS	X-ray photoelectron spectroscopy
NMR	Nuclear Magnetic Resonance spectroscopy
GNS	Graphene nanosheet
2D	Two-dimensional
3D	Three-dimensional
4D	Four-dimensional
HEA	High entropy alloy
HEO	High entropy oxide
M	Metal
MO	Metal oxide
GB	Grain boundary
CV	Cyclic voltammetry

1. Introduction

1.1. Introduction

Since the middle of the last century, accelerated population growth and rapid economic development have substantially increased the consumption of fossil-based energy. Establishing cleaner energy systems, such as solar energy[1,2], wind energy[3,4], and geothermal energy[5,6] has become of significant technological interest and, in the last two decades, major scientific and technological advancements in greener energy production have been made. However, varying energy output is a significant problem for these new energy sources due to the intermittent nature of sunlight and wind power. The intermitted energy output has increased the demand for a cheaper and more powerful large-scale energy storage grid. Physical[7–12], electrochemical[13–18], supercapacitor[19–24] and superconducting[25–30] energy storage-based technologies are the current or promising approaches for solving this problem. Figure 1-1 present a comparison of different energy storage systems, in which electrochemical energy storage systems show a good balance between discharging time and power capacity.[1] The electrochemical energy storage systems also have the advantage of a high energy density and relatively low cost.[31–33] Moreover, the interest in advancing electrochemical energy storage technologies is also driven by the need of increasing the specific and volumetric capacity of batteries used in portable electronic products and electric vehicles (EV), asking for an ever-increasing energy density. Rechargeable ion batteries, such as lithium ion batteries (LIBs) and sodium ion batteries (SIBs) show the right characteristics for an extensive usage in both portable electronics and electric vehicles and also in the large-scale energy storage grids.

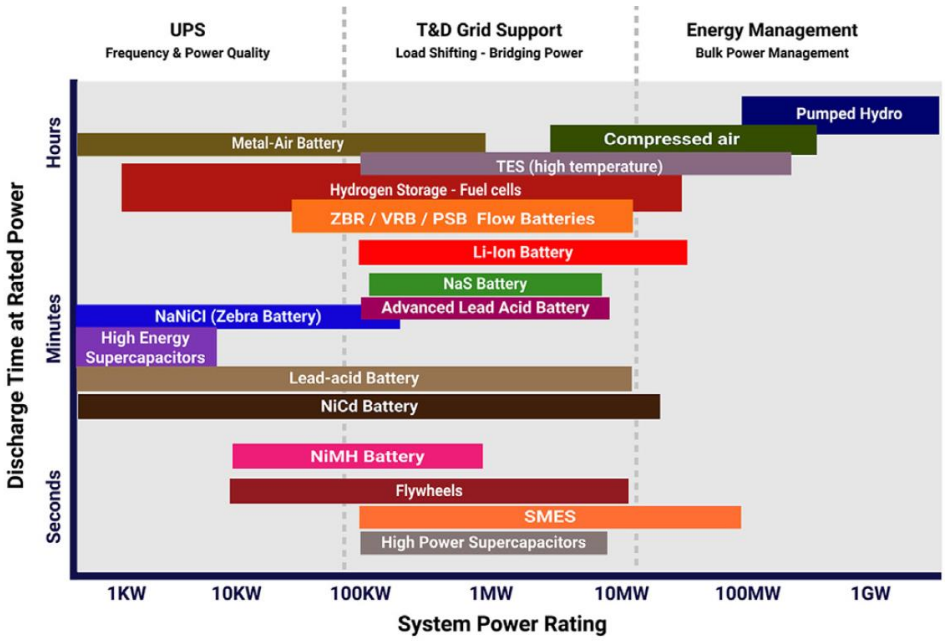

Figure 1-1: Summary of the energy storage technologies based on their power capacity and discharge time, adopted from[1].

Rechargeable ion batteries relay on the concept of ionic shuttling between cathode and anode through a solid or liquid electrolyte with the energy stored and released due to the different electrochemical potential between electrodes.[34] The anode, as one important component in rechargeable ion batteries, strongly affects the battery performance. Carbon based materials offer high specific capacity and cycling stability and are currently the most commonly used anodes in the rechargeable ion batteries. However, the need of higher energy density trigger intensive research of anode materials as there is still large room for improvement towards a higher weight and volume energy densities. Based on the reaction mechanism of the anodes, they can be grouped into three categories including intercalation reaction anodes, alloy reaction anodes and conversion reaction anodes. Among them, the conversion reaction anode materials exhibit a higher specific capacity (compared with intercalation reaction anodes) and higher cycling stability (compared with the alloy reaction anodes), thus obtained wide attention in recent years.[35] Understanding the reaction mechanism including the ion diffusion processes, electrochemical reaction products and the role of the constituting elements (in the multi-cations materials) is vital for the materials designing and optimization. However, characterization of the conversion reaction anodes after battery cycling is more complicated compared with intercalation and alloy reaction materials due to the large amount of amorphous products formed, which restricts the clarification of the reaction mechanism. The difficult characterization originates from the limitations of traditional characterization techniques. Conventional TEM measurements, such as SAED and HRTEM, and XRD are not capable to provide structural information on the amorphous products. Although many characterization techniques, such as X-ray absorption spectroscopy (XAS), nuclear magnetic resonance spectroscopy (NMR) and X-ray photoelectron spectroscopy (XPS), can provide bonding information directly or indirectly and are widely used for studying electrode materials, a characterization with sub-nanometer spatial resolution, such as grain boundaries and phase interfaces, cannot be provide by these bulk techniques. Modern transmission electron microscopes equipped with various imaging and analytical techniques are ideal characterization tools for the chemical composition, structural information and valence states with nanometer level resolution. Therefore, the aim of this thesis is to understand the fundamental ion migration processes in conversion reaction anodes during battery cycling using TEM techniques assisted by bulk information from measurements including XRD, XAS, electrochemical testing.

Metal oxides (MOs) and transition-metal dichalcogenides (TMDs) as typical conversion reaction anodes for LIBs and SIBs were intensively studied in past two decades as alternative anodes for the next generation high energy density rechargeable ion batteries.[36–39] Two state-of-art MO and TMD type materials, high entropy oxide (HEO) $(Co_{0.2}Cu_{0.2}Mg_{0.2}Ni_{0.2}Zn_{0.2})O$ and MoS_2/C composites, were selected to study the electrochemical cycling. Revealing the reaction mechanism is not only beneficial for better understanding the two materials, but it can be used for materials optimization and to design new materials. In this chapter, a brief history of rechargeable ion batteries, their basic concepts and working

principles will be introduced. This will be followed by a review of the different classes of cathode and anode materials, including the currently employed commercial ones and ongoing research in developing next generation high energy density batteries. A brief overview of the contribution of TEM measurements on elucidating battery reaction mechanisms and material properties is given at the end of the introduction chapter. The fundamental principles of the characterization techniques used in this thesis are presented in the second chapter. Following that the detailed research results are presented in three experimental chapters.

1.2. Rechargeable batteries

The idea of rechargeable ion batteries was first applied by Michel Armand in LIBs that use the migration of lithium ions between two intercalation electrodes operating at different potentials. As shown in Figure 1-2 a typical rechargeable liquid battery can be divided into five major components: current collectors, cathode electrode, separator, anode electrode and electrolyte. The separator and the liquid electrolyte are replaced by a solid electrolyte in all-solid-state batteries. For the electrodes, both cathode and anode, binder and conductive additives are necessary to be added in order to facilitate the contact with the current collectors and the electrical and ionic connection between electrochemically active particles. During cycling, redox reactions are taking place at cathode and anode with Li^+ ions transferred between the two counter electrodes through the electrolyte/separator. At the same time, the electrons shuttle through the external circuit. Based on the concept summarized above, various kinds of alkali metal batteries including LIBs[40–44], SIBs[45–49] and potassium ion batteries (PIBs)[50–54] and some more exotic system, such as aluminum ion batteries (AIBs)[55–58] and magnesium ion batteries (MIBs)[59–63], have been developed in the past several decades. Among them, LIBs have become the battery used in virtually all important applications due to their strong advantages compared with other ion batteries. These advantages include a high discharge voltage, stable long term cycling, and high energy density. Since the first commercialized LIBs using $LiCoO_2$ and graphite as cathode and anode materials were launched by Sony in the 90s, LIBs have rapidly developed and nowadays are an indispensable technology for our modern way of life. The principle reaction is schematically shown in Figure 1-2:

Cathode: $LiCoO_2 \rightleftharpoons Li_{1-n}CoO_2 + nLi^+ + ne^-$ *1-1*

Anode: $C_6 + nLi^+ + ne^- \rightleftharpoons Li_nC_6$ *1-2*

Cell reaction: $LiCoO_2 + C_6 \rightleftharpoons Li_nC_6 + Li_{1-n}CoO_2$ *1-3*

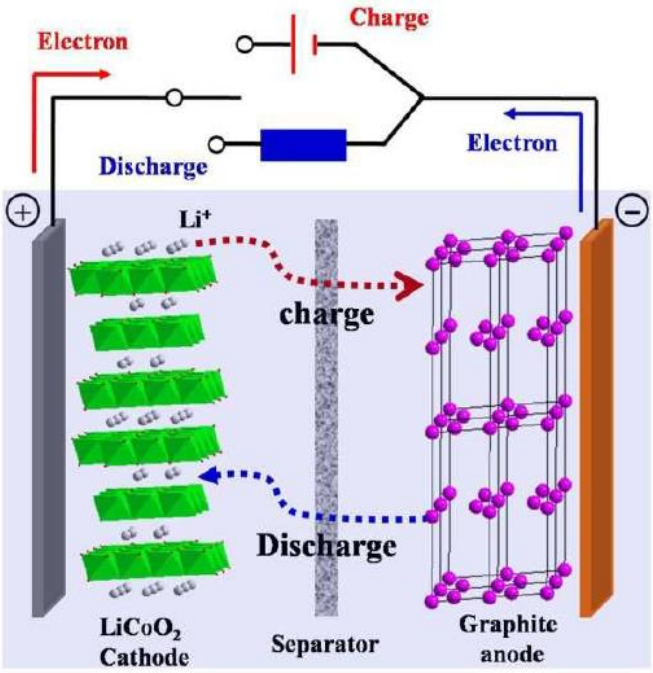

Figure 1-2: components of a rechargeable Li-ion battery. In this schematic, $LiCoO_2$ and graphite are used as cathode and anode materials, respectively. An electronically insulated separator is mounted between the electrodes. During battery cycling, the lithium ion shuttle between cathode and anode through the electrolyte along with the transfer of electron in the external circuit, adopted from reference[64].

1.3. Cathode materials

The electrode materials employed in LIBs have been greatly diversified and include novel materials targeting higher energy density, steady cycling, low cost and environmentally friendly materials and technologies. After the successful commercialization of $LiCoO_2$, olivine $LiFePO_4$, layered $LiNi_xCo_yMn_{1-x-y}O_2$ (NMC), and spinel $LiMn_2O_4$ were commercialized in recent years. All of these commercial cathode materials have a high theoretical specific capacity, i.e., $LiCoO_2$ (274 mAh/g), $LiFePO_4$ (170 mAh/g), NMC (278 mAh/g, calculated for $LiNi_{1/3}Co_{1/3}Mn_{1/3}O_2$), and $LiMn_2O_4$ (148 mAh/g). However, their practical capacity varies between 100 to 180 mAh/g.[65] The excellent long cycling performance, low cost, and high safety levels are the main advantages of $LiFePO_4$ based materials, which are widely used in EV technology. [66–69] Using the redox reaction of Fe^{2+}/Fe^{3+} during battery reaction, the cycle life of $LiFePO_4$ reaches beyond 2000 times at a current corresponding to 0.2C with a stable operating voltage of 3.0 to 3.3 V. However, the rate performance is limited by the 1D lithium ion transport path in the olivine structure (Figure 1-3) and its inherent low electric conductivity. In addition, the poor tapped density (only about 1.3 g/cm^3)[70] compared with the commercial $LiCoO_2$ (about 3.9 g/cm^3)[71] makes it difficult to be used in portable electronics. Ternary NMC materials, which are isostructural with the layered oxide $LiCoO_2$ (Figure 1-3), received much attention and reached a record high of 90% global market share of electric vehicle batteries in 2019.[72] Compared with $LiCoO_2$ cathodes, NMC materials corresponding to a composition of $LiNi_xCo_yMn_{1-x-y}O_2$ ($0< x, y< 1$)[73–76] show superior properties due to their competitive

electrochemical performance, lower cost and being more environmentally friendly due to the lower Co content. In NMCs, nickel, cobalt and manganese have their specific functions, e.g. nickel increases the specific capacity, the cobalt concentration is beneficial for the electric conductivity and manganese is important for the structural stability during battery cycling.[65] The nickel rich NMC materials are believed to be the future LIB cathode materials, as with an increasing nickel concertation higher specific capacities can be achieved and a lower amount of the expensive and toxic cobalt would need to be used.[77] However, due to the similar ionic radius of lithium and nickel atoms, a significant Li/Ni mixing occurs during synthesis and is enhanced during cycling which increases at higher nickel concentrations. Spinel type $LiMn_2O_4$ is another commercialized SIB cathode material with fast ion diffusion due to its 3D ion transport paths (Figure 1-3) and high operation voltage.[78,79] However, it suffers from a low cycle stability due to the well-known Jahn-Teller effect of manganese.[65] Lithium rich materials have also been regarded as promising next generation LIB cathode materials due to their practical capacity exceeding 250 mAh/g.[80–83] However, the unsolved problem of fast capacity fading caused by the microstructural degeneration during cycling still needs to be solved before it can be used commercially.

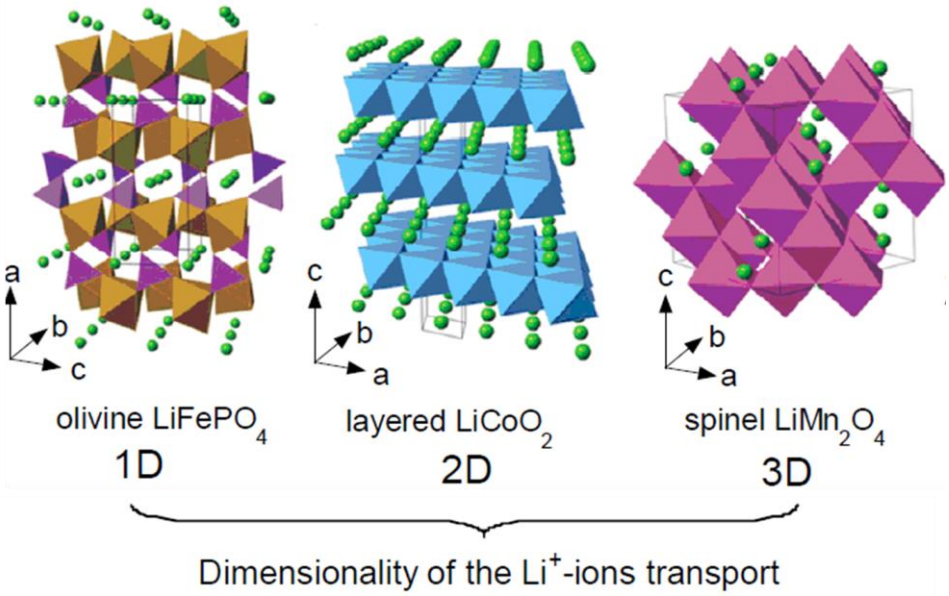

Figure 1-3: Crystal structure of the three lithium-insertion compounds in which the Li ions are mobile through the 1-D (olivine), 2-D (layered) and 3-D (spinel) frameworks, modified from reference[84].

Although LIBs can be regarded as a revolutionary invention, an ever increasing energy storage demand has led to a rise of production costs. Moreover, lithium reserves are unevenly distributed around the globe and the resources are very limited compared with other elements that could be used in rechargeable batteries. Sodium is a member of the same period and has similar chemical and physical properties as lithium, e.g. charge and electrical potential. Therefore, the development of SIBs seems to be a fairly straightforward idea because of the lower cost and higher availability of sodium and its acceptable electrochemical properties. Similar to LIBs, layered oxides[85–89] and prussian blue and its

analogs (PBAs)[90–92], are the most commonly used cathode materials in SIBs. Both types of materials have been considered for commercial application.[93] P2 type, O3 type and some multiphase P/O composite materials, e.g. P2/O3, P2/P3 and P2/O3/O1, have been intensively investigated due to the high theoretical specific capacity and low cost, where P (prismatic) and O (octahedral) represent the sodium sites in the layers and the number reflects the number of layers in one unit cell. The structure of some typical layered oxide SIB cathode materials are shown in Figure 1-4a. Both P and O type layered oxide materials undergo complicated phase transitions during cycling, which results in capacity fading.[93] Although the cycling stability can be enhanced to some extent using special strategies, such as doping the layered oxide materials with electrochemically inactive transition metals[94–97] and designing multiphase composite materials[98,99], the limited cycle life is still the main barrier for their commercial application. PBAs formulated as $(A_xM[M'(CN)_6]_{(1-y)} \cdot \square_y \cdot nH_2O$; with A alkali metal, M N-coordinated transition metal ion, M′ C-coordinated transition metal ion, and □ vacancy occupied by coordinating water; $0 \leqslant x \leqslant 2$, $0 \leqslant y < 1$), show high cycling stability and stable operation voltage. Amperex Technology Co. Limited announced that they will introduce the first generation commercial SIBs, where Prussian white (a high sodium content PBA) will be used as cathode material. However, the water content present in the PBA materials is the biggest problem for their large scale application. Water exists in three kinds of forms within the PBA framework, adsorbed water on the surface, zeolitic water on the interstitial sites and coordinated water bonded to metal ions, which not only reduce the specific capacity but also block the sodium diffusion path. Coarsening of the particles, dehydration of the PBA samples, and introduction of more alkaline ions into the framework are commonly used to reduce the aforementioned water.[100]

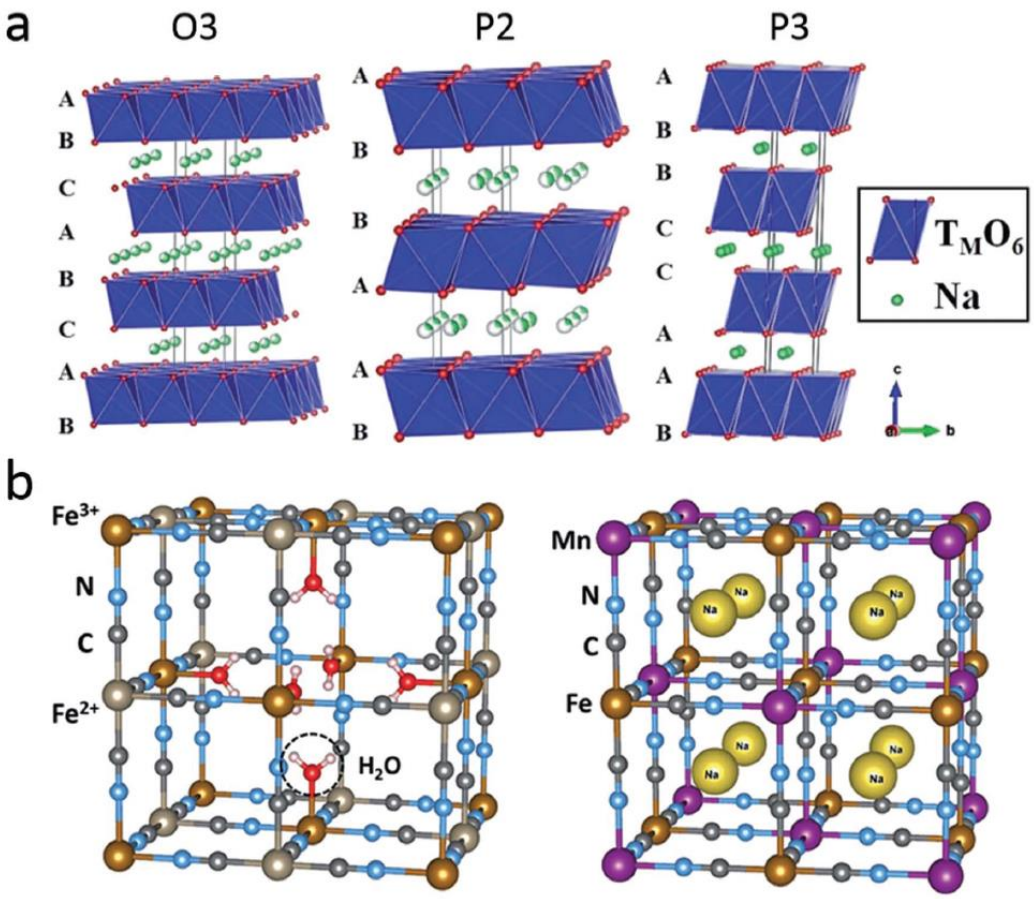

Figure 1-4: **a**) crystal structure schematics of layered Na_xMO_2: **b)** PB ($Fe_4[Fe(CN)_6]_3 \cdot nH_2O$) and typical PBAs ($Na_xMnFe(CN)_6$), modified from reference[93].

1.4. Anode materials

As mentioned above, the anode is one of the most important parts in a battery system, which affects the capacity, the energy density and the rate performance of batteries together with the cathode and the electrolyte. Carbon based materials are still the mainstream anode materials for LIBs. However, to meet the rapidly increasing needs for high energy density, novel anode materials are designed with promising prospects for next generation LIBs and SIBs. Depending on their de/lithiation (sodiation/desodiation) reaction mechanism, anode electrode materials are typically classified as intercalation type [101–104], alloying type [105–108] or conversion type anodes [109–112].

Carbons can be roughly grouped into three categories, graphitic carbon (soft carbon), disordered carbon (hard carbon) and nanostructured carbon. Graphitic carbons are the typical intercalation anode materials used currently in commercial LIBs, in which the Li^+ can be de/intercalated repeatedly between the graphitic layers.[113–116] In graphite, the sp^2 hybridized graphene layers are linked by van der Waals forces and π-π bonds in the sequence ABAB or ABCABC forming the hexagonal and rhombohedral structure (Figure 1-5a). During lithiation, at the potential range of 0.1 to 0.2 V the AA packing lithium-intercalated graphitic compounds (Figure 1-5b) form and offer a theory capacity of 372 mAh/g, calculated

using the formation of LiC_6. Although the practical capacity has already approach the theoretical capacity, compared to other newly proposed anodes it is still low. Much higher capacities have already been obtained using disordered or nanostructured carbon materials. Matsumura et al. suggested that not only the space between and the edges of the graphitic layers, but also the exposed crystallite surfaces can be used to store Li species.[117] It has also been speculated that all interstitial sites in carbon nanotubes, e.g. the inter-sheet van der Waals spaces, inter-tube channels and inner cores are accessible for lithium intercalation, as single walled carbon nanotubes have been proven to exhibit a capacity of more than 1000 mAh/g as LIBs anode.[118] Different from LIBs, graphitic carbon cannot be used as anode material in SIBs due to the larger ionic radius of sodium.[119] However, disordered and nanostructured carbon materials exhibit reasonable capabilities and have been intensively studied in SIBs.[120–122] Li et al. reported that porous nitrogen doped carbon spheres can deliver about 200 mAh/g capacity after 600 cycles using a current of 200 mA/g and show excellent rate performance, so that a capacity of 155 mAh/g was obtained at an ultra-high current of 1 A/g.[120]

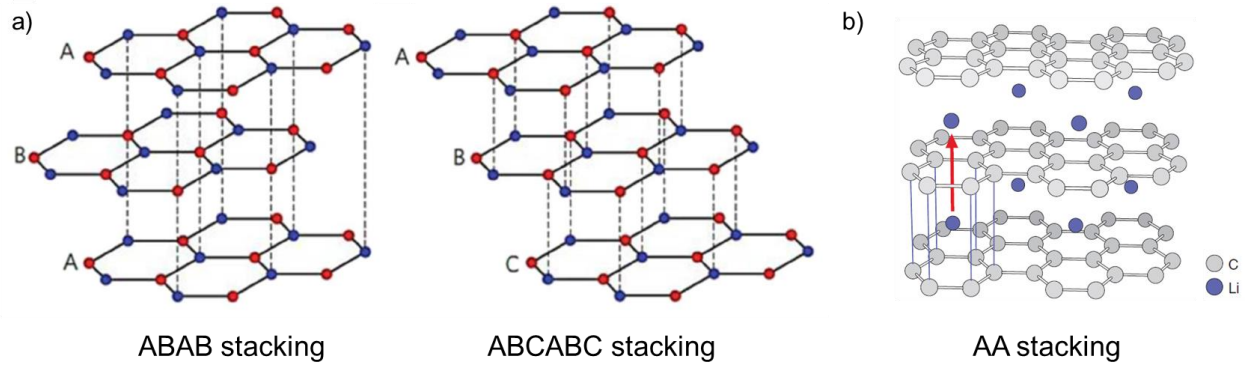

Figure 1-5: **a)** schematic representation of the stacking sequence in graphitic carbons, modified from reference[123]; **b)** schematic of AA stacking of graphite after lithiation, adopted from reference[124].

In addition to carbon based anodes, some other intercalation materials show promising prospects as anodes, e.g. MoO_2[125,126] and TiO_2[127,128]. TiO_2 as a near-zero strain material has been widely reported as intercalation host for lithium/sodium ions.[127,128] Wu et al. reported that N-doped carbon coated TiO_2 exhibited a remarkably high capacity of 462 mAh/g after 300 cycles in LIBs using a current of 0.5 A/g.[128] The capacity is not substantially higher than that of graphite anodes in LIBs, but the high tapped density (4.23 g/cm^3) compared with graphite (0.97 g/cm^3) is a major advantage considering the volumetric energy density, which is another important performance indicator, especially for batteries for portable electronics. Although the aforementioned single-wall carbon nanotubes can deliver more than 1000 mAh/g capacity, nanostructuring the active material is sacrificing tapped density. Wu et al. also explored the electrochemical performance of TiO_2 in SIBs. The N-doped carbon coated TiO_2 showed a capacity of 140 mAh/g after 400 cycles at a current density of 1 A/g.[128]

Compared with intercalation materials, alloying and conversion reactions result in a higher capacity due to multi-electron transfer. For instance, an ultrahigh theoretical capacity of 4200 mAh/g ($Li_{22}Si_5$) and 2600 mAh/g (Na_3P) can be obtained for silicon and phosphorus anodes in LIBs and SIBs. However, the high capacity means that large amounts of lithium/sodium ions are transferred into the anode, which results in an extensive volume expansion, e.g. the volume expansion can reach 400% in Si anodes in LIBs.[129] The volume expansion during cycling will destroy the connections between active particles and thus leads to the formation of dead volume within the anode resulting in capacity fading. Furthermore, breaking of silicon particles lead to SEI generation at the new surface, resulting in low columbic efficiency and further volume expansion. In addition, the low electric and ionic conductivity limits the rate performance of silicon anodes. Designing Si/C composites is one strategy to tackle the above problem. Here, silicon acts as active material to provide capacity and the carbon is used to buffer the huge volume expansion of Si. Meanwhile, the high electric and ionic conductivity can improve the rate performance. Encapsulated structures such as core-shell or yolk-shell structures and embedded structures (nano-size silicon embedded in a continuous carbon matrix) are two commonly used structures for Si/C composites.[130] Figure 1-6 shows a comparison of the reaction mechanism of silicon particles, Si/C core-shell particles and Si/C yolk-shell particles. Compared with bare silicon, the core-shell structure (Figure 1-6b) can mitigate the cracking and crushing of silicon and improve the conductivity. The yolk-shell structure is inspired by the core-shell structure, but a void space exist between the silicon core and carbon shell (Figure 1-6c). After careful design and accommodation, state-of-art Si@C yolk-shell composite can exhibit an ultrahigh initial capacity of about 2800 mAh/g at 0.1 C and a 76% capacity retention after 1000 cycles.[131] The low cost of the raw materials and the excellent performance makes these Si/C composite excellent candidates for LIB anodes. Increasing the amount of carbon and/or of voids results in a more stable cycling behavior, but also results in a lower capacity and tapped density. Nanostructures that are designed to compensate for the above presented drawbacks can be very beneficial for the electrochemical performance, but also increases the cost of production.

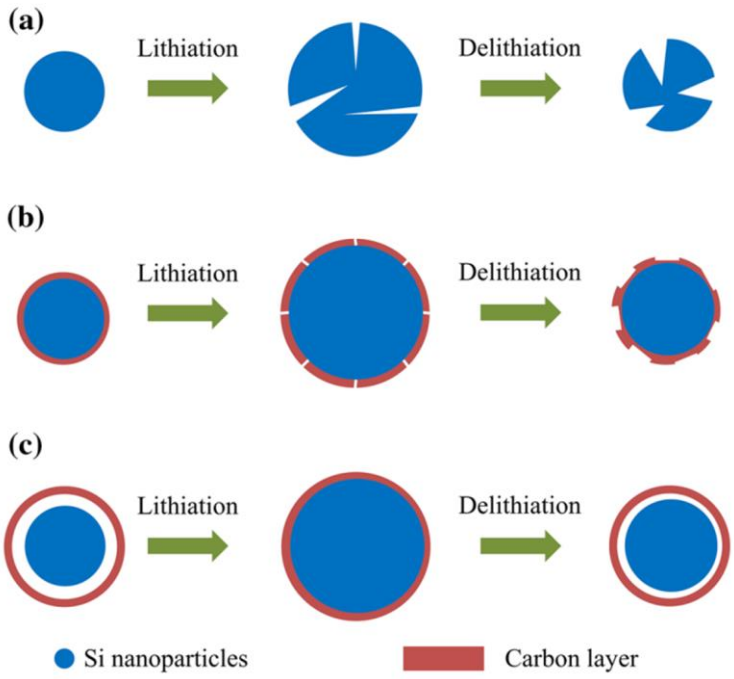

Figure 1-6: Reaction mechanism comparison of three types of Si and Si/C composites. **a)** Si particles; **b)** Si/C core-shell structure; **c)** Si/C yolk-shell structure, modified from reference[130].

Metal oxides used as conversion materials are regarded as another promising candidate for next generation anode materials because of their high theoretical capacity, stable battery cycling performance and high tapped density. However, the low electrical conductivity is one of the main obstacles for their commercial application.[35,132–134] Various metal oxides were explored as anode materials, such as CoO, NiO and ZnO, and show high specific capacity and stable cycling behavior. K. Bindumadhavan et al. reported on CoO/reduced graphene oxide hybrids with ultrafine CoO nanoparticles of 4–6 nm homogenously loaded on a reduced graphene oxide network.[135] The composite exhibited an ultra-high capacity of 900 mAh/g at 150 mA/g after 60 cycles. The egg shell-yolk NiO/C porous composite was also proven to deliver outstanding performance in LIBs where about 600 mAh/g capacity could be retained after 100 cycles at a current density of 100 mA/g.[136] However, the nanostructuring approach reduces the tapped density of materials and increase the production cost. Recently, the concept of high entropy was applied to metal oxides used as anode materials for lithium ion batteries, and they showed excellent battery performance.[137–140] As another type of conversion material, transition-metal dichalcogenides (TMDs) have been widely investigated. Their composition can be described as MX_2, where M represents a transition metal from group 4 to 6 (Ti, V,and Mo, etc.) and X is a chalcogen (S, Se and Te). These materials exhibit promising prospects for the application in LIBs and SIBs with high capacity and fast ion conduction compared with carbon-based materials.[141–143] An MoS_2/WS_2 nitrogen doped graphene composite exhibited about 1200 mAh/g capacity at 100 mA/g in LIBs and showed a good cycling stability with 99.8% retention after 100 cycles.[144] A reversible capacity of 590 mAh/g using a current of 50 mA/g has been also achieved for MoS_2 in SIBs.[145]

Unlike the intercalation and alloying anode materials where the reaction mechanisms are relative straightforward, understanding the mechanisms of conversion reactions is more difficult due to the multitude of disordered products typically obtained after cycling. HEOs exhibit interesting prospects, but the reaction mechanisms are still unclear. Moreover, although MoS_2 was applied in lithium and sodium storage for more than 20 years, a clear understanding for sodiation/desodiation mechanism is still lacking. As this thesis is aiming to clarify the reaction mechanisms in HEO and MoS_2, among others, the detailed background of this two type materials will be given in following sections.

1.4.1. High entropy oxides

The high entropy concept for material design received increasing attention after the discovery of high entropy alloys (HEA) by Yeh at al. in 2004.[146] The introduction of HEOs (also named entropy stabilized oxides) in analogy to HEAs, has created a strong excitement in the materials community.[147] The Gibbs free energy (ΔG) of a system, $\Delta G = \Delta H - T\Delta S$, is determined by the enthalpy (ΔH) and the entropy (ΔS), and a single phase reaction is thermodynamically only feasible when ΔG of the reaction is negative. In contrast to low entropy materials, where ΔG is mainly affected by enthalpy, in high entropy materials the large configurational entropy plays an important role and drives the structure to form a single solid solution at sufficiently high temperatures. Synthesizing entropy stabilized oxides is possible by a simple calcination of a mixture of different elements at high temperature (T), where the entropy becomes the dominant term determining the total Gibbs free energy.[148,149] The configurational entropy reaches a maximum when metal atoms randomly occupy the lattice sites with equal ratio. To maintain the structure requires quenching of the sample at high temperatures to prevent phase separation as the positive enthalpy becomes the main factor again at low temperature. This is shown in Figure 1-7a for the synthesis of single phase $(Co_{0.2}Cu_{0.2}Mg_{0.2}Ni_{0.2}Zn_{0.2})O$, which can only be obtained by quenching, otherwise phase separation will occur during slow cooling. The homogeneous elemental distribution in HEO materials synthetized by fast quenching has been proven experimentally. For instance, STEM-EDX elemental mapping revealed that in the perovskite type $(Gd_{0.2}La_{0.2}Nd_{0.2}Sm_{0.2}Y_{0.2})(Co_{0.2}Cr_{0.2}Fe_{0.2}Mn_{0.2}Ni_{0.2})O_3$ HEO, the rare earth elements (Gd, La, Nd, Sm and Y) are distributed homogeneously on the A sites and the transition metals (Co, Cr, Fe, Mn, Ni) on the B sites (Figure 1-7b to 3d).[150] In such a highly disordered but homogeneous crystalline single phase, the large configurational entropy caused by the disordered cation mixing is considered to result in new relationships between composition, phase stability, and reactivity, potentially in combination with further synergistic effects between different cations, making it possible to develop special functional properties.[151–153]

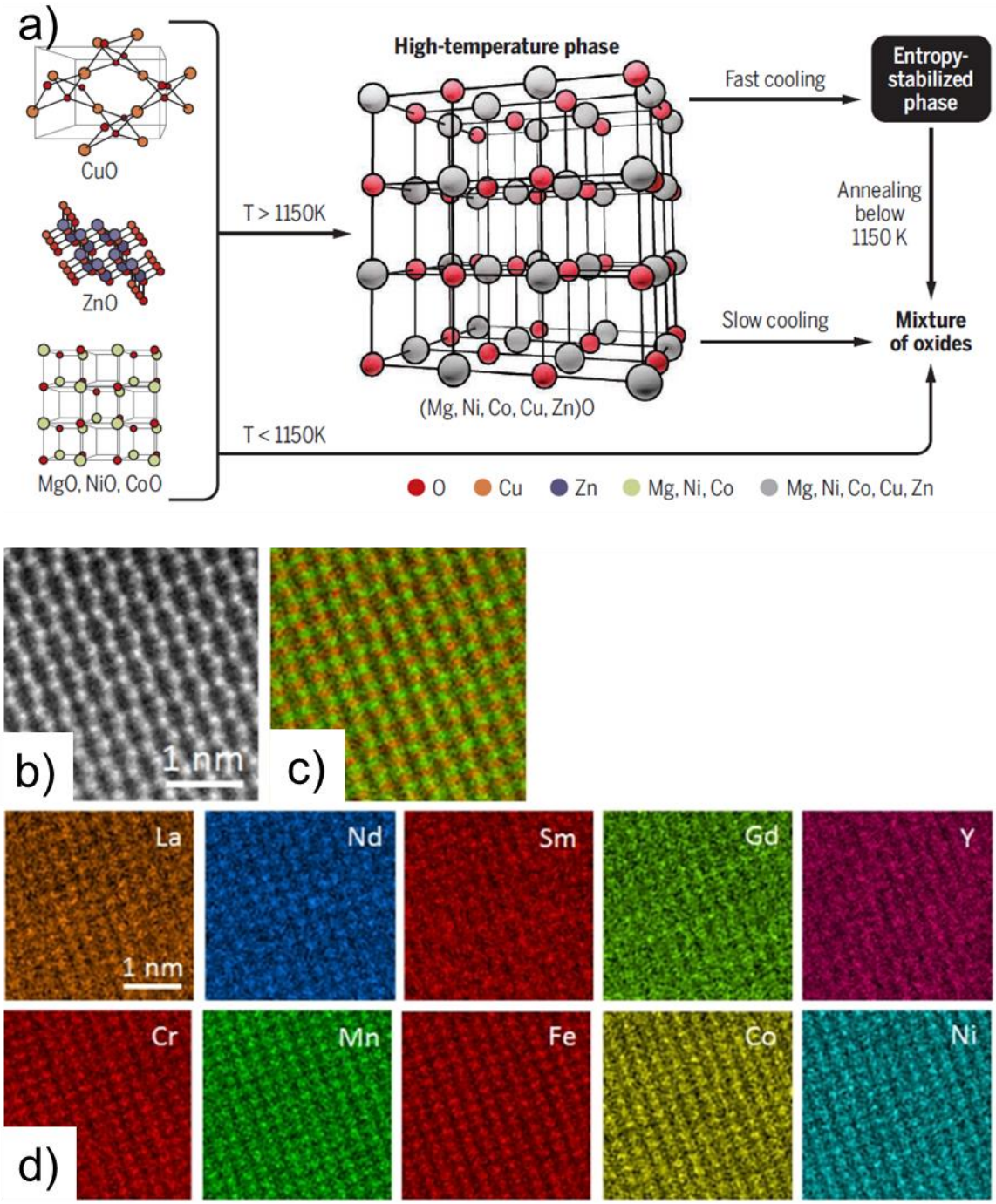

Figure 1-7: **a)** schematic representation of the heat treatment temperature and cooling conditions influence on the HEO phase formation, adopted from reference [148]; **b)** to **d)** atomic resolution STEM-EDX and elemental mapping of perovskite type $(Gd_{0.2}La_{0.2}Nd_{0.2}Sm_{0.2}Y_{0.2})(Co_{0.2}Cr_{0.2}Fe_{0.2}Mn_{0.2}Ni_{0.2})O_3$. The color mixed map (**c)**) shows in green the A sites (upper row in **d)**) and in red the B sites (lower row in **d)**), adopted from reference [150].

In the energy storage field, high entropy oxides (HEOs)[137,138,140,154–159] and high entropy oxyfluorides (HEFs)[160–163] that can be used both as anodes and cathodes depending on the metal ions incorporated, showed promising results indicating that entropy and synergistic effects could play a key role to stabilize materials during battery cycling. For example, a high lithium ion conductivity of

$(Co_{0.2}Cu_{0.2}Mg_{0.2}Ni_{0.2}Zn_{0.2})O$, exceeding 10^{-3} S cm^{-1} at room temperature, was revealed by D. Berardan et al.[157] Together with the known high capacity of metal oxides, this high lithium ion conductivity implies the material could be a promising candidate for application in energy storage systems acting as anode materials. This was confirmed by S. Abhishek at al. who successfully used $(Co_{0.2}Cu_{0.2}Mg_{0.2}Ni_{0.2}Zn_{0.2})O$ in LIBs and achieved excellent electrochemical performance as shown in Figure 1-8a and 8b.[159] At a current of 200 mA/g, the HEO could deliver about 500 mAh/g capacity and showed almost no capacity fading after 300 cycles. A quasi-conversion reaction of the metal oxide/metal and lithium oxide was proposed as the reaction mechanism. The excellent battery performance of $(Co_{0.2}Cu_{0.2}Mg_{0.2}Ni_{0.2}Zn_{0.2})O$ was also demonstrated in a full-battery system using NCM111 as cathode (as shown in Figure 1-8c).[140] A spinel structure $(Mg_{0.2}Ti_{0.2}Zn_{0.2}Cu0.2Fe_{0.2})_3O_4$ anode material was also successfully synthesized using high-energy ball milling.[137] Acting as anode material in a LIB, it could deliver more 250 mAh/g capacity at an ultra-high current density of 2000 mA/g with almost no capacity fading after 800 cycles (Figure 1-8d). The superior cycling stability and fast reaction kinetics of HEOs were attributed to the high entropy effect that could stabilize the structure and provide a single solid solution phase enabling the ion transportation.[160,164] However, as we introduced previously (see Figure 1-7) the HEOs need to be synthesized at high temperature to overcome the enthalpy of mixing but the batteries are cycled at room temperature. This suggests that reestablishing the initial HEO structure could be impossible during battery cycling at room temperature. Therefore, the entropy effect is not enough to explain the excellent battery performance. The 'cocktail effect' or 'synergetic effect' among different metal elements was mentioned in various studies of the HEO materials, and was proposed to be responsible for the excellent battery performance. [164–167] The primary benefit of multi-cations metal oxides consists of higher electric conductivity than the binary metal oxides due to the lower activation energy for electron transfer between cations.[168–170] In addition, the 'cocktail effect' was frequently observed in the multi-cations metal oxides. For instance, different metal elements have diverse expansion coefficients while reacting with Li ions. The lower expansion coefficient and stabilizing inactive elements provide a mechanical buffer to relieve the volume changing during battery reaction.[171–173] More significantly, in a complex elemental environment there are more possibilities of improving battery performance. The reaction mechanism of $Ni_{0.9}Zn_{0.1}O$ was verified to be different from that of individual NiO/ZnO and that of their mixture, with the $Ni_{0.9}Zn_{0.1}$ alloy phase partially contributing to the system capacity.[174] Moreover, the self-built up NiO and Sn matrix during battery cycling was demonstrated to be responsible for excellent battery performance of $NiSnO_3$ anode in LIBs.[175] HEOs combine the properties of diverse cations and provide more possibilities for improving battery performance in the complex elemental environment, i.e. the 'cocktail effect'. However, a clear understanding of 'cocktail effect' is still missing in the previous studies and further investigations are required. Clarifying the contribution to the 'cocktail effect' among different metal elements would be helpful for the designing of multi-cations battery electrode materials.

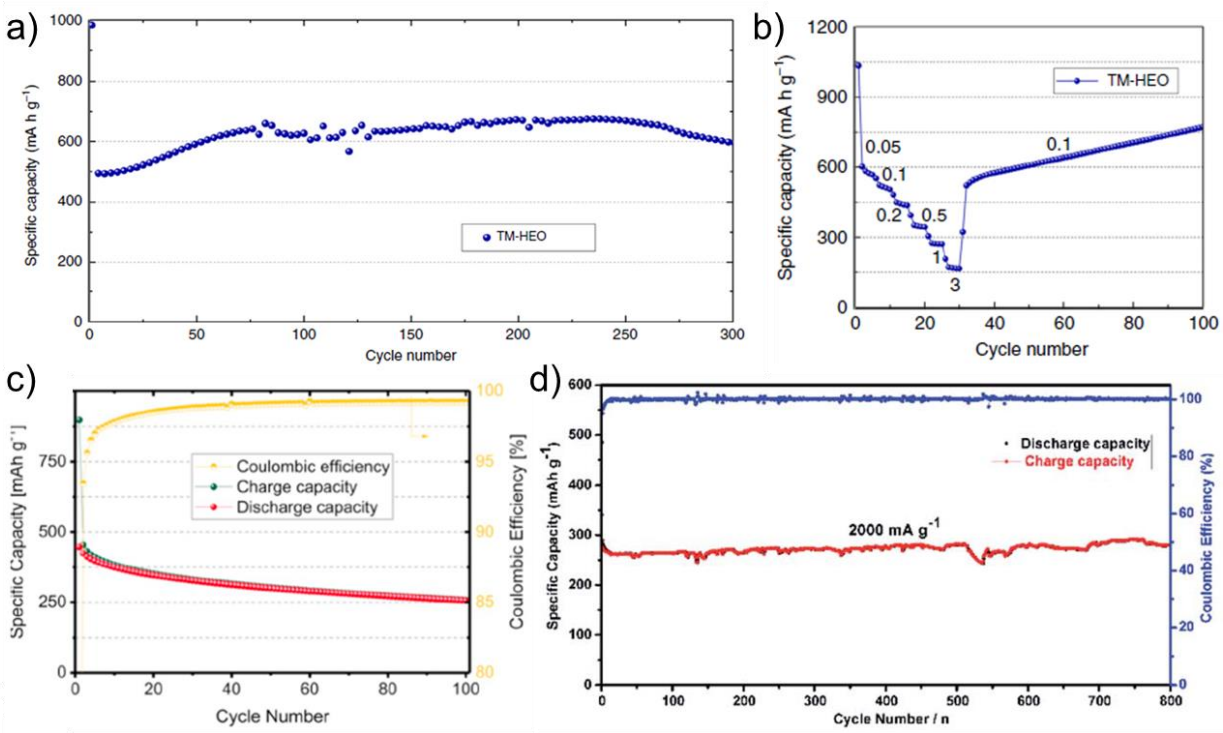

Figure 1-8: the battery performance of HEOs as LIBs anode materials. **a)** the long-term cycling performance of HEO $(Co_{0.2}Cu_{0.2}Mg_{0.2}Ni_{0.2}Zn_{0.2})O$ at 200mA/g, adopted from[159]; **b)** the rate performance of HEO $(Co_{0.2}Cu_{0.2}Mg_{0.2}Ni_{0.2}Zn_{0.2})O$, adopted from [159]; **c)** the cycling performance of the full-battery using HEO $(Co_{0.2}Cu_{0.2}Mg_{0.2}Ni_{0.2}Zn_{0.2})O$ as anode, adopted from[140]; **d)** cycling performance of $(Mg_{0.2}Ti_{0.2}Zn_{0.2}Cu0.2Fe_{0.2})_3O_4$ at 2000 mA/g, adopted from[139].

1.4.2. Molybdenum disulfide

MoS_2, as a member of transition-metal dichalcogenides (TMDs), exhibits promising properties for application in both lithium and sodium ion batteries.[141–143] Compared with common anode materials like carbon-based structures and transition metal oxides, MoS_2 has the advantage of high electrochemical capacity and rate performance.[176–179] It has been reported that a composite of MoS_2 with graphene nanosheets can deliver a capacity as high as 1290 mAh/g, as shown in Figure 1-9a.[180] A capacity of 1040 mAh/g can still be retained even at a high current density of 1000 mA/g. Moreover, MoS_2 exhibits the same remarkable properties when used in SIBs. MoS_2 nanosheets/reduced graphene oxide/hollow carbon spheres (MoS_2-rGO/HCS) delivers about 1000 mAh/g and 750 mAh/g capacity at a current density of 100 mA/g and 2000 mA/g with a stable cycling performance as shown in Figure 1-9.[181]

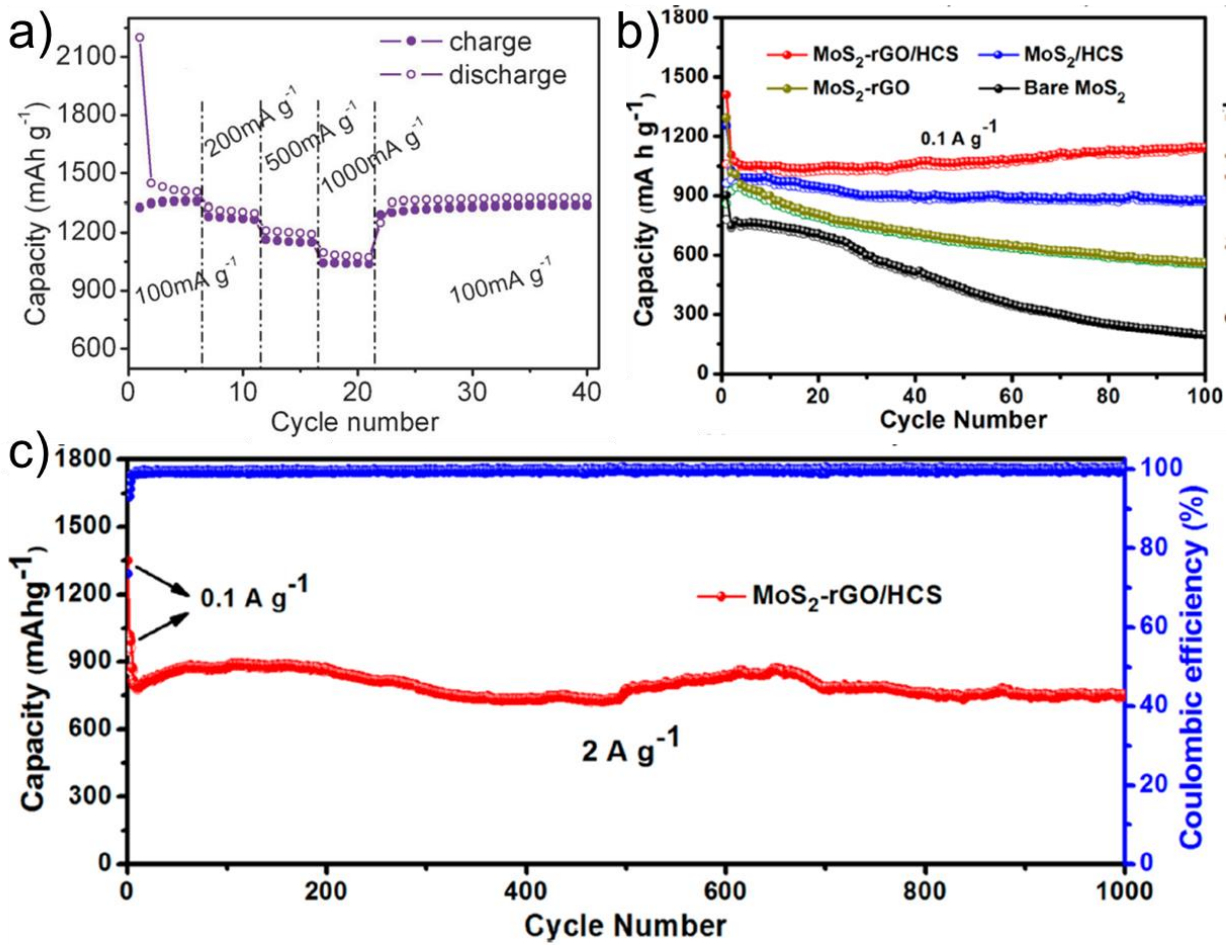

Figure 1-9: lithium and sodium battery performance of MoS_2 based composites. **a)** cycling behavior of MoS_2/GNS at various current densities, adopted from[180]; **b)** cycling performance comparison of MoS_2-rGO/HCS, MoS_2/HCS, MoS_2/rGO and bare MoS_2 materials; **c)** long-term cycle performance of MoS_2-rGO/HCS at the current 2000 mA/g. The **b)** and **c)** are adopted from[181].

Similar to other TMDs materials, MoS_2 exist in many different polymorphs, such as 2H, 1T, 3R, 1T', 1T''.[141,182–184] With a trigonal prismatic coordination MoS_6 units, the layers show ABAB and ABCABC stacking in the 2H and 3R structures.[141,185] In the 1T structure, the MoS_6 units change the coordination symmetry to octahedral and show an AAA stacking pattern. [186] Although the stacking patterns and MoS_6 unit symmetry are different in the above three MoS_2 polymorphs, the direct Mo-S and Mo-S-Mo/S-Mo-S bonds show constant distance in all structure. Except for those three structures, some distorted 1T structures were also found and termed as 1T', 1T'', 1T''' etc.[141,143] In these distorted T type structures, the Mo-S bond changes its length and leads to inhomogeneous Mo-S-Mo and S-Mo-S distances. Figure 1-10 shows the atomic arrangement for three of these polymorphs. Among them, the 2H MoS_2 has the best thermodynamic stability and is found in nature as the mineral molybdenite.[187,188] The T type MoS_2 was proven to be quite challenging to synthesize as pure bulk phase because of its inherent instability[143]. However, multiple studies have reported that the 2H structure could change to a 1T phase during lithiation and sodiation using various research methods including XRD, Raman spectroscopy and TEM.[145,189–

191] The phase transition between 2H and 1T was also demonstrated to be reversible during battery cycling.[142,192,193]The MoS_6 slabs shift and change the symmetry during the de/intercalation of alkali metal ions, which could lead to changes of the electric field between the MoS_6 slabs affecting the electric conductivity. However, the structural transition induced during the lithiation/sodiation processes is seldom reported because the products generated at the fully discharged state always show an amorphous structure.[143,182,186]

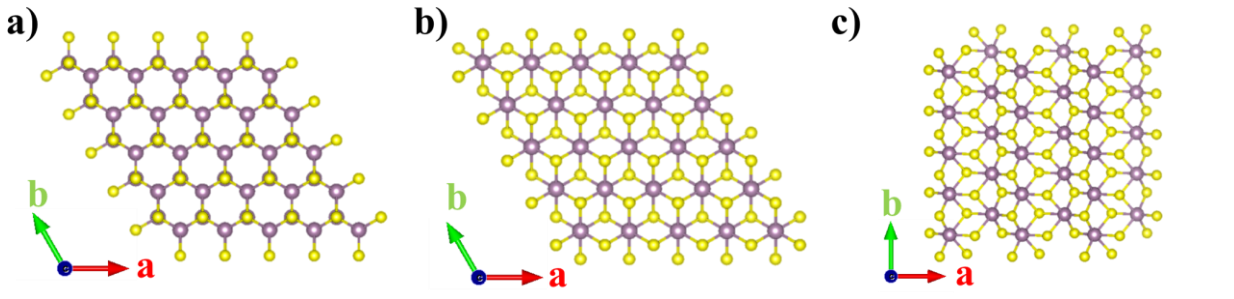

Figure 1-10: structural unit representation for the 2H (**a)**), 1T (**b)**) and 1T' (**c)**) polymorphs of MoS_2.

A few recent studies using HR(S)TEM measurements have identified the storage mechanism of MoS_2 in LIBs as conversion reaction type.[194,195] This was also verified by XAS results, in which the disappearance and reappearance of Mo-S shells can be clearly observed during the delithiation and lithiation processes.[196] Considering the similarities between LIBs and SIBs, MoS_2 was always thought of as a conversion material when used in sodium batteries. This speculation has been mainly supported by Raman measurements and some measurements of the crystalline structure by XRD and TEM. Raman data interpretation was based on the disappearance of specific peaks (E^1_{2g} and A_{2g} at about 380 and 400 cm^{-1}) of MoS_2 during the discharge process followed by its reemergence in the charge process indicating fracture and regeneration of the Mo-S bond, which was regarded as an indicator of the expected conversion reaction between MoS_2 and metallic Mo plus Na_2S.[193,197] In addition, HRTEM exhibiting a single type of lattice plane was also used as indicator for a conversion reaction. However, this interpretation is not necessarily the only explanation of the observations and thus the conversion model unambiguously confirmed. In general, characterization of the amorphous products in the MoS_2 battery system is not straightforward due to lack of long-range order, making the conventional imaging and diffraction analysis less reliable. Overall, the understanding of the reaction mechanism of MoS_2 in SIBs is still not clear. This would be highly beneficial for the overall understanding of these materials and for developing of novel strategies in material optimization and design.

1.5. Materials characterization in battery studies

A deeper understanding of the active materials, their transformations and interactions can be achieved by following their structural and chemical properties both in the bulk and locally at interfaces.

Due to their different inherent properties, materials face different problems when employed in batteries as active materials. For instance, oxygen release is one major concern for the safety of the NMC materials in LIBs and it's accompanied by structural degradation when the layered oxide structure is transformed to a rock salt phase.[198,199] This phenomena is also responsible for the capacity fading during battery cycling. Another example is the irreversible phase transition between the P type and O type structures, resulting in a reduced cycling stability of P and O type layer oxide cathodes in SIBs.[95,200] For most anode materials, their initial morphology is a crucial factor controlling their performance during battery cycling, as it has been shown that a properly designed morphology is e.g. beneficial for increasing reaction sites, decreasing ion and electron diffusion path length and avoiding severe volume expansion during lithiation/sodiation.[136,201] In addition, the characterization of electrode products forming during the conversion reactions is always difficult but very important for revealing the involved mechanisms. To study the different aspects in different materials, various characterization are needed. And the different techniques always need to be combined to interpret the scientific questions in battery reaction. Generally, we can classify the active material characterization into several categories, i.e. morphology studies, structure determination, phase distribution and valence state/bonding analysis.

1.5.1. Morphological characterization

For the active materials in a battery, the evolution of secondary and primary particle morphology, e.g. as described by their porosity and their contact surface, is a very important factor that affects the diffusion path length of ions and electrons in the electrochemical system. Moreover, morphological changes could be a first indicator for structural or compositional degradation during battery cycling. SEM and TEM are most commonly used to image the particle morphology of battery materials. As mentioned before, the particle morphology is an important parameter that can affect ion and electron transfer length and volumetric expansion during cycling. Nanostructuring the active material is a widely recognized method to shorten the ion and electron transfer length and avoid large volume expansion. Figure 1-11a shows a SEM image of bare Co_3O_4, which exhibits fast capacity fading during electrochemical testing with only about 200 mAh/g capacity retained after 100 cycles in a LIB.[201] However, after nanostructuring to produce a Co_3O_4/graphene composite, the material exhibits about 1200 mAh/g capacity after 100 cycles. Figure 1-11b displays the morphology of the Co_3O_4/graphene composite revealing a higher reaction surface and shorter reaction distances than the bare Co_3O_4. The formation of dead volume is regarded as another important reason leading to capacity fading in many conversion and alloy reaction anodes. Morphological observations are convenient and efficient way to follow this. Fig. 1-11c – left image shows the pristine state of an ordered mesoporous nickel oxide, in which 8–10 nm diameter nanorods are clearly visible. However, after 7 cycles (Figure 1-11c – right) a substantial SEI layer is coating the surface of cracked particles resulting in a loss of electric connectivity of the cracked particles on the material surface in the electrode. This phenomena could be one explanation the capacity fading in the conversion and alloy

reaction electrode materials. In addition, morphology observations are an effective method to characterize the reaction progression in *in-situ* experiments. E. R. Adkins et al. used *in-situ* TEM to study the lithiation and delithiation process in silicon oxide coated silicon nanowires.[202] A time series of the lithiation process is shown in Fig. 1-11d, where the volume expansion of the Si nanowires during lithiation can be clearly observed and proved that the mechanically robust silicon oxide shell could limit the extent of volume expansion caused by lithiation.

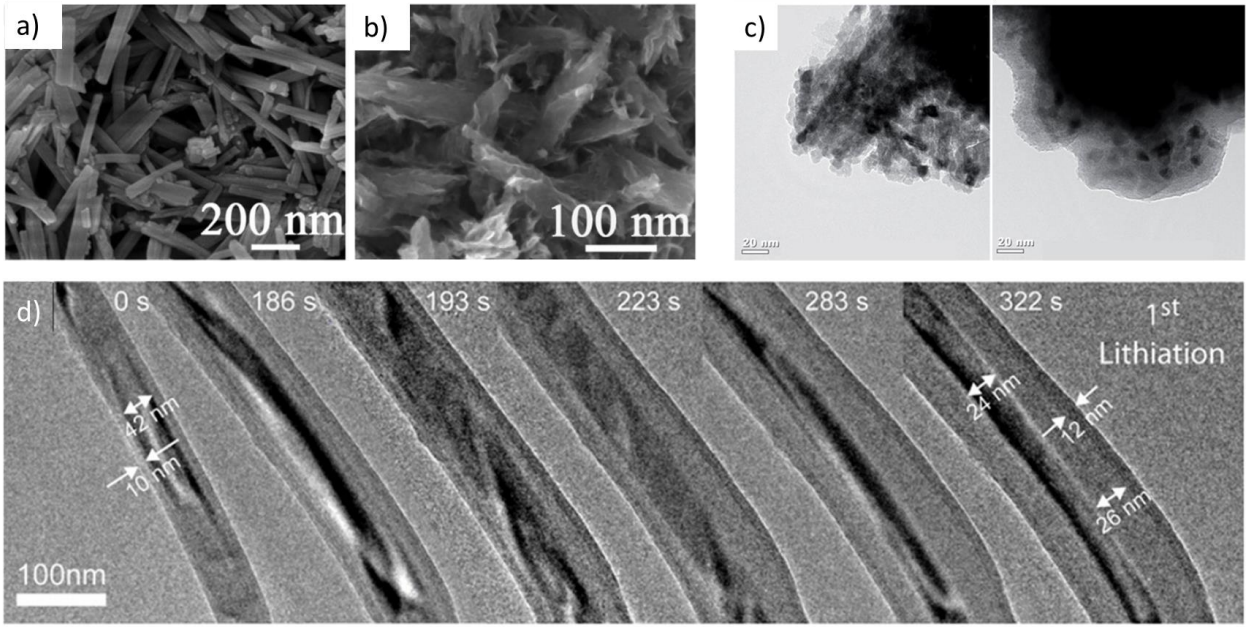

Figure 1-11: morphological and structural characterization of the battery materials by SEM and TEM. **a)** SEM image of ZnO@C nanoflower, modified from reference[203]; **b)** SnS nanoflowers, adopted from reference[204]; **c)** TEM imaging of OMNiO (ordered mesoporous nickel oxide) before cycling (left) and after 7 cycles, adopted from reference [205]; **d)** time-lapse of *in-situ* TEM imaging showing the lithiation process of the silicon oxide coated silicon nanowires, adopted from reference [202].

1.5.2. Structural characterization

Determining the crystal structure of pristine active materials and their evolution throughout the battery cycling is an important tool for understanding and improving the performance of batteries. One example are the bi- or multi-phase layered oxide cathode materials in SIBs that show superior battery performance compared with their single phase counterparts.[98,206] Z. Yan et al. reported a P2@P3 biphasic material giving a better rate and cycling performance than the pure P2 and P3 materials.[207] Although XRD measurements (Figure 1-12a) undoubtedly confirmed the different phases in $Na_{0.78}Cu_{0.27}Zn_{0.06}Mn_{0.67}O_2$, the bulk information obtained from XRD could not describe the spatial distribution of the two phases, and more importantly characterize their interface. S/TEM high resolution imaging was used to fill this gap. Fig. 1-12b presents the scanning transmission electron microscopy-high angle annular dark-field image (STEM-HAADF) (left) and bright field (BF) image (right) of the material,

which clearly identifies the interfaces along the [003] direction. Another example are the complex reversible or irreversible phase transitions that layered oxide cathodes in LIBs and SIBs experience during the intercalation reactions, which can lead to drastic capacity fading. *In-situ and ex-situ* XRD measurements are widely used to study these phase transitions with the same drawbacks of bulk information averaging. Figure 1-12c presents one example of an *in-situ* XRD study for an O3 type $NaNi_{2/3}Sb_{1/3}O_2$ SIBs cathode material, which shows that the sample undergoes a series of phase transition from the O3 phase to a P3 phase and further to a O1 phase during the desodiation process. In the following sodiation process, the O1 phase obtained at the maximum desodiated state experiences a reverse phase transition and transforms to the O3 phase at the fully sodiated state. Although the global phase transition can be clearly described by these measurement, XRD lacks the ability to spatially resolve the phase distribution. TEM can not only characterize the structural evolution with high resolution, but can also provide information on the ion migration behavior with similar resolving power. Y. Nomura et al. recorded an orientation map (Figure 1-12d-left) in a $LiNi_{0.8}Co_{0.15}Al_{0.05}O_2$ LIBs cathode material using 4D-STEM at an intermediate point during battery cycling. Combing these results with the lithium elemental map obtained from EELS data (Figure 1-12d-left) they proved that the lithium diffusion in the polycrystalline secondary cathode particles is limited by the grain boundaries along the *c-axis.*[208]

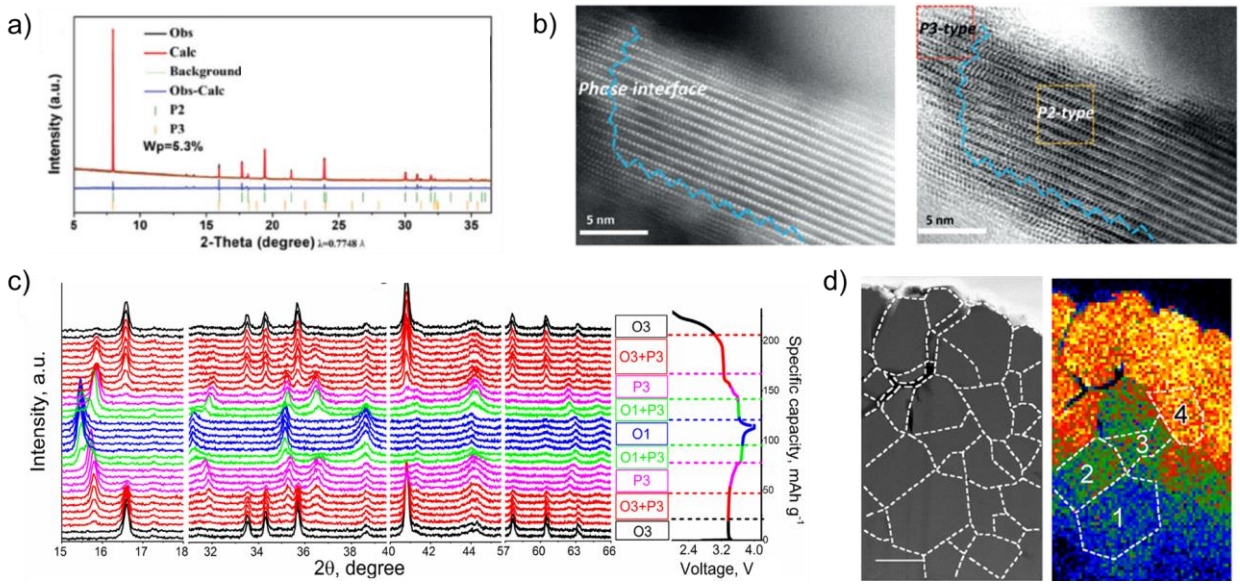

Figure 1-12: **a)** Rietveld refinement of synchrotron XRD pattern of P2@P3 $Na_{0.78}Cu_{0.27}Zn_{0.06}Mn_{0.67}O_2$, **b)** STEM-HAADF (left) and STEM-BF (right) images of the phase interface, adopted from reference [207]; **c)** *in-situ* electrochemical XRD analyzes of $NaNi_{2/3}Sb_{1/3}O_2$ sample during the initial cycle stacked against the voltage profile, adopted from reference[209]; **d)** STEM-ADF image (left) and Li elemental map (right) of the $LiNi_{0.8}Co_{0.15}Al_{0.05}O_2$, the white dash line in STEM-ADF image is to mark different orientations based on 4D-STEM date, the scale bar is 500nm, adopted from reference[208].

The structural characterization of non-crystalline composites is also very important for understanding reaction mechanism in batteries, as many battery materials can lose their long range order

during cycling. However, many of the traditional structural characterization methods, such as X-ray and electron diffraction or HRTEM, are limited in studying non-crystalline phases. For instance, Z. Li at al. successfully applied MoS_2/C composites in MIBs, but the amorphous products formed during cycling increased the difficulty of understanding the structural evolution. However, the authors employed a pair distribution function (PDF) analysis derived from SAED to understand the products formed during the battery cycling and reported a solvated magnesium-ion intercalation mechanism for their system. The experimental and simulated PDFs are shown in Figure 1-13. Although the simulated PDFs from 2H and 1T structures look quite similar, some relevant different features appears such as the peak at about 4.5 Å observed only for the 2H phase and the different ratio of the peaks at about 6.3 Å and 6.7 Å. The results show that the pristine MoS_2 has a 2H structure that changes to 1T structure at discharge and returns to 2H structure after charging. In addition, the evolution of the peak located at 1.9 Å attributed to the Mg-O bonds was correlate with the discharge and charge mechanism indicating the magnesium could shuttle between electrodes in the form of an organic molecular cluster instead of the expected Mg^{2+}.

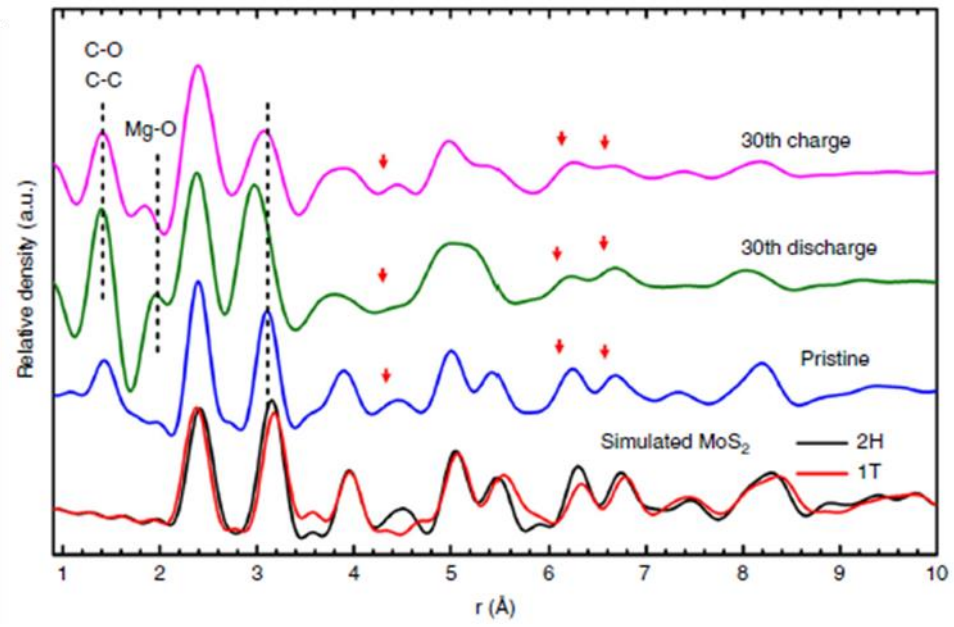

Figure 1-13: PDF analysis for as-prepared and cycled materials of the MoS_2 in MIBs at 30 cycles, adopted from[210].

1.5.3. Elemental distribution observed by S/TEM

Imaging and diffraction analysis provide morphological and structural information. However, the exact chemical composition cannot be directly extracted from these data. Analytical S/TEM techniques such as EDX, EELS and energy filter TEM (EFTEM) are wildly employed in battery research for elemental analysis including qualitative and quantitative measurements.[211–215] EDX chemical mapping is frequently used to monitor elemental diffusion and to reveal phase separation. One example is shown in Figure 1-14a where STEM-EDX mapping of $Li_4Ti_5O_{12}$ nano-particles was used to follow the sodiation and desodiation evolution during discharging and charging of the anode.[216] The uneven distribution of

sodium (yellow map in Figure 1-14a) in the discharged state implies a phase separation after sodiation. Figure1-14b is another example for application of STEM-EDX in the battery field, where the poor infiltration efficiency of microporous carbon by sulfur during the high temperature synthesis is clearly shown in a cryo-TEM experiment.[217] It can be observed that a majority of sulfur has not infiltrated the carbon, and remained external to the carbon particles. Although EDX is a relatively simple technique and powerful for detecting most elements, the low energy resolution and absorption problems caused by the detector window and the specimen itself, make it difficult to be used for monitoring light elements. The possible to map Lithium is one of the advantages EELS is offering. J. Yoshida et al. investigated the relationship between particle size and the battery performance of a spinel type $LiMnPO_4$ LIBs cathode material.[218] The results show that a significant amount of lithium ions are trapped inside the secondary particles (Figure 1-14c) in the fully delithiated state, indicating that the large particle size lengthens the lithium transition path and is harmful for the battery performance.

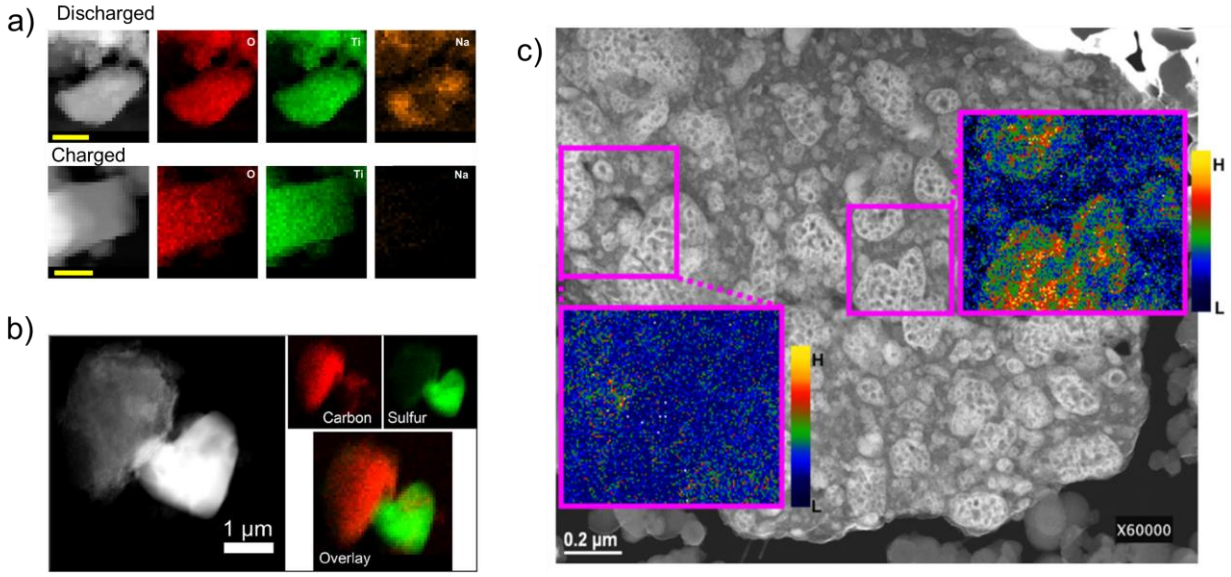

Figure 1-14: **a)** elemental map of $Li_4Ti_5O_{12}$ anode nano-particles in SIBs at discharged and charged statues after 5 cycles, adopted from reference[216]; **b)** investigation of carbon and sulfur distribution in sulfur battery cathode acquired by cryo-scanning transmission electron microscope, adopted from reference[217]; **c)** STEM image of the $LiMnPO_4$ secondary particle at delithiated states. Insets show the Li-EELS maps measured in the part enclosed with the square, adopted from reference[218].

1.5.4. Oxidation state analysis

For battery electrode materials, the elements in the host structure change their valence state to compensate the charge imbalance caused by the de/lithiation (de/sodiation) processes during cycling. Therefore, determination of the oxidation state is important to understand the reaction mechanism, especially in complicated multi element systems. An interesting example shown here is the investigation of the capacity fading of a NMC8111 ($LiNi_{0.8}Mn_{0.1}Co_{0.1}O_2$) cathode material in a LIB. X. Li et al. examined

the valence state changes of the transition metal elements during the delithiation and lithiation process.[219] The *in-situ* XAS spectrum is shown in Figure 1-15a. The near edge spectrum of Mn slightly shifts to higher energy during the charge and following discharge process indicating the local environment of Mn changes. The difference in the Mn XAS spectrum between 'before charge' and 'after discharging' (shown in the insert in Figure 1-15a) implies some irreversibility and explains the capacity fading to some extent. However, the XAS measurements here can only give average bulk information without spatial resolution. EELS mapping (Figure 1-15b) was carried out to study the local distribution of different Mn states. The EELS spectra were acquired at different areas from the bulk to the particle surface showing a clear evolution of the O K-edge and the Mn L-edge. The L3/L2 ratio of Mn L-edge constantly increases from the bulk to the surface, a change that is attributed to a reduction of the Mn oxidation state at the particle surface. The finding extracted from the L3/L2 ratio is backed up by the evolution of the O K-edge pre-peak, which shows a decreased intensity from the bulk towards the surface. Combined with the structural study in this work, the authors come to the conclusion that the surface of the particle in bare NMC111 material undergoes a structural evolution from a layered oxide to a rock salt structure, which is responsible for the capacity fading. In the NMC materials, all transition metals can contribute to the battery capacity at different voltage windows. Revealing the reaction sequence of the transition metal is critical for understanding the de/lithiation mechanism and tuning the electrochemical performance by changing the stoichiometry of the transition metals. H. Liu et al. studied the transition metal state during delithiation and lithiation by *ex-situ* high resolution EELS.[220] As shown in Figure 1-15c, the L3 edge shape and position of Ni is shifting during cycling (no clear changes can be observed in the spectra of Mn and Co) indicating that Ni primarily contributes to the capacity for this $LiNi_{1/3}Mn_{1/3}Co_{1/3}O_2$ in the voltage window of 2.5-4.5 V. The valence region of EELS spectra can also be used in battery studies, as this region will give information on the band gap and can help to identify different phases in cycled electrodes. For an electrode with known components, valence EELS can be carried out to map the phase distribution. Figure 1-15d shows valence EELS spectra of different electrodes, in which we can see that valence EELS can be used as a finger-print technique to identify these phases.[221] Clear differences can be seen in relatively similar compounds, such as $LiCo_{0.9}Ni_{0.1}O_2$/$LiCoO_2$ and $LiFePO_4$/$FePO_4$.

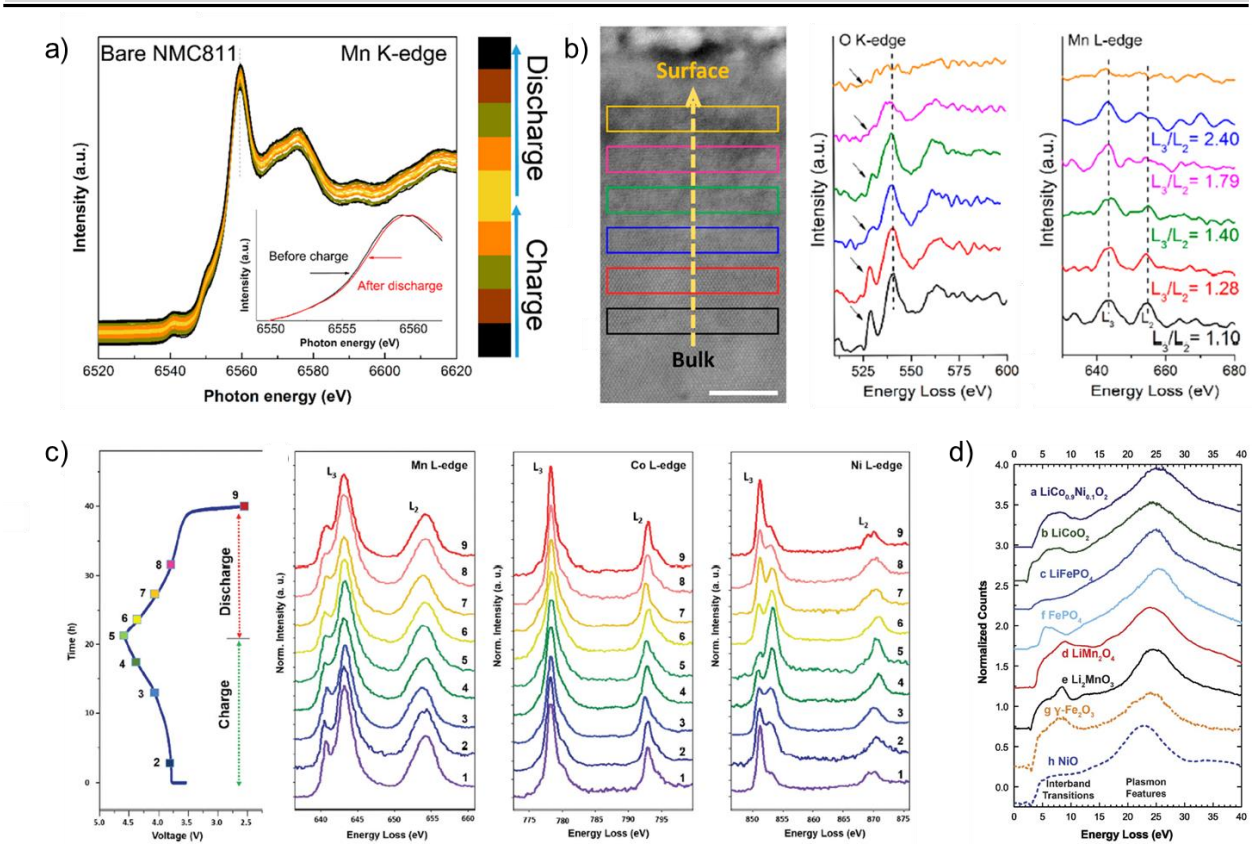

Figure 1-15: EELS characterizations for battery materials. **a)** operando XANES spectra of Mn of bare NMC811 cathode, **b)** STEM-HAADF image and corresponding EELS spectra acquired from the regions in cycled NMC811 material, scale bars in **b** 5 nm, **a)** and **b)** are modified from reference[219]; **c)** voltage profile and the normalized EELS spectra of Mn, Co and Ni, adopted from reference[220]; **d)** valence EELS spectra of several lithium ion battery materials, adopted from reference[221].

1.6. Motivation and outline of this PhD work

As mentioned in Section 1.1, the anode is an important component of the rechargeable batteries but requires significant improvements in order to meet the continuously increasing demand for high energy density. MOs and TMDs are receiving increasing attention as conversion reaction anodes due to the high theoretical capacity, tap density and cycling stability. Due to their outstanding battery performance as well as the incomplete available model for their reaction mechanism, the HEO $(Co_{0.2}Cu_{0.2}Mg_{0.2}Ni_{0.2}Zn_{0.2})O$ and MoS_2 were selected as two representative materials for MOs and TMDs to be studied in this thesis.

Although significant progress has been made recently in understanding the mechanisms controlling the electrochemical properties of HEO, a clear understanding of the role played by entropy-stabilization and other additional effects is still missing. The high entropy effect can stabilize multi-cations into a single solid solution phase, which is favorable for ion migration. Nevertheless, the entropy effect is insufficient to explain the excellent battery performance of the HEO in the conversion reaction as the initial HEO structure cannot be reestablished during delithiation at room temperature due to the positive enthalpy of mixing. A 'cocktail effect' is regarded as another possible reason for the good battery performance,

which was mentioned frequently in previous studies,[164–167,222] The complex chemical composition in HEOs provides lots of possibilities for synergetic effect of different elements. However, a 'cocktail effect' in multi-cation HEOs has not been understood so far. The $(Co_{0.2}Cu_{0.2}Mg_{0.2}Ni_{0.2}Zn_{0.2})O$ was used in this thesis to study the 'cocktail effect' during battery reaction in this HEO. Understanding the reaction mechanism of this typical HEO $(Co_{0.2}Cu_{0.2}Mg_{0.2}Ni_{0.2}Zn_{0.2})O$ can be used to guide material optimization and design of analog high entropy systems.

The failure of graphite anodes implementation in SIBs accelerates the research for non-graphitic carbon materials, such as TMDs. As one typical TMD, MoS_2-based electrodes show good prospects and have high theoretical capacity of about 660 mAh/g in both LIBs and SIBs, even larger than that of the commercial graphite in LIBs. However, understand the reaction mechanism of MoS_2-based electrodes in SIBs is still limited. Figuring out the reaction mechanism could be helpful for further materials optimization. In addition, as mentioned before, the MoS_2/C composites always show superior battery performance compared to the bare MoS_2 without carbon. Uncovering the role of carbon in MoS_2/C composites will help to design TMDs/C composites for rechargeable battery anodes. To study the reaction mechanism of MoS_2 and the carbon function, two samples, MoS_2-C@C and bare MoS_2 were prepared in this thesis and characterized comprehensively at different batteries states.

To answer the above highlighted questions, many techniques can contribute to the characterization of the morphology, structure, composition, valence state. Among them, modern TEMs integrating different analysis options can provide valuable information about all the above mentioned functions with sub-nanometer resolution. However, the fairly localized characterization potentially yields not statistically relevant data. To compensate for this, the results were supplemented by bulk characterization techniques including XRD, XAS and electrochemical testing.

The basic principles of TEM including the image formation, spectroscopic techniques and PDF are introduced in **Chapter 2**. Moreover, a brief presentation of the equipment, such as XRD, XAS and electrochemical testing methods, and their setups used throughout this thesis is also provided.

As introduced above, many questions about the HEO phase formation during the synthesis process are unclear. For instance, the detailed microstructural evolution along with the elemental diffusion during annealing is missing in the previous reports. Clarifying that is beneficial for understanding the reaction sequence of individual MOs and for optimizing the synthesis conditions. In addition, unraveling the reaction sequence of different raw metal oxides, could be helpful to design other HEOs. In **Chapter 3**, we try to answer some of these questions including the microstructure evolution, elemental diffusion sequence and possible prior phase formation before HEO generation. This is achieved by studding the calcination of HEO $(Co_{0.2}Cu_{0.2}Mg_{0.2}Ni_{0.2}Zn_{0.2})$ using a combination of *in-situ* TEM and *in-situ* XRD measurements as the main characterization techniques.

The de/lithiation mechanism of the HEO $(Co_{0.2}Cu_{0.2}Mg_{0.2}Ni_{0.2}Zn_{0.2})O$ was investigated in **Chapter 4**. In this chapter, many complementary TEM methods, such as PDF, STEM-EELS, HRTEM, electron tomography and 4D-STEM, were used to characterize as-prepared and cycled HEO samples. The behavior and the electrochemical contribution or inertia of each of the five transition metals in the material are explained. The synergetic effects between different elements are explained based on the results presented in this chapter. They are considered to be the reason of the outstanding electrochemical performance of HEO in LIBs.

Taking the advantage of the methodology employed in the previous chapter with a focus on the characterization of amorphous products in the conversion anodes, the de/sodiation mechanism of MoS_2 was studied and the findings presented in **Chapter 5**. The results obtained in this chapter provide a new insights into the MoS_2 sodiation mechanism. After cycling, the MoS_2 structure losses the long range order and fragments into MoS_x clusters, which act as active components in the following de/sodiation cycles. The carbon was demonstrated to be independent of the reaction mechanism of MoS_2, but prevents leaching of MoS_x clusters into the electrolyte during battery cycling.

2. Methods and characterization techniques

As seen in the previous chapters, a deeper understanding of the reactions and transformations of the active material requires information on their structure and chemical properties, both in the bulk and at interfaces, at different states or ideally *in-situ*/operando. This thesis aims to understand the ion migration and microstructural evolution of battery materials during materials synthesis and during battery cycling. TEM is a powerful tool that can provide structural information down to the atomic level. Combining the imaging and diffraction capabilities of electron microscopy with analytical tools such as Electron Energy Loss Spectroscopy (EELS) and Energy-dispersive X-ray spectroscopy (EDX) allows a chemical characterization of materials with sub-nanometer resolution. However, the information provided by TEM is always limited to some local areas in the material. Compared with TEM, other techniques, such as X-ray diffraction (XRD), X-ray absorption spectroscopy (XAS), provide an average bulk characterization including structural and bonding properties and information on the chemical state, but with limited spatial resolution.

TEM measurements complemented by bulk techniques including XRD and XAS were used in this thesis to answer multiple questions regarding the reactions during battery cycling and materials synthesis. Electrochemical measures, e.g. galvanostatic charge-discharge tests and electrochemical impedance spectroscopy (EIS), are used to prepare the sample at the targeted states and reveal the electrochemical performance. Different sample preparation method including focus ion beam (FIB) and ultramicrotome were used to prepare the specimens suitable for TEM measurements. The setups and the equipment used for the characterization and sample preparation are introduced in this chapter together with a background on the techniques.

2.1. Equipment used in this thesis

2.1.1. Galvanostatic charge-discharge test

Galvanostatic measurements were performed using an Arbin battery test system (BT-2000) at 25°C. The measurements were performed with a voltage window of 0.01 to 3.0 V with a current of 0.1 C. 1 C corresponds to 500 mA/g for the HEO batteries in **Chapter 5** and 600 mA/g for the MoS_2 batteries in **Chapter 6**.

The theoretical capacity was calculated using the following equation**:**

$$Q = \frac{nF}{3.6M_w} \qquad 2\text{-}1$$

where Q is the theoretical capacity, n is the number of transferred electrons during the electrochemical reaction, F present the Faraday constant (96500 C/mol), and M_w is the equivalent molecular weight.

2.1.2. Electrochemical impedance spectroscopy measurements

EIS measurements were performed using a BioLogic VSP-300 potentiostat. The impedance data was acquired by applying 10 mV AC perturbation signal over a frequency range of 1 MHz to 1 Hz (6 points/decade).

2.1.3. Power diffraction

In-situ **high-temperature XRD** was performed using a STOE/STADIP diffractometer (Mo K_α, λ= 0.7093 Å) equipped with a Dectris Mythen detector and Ge (111) monochromator calibrated with a LaB_6 standard. *In-situ* diffraction patterns were collected while keeping the samples at the target temperature during acquisition. Temperature corrections were made based on the thermal expansion of NaCl using a NiCr thermocouple. The XRD patterns were recorded from 5 to 40 ° (2 theta) using a step size of 0.015 °. The collection speed is 1 ° per min.

The ***ex-situ*** **XRD** characterization employed in **chapters 4** and **5** was conducted using a Bruker D8 diffractometer with Bragg-Brentano geometry using Cu K_α, λ = 1.54 Å) radiation. The XRD patterns were collected from 10˚ to 80˚ using a step size of 0.2˚. The collection speed was set to 0.6 ° per min.

The XRD patterns **in chapter 6** were recorded using an STOE Stadi P diffractometer, equipped with a Ga-jet X-ray source (Ga-K_β radiation, λ = 1.2078 Å). Cycled samples were prepared in a glove box to avoid exposure to air and protected by a kapton film.

2.1.4. X-ray photoelectron spectroscopy

The XAS data were recorded at the Mo K-edge (20,000 eV), Co K-edge (7709 eV), Ni K-edge (8333 eV), Cu K-edge (8979) and Zn K-edge (9659). X-ray absorption near edge spectra (XANES) of the XAS spectrum were obtained by subtracting the pre-edge background from the overall absorption and normalizing with a spline fit using the ATHENA software package. The k2-weighted extended X-ray absorption fine structure (EXAFS) was Fourier transformed over the limited range of k from 3 to 10 $Å^{-1}$ with a hanning window (dK =1 $Å^{-1}$). The XAS measurements in **chapter 5** were performed at the XAS beamline of the synchrotron radiation source at Karlsruhe Institute of Technology (KIT), beamline P64 and P65 at PETRA III (Hamburg). XAS measurements in **chapter 6** were performed at the P64 beamline at PETRA III Extension of DESY (Hamburg).

2.1.5. Transmission electron microscopy

A Titan 80-300 and a Themis Z were used in this thesis. The image corrected Titan 80-300 was equipped with an EDAX s-UTW EDX detector and a Gatan UltraScan CCD camera. The microscope was operated at 300 kV. The image and probe corrected Themis Z is equipped with a Super-X EDX detector, a Gatan OneView CMOS camera and a Gatan imaging filter with a Continuum and K3 IS camera. The Themis

Z was also operated at 300 kV. The detailed parameters for EDX and EELS acquisition are described in each chapter as different setups were used. The design of the special TEM holders used in this work will be displayed in the corresponding experimental chapters. The data analysis was performed using TEM Imaging & Analysis (TIA), DigitalMicrograph, and Velox software.

2.1.6. Scanning electron microscopy

The scanning electron microscope (SEM) and focus ion beam (FIB) system used in this thesis was a FEI Strata 400 S equipped with a (Schottky) field emission gun as electron source and a Gallium liquid metal ion source. The detectors included a through-the-lens detector (TLD), an Everhart-Thornley detector (ETD), a back scatter electron detector (BSD), a continuous dynode electron multiplier (CDEM) and a scanning transmission electron microscopy (STEM) detector. The Gas Injection System (GIS) includes Pt, C and W. The high tension used for SEM imaging was 5 kV and the range for FIB was between 2 kV - 30 kV.

2.1.7. Ultramicrotome

The dismounted electrodes were embedded in a polyethylene BEEM® capsule using a cold mounting epoxy resin (STRUERS SpeciFix-20) and cured for one week. The four faces and the front face of the hardened resin/sample block were trimmed with a Diatome 45° diamond trimming knife to sharpen the tip and to reach the sample. A Leica ultramicrotome (Ultracut UCT) was used for the final slicing a with a Diatome low angle diamond knife type “MT Ultra 35°”, a cutting velocity of 2 mm/s, and distilled water as trough liquid at room temperature. Slices with a nominal thickness of 70 nm were cut. The microtomed slices were picked up with the aid of a “Perfect Loop” tool and transferred to TEM Cu grids.

2.1.8. In-situ gas heating system

The *in-situ* gas heating experiment conducted in **Chapter 3** was performed with the help of a Protochips™ Atmosphere 210 system with integrated gas mixing capabilities. A gas composition of 21% oxygen in an argon flow was used to simulate similar oxygen levels as in air. The experiment was run at a pressure of 740 Torr with a gas flow rate of 0.1 sccm. The temperature was increased from 300˚C up to 850˚C with a heating rate of 2˚C s^{-1}. Each time the temperature was increased in steps of 50˚C and at each temperature a full morphological, structural and chemical (EDX-based) analysis was performed.

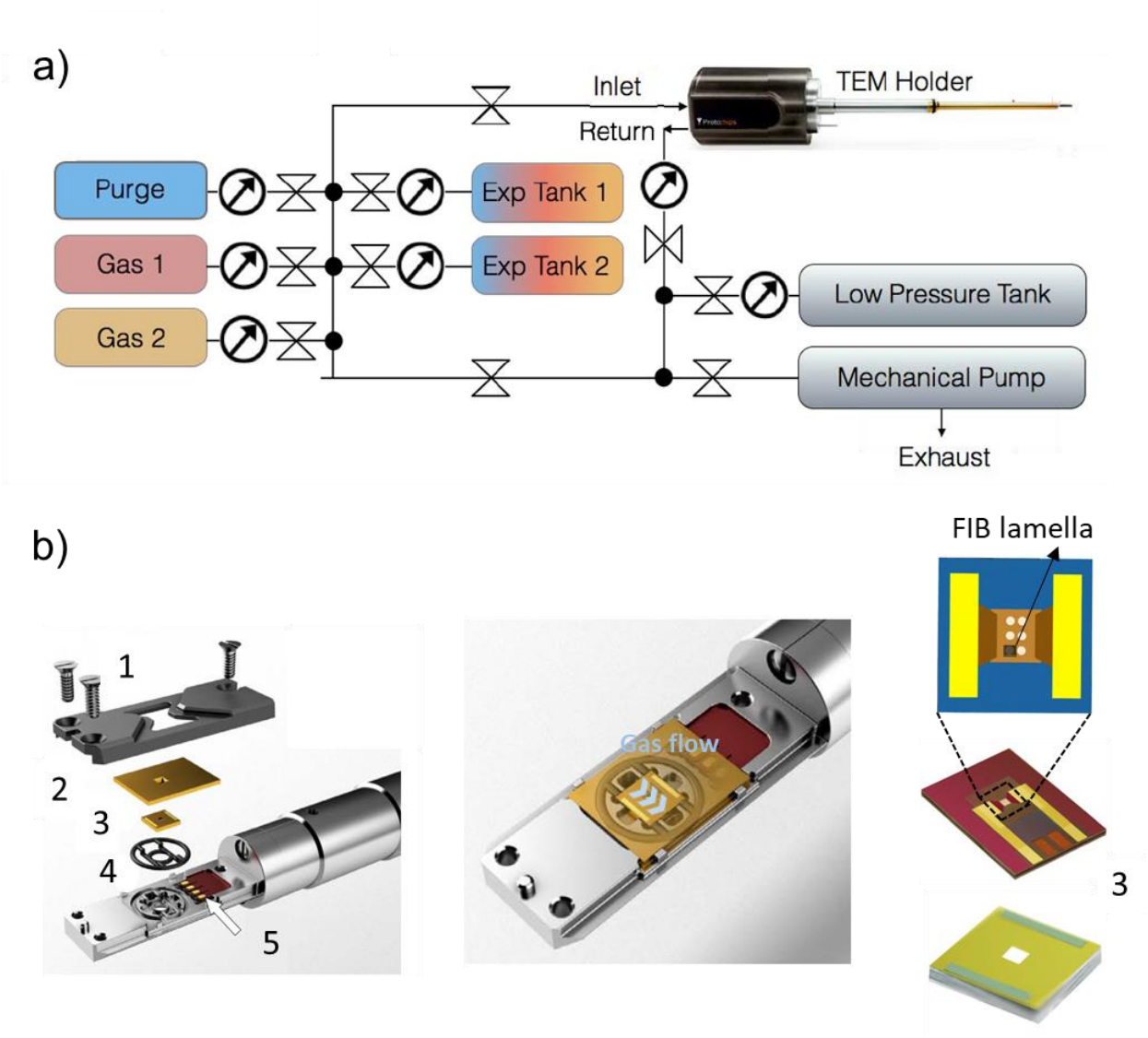

Figure 2-1: presentation of the Atmosphere 210 gas manifold and the gas heating holder. **a)** diagram of the Atmosphere 210 gas manifold; **b)** visual presentation of the gas holder tip main components and assembling order: 1- lid screws, 2 - lid, 3 - small/large chip pair, 4 - gasket, 5 - flex-circuit, adapted from reference [223].

2.1.9. STM holder

In-situ TEM electrical measurements applied in **Chapter 5** were carried out in order to test the electrical conductivity with the help of a double tilt *in-situ* TEM-STM holder (TE02-DT).[224] A schematic of the STM holder is shown in Figure 2-2. The holder has a fixed slot for a sharp nanoscale gold tip opposite to a second slot for a TEM half grid. The tip can move in x, y and z direction with sub-nanometer precision using a piezo based device. The two positions are connected with an integrated circuit inside the ceramic head of the holder. For the experiment, the sample was dropped on a TEM half grid coated by a carbon membrane. Under STEM imaging control, the gold tip was brought in contact with a selected sample on the TEM grid. After fixing the contact position, an external voltage was applied. In this experiment, the selected voltage scan was ranged from -15 V to 15 V.

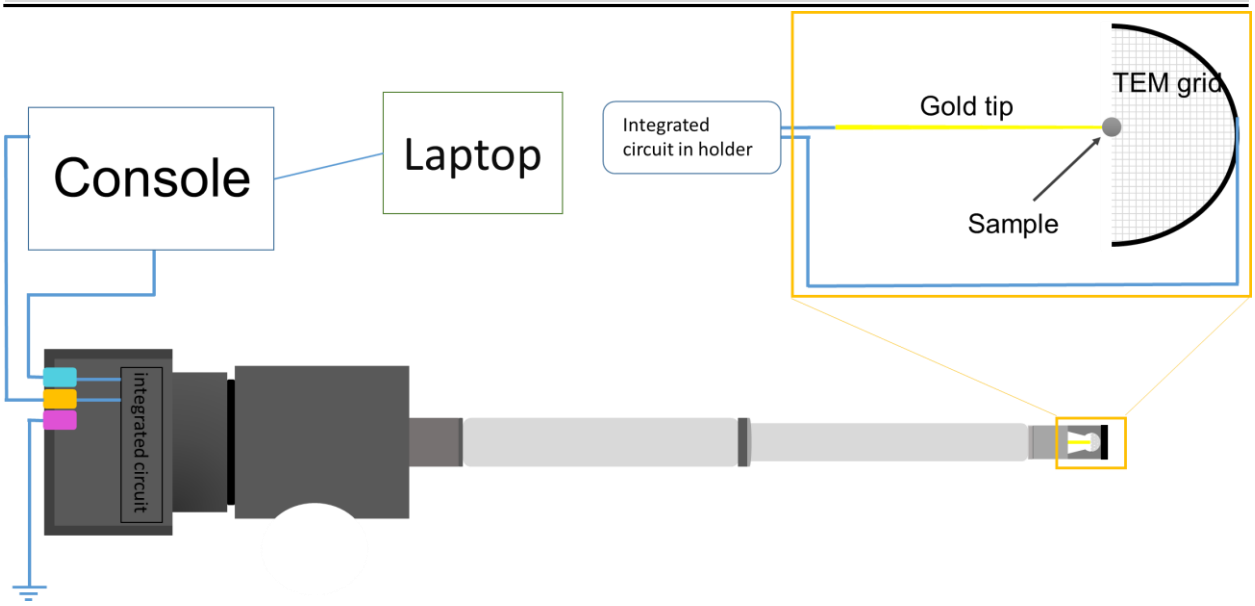

Figure 2-2: schematic of STM holder and the working principle of electric conductivity testing.

2.1.10. Electron tomography

The electron tomographic analysis was carried out by Xiaohui Huang, a PhD candidate in our group. It was performed using a Fischione 2020 tomography holder on a probe-corrected ThermoFisher Scientific Themis 300 microscope operated at 300 kV in STEM mode. STEM-HAADF tilt series were recorded over a range of ±72º with a tilt step of 2º. Projections were then aligned in IMOD using 6.5 nm Au colloidal particles as fiducial markers with a mean residual alignment error of 0.45 voxels. The aligned tilt series were reconstructed using the simultaneous iterative reconstruction technique (SIRT) within Inspect3D 4.4 (ThermoFischer Scientific). 3D visualization was performed in Avizo (ThermoFisher Scientific).

2.1.11. Ball mill

The ball milling used in **Chapter 3** was done using a Chishun Tech ball mill machine. The raw materials, CoO, CuO, MgO, NiO and ZnO, were ground for 2 hours at 300 rpm/min using ethanol as dispersant.

2.2. Electron-matter interaction

According to the particle–wave duality in quantum mechanics, electrons can be regarded as waves and particles. When they interact with matter the resulting scattering events produce a wide variety of signals as illustrated in Figure 2-3. The scattered electrons carry specific structural and chemical information due to the interaction with the specimen and these signals can be used in different imaging, diffraction and analytical techniques.

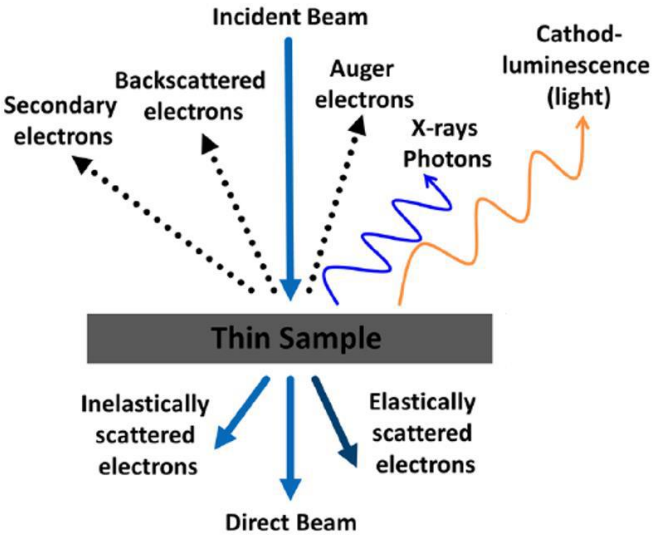

Figure 2-3: interaction of electron with a specimen and the generated signals, adopted from reference[225].

The interaction between the incident beam and the electrons/nucleus of the atoms in the specimen, can cause a loss of energy and change in momentum of the incident electrons. Depending on the transferred energy during scattering, the events can be classified into two categories: elastic scattering, involving no energy loss and inelastic scattering, when incident electrons lose energy. In both cases, the interaction of the incident electron with the atoms results in a change of direction as summarized in Figure 2-4. The direct transmitted beam refers to the electrons that pass the sample without any detectable interaction with the atoms, and thus experience no change in direction and energy. Elastic scattering can occur when the incident electrons are scattered either by the interaction with the electron cloud (low angle scattering) or by Rutherford scattering at the atomic nucleus (high angle scattering). In some cases, the scattering angle can be larger than 90 °, an event named backscattering, when the incident electron is directly hitting the nucleus.[226] The dominating scattering angle is in the range of 10-100 mrad for an incident beam energy of 100 keV.[227] Considering the wave-like nature of the electrons, the electrons scattered coherently by a crystalline structure lead to constructive and destructive interfere, which gives rise to a diffraction pattern. It should be mentioned that the energy transferred from the electron beam to the atomic nuclei can be negligible only for low angle scattering. In the extreme case of a head-on collision, the energy transition could be higher than 1 eV (for 100 keV beam energy). Such an energy may exceed the required energy for displacing the atom from its lattice site and results in displacement damage.[228]

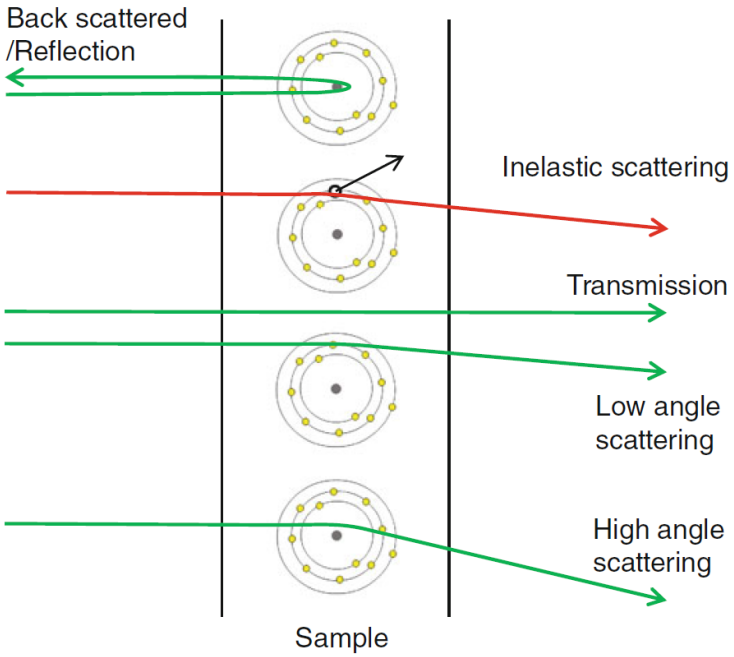

Figure 2-4: schematic of electrons-matter interaction, from up to down the arrows present the back scattering, inelastic scattering (the incident electron interacts with the out shell bond electron), transition electron, and the elastic scattering (low angle and high angle scattering), adopted from[226].

When a fast incident electron interacts with a bound electron the incident electron can lose a non-negligible amount of energy and change its momentum resulting in a characteristic scattering angle and give rise to a wide series of signals as shown in Figure 2-3. When the energy transferred from the incident electron to a bound electron is similar or greater than the energy difference between an unoccupied orbital and its current orbit, the bound electron can be excited to a higher energy level and leave behind a 'core hole'. If the electron is weakly bound (in the valence or conduction band) it will gain enough energy from its interaction with the incident electron so that it can escape to the vacuum. These electrons are called secondary electrons and are widely used in SEM imaging. After the excitation process, the excited (ionized) atom will loss the excess energy through the transition of an electron from a higher energy level to the core hole. Figure 2-5a presents a schematic of excitation and de-excitation process of the bound electron, in which one electron in the K inner-shell is excited to a state above the Fermi level. Afterwards, an electron from a higher energy level moves into the core hole in the K shell, accompanied by release of the excess energy, e.g. through emission of a photon (characteristic X-rays, cathodoluminescence) or by emission of an auger electron. The X-ray energy emitted during the de-excitation process is characteristic for every atom and can be used for elemental identification. The correlation between the atomic shell structure and the characteristic X-ray energy emitted can be seen in Figure 2-5b obeying the electronic dipole transitions rules with Δn (principal quantum number)$\neq$0, Δl (azimuthal quantum number)=±1 and Δm (magnetic quantum number)=0, ±1.

g

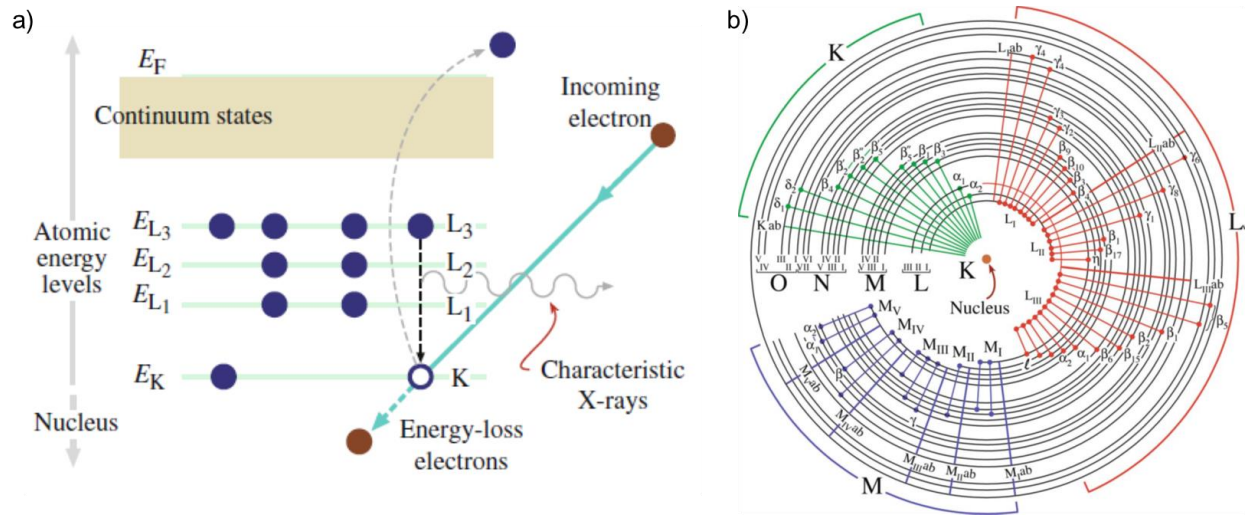

Figure 2-5: **a)** schematic of the inelastic scattering process of an incoming electron and an inner-shell electron of an atom and the process of characteristic X-ray emission, adopt from[225]; **b)** a range of possible electron transitions that give rise to K, L, and M characteristic X-rays, adopted from reference[225]

As the total energy is conserved during the interaction, the energy loss of the incident electron is equal to the energy transferred to the bound electron. Therefore, the energy loss of the inelastic scattered electron is characteristic and can be used to identify the composition, the structure and the bonding of the specimen, a technique known as electron energy loss spectroscopy (EELS). The energy loss process described in Figure 2-5a, i.e. an electron transition from the inner-shell to an unoccupied state, which is widely used for chemical composition and oxidation state determination. In addition to this excitation, the energy loss caused by an interband transition across the energy gap of a valence electron in an insulator/semiconductor or the transition of an electron from the conduction band to a higher state in a metal, contains information about the optical properties, the band gap, the chemical environment and bonding information of the specimen, a spectroscopic region known as valence EELS. This technique can be used to map different phases with a higher electron dose efficiency compared with other techniques, i.e. core-loss EELS and EDX.[229] Moreover, when the incident electron interacts with the electrons in the valence or conduction band this results in collective oscillations of the electrons known as plasmon resonance. The plasmon signal dominates in materials with significant free-electrons, e.g. in metals. However, plasmon-like transitions occur to some extend in all types of materials, even if in insulators.

2.3. X-ray-matter interaction

Similar to the electron-matter interactions, the X-rays-matter interactions can be classified as elastic and inelastic scattering. The main distinction appears in the strength of these interactions as X-ray scattering is much weaker than electron scattering. Therefore, X-rays can be used to study thicker materials than possible using electron microscopy techniques. During the inelastic scattering of X-rays with bound electrons in atoms, the energy of the incident photon can be partially absorbed and the

electron can be knocked-out into the continuum or to a higher unoccupied state. The X-ray loses the same amount of energy and is deflected from its original direction to one opposing the direction of the knocked-out electron in order to conserve momentum. This phenomenon is known as Compton scattering. Moreover, the interaction between an incident photon and electrons from an inner shell electron can lead to the absorption of the entire photon energy. An electron ejected by the initial photon absorption is known as a photoelectron. Analogous to EELS spectroscopy, the X-ray absorption energies can be related to the elemental composition and valence state of each element and thus be used to analyze the composition and the oxidation state of materials and even quantitatively determine the chemical composition. Coherent scattering by a periodic lattice is the basis for diffraction, which can be used to analyze crystal structures.

2.3.1. X-ray absorption spectroscopy

In XAS the energy dependent X-ray intensity is measured before and after the X-rays penetrate a sample. It is a widely used technique to analyze the chemical composition, valence state and for structural characterization of bulk specimens. Figure 2-6 shows a XAS spectrum, in which the *y-axis* represents the absorbance and the *x-axis* the energy. One can observe that the XAS spectrum is composed of two distinct regions: one where the absorption coefficient changes suddenly and a second region where it is gradually decreasing. When the incident x-ray has an energy equal to the binding energy of a core-level electron, resonant scattering strongly enhances the scattering cross-section and results in a sharp absorption rise. After the absorption edge, the absorption coefficient decreases drastically with increasing energy due to the relationship between the absorption probability (μ) and energy in a given specimen, which can be expressed by the following equation:

$$\mu = \frac{\rho Z^4}{AE^3} \qquad 2\text{-}2$$

where ρ is the sample density, Z is the atomic number, A is atomic mass and E is the x-ray energy.

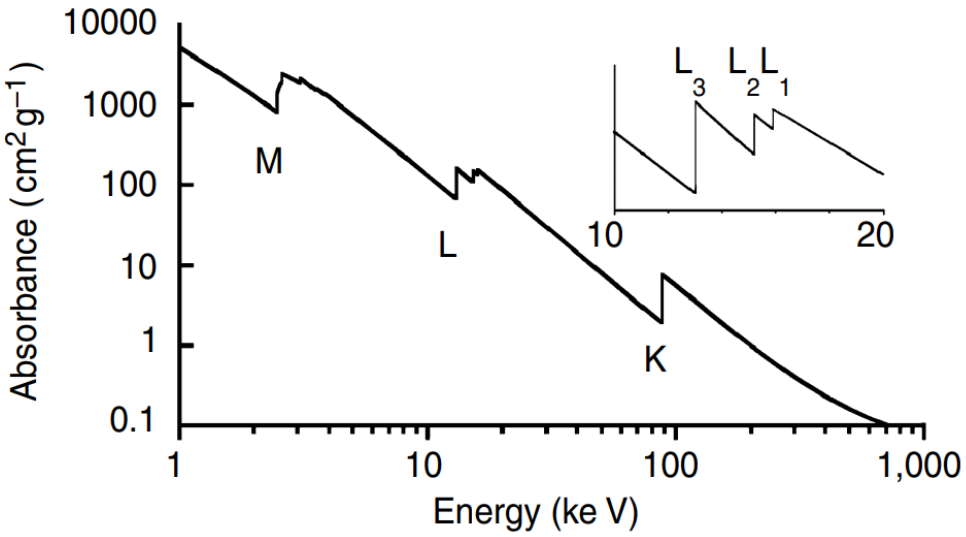

Figure 2-6: example XAS spectrum presenting the Pb absorption characteristics, adopted from reference [230].

At higher energy resolution, one can see that the absorption spectrum near the absorption edge does not decrease monotonously but oscillates. This oscillation originates from the scattering of photoelectrons excited by the X-rays in the surrounding coordinated atoms, causing the intensity of the X-ray absorption to change. The energy range up to 50 eV from pre-edge is called X-ray absorption near edge structure (XANES), which normally includes the pre-edge and the rising edge. In XANES, a pre-edge can be detected in some cases, which is caused by a photoelectron emitted from core state 1s to the unoccupied state *n*d, as shown in Figure 2-7. This can reflect the symmetry of atomic coordination that can be further used as a fingerprint for electronic structure determination. In a XAS spectrum the sudden vertical appearance at the binding energy regime of a core shell electron is so-called rising edge (Figure 2-7). The absorption edge will be shifted to a higher energy with increasing oxidation state of the atoms, which can be simply explained by considering that it is increasingly difficult to remove an electron from an atom that bears a higher positive charge. After the rising edge, the strong oscillation in XANES corresponds to low-energy photoelectrons scattered by coordination atoms, which interfere with the outgoing inelastically scattered electrons leading to strong oscillations. XANES can be used to quickly identify the elements and is sensitive to chemical information such as valence state, unoccupied electron orbitals and charge transfer. Moreover, XANES is also suitable for time-resolved and temperature-resolved *in-situ* experiments due to the short spectrum acquisition time and the weak temperature dependence peculiarity.

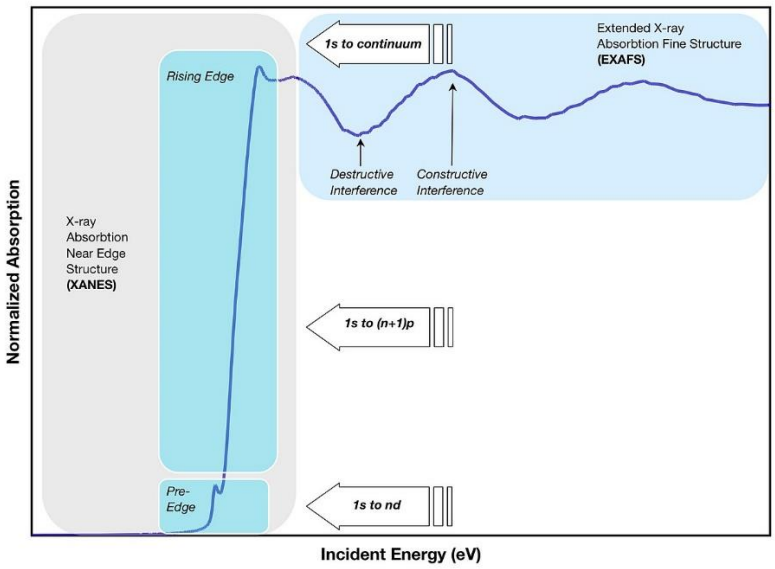

Figure 2-7: two distinct regions forming the XAS spectra and their basic characteristics, adopted from reference [230].

The energy range of 50 eV - 1000 eV above the absorption edge is called EXAFS and can be described by high-energy photoelectrons undergoing single scattering events by the coordination atoms around the absorbing atom, returning to the absorbing atom and interfering with the outgoing wave. The reason why EXAFS originate from single scattering of photons and XANES from multiple scattering is that photons with higher kinetic energy are less affected by the surrounding environment/neighbor coordination atoms, and are generally only single-scattered by neighbor coordination atoms. The characteristic shape of the EXAFS is given by a reduced amplitude, like a sinusoidal wave, that contains the information about the atomic surrounding. Standard data processing for EXAFS-PDF includes normalization of the absorption coefficient, conversing the oscillation from energy space to wave vector space and Fourier transformation. The PDF data thus obtained represents the coordination around a specific element.

2.3.2. X-ray diffraction

In 1912, M. Laue et al. have experimentally proven that X-rays undergo diffraction when passing a crystalline structure, proving the theoretical predication of the electromagnetic wave nature of X-rays.[231] X-ray diffraction has since proven to be a highly valuable technique in materials research that can offer precise information on the crystal structure of materials. Modern XRD setups can be divided into three main components including the X-ray source, the sample stage and the detector. The X-ray radiation in XRD equipment is generated by impacting a target metal, such as Cu, Mo and Ag, with an accelerated electron beam of 30-60kV in an X-ray tube. Using a monochromator, the polychromatic radiation emitted is filtered and directed towards the specimen. The working principle of a monochromator crystal is based on the selection of a specific photon energy by coherent diffraction satisfying the Bragg condition (Equation 2-3) for specific lattice planes. The Bragg-Brentano geometry was applied in the diffractometers used in this thesis with the detector is mounted in a position that is mirror-symmetrical to the X-ray source

(as shown in Figure 2-8a). The angle θ between detector and sample stage is the same as the angle between source and sample stage. During measurements, the X-ray source and the detector move symmetrically in order to illuminate and collect the deflected X-rays.

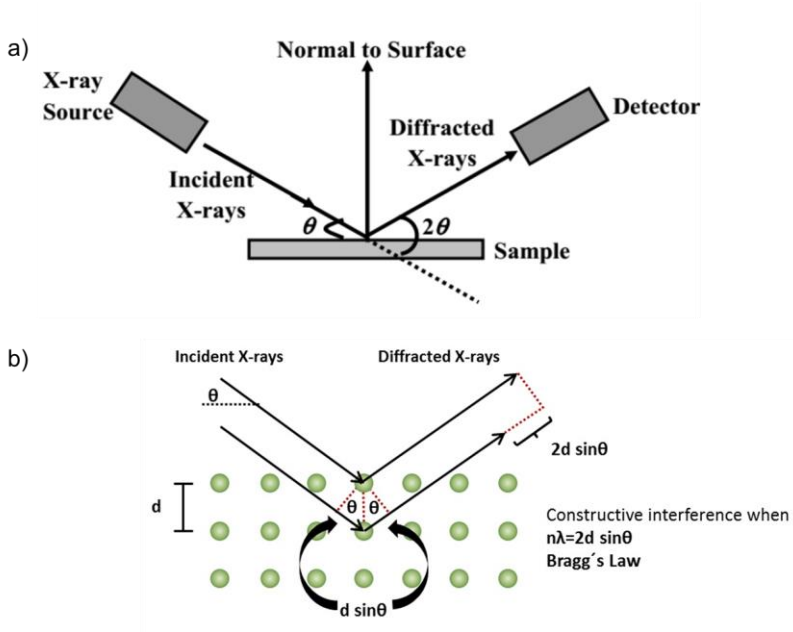

Figure 2-8: **a)** schematic presentation of the working principle of the X-ray diffraction, adopted from reference[232]; **b)** schematic representation of the Bragg equation, adopted from reference[233].

As shown in Figure 2-8b, the path length difference of the two waves diffracted by adjacent lattice planes is equal to $2dsin\theta$. When the path length difference is a multiple of the wave length, constructive interference occurs, which is described by the Bragg equation:

$$n\lambda = 2dsin\theta \qquad 2\text{-}3$$

where n is an integer, λ the wavelength of the incident X-ray, *d* the lattice distance, and θ the scattering angle. By continuously scanning the incident angle θ a typical XRD spectrum including the continuous background and a series of discrete reflections is obtained.

2.4. Electron microscopy (EM)

Electron microscopes (EM) use signals formed by the interaction of an electron beam with the specimen in order to obtain information on structure, morphology, and composition. The basic optical setup is similar to that in transmission light microscopy. However, the achievable resolution is significantly higher due to the short wavelength of the electrons. Using the Rayleigh criterion, the diffraction limited resolution can be estimated according to

$$\delta = \frac{0.61\,\lambda}{\mu\ sin\,\beta} \qquad 2\text{-}4$$

where λ is the wavelength of the radiation, μ the refractive index of the medium between the object and the objective lens and β the collection semi-angle. The term $\mu \sin \beta$ is called numerical aperture. Form the equation 2-4, it easy to understand that decreasing λ and increasing μ or β can improve the resolution. In a modern EM, the acceleration voltage can be as high as 300 kV corresponding to an electron wavelength of 1.97×10^{-2} Å, which, in principle, allows sub-Ångstrom resolution imaging. However, the optical aberrations of the electromagnetic lenses and their stability are limiting the achievable resolution, as will be discussed in more detail later.

An electron source, electromagnetic lenses, vacuum system and detectors are the main components of an EM. Electrons are emitted from an electron source on top of the EM. Two different types of electron sources, thermionic source and filed-emission source (FEGs), are typically used in EM. In thermionic sources the electrons are generated by heating an emitter material that has high thermal stability and possess a low work function. Typical thermionic emitter materials used in EM are tungsten and LaB_6. In a FEG, electrons are generated by applying a high voltage to a very fine needle-like tip that extracts free electrons located near the Fermi level through tunneling. Schottky sources, which are adopted in the SEM (Strata) and TEMs (Titan, Themis 300 and Themis Z) used in this thesis, make use of both heating the source materials and applying the field emission in order to generate an electron beam with higher brightness, greater coherence and lower energy spread compared with a thermionic source. Moreover, it offers higher stability and is less sensitive to contamination compared with cold FEGs sources. The extracted electrons are accelerated to 0.2 - 30 kV (in Strata SEM) and to 60kV to 300kV in the TEMs. In EMs the electron magnetic lens are used to either demagnify the source image on the specimen (in SEM and STEM) or magnify the image or diffraction pattern and project them on the viewing screen (in TEM). An inhomogeneous rotationally symmetric magnetic field is created by a magnetic electron lens, in which the magnetic field is weak in the center and becomes stronger further away from optical axis. Therefore, electrons entering the lens are focused along the axis by the magnetic field. The focal length of the electromagnetic lens is controlled by varying the current through the electromagnetic coil in the lens. In EMs, a high vacuum environment is necessary to avoid scattering of electrons by gas molecules. Different detectors are mounted on EMs to detect various signals and provide corresponding images or spectra.

2.4.1. Scanning electron microscopy

SEMs use a finely focused electron beam with a narrow energy range scanned across the sample. All modern SEMs are equipped with a secondary electron detector and most of them with additional detectors for backscattered electrons and X-rays, making the SEM able to study the sample topography and composition. Figure 2-9 shows a schematic of a typical SEM layout, in which the accelerated electron beam is focused by the condenser and objective lenses to form an electron probe with a defined energy, intensity and size that scans the surface of the sample controlled by scanning coils. The generated

secondary electrons contain topographic information of the sample surface. SEM microscopes do not require imaging lenses, but form the image by detecting the selected signal point by point along the scanned beam.

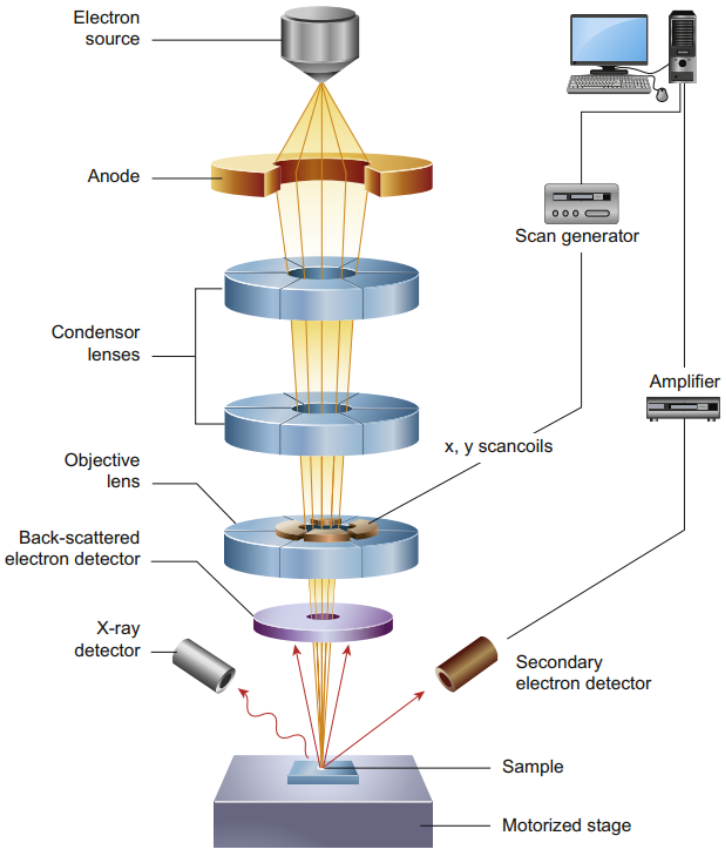

Figure 2-9: schematic diagram of the core components of an SEM microscope. The electrons are emitted from the electron source and accelerated by the anode. After being focused by the condenser and objective lens, the electron beam is scanned across the sample. Three typical detectors types including a secondary electron detector, X-ray detector and backscattered electron detector are displayed, adopted from reference [234].

The spatial resolution of state-of-art scanning electron microscope can reach below 1 nm. The magnification has a wide range and the field of view for observation can be adjusted from the nm to mm range depending on the requirements. The secondary electron detection helps creating an image showing the 3D morphology of samples that is dominated by the surface roughness. This is because the detected secondary electrons come from a thin region below the specimen surface. Another imaging mechanism based on the detection of backscattered electrons is more sensitive to the chemical composition of specimens due to the fact that heavier atoms scatter electrons stronger than light atoms.

2.4.2. Focus ion beam

A FIB instrument is similar to a SEM, but uses an ion beam (typically Ga^+) and electrostatic lenses in addition to the electromagnetic lenses. In a standard FIB, a liquid metal is used as ion source. The heated

liquid metal wets a tungsten needle and when a strong electric field is applied, this results in the formation of a Taylor cone and emission of positively charged ions from the cone.[235] The focused ion beam can directly modify the specimen surface by sputtering due to the high mass of Ga^+ ions. By carefully controlling the energy and intensity of the ion beam, one can perform precise nanomachining that can be used to remove unwanted material or more often to fabricate special microsized structures. In addition, if supplemented by chemical vapor deposition, ion beams can be used to deposit various materials with a precision close to FIB milling. When a small amount of a selected precursor gas is injected close to the specimen surface and exposed to the electron or ion beam, the gas is decomposed by the beam and the non-volatile products will be deposited on the surface of the specimen while the volatile products will be extracted by the vacuum system, as illustrated in Figure 2-10.

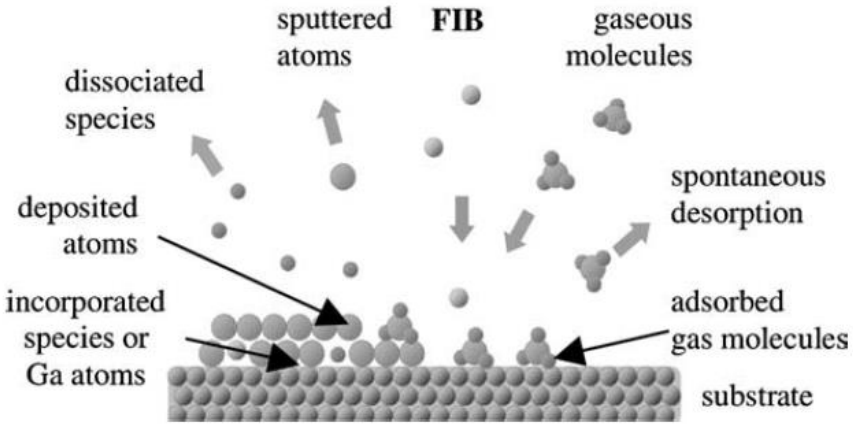

Figure 2-10: schematic process of FIB deposition, adopt from[236]

In a dual beam system, an electron and ion beam intersect at the coincidence point at the sample surface at an angle of 52°, and a high-resolution SEM image of the FIB milled surface can thus be formed. These systems combine the advantages of SEM and FIB, i.e. the complementary functions for imaging and nanofabrication. Figure 2-11 presents the typical process of preparing and lifting out a FIB lamella from a selected specimen area. First, the area of interest is identified by SEM. Then, Pt is deposited as protective layer on the sample surface. A TEM lamella can be obtained by milling two trenches on both sides of the sample and afterwards an initial relatively thick lamella is cut off from the bulk sample. The lift out is performed using a pieozo controlled nanomanipulator and the thick lamella is mounted on a TEM grid with a special finger design. Further thinning is necessary to obtain a TEM suitable lamella, which is done by using a low current ion beam in order to avoid surface damage. Finally, a cleaning step at low acceleration voltage is added in order to minimize the thickness of the embedded Ga ion and damage layer on both sides of the specimen surface.

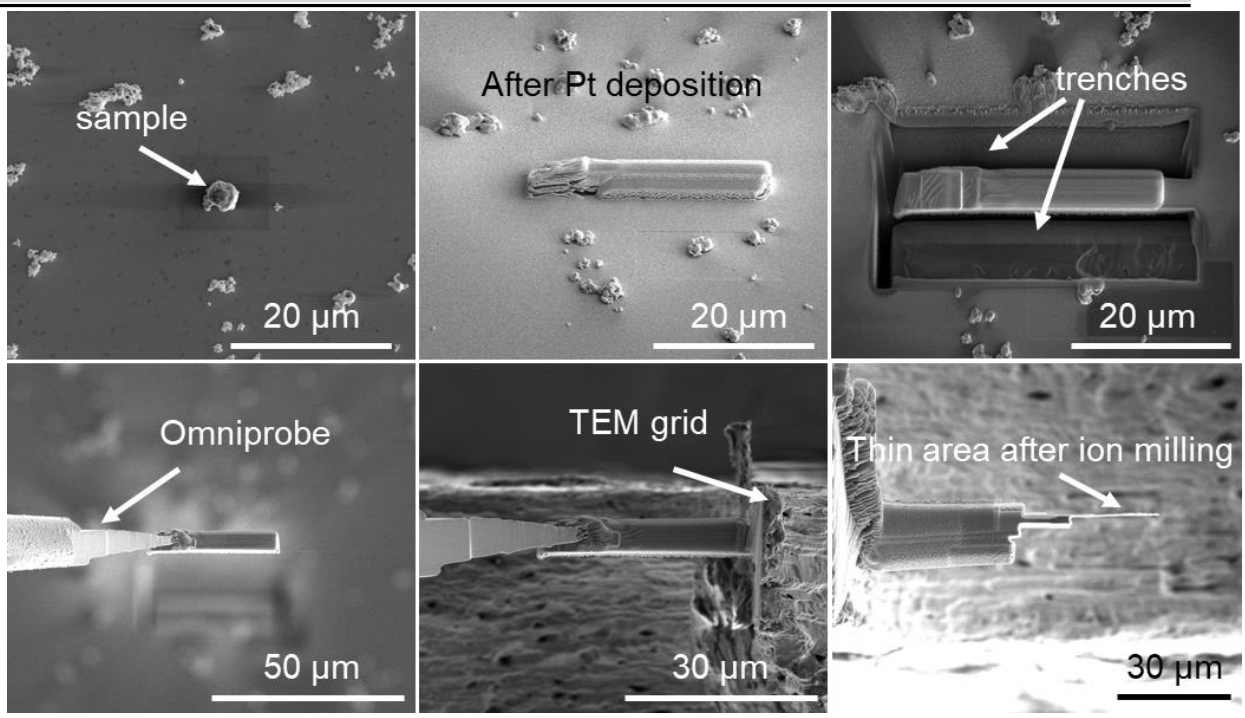

Figure 2-11: step by step procedures of TEM lamella lifting out: the desired particle was found in the SEM mode (shown in the top left image); Pt was deposited on the sample surface to protect the sample (top center image); two trenches were milled to remove the connection between the particle and the substrate (top right image); An Omniprobe was used to lifted out a thick lamella (bottom left image); the lamella was mounted on a TEM grid (bottom center image); the ion beam was used to thin the lamella (bottom right image)

2.4.3. TEM components and lens system

Figure 2-12 shows the overall optical setup of a TEM with the different components including an electron gun, condenser lenses, objective lens and projection lens system. An electron beam is emitted from the electron source and roughly shaped by the electron gun lens. The gun produces an image of the source emitting the electrons from the surface. In modern TEMs, the condenser system consisting of three electromagnetic lenses and apertures is used to tune the beam characteristics such as desirable intensity and convergence angle. The spot size is controlled by the strength of the C1 lens and its aperture. By strengthening the C1 lens an increasing part of electron beam will be blocked by the aperture and only the central more coherent part passes. Thus, a smaller probe will be obtained. The desired convergence angle is obtained by the combination of the C2 and C3 lens and their apertures. A mini condenser lens positioned below the C3 lens and above the objective lens is used for rapid switching between TEM and STEM mode. The objective lens is split into two parts, the upper and lower objective lens. In STEM mode, a convergent beam and, in TEM mode a parallel beam is formed by the upper objective lens to illuminate the specimen. An objective aperture positioned above the lower objective lens can be used to block certain parts of the transmitted beam to create contrast for bright field TEM imaging. The image formed in the image plane or the diffraction pattern formed in the back focal plane of the lower objective

lens are further magnified by the intermediate and the projection lenses to be projected on the camera as explained below.

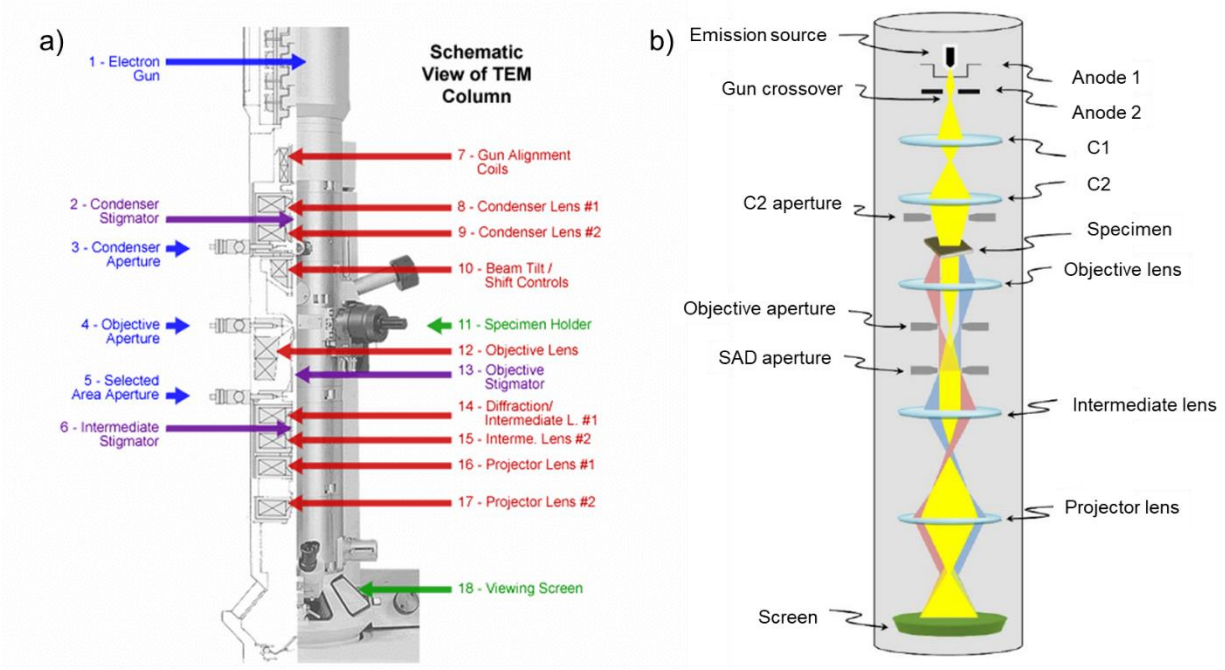

Figure 2-12: **a)** schematic representation of a TEM microscope including the main lens systems and apertures, adopted from[237]; **b)** schematic of the beam path diagram in a conventional bright-field TEM mode, adopted from[238].

2.5. Operating modes in TEM

In TEM imaging mode, the upper objective lens form a parallel beam illuminating the area of interest of the sample. As shown in the Figure 2-13, after exiting the specimen the scattered rays with the same propagation direction are focused at the same point in the back focal plane of the objective lens creating a diffraction pattern of the illuminated region. All rays emanating from one point in the specimen plane are brought to a point in the image plane of the objective lens, thereby forming a conjugate image of the illuminated area using the electrons passing the objective aperture. The objective aperture located in the back focal plane of the objective lens is used to enhance the image contrast by excluding high-angle scattered electrons. Following, the image is magnified and projected on the view screen by the projection system. The progress is shown in Figure 2-13-left. Diffraction mode can be activated by changing the strength of the intermediate lens. In diffraction mode, the focal length of the intermediate lens will be adjusted so to image the back focal plane of the objective lens onto the image plane of the projection lens and this will be further magnified and projected on the viewing screen by the projection lens system. In diffraction mode, a selected area aperture, which is placed in the image plane of the objective lens is used for selecting a specific region on the specimen. As the image plane is conjugated with the specimen plane, the insertion of the selected area aperture only allows the passage of electrons originating from the region of interest.

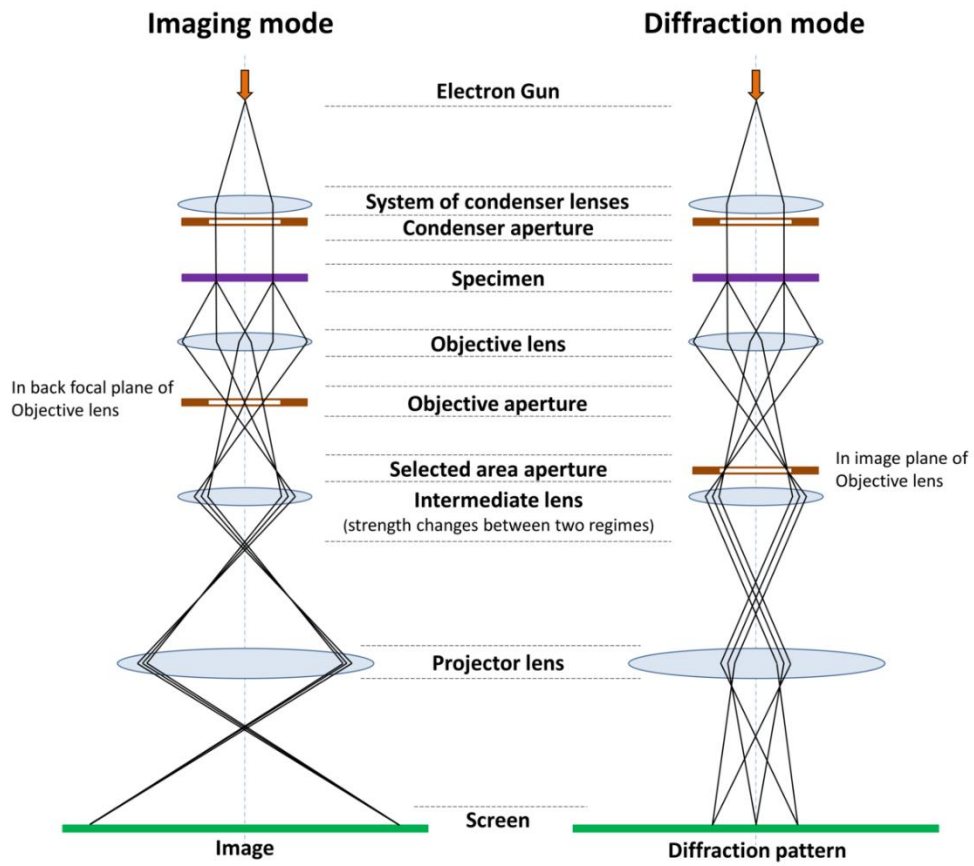

Figure 2-13: two basic operations modes of a TEM: image mode and diffraction mode, adopted from[239].

2.5.1. Bright field and dark field TEM

In imaging mode, both bright-field (BF) images as well as dark-field (DF) images can be acquired. The BF image originates from mass-thickness contrast and diffraction contrast. Mass-thickness contrast is a type of the amplitude contrast and usually dominates at low and intermediate magnification imaging of non-crystalline samples. Due to the characteristic of the electron-matter integration, higher Z or thicker areas scatter electrons more strongly. Therefore, the direct beam intensity will be reduced and those areas appear darker in a BF image. As shown in Figure 2-14a, in BF-TEM, the direct beam selected by the objective aperture is used to form the image that will be projected on the viewing screen after magnification by a series of projector lenses. Therefore, in the BF image the areas with lower Z elements and thinner thickness will show higher brightness as the objective aperture blocks the higher angle scattered electrons. Diffraction contrast is another type of amplitude contrast, which typically dominates the image contrast in crystalline materials. When a crystalline sample is irradiated by an electron beam and some crystal planes in the sample fulfill the Bragg condition, diffraction will occur and thus reduce the intensity of the primary beam. When the transmitted beam is imaged (the objective lens aperture is used to cover the transmission beam in the back focal plane of the objective lens to block all diffraction beam as shown in Figure 2-12a), the intensity of the areas containing crystal planes that fulfilled the Bragg

condition is reduced on the viewing screen. In DF mode, the primary beam is tilted so that one diffracted beam is centered in the objective aperture as shown in Figure 2-14b. A DF image is formed and projected on the view screen after the intermediate lens system. In a DF image, only the parts of crystals where the chosen diffracted beams are excited will show a high intensity.

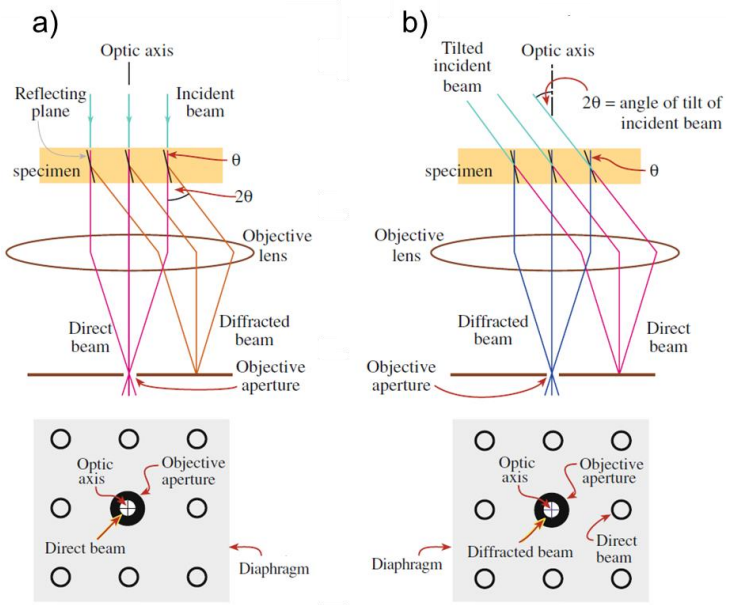

Figure 2-14: ray diagrams of the objective lens and objective aperture: **a)** BF image forming; **b)** DF imaging forming, adopted from[225].

2.6. HRTEM imaging

In HRTEM mode, the incident beam exiting the specimen will interfere with the different diffracted beams to form an interference pattern containing structural information of the specimen. The resolvable details of the image depend on the phase change caused by the incident wave scattered by the sample, the spherical aberration of the objective lens and the selection of additional phase difference caused by the defocus.[225] When a uniform incident beam passes through the specimen, a modulation of the incident wave is caused by the interaction with the potential of the specimen. The outgoing wave at the exit plane of the specimen can be described using following equation:

$$\psi(r) = A(r)e^{i\sigma V_p(r)t} \qquad 2\text{-}5$$

where $A(r)$ is the amplitude, σ is an interaction parameter, V_p is the projected potential, and t is the thickness of the sample. For very thin specimens an approximation is that no absorption occurs, $A(r)$ is constant, which is called as 'phase object approximation'. With this the wave function can be rewritten as:

$$\psi(r) = e^{i\sigma V_p(r)t} \qquad 2\text{-}6$$

If the thickness of the specimen is limited and the interaction parameter small enough, the exponential term is much smaller than 1. Equation 2-6 can then be approximated using only the first order term of the Tayler expansion of the exponential function:

$$\psi(r) = e^{i\sigma V_p(r)t} \approx 1 - i\sigma V_p(r)t \qquad 2\text{-}7$$

Equation 2-7 is called the 'week-phase object approximation'.

To understand how this exit wave is imaged by the microscope, the transfer by the optical system has to be considered. The lenses introduce aberrations, which modify the phase and can be described using a convolution of the exit wave with the transfer function describing the lens aberrations in real space , as shown in equation 2-8.

$$\psi_{image}(r) = \psi(r) \otimes T(r) \qquad 2\text{-}8$$

where T(r) is an aberration function of the general form $e^{-i\chi(r)}$, ignoring the aperture function.

Combining equation 2-7 with 2-8, the wave function in the image plane can be calculated:

$$\psi_{image}(r) = \left[1 - i\sigma V_p(r)t\right] \otimes e^{-i\chi(r)} = \left[1 - i\sigma V_p(r)t\right] \otimes [cos\chi(r) - isin\chi(r)] \qquad 2\text{-}9$$

The image intensity is the wave function multiplied by its complex conjugate and can be expressed as:

$$I(r) = \psi_{image}(r) * \psi^*_{image}(r) = 1 + 2\sigma V_p(r)t \otimes sin\chi(r) + |2\sigma V_p(r)t \otimes e^{-i\chi(r)}|^2 \qquad 2\text{-}10$$

In the weak-phase object approximation, $\sigma V_p(r)t$ is much smaller than 1 and thus the squared term in equation 2-10 is much smaller than the linear term. The leads to the linear imaging approximation, where the squared term is neglected.

$$I(r) = \psi_{image}(r) * \psi^*_{image}(r) = 1 + 2\sigma V_p(r)t \otimes sin\chi(r) \qquad 2\text{-}11$$

In Fourier space, equation 2-11 can be represented as:

$$I(g) = \delta(g) + 2\sigma V_p(g)t * sin\chi(g) \qquad 2\text{-}12$$

Where $V_p(g)$ is Fourier transform of $V_p(r)$, $\chi(g)$ is description of the aberrations in Fourier space. If only the spherical aberration Cs and defocus Δf are considered, $\chi(g)$ can be described using following equation:

$$\chi(g) = \pi C_s \lambda^3 \frac{g^4}{2} + \pi\lambda\Delta f g^2 \qquad 2\text{-}13$$

In equation 2-13, the first term presents the effect of the spherical aberration caused by the inhomogeneous magnetic field of a round electromagnetic lens. The electrons passing through the center of the lens and those passing further away from the optical axis are focused into a disk of a finite size

instead of a point. The second term in equation 2-13 describes the effect of defocus, which is leading to the formation of a disk in the image plane.

From the equation 2-12 and 2-13, we know that the image intensity represents the exit wave modulated by the phase shift $sin\chi(g)$ due to spherical aberration and defocus (Δf). The term $sin\chi(g)$ is referred to as contrast transfer function (Figure 2-15a). In a TEM the Cs of a classical lens is fixed, but the focus can be change and thus the frequency of the CTF. Figure 2-15b shows two CTF curves at different focus for a Tecnai F30 (high tension 300 kV, Cs 0.6 mm), together with the lattice distances for gold. The CTF has different signs at the (111) and (200) at different focus meaning that these planes will appear bright or dark in the final image at these two focus setting. The oscillation (negative or positive) in the CTF results in difficulties in interpreting HRTEM images. To avoid this ambiguity, the CTF should be constant or at least have the same sign over a wide range of spatial frequencies, which can be achieved with a particular defocus value, known as 'Scherzer focus' (Δf_{sch}).

$$\Delta f_{sch} = -1.2(C_s\lambda)^{1/2} \qquad 2\text{-}14$$

At the 'Scherzer focus', the point resolution (marked in Figure 2-15a) is defined as the first zero transition of the CTF. The information in the HRTEM images can be directly interpretable until the point resolution.

In addition, the oscillations of the contrast transfer function are damped by the coherence of the electrons and various instabilities, as shown in Figure 2-15a. The limited temporal coherence (E_t) is due to the energy spread of the electrons. Electrons with different energy will be focused at different heights resulting in a focus spread in the image plane. The limited spatial coherence (E_s) is caused by the size and angular spread of the electron source that leads to a slight phase shift of the illuminating wave. Mathematically, both act as a envelop function to the CTF, dampening the oscillation at high spatial frequency region, where the CTF varies rapidly. The so called 'information limit' refers to the envelope function falling off to $1/e^2$ (~13.5%), resulting in an image contrast considered too weak to transfer significant image information.

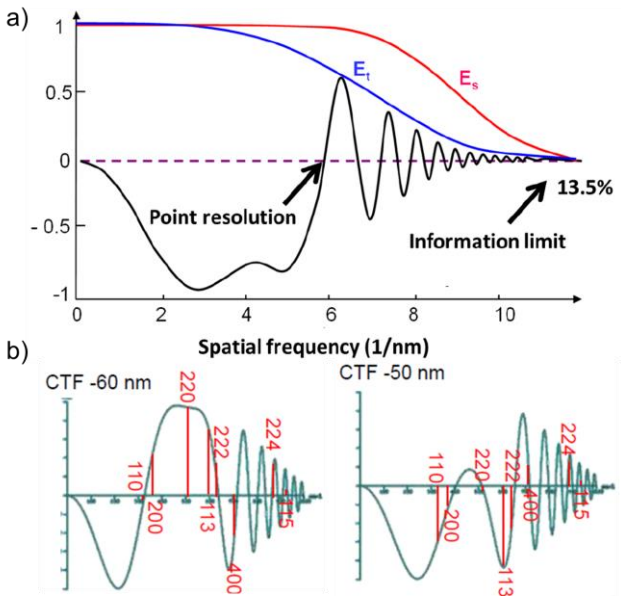

Figure 2-15: **a)** CTF of a microscope at Scherzer defocus with coherence envelop functions, adopted from reference[240]; **b)** contains two CFT at different focus of Tecnai F30 under the situation high tension of 300 kV and Cs of 0.6 mm, the red lines present the planes of *fcc* Au crystal, adopted from reference[241].

2.7. Scanning transmission electron microscopy

In addition to the conventional BF/DF and HRTEM imaging modes in TEM, most modern microscopes also allow imaging in STEM. The two operation modes, TEM and STEM, can be differentiated by the way the image is generated. In TEM mode a stationary almost parallel electron beam continuously illuminates the viewing area, whereas in STEM a (typically highly convergent) beam with a small probe size is scanned across the viewing area. A schematic of the beam convergence differences is show in Figure 2-16. In STEM the beam position is controlled by the scanning coils, which allows for a pixel-by-pixel scanning of the area of interest, illuminating the specimen at each scan point and collecting the scattered beam with the help of various (conventionally annular) detectors.

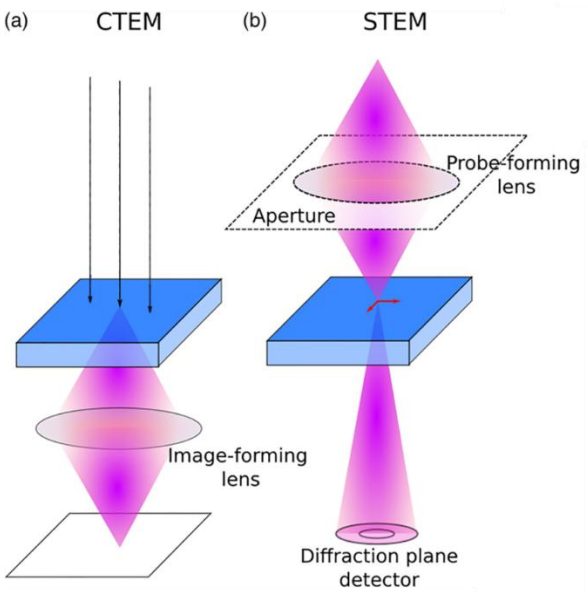

Figure 2-16: **a)** ray diagram of the beam path of CTEM mode; **b)** ray diagram of the beam path of STEM mode, adopted from[242].

In TEM mode, the resolution is limited by the objective lens aberrations as we discussed in the last section. In STEM mode, the resolution is controlled by the size of the scanning probe, which is determined by the aberrations of the probe forming system and the convergence angle (tuned by the combination of the condenser and upper objective lenses). In addition, a defocus directly leads to a beam not perfectly focused on the sample and generates a disk instead of a point, which can be tuned by looking at the sharpness of the image or the Ronchigramm, which will be explained later. For a hypothetical aberration free lens, the probe size is diffraction limited as described by Rayleigh criterion (equation 2-15).

$$d = 0.61\lambda / \sin\alpha \qquad 2\text{-}15$$

where *d* is the probe size, λ is wavelength, and α presents the convergence angle. However, in a real lens, spherical aberration has to be considered, which dramatically increases the probe size with a relationship proportional to the third power of convergence angle, as well as higher order aberrations. In addition, a large convergence angle will also increase chromatic aberration effects for the probe. Therefore, in an uncorrected STEM microscopes a trade-off between the convergence angle and the spherical aberration has to be made by selecting the right probe forming aperture. This is illustrated in Figure 2-17, which presents the influence of the size of condenser aperture and thus of the convergence angle, on the size and the intensity profile of the STEM probe. In practice, only considering the effect of Cs and convergence angle the best resolution can be achieved using following equation:

$$\alpha_{opt} = 1.41(\lambda/Cs)^{1/4} \qquad 2\text{-}16$$

where α_{opt} is the convergence angle for a given spherical aberration. By combing equation 2-15 and 2-16 the resolution in STEM can be determined:

$$d = 0.43\lambda^{3/4}Cs^{1/4} \qquad 2\text{-}17$$

Ignoring higher order aberrations, equation 2-17 means that the optimum resolution (*d*) is limited by the spherical aberration (Cs) for a given wavelength.

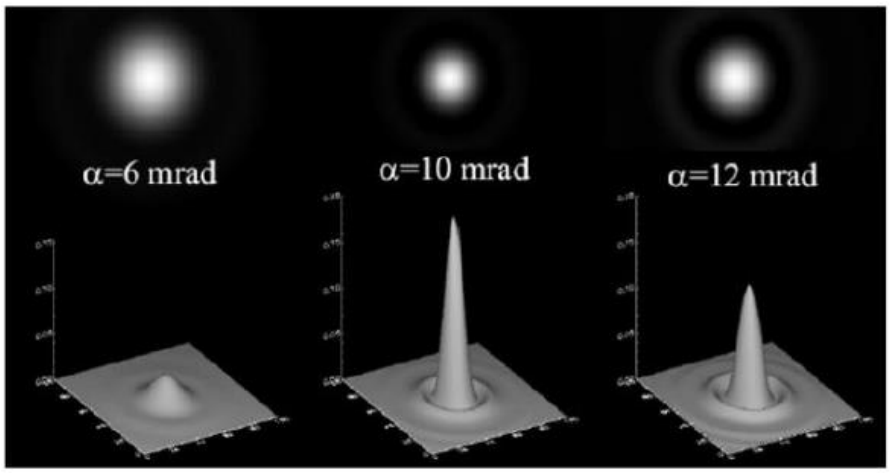

Figure 2-17: influence of convergence angle to the probe shape and brightness, adopted from reference[243].

In STEM mode, bright field (BF) and annular dark field (ADF) detectors, are most commonly used for imaging, and are mounted underneath the specimen to collect the electrons at different scattering angles. Figure 2-18 schematically presents the position of the three most commonly used integrating detectors in STEM mode. STEM-BF images formed by the BF detector are similar to BF-TEM images. At higher collection angles, the electrons collected by ADF detectors are dominated by electron diffraction, resulting in similarly complex contrast mechanism for STEM-ADF images as in DF-TEM. A high angle annular dark field (HAADF) detector is used to collect signals at even higher scattering angles (θ>50 mrads) (Figure 2-18), which is dominated by Rutherford and thermally diffuse scattering. The HAADF signal is considered to be incoherent for sufficiently large inner collection angles (about 3 times the convergence angle). The ADF image intensity can be approximated as[244]:

$$I_{ADF}(R_o) = |P(R_o)|^2 \otimes O(R_o) \qquad 2\text{-}18$$

where R_o is the probe position, $P(R_o)$ is the probe function and $O(R_o)$ is the object function. Equation 2-18 means the ADF image intensity ($I_{ADF}(R_o)$) is the object function ($O(R_o)$) convoluted by the intensity of the illuminating probe ($|P(R_o)|^2$), which describes incoherent imaging.

During the electron-matter interaction, high *Z* elements are more likely to scatter the incident electrons to larger angles. The differential cross section for high-angle scattering can be expressed by equation 2-19.

$$\delta_R(\theta) = \frac{e^4 Z^2}{16(4\pi\varepsilon_0 E_0)^2} \frac{d\Omega}{sin^4\frac{\theta}{2}} \qquad 2\text{-}19$$

where *e* is the charge of an electron, *Z* presents the element number, E_0 is the incident beam energy, ε_0 is the vacuum permittivity, Ω is the total solid angle of scattering and ϑ is the angle of scattering. In reality, the nucleus is partially shielded by the electrons leading to a scattering probability proportional to $Z^{1.6}$ - Z^2.[245] Therefore, the images generated using a HAADF detector show higher intensity for high Z

elements. The intensity in STEM-HAADF is also affected by the thickness of the specimen as the total scattering probability increases with increasing specimen thickness.

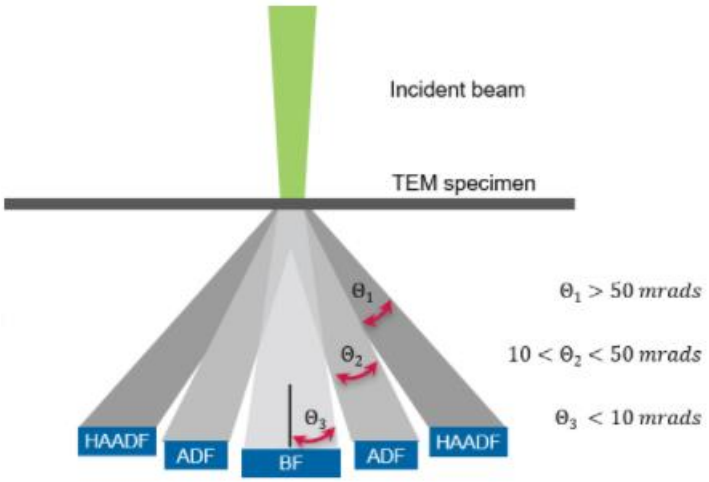

Figure 2-18: diagram of the angular arrangement of the three most used detectors in STEM, adopted from[246].

In addition to imaging, the combination of STEM with analytical techniques such as EDX and EELS provides analytical information about the specimen with high spatial resolution. More recently, 4D-STEM, where the complete 2D diffraction pattern is recorded for every pixel in a 2D real space map, was developed and is now widely used to obtain virtual STEM images and to study crystal orientations, phase and strain in large areas of a given specimen.[247] Pixelated direct electron detectors with complementary metal oxide semiconductor (CMOS) technology, which have a very high frame rate, are commonly used for collecting the diffraction patterns. By applying different processing of the 4D data set, virtual STEM images with customized detection angles can be generated at any time post-acquisition[246]. Therefore, this virtual STEM imaging is not limited by the shape and the number of the detectors, which are fixed during conventional STEM imaging. When 4D-STEM is used to study the crystallographic orientation or phase information, orientation or phase maps are produced by indexing the diffraction patterns of each scanned point. An almost parallel beam, that forms much smaller diffraction spots compared with a highly convergent beam, is selected for obtaining better resolution in the reciprocal space. However, this will generate a larger probe size and thus sacrifice the resolution in real space. Therefore, in 4D-STEM data acquisition a compromise needs to be achieved between the spatial resolution and the diffraction resolution.

2.8. High order aberrations and aberration correction in (S)TEM

Form the last two sections, we can see that spherical aberration and defocus significantly affect the resolution in both TEM and STEM mode. However, other aberrations introduce additional phase shifts and thus affect the experimental resolution. Two-fold astigmatism and coma are the two most important aberrations. Astigmatism is caused by an inhomogeneous magnetic field of the lens resulting in a different

focal strength in different directions. The two-folder astigmatism can be easily corrected by stigmators that can induce fields to counter these inhomogeneity. Coma as one aberration appears when the electron beam is tilted away from the optic axis of the objective lens. It results in an additional inverse phase shift for +g to –g reflections. It can be corrected by tilting the beam to be parallel to the optical axis of the objective lens.[248]

In addition, high order aberrations with higher rotational symmetry, such as higher order spherical aberrations, astigmatism and coma as well as star aberration, need to be considered for sub-Angstrom resolution in modern TEMs as they induce a phase shift at high spatial frequencies. Following the common notation, ordering the aberrations in terms of scattering angle $\omega=\lambda g$ and its complex conjugate $\overline{\omega}$, the aberration wave function $\boldsymbol{\chi}(g)$ can written as[249]:

$$\chi(\omega) = Re\{\tfrac{1}{2}\omega\overline{\omega}C_1 + \tfrac{1}{2}\overline{\omega}^2A_1 + \omega^2\overline{\omega}B_2 + \tfrac{1}{3}\overline{\omega}^3A_2 + \tfrac{1}{4}(\omega\overline{\omega})^2C_3 + \omega^3\overline{\omega}S_3 + \tfrac{1}{4}\overline{\omega}^4A_3 + \omega^3\overline{\omega}^2B_4 + \omega^4\overline{\omega}D_4 + \tfrac{1}{5}\overline{\omega}^5A_4 + \tfrac{1}{6}(\omega\overline{\omega})^3C_5 + \tfrac{1}{6}\omega^2\overline{\omega}^4S_5 + \tfrac{1}{6}\overline{\omega}^6A_5 + \cdots\} \quad \textit{2-20}$$

According to the nomenclature introduced by CEOS, C_1, A_1, B_2, A_2, C_3, S_3, A_3, B_4, D_4, A_4, C_5 and A_5 present the residual aberration coefficients due to defocus, two-fold astigmatism, axial coma, three-fold astigmatism, spherical aberration, star aberration, four-fold astigmatism, fourth-order axial coma, three lobe aberration, five-fold astigmatism, five-order spherical aberration, six-fold astigmatism. The effect of the aberrations can be understood by representing the phase changes introduced by them as phase plates (Figure 2-19).

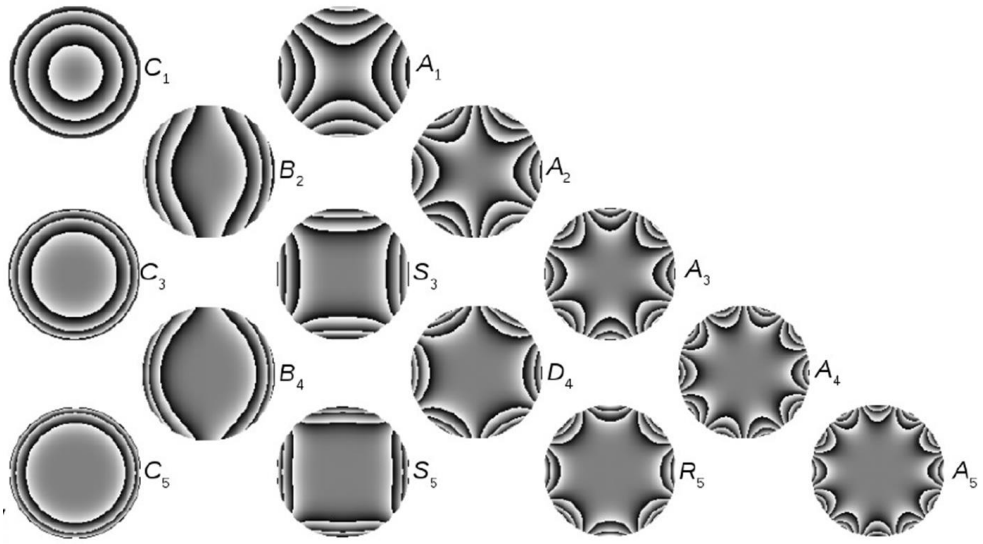

Figure 2-19: table of axial aberrations visualized as phase plates, modified from reference[250].

When high resolution in real space images is desired, the information contained at high scattering angles needs to be transferred. Considering equation 2-20, with increasing power of ω, the higher order aberrations become increasingly dominant for the phase shift introduced by the aberrations. To achieve

the sub-angstrom resolution, aberration correctors are used to compensate both low- and high-order aberrations using a complex combination of non-round lenses. The corrector consists of non-round optics such as hexapoles and/or octupoles, to induce negative spherical aberration to compensate the positive aberrations of the round objective lens (for TEM) or the probe forming lenses (for STEM). In practice, the correction is implemented using a Zemlin Tableau that makes use of a series of diffractograms at different beam tilts. During tilting, the apparent astigmatism and defocus changes, from which the different aberrations can be calculated. Correctors can dramatically improve the point resolution of TEMs and allow the CTF to exhibit the same sign over a wide range of spatial frequencies (Figure 2-20a). Thus, C_s corrected microscopes help in the more intuitive analysis of the HRTEM image contrast. For STEM, figure 2-20b shows that the probe size and the intensity profile of the probe are significantly improved using probe aberration correctors, meaning that much higher resolution and probe current can be obtained.

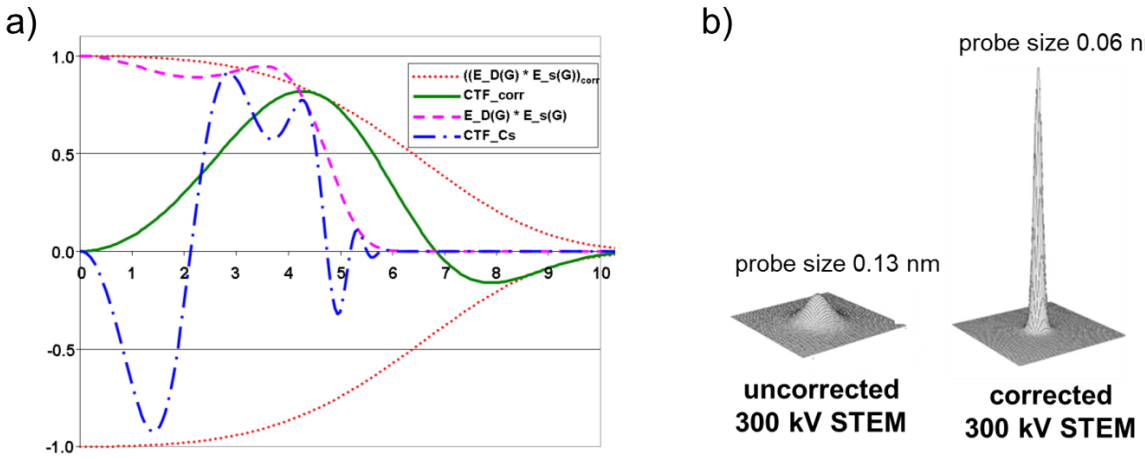

Figure 2-20: **a)** CFTs and the envelop functions from the Cs corrected and uncorrected TEM, red dot and green solid line present the envelop function and CTF of corrected system, the pink dash line and blue dot-dash line are the envelop function and CTF with Cs aberration, adopted from reference[251]; **b)** comparison of the probe size and intensity between the uncorrected and corrected STEM, adopted from reference[241].

2.9. Spectroscopic techniques

As presented in section 2.2., the interaction of the primary electrons with matter gives rise to a multitude of signals that can be used for imaging and analytical TEM techniques. The following section will deal with the fundamentals and some practical aspects of the two most important analytical techniques in TEM, e.g. energy-dispersive X-ray spectroscopy and electron energy loss spectroscopy.

2.9.1. Energy-dispersive X-ray spectroscopy

Figure 2-21 schematically shows the classical geometry of an EDX detector in a TEM column. The detector is mounted between the upper and lower objective pole pieces to collect the X-ray signal with a solid angle Ω, which is related to the active area of the detector and the distance of the detector to the emitting surface.[252] After the interaction of the primary electrons with the specimen, X-rays will be

emitted in all directions. Compared with the full solid angle of characteristic X-ray generation, the desired solid angle of Ω of the detector is only covering a small fraction. By increasing the number of detectors, shortening the detector-specimen distance and optimizing the geometry of detector system, the efficiency of EDX detectors in modern TEMs has been enhanced dramatically, but there is still room for improvement.[253]

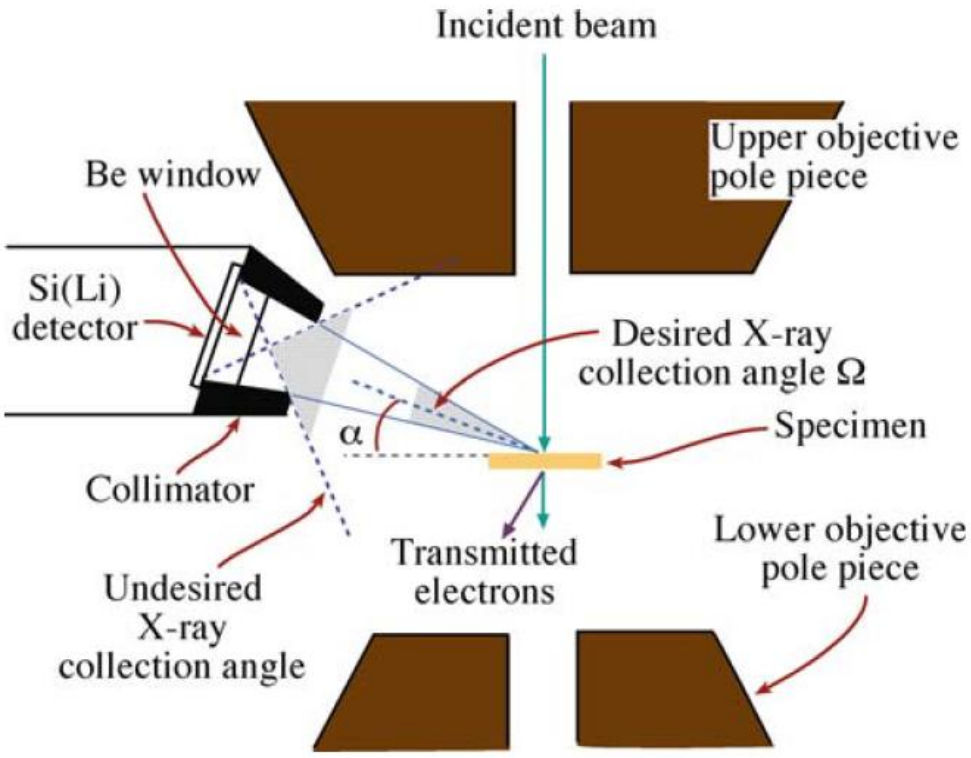

Figure 2-21: schematic representation of a conventional geometry of a single X-ray detector positioning in the TEM column, adopted from[225].

The most common X-ray detectors are based on lithium drifted silicon (Si(Li)) technology, and more recently an improved technology based on silicon drift detectors (SDD) have been implemented. Figure 2-22 shows a cross section of a Si(Li) detector. When a X-ray hits the detector, many electron-hole pairs will be generated in the silicon crystal of the detector. An electrical bias applied across the detector will separate the electron-hole pairs: the electrons are attracted in one direction and the holes moved in the opposite direction, which will generate an electrical pulse. The charge pulse is converged to a voltage pulse and amplified by a field-effect transistor. Higher X-ray energies gives rise to more electron-hole pairs and thus result in a stronger signal. This signal is converted to the X-ray energy and plotted as EDX spectrum with the energy as one axis and the number of counts on the other axis. In EDX spectra, each element gives rise to specific peaks while a continuum background is due to the Bremsstrahlung. EDX detectors require cooling to reduce the thermal excitation that leads to high background noise. Moreover, the lower temperatures will also reduce the diffusion of lithium inside the Si crystal that occurs when the voltage is applied.

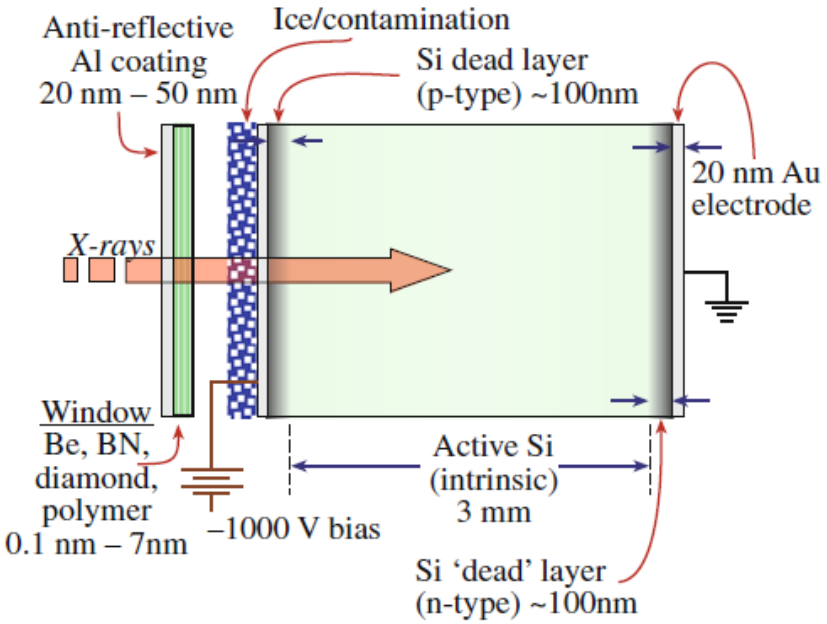

Figure 2-22: cross section of a Si(Li) detector, adopted from reference[225].

In practice, artifacts are present in the spectra, which can be divided into signal-detection artifacts and signal-processing artifacts. The 'internal fluorescence peak' and 'escape peak' are two types of signal-detection artifacts, which appear in the spectra due to the interaction between the incoming X-rays and the detector itself. The 'internal fluorescence peak' is a characteristic peak from Si (in Si containing EDX detectors). The 'escape peak' is the counterpart occurring when high-energy x-ray photons are exciting the Si-K X-rays. The associated energy loss results in a new peak in the X-ray spectrum with an energy equal to the elemental characteristic X-ray minus Si-K edge energy. Fortunately, they are efficiently reduced in the modern SDD detectors. One typical signal-processing artifact is 'sum peak', which is caused by more than one X-ray hitting the detector within the processing time and are thus counted as a single signal. In addition, characteristic X-ray signals can be generated from the objective lens pole pieces, sample grid and the specimen holder itself as well, because of interactions with secondary electrons and X-rays. A collimator is assembled in front of the detector to shield it against the entry of undesired parasitic X-rays as shown in Figure 2-21. When the EDX is used for a qualitative analysis, these artifacts need to be considered.

Besides qualitative elemental identification, EDX can also be used as a quantitative technique after the continuum Bremsstrahlung background in the spectra has been properly subtracted. This is because the intensity of each of the characteristic lines of an element is proportional to the elemental concentration in the illuminated volume. However, the detector efficiency for the detection at different energies, the elemental characteristics, and the density and thickness of the specimen need to be consider. To quantify an EDX spectrum, so called K factors are used as correction parameters, which depend on the atomic number, absorption and fluorescence of X-rays within the specimen and the detector

characteristics. The *K* factors can be determined by measuring the intensity ratio in a standard sample with known elemental ratio. In practice, the *K* factor calculation is embedded in the processing software used for EDX quantitation. Based on the Cliff-Lorimer equation, for two given elements (A and B) the concentration ratio (C_A/C_B) can be measured based on the intensity ratio (I_A/I_B) in the spectrum. It can be expressed as $\mathrm{C}_A/C_B = K_{AB} * \mathrm{I}_A/I_B$, where K_{AB} are the K factor (or Cliff-Lorimer factor) between the elements A and B.

2.9.2. Electron energy loss spectroscopy

As previously described, the energy lost by the primary electron beam during inelastic interaction with the sample, can be used in electron energy loss spectroscopy to characterize the chemistry of materials complementing EDX analysis. EELS is especially powerful for identifying low Z elements and has a much higher energy resolution. In addition to the chemical composition, the higher energy resolution in EELS enables to get additional information on the specimen, such as bonding/valence state, nearest-neighbor atomic structure, dielectric response, free-electron density, band gap and specimen thickness.

Figure 2-23 shows a schematic of a Gatan Image Filter (GIF) spectrometer. The transmitted electron beam, including the inelastically and elastically scattered electrons and the direct beam is selected by an entrance aperture. Due to the different energy of the scattered electrons, they are dispersed to different positions in the dispersion plane after the magnetic prism. With increasing energy loss, the electrons will be deflected more strongly due to the Lorentz force of the magnetic prism. In spectrum mode, the specific energy loss spectra from the illuminated area of the specimen will be shown, which integrates the signals with different energy loss perpendicular to the energy plane. The spectrometer is also equipped with an energy slit after the magnetic prism, selecting the electrons with desired energy loss. The electrons passing through the energy slit and a complex lens system can be used to form an energy filtered TEM (EFTEM) image.

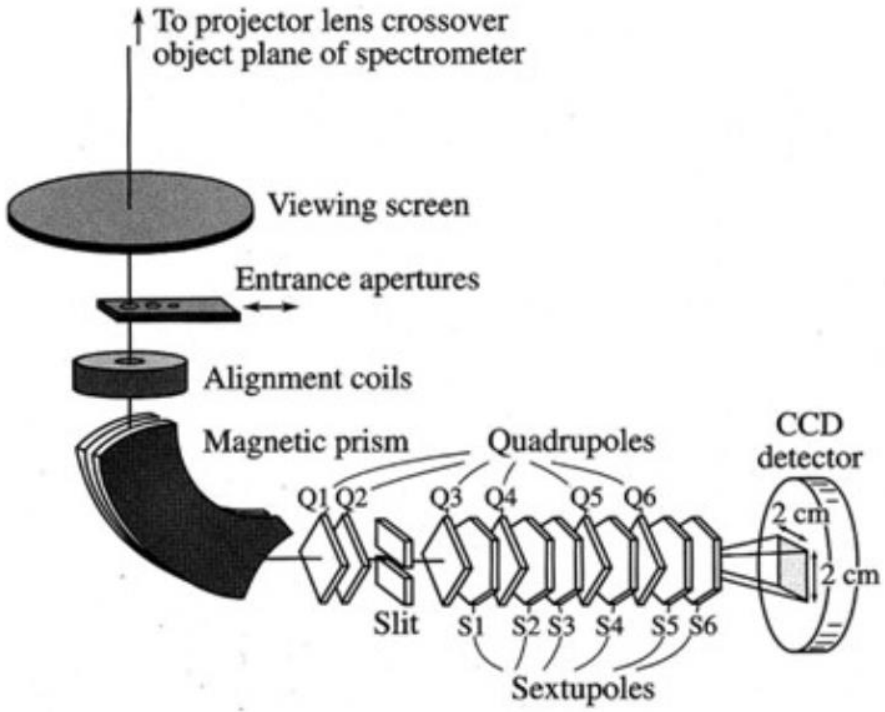

Figure 2-23: schematic image of the Gatan image filter (GIF). This spectrometer is mounted at the bottom of the microscope column, beneath the views screen, adopted from reference[254].

The collection angle β is the most important parameter for EELS, which affects the collection efficiency, the signal to noise ratio and the elemental quantification.[225] Larger collection angles enable gathering of more scattered electrons, but with a trade-off in energy resolution of the spectra. In practice, it is recommended that the EELS collection angle should be set to 3 times of characteristic scattering angle (ϑ_E) for an optimal signal to background ratio.[255] ϑ_E can be calculated by:

$$\theta E = \frac{E_{edge}}{2E_0} \qquad 2\text{-}21$$

where the E_{edge} and E_0 are the energy loss at the specific edge and the primary beam energy. As shown in the Figure 2-24a, in diffraction mode, the size of the entrance aperture is the final element controlling the collection angle, with larger apertures resulting in larger collection angles. However, in TEM image mode, a magnified image of the specimen is present at the GIF entrance plane, and the angular distribution of the electrons is controlled by the objective aperture in the back-focal plane of the objective lens. Therefore, the spectrometer aperture does not limit the collection angle, which can be calculated by the specific value of the maximum radius (r_0) of the DP in the back focal plane and the camera length L as shown in Figure 2-24b.

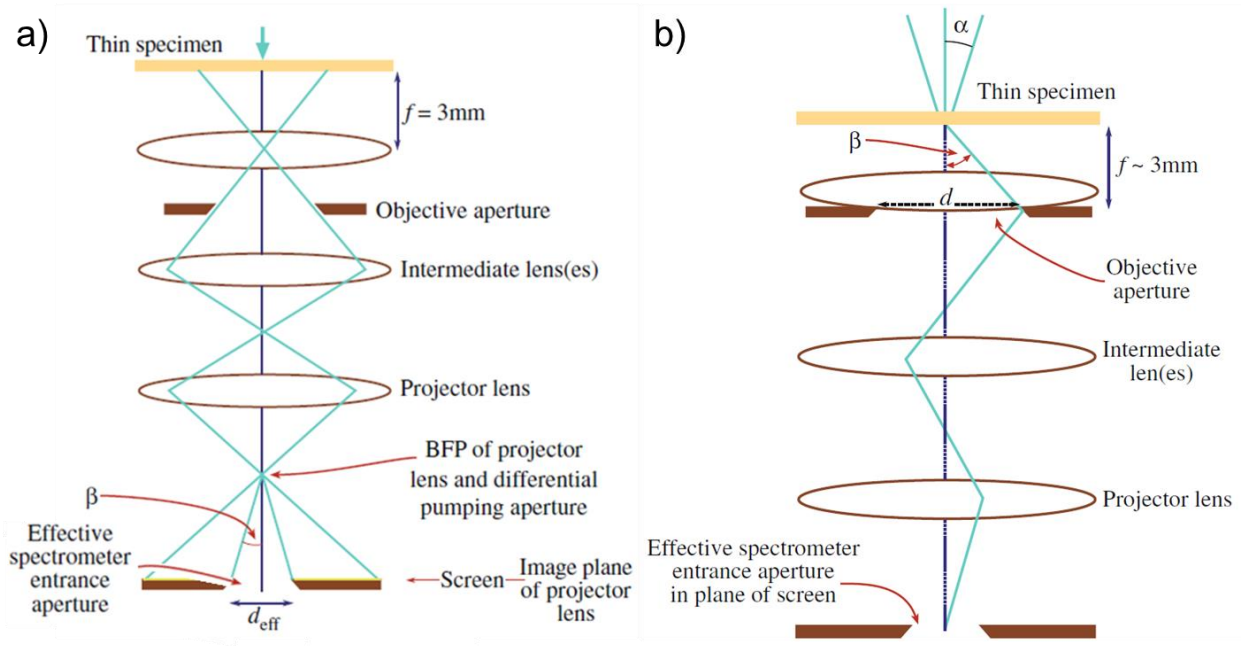

Figure 2-24: diagrams illustrating the factors influencing the collection angle (β) in EELS. **a)** S/TEM diffraction mode where, for a fixed camera length β is given by the spectrometer entrance aperture; **b)** TEM mode where β is independent of the entrance aperture and controlled by the objective lens, adopted from[225].

After the dispersion of the electron beam by the magnetic prism based on the energy loss, an EELS spectrum is obtained where the energy is plotted along the x-axis (energy loss axis) and the intensity is plotted on the y-axis (Figure 2-25). Based on the different processes leading to the energy loss, EELS spectra can be divided into a low energy loss and a high energy loss region. The low loss region that generally extends up to 50 eV contains the zero loss peak (elastically scattered electrons), the valence loss and plasmon peaks. As can be seen in Figure 2-25, the intensity of the high energy loss region generated by the core losses, is much lower than in the low energy loss region, meaning that the vast majority of the electron-matter interaction is represented by phenomena represented in the low energy loss region.

A simple but important practical application of the low energy loss region is thickness determination, which can be done using:

$$t = \lambda \, ln \frac{I_t}{I_0} \qquad 2\text{-}22$$

where t the specimen thickness, I_t is total EELS intensity, I_0 is intensity of zero loss, λ is average inelastic mean free path of the primary electrons. Based on many experimental measurements, Malis et al. have given an empirical equation for the mean inelastic mean free path[256]:

$$\lambda = \frac{106F(E_0/E_m)}{ln(2\beta E_0/E_m)} \qquad 2\text{-}23$$

where λ is in nm, F a relativistic correction factor that is described in equation 2-24, E_0 is the incident electron energy in keV, E_m is the average energy loss in eV and equal to $7.6Z^{0.36}$, β is collection semi-angle

in mrad. Form equation 2-23, we see that the mean free path λ increases with incident electron energy and decreasing average atomic number. However, orientation and channeling effects are not considered in equation 2-23, which affect the mean free path and thus the thickness calculation as well. The simplest way to avoid it is to operate under kinematical conditions and stay away from the Bragg condition.

$$F = \frac{1+E_0/1022}{(1+E_0/511)^2} \qquad 2\text{-}24$$

The high loss region is the result of the excitations of electrons in a core shell of an atom to an unoccupied states or to the continuum. When the incident electron interacts with a core shell electron and excites it to an unfilled empty state, a specific energy E_{edge}, the difference between the two states, will be transferred to the bound electron. It is also possible to ionize an atom by transferring a higher energy than E_{edge}. However, the ionization cross section decreases with increasing energy above E_{edge}. As a result, the core loss electrons have an energy distribution that ideally shows a sharp rise to a maximum at E_{edge} followed by a slow decrease in intensity toward the background. However, some oscillations occur after the ionization edge in an EELS spectrum. The oscillations occurring within about 30-50 eV after E_{edge} is termed as energy-loss near edge structure (ELNES) and the weaker oscillations extending out of several hundred eV after ELNES is termed as extended energy-loss fine structure (EXELFS), which present the bonding information and the nearest atom coordination information as discussed previously for X-rays in section X.XX.

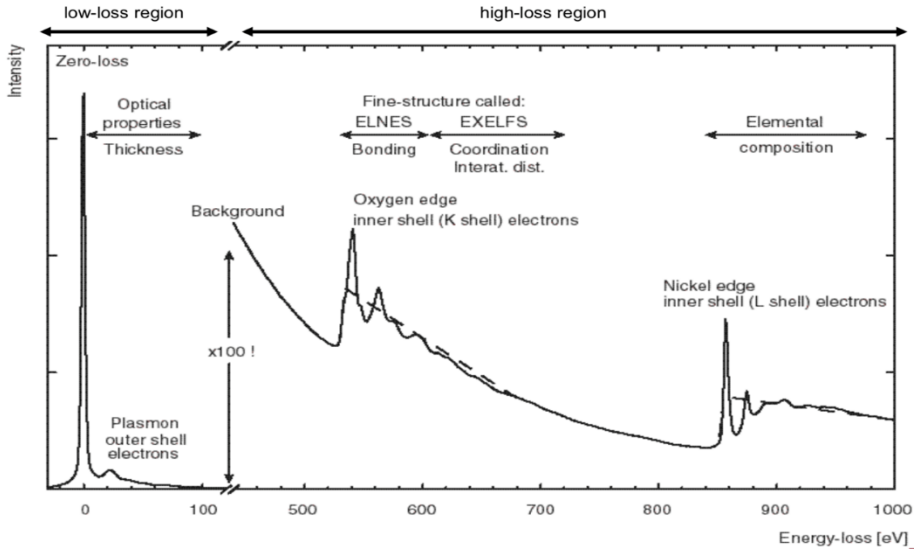

Figure 2-25: typical EELS spectrum of a NiO thin specimen. The energy loss range is from -15 eV to 1000 eV and the intensity is multiplied by 100 times after 200eV, adopted from reference[227].

Based on Fermi's golden rule for the electric dipole transition probability and the density of states, the probability of an electron to be excited to an empty state is not uniform.[257] The oscillations in the ELNES reflect the density of available states (modulated by the dipole selection rules) of an element above the Fermi level. The density of states is highly sensitive to the type of bonding as well as the charge state.

Therefore, details in ELNES can offer information on chemical bonding and oxidation state of the elements. For most transition metals, the intense near-edge structure of the L-edges (named white lines) corresponding to an electron transition from 2p to 3d can be clearly observed.[258] The L3/L2 peak ratio or their energy loss position reflect the state of the outer-shell electrons and are very useful for valence analysis. If a much higher energy than E_{edge} is transferred to an electron in the filled states, the electron will escape and act like a free electron. The excess energy can be regarded as an electron wave, which can be diffracted by the atoms in the structure around the original ionization site, thus contains structural information. This type of weak oscillations in EELS spectra is studied by EXELFS.

In addition to the above mentioned information, EELS is a powerful tool for elemental quantification. After background removal and plural scattering deconvolution, the edge intensity above the background I_{edge} can be obtained from the integration of the spectrum over a certain energy range. By assuming that the electrons contributing to the edge have only undergone a single ionization event, the number of the atoms in per unit area in a specimen can be calculated by:

$$N = \frac{I_{edge}(\beta,\Delta)}{\sigma_{edge}(\beta,\Delta)I_t} \qquad 2\text{-}25$$

where $I_{edge}(\beta,\Delta)$ is the integral edge intensity without plural scattering over an energy window Δ with an effective collection angle β, $\sigma_{edge}(\beta,\Delta)$ is the partial inelastic scattering cross-section meaning the probability for an individual ionization process that can be obtained by either theoretical calculations or comparing experimental spectra with known standards. Two computer programs, SIGMAK and SIGMAL, are embedded in Gatan software to theoretically model the K and L shell partial cross sections[225,227] I_t is the total transmitted intensity. The ratio between different atoms (A and B) can be calculated by equation 2-26.

$$\frac{N_A}{N_B} = \frac{I_A(\beta,\Delta)\sigma_B(\beta,\Delta)}{I_B(\beta,\Delta)\sigma_A(\beta,\Delta)} \qquad 2\text{-}26$$

Compared with EDX, EELS has higher signal collection efficiency. In EELS the collection angle is normally larger than the characteristic scattering angle, while the EDX detectors can only obtain the X-ray from a limited solid angle of the full spherical space. However, EELS has a lower signal to background ratio due to the higher plural scattering and has a strict requirement for the sample thickness. The accuracy of EELS quantification depends on the background removal, peak shape and plural scattering deconvolution. In practice, the two techniques should be chosen based on the specimen condition, such as the type of elements contained, their concentration, specimen thickness and the scientific question that need to be answered.

2.10. Pair distribution function

Electron diffraction is a common and important approach to study the crystalline structure of specimens. By indexing the peaks in a diffraction pattern, considering distances and angles between different planes, the crystal structure of specimen can be identified. Amorphous materials are missing long-range order making their structural characterization compared to crystalline samples. However, the short range order in amorphous materials is characterized by specific bonding distances and bonding angles. This short range order information is embedded in electron diffraction patterns and can be used for structural analysis. This can be achieved using pair distribution function (PDF) analysis that resolves the distribution of distances between pairs of atoms contained within a given volume and is an effective way to describe the short range order in a material. An example for a PDF is shown in Figure 2-26a where the *x*-axis represents the atomic distances and the y-axis represents the number of pairs with a specific distance. Assuming that the distributions of atomic pairs is isotropic when averaged for a sufficiently large volume, the PDF can be represented using a delta function:

$$P(r) = \sum_m^N \sum_{m \neq n}^N \delta(r - r_{mn}) \qquad 2\text{-}27$$

where the r_{mn} represents the distance between atom *m* and *n* and *N* presents the total number of atoms in the illuminated volume. Equation 2-27 describes the PDF, which is counting the cumulative number of atomic distances in the sample. With increasing pair distance, the probability of finding atoms increases due to the increasing surface, which is causing a continuously increasing background in the PDF (Figure 2-26b). The intensity of the PDF will fluctuate around this background. After removing the background, the resulting function is called reduced PDF. This PDF represents the boding distances and is used characterize amorphous materials. The distribution is then defined as [259,260]:

$$G(r) = \frac{1}{4\pi r}\left[\frac{1}{2N}P(r) - 4\pi r^2\rho\right] = \frac{1}{4\pi r}\left[\frac{1}{2N}\sum_m^N \sum_{m \neq n}^N \delta(r - r_{mn}) - 4\pi r^2\rho\right] \qquad 2\text{-}28$$

where ρ is average atomic density in the material and *r* is set of all possible r_{mn}.

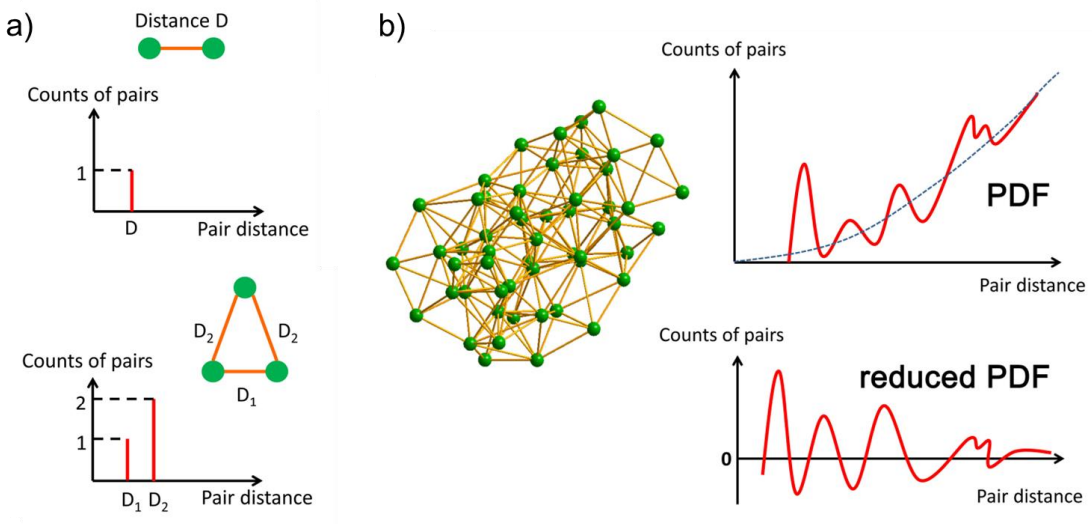

Figure 2-26: **a)** a simple example of PDF in two (up) and three (down) atoms systems; **b)** PDF (P(r)) and reduced PDF ($G(r)$) in an amorphous structure, modified from reference[261].

Experimentally, the PDF can be derived from various of types of measurements including XRD[261], SAED[262], XAS[263] and EELS fine structure[225]. Electron diffraction based PDF was used in this thesis. Here we explain the process of extracting the PDF from TEM diffraction data. According to the Debye formula[264], the diffraction intensity $I(s)$ can be described as:

$$I(s) = \sum_m^N f_m(s)^2 + \sum_m^N \sum_{m \neq n}^N f_m(s) f_n(s) \frac{sin(2\pi s r_{mn})}{2\pi s r_{mn}} \quad \textit{2-29}$$

where m and n present all atoms, $s = 2\theta/\lambda$, θ is scattering semi-angle and λ the wavelength, $f_m(s)$ represent the single atomic scattering intensity of element m, r_{mn} is the pair distance between atom n and m. The first term in equation 2-29 is called single atomic scattering factor, which gives rise to a steadily decreasing background in the SAED profile. The second term represents the scattering contribution of the atomic pairs with the corresponding phase factor. This contains the information about the atomic distances and produces the oscillations around the background in the SAED profile. Following the procedure in reference[264,265], a diffraction profile can be normalized to:

$$\varphi(s) = \frac{I(s) - N f(s)^2}{N f(s)^2} s \quad \textit{2-30}$$

where N is the number of atoms irradiated by the electron beam, $f(s)$ is the average atomic scattering factor of all elements contributing to the diffraction pattern. $\varphi(s)$ is referred to as the structure factor, describing the structural information in reciprocal space, which is the inverse sine transform of the PDF. Figure 2-27 displays the processes to obtain a PDF from a diffraction pattern. A 1D profile can be acquired in radial direction of a 2D diffraction pattern by azimuthal averaging of the intensity. The profile is fitted at high diffraction angles to extract the single atomic scattering background using equation 2-30. Multiple scattering also needs to be considered as it contributes to the diffraction background without introducing additional structural information. It causes oscillations with low spatial frequency. These artifacts introduced by multiple scattering can be effectively suppressed by applying a polynomial function correction to the structure factor.[266] Finally, the reduced PDF can be obtained by a simple reversed Fourier sine transform of the structure factor.

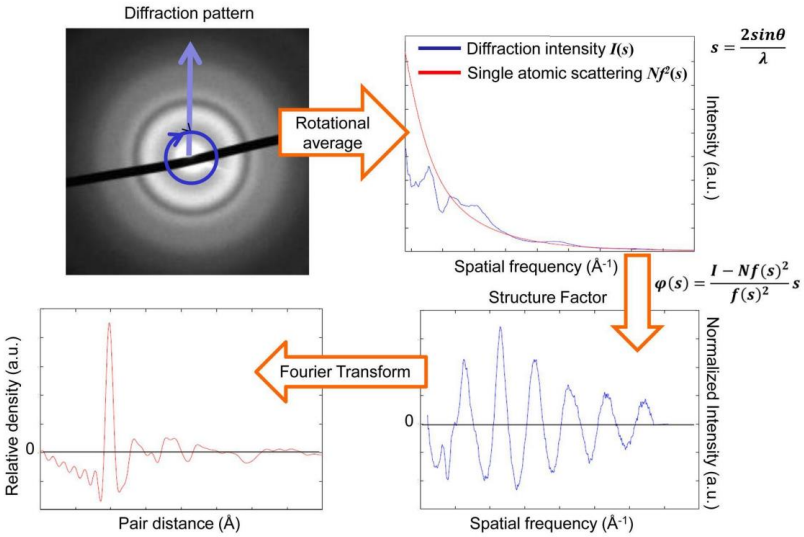

Figure 2-27: schematic of the step by step procedure of t extracting the PDF data from a 2D electron diffraction pattern, adopted from reference[261].

3. Chemical and microstructural evolution during synthesis of a high entropy oxide observed by *in-situ* gas heating transmission electron microscopy

3.1. Introduction

High entropy materials (HEO) are exhibiting promising application prospect in various fields. Among this new class of materials, $(Mg_{0.2}Co_{0.2}Ni_{0.2}Cu_{0.2}Zn_{0.2})O$ HEO has shown outstanding battery performance. The synthesis of $(Co_{0.2}Cu_{0.2}Mg_{0.2}Ni_{0.2}Zn_{0.2})O$ was first reported by C. Rost et al.[267] In their study, a mixture of metal oxides (CoO, CuO, MgO, NiO and ZnO) was demonstrated to transform into a single high entropy phase $(Co_{0.2}Cu_{0.2}Mg_{0.2}Ni_{0.2}Zn_{0.2})O$ at high temperatures due to the entropy-stabilization of this phase, after a transition of ZnO (wurtzite) to ZnO (rocksalt) and CuO (tenorite) to CuO (rocksalt). However, the detailed picture of the structural evolution from the constituent oxides to the high entropy phase is missing, in particular the reaction sequence of the metal oxides and the presence of any potential intermediate phases during high temperature heating in air prior to HEO generation. Moreover, diffusion of the different elements leading towards the homogenous phase has not been observed directly to the best of knowledge. Understanding the fundamental reaction steps and the microstructural evolution is not only helpful for optimizing the synthesis conditions, but also for designing and tuning analogous materials. XRD measurements are a powerful and straightforward tool to study the structural evolution. However, its lack in spatial resolution is limiting the information, especially in revealing processes due to elemental diffusion at the micro- and nano-scale. This chapter investigates the mechanism active during HEO formation during heat treatment in air with the help of an *in-situ* TEM gas heating setup. Moreover, *in-situ* and *ex-situ* XRD were performed in order to follow the structural evolution. The information revealed in this chapter, with a focus on the structural transformation and diffusion of the elements can be beneficial for understanding the HEO formation mechanisms and synthesis of analogous materials. Meanwhile, the successful application of the environmental TEM method could open new perspectives to investigate the microstructural evolution of other important battery materials, such as lithium and sodium layered oxide materials.

3.2. Experimental

3.2.1. Sample preparation

CoO, CuO, MgO, NiO and ZnO were mixed in stoichiometric amounts using a planetary ball mill. The mixed sample was dried for 1 hour at 120 °C and then used for *in-situ* heating XRD, calcined in an oven at different temperatures for *ex-situ* XRD and TEM characterization. The dried mixture was press into 2 mm thick pellets with a diameter of 10 mm at 1 GPa pressure for 5 minutes. The pressed pellet was transferred

into the FIB and TEM suitable thin lamellas were fabricated. The lamellas were transferred to a heating MEMS chip adapted for gas experiments inside a closed gas cell (Figure 3-1) and exposed to a gas composition of 21% oxygen / 79% argon, resembling the *ex-situ* synthesizing process of HEOs in air. The setups of TEM and XRD used in this chapter have been described **in Chapter 2.**

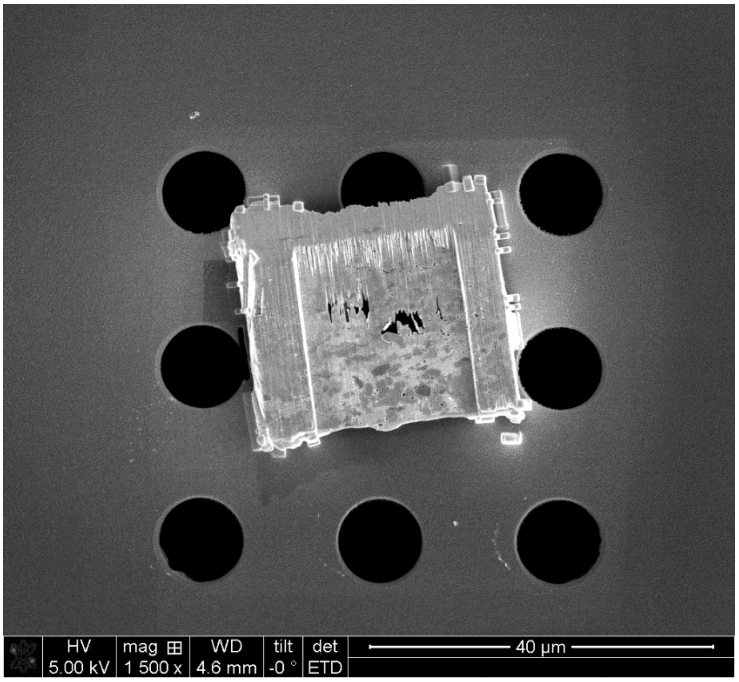

Figure 3-1: Low magnification image of a FIB prepared lamella of mixed oxides attached to the heating MEMS chip. The sample was cut from a pressed pellet of mixed oxides and the lamella was fixed on the MEMS chip with the help of Pt deposition on the sample edges.

3.3. Results

The as-prepared FIB lamella was initially analyzed to confirm its composition, structure and the presence of all oxide phases. The STEM-EDX map (Figure 3-2a) of the raw mixed materials was acquired at 300˚C in order to avoid carbon contamination building up. It reveals that the sample is composed of particles with different sizes and morphology tightly pressed together. The initial morphology of each oxide can be identified. Zn and Mg oxides have small particle sizes that seem to form a percolated continuous network, while CoO consists of a relatively uniform distribution with 1-2 µm sized particles. NiO and CuO have a larger particle size that can reach a few micron. It is worth to mention the limited statistical relevance of the thinned area as the number of particles is small. Nevertheless, the composite map clearly shows a good mixture of the oxides, as all five oxide phases are distributed in an area of around 100µm^2. The corresponding integrated EDX spectrum from the entire thinned area, in which all the K edge peaks of Mg, Co, Ni, Cu and Zn can be clearly observed, is shown in Figure 3-2b. The EDX quantification gives an elemental ratio of 15: 17: 33: 12: 21 (Mg: Co: Ni: Cu: Zn) for an assumed thickness of 120 nm of the TEM lamella. Thus, the EDX quantification shows that all transition metals are present in significant amounts. Although they are not exactly stoichiometric, especially Ni and Cu are deviating from

the others, the FIB lamella contains a large amount of fairly homogenous material in the thick areas, which can also contribute the HEO generation at high temperature through elemental migration. The XRD pattern of the mixed sample before calcination is shown in Figure 3-2c together with the standard rock salt MgO, CoO, NiO, monoclinic CuO and hexagonal ZnO structure. The experimental XRD pattern corresponds to the mixed oxide phases and shows that the structure of the metal oxides was not altered during physical mixing.

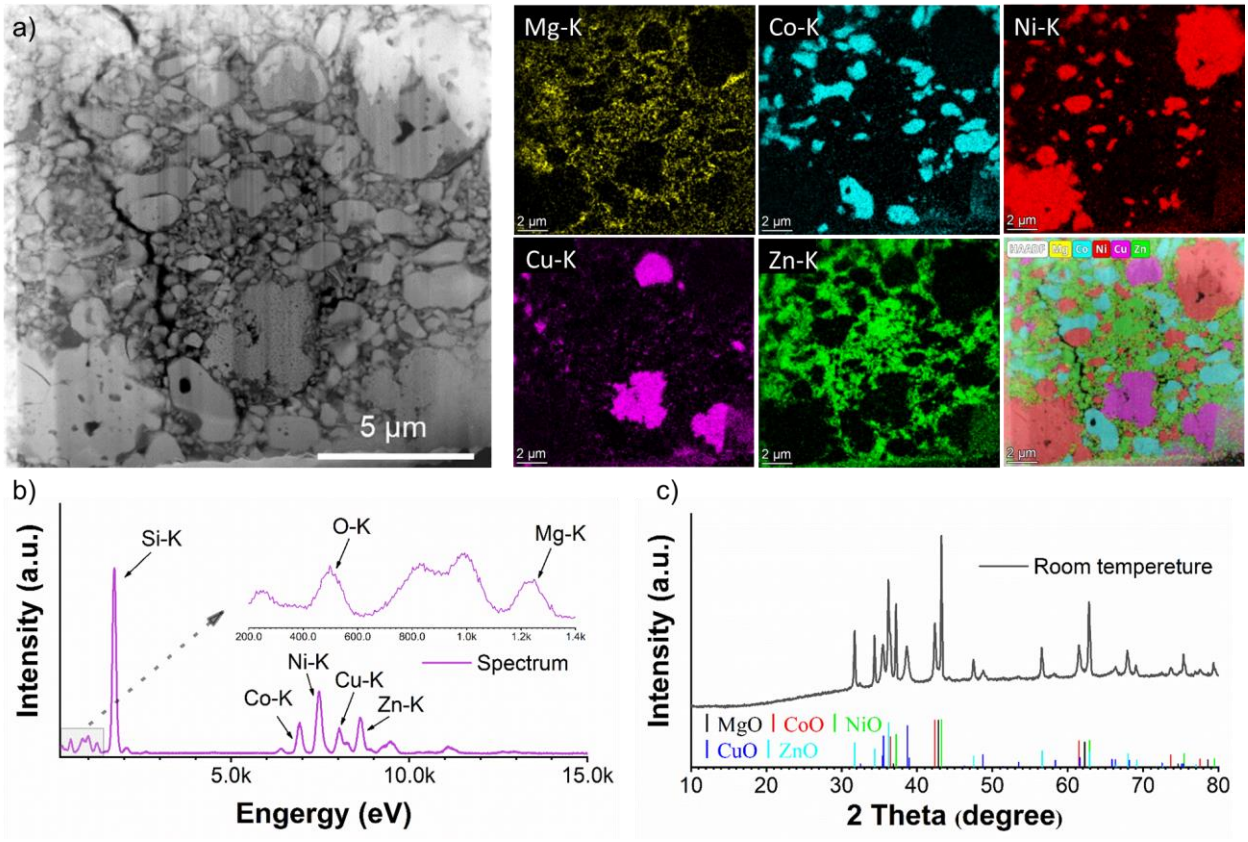

Figure 3-2: Compositional and structural characterization of mixed raw material at 300 ˚C. **a)** EDX map of the as-prepared sample on a Protochip MEMS substrate of the gas holder; **b)** EDX spectrum from the entire area in **a)**; **c)** XRD pattern of as-prepared sample.

In-situ heating XRD was carried out to monitor the structural evolution during heating. As shown in Figure 3-3a, below 600 ˚C, the positions of the reflections at different temperatures are highly consistent. The peaks in the raw material shift slightly and continuously to the left as the temperature is increased, due to the increasing lattice parameters with temperature. A distinct structural change happens beyond 600 ˚C. A set of new reflections appears in the XRD pattern at 650 ˚C when compared with that at 600 ˚C, e.g. the reflections at 14.1, 16.7 and 20.0 ˚, which can be indexed by the spinel structure (shown as pink lines between the XRD patterns at 600 and 650 ˚C in Figure 3-3a). Simultaneously, the reflection at 19.1 ˚ corresponding to the {002} reflection of rock salt CoO decreased dramatically indicating that CoO was involved in the spinel phase formation. To display the structural evolution of the metal oxides during

calcination more clearly, the *in-situ* XRD patterns are plotted as contour plot (Figure 3-3b), in which the emerging reflections of spinel phase and the decreasing intensity of the reflection at 19.1 ˚ can be observed more clearly. With continuing heating, above around 700 ˚C, the intensity of all the reflections of the individual metal oxides become weaker. At the same time, the reflections of the HEO {111} at about 16.5 and {002} at about 19.1 ˚ appear, indicating the generation of the rock salt HEO structure. These observations indicate that all oxides took part in the phase incorporation in a narrow temperature range. The reflections of all oxides decrease further with increasing temperature and most of them completely disappear at about 800 ˚C. However, some reflections at about 16.1, 16.9, 17.5 and 19.2 ˚can be still observed in the pattern at 750 ˚C and correspond to CuO and NiO phases. The presentence of these reflections indicates that the phase transition of CuO and NiO need a longer time/higher temperatures than others to complete, which could be caused by the larger particle size of CuO and NiO in the mixture. One should also mention, that the two peaks that appear at about 12.0 and 22.2 ˚, which are highlighted by stars can be indexed as hexagonal SiO_2 (space group P6222), which is due to the glass capillary crystallizing at high temperature.

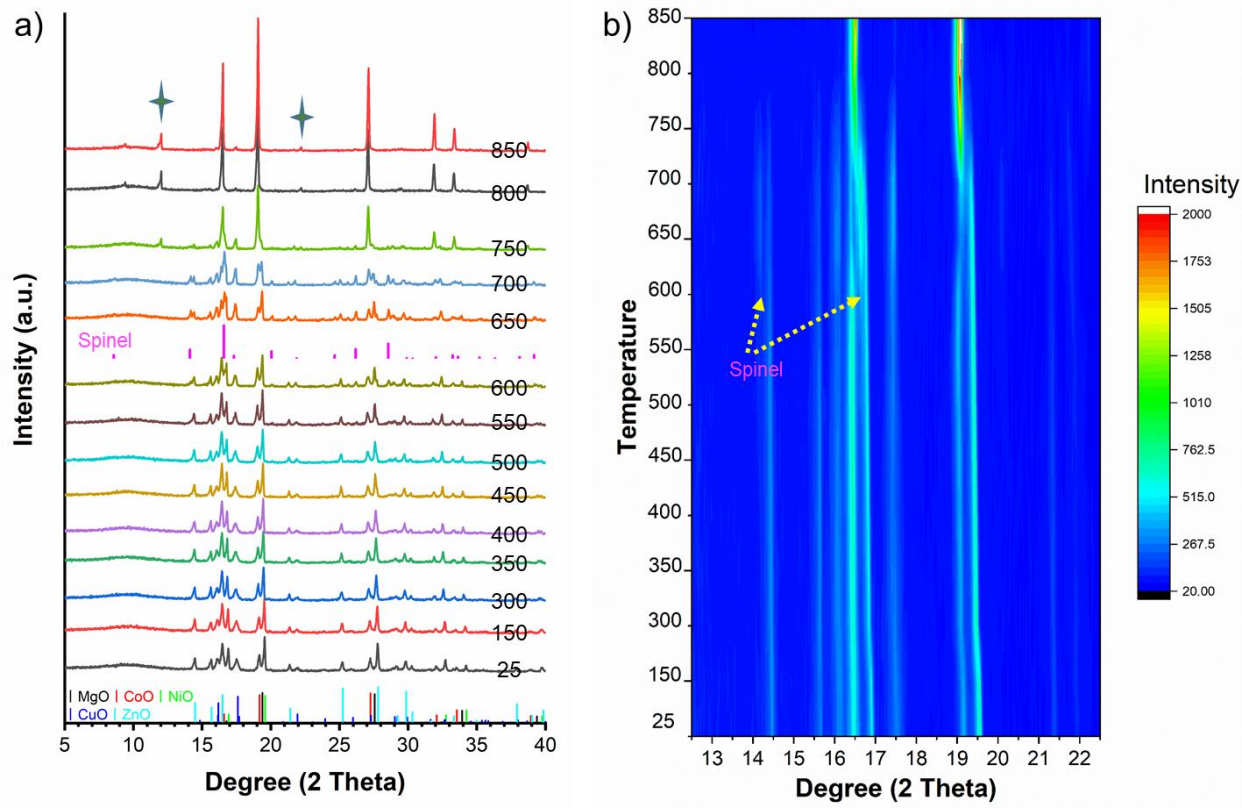

Figure 3-3: *In-situ* heating XRD results using MgO, CoO, NiO, CuO and ZnO as metal sources, which are plotted in normal mode (**a)**) and contour mode (**b)**). The reflections marked by stars in **a)** are from high temperature SiO_2 that could be introduced by glass capillary.

As the glass capillary used in the *in-situ* heating XRD, only give very limited space for the analyzed materials, the small amount of material and the short acquisition time gives a low signal to noise ratio for

the *in-situ* XRD patterns. However, the structural evolution extracted by these measurements were also confirmed by *ex-situ* XRD experiments (Figure 3-4a and 4b). It shows that the individual oxide patterns are present with few changes up to 700˚C followed by an abrupt decrease at 800˚C. At 850˚C the HEO structure seems to be fully formed. The temperature of HEO generation detected in *ex-situ* XRD roughly agrees with that observed during the *in-situ* XRD experiment. Consistently, the Cu seems to need longer times or higher temperature to be fully incorporated into the HEO structure than the other oxides, i.e. distinct reflections corresponding to CuO can be detected at 850 ˚C in the *ex-situ* XRD experiment. The sluggish disappearance of the CuO reflections agrees with previous reports[268,269]. One potential explanation for the sluggish reaction of CuO could be related to the different enthalpy of mixing among the metal oxides. Based on the simulation results reported by G. Anand et al.[270], removing CuO from the complete HEO will result in a reduction of the positive enthalpy of mixing, indicating that the introduction of CuO increases the enthalpy of mixing and is thus unfavorable for the reaction. They also reported that removing ZnO would decrease the enthalpy of mixing as well. However, a slow fading of the ZnO reflections cannot be detected. That implies that the enthalpy of mixing cannot be the only explanation for the sluggish phenomenon. Aside from the larger particle size of the initial precursor, it may also be caused by the larger driving force needed to incorporate Cu ions. The extra energy required is due to the large lattice distortions the Cu incorporation creates. In the work of J. Sushil et al., simulations showed that removal of from the HEO reduces the standard deviation of the cation-oxygen and cation-cation distances to reach a minimum value.[270] Different from the *in-situ* XRD data, the spinel structure started to appear at lower temperature (at about 400 ˚C) in the *ex-situ* experiments. This could be caused by the longer sintering time and a better exposure of powder sample to air, but also because of a better data quality of the *ex-situ* experiments. However, the correlations between the emerged spinel phase and rock salt CoO is consistent in both *in-situ* and *ex-situ* XRD experiments, with the reflections of CoO (at about 16.2 and 19.1 ˚ in Figure 3-4a) disappearing at the same time as the formation of the spinel phase. The results from both *in-situ* and *ex-situ* XRD indicate that the spinel phase should be dominantly a Co_3O_4 phase, which is due to the rock salt CoO oxidizing at high temperature in the presence of oxygen.

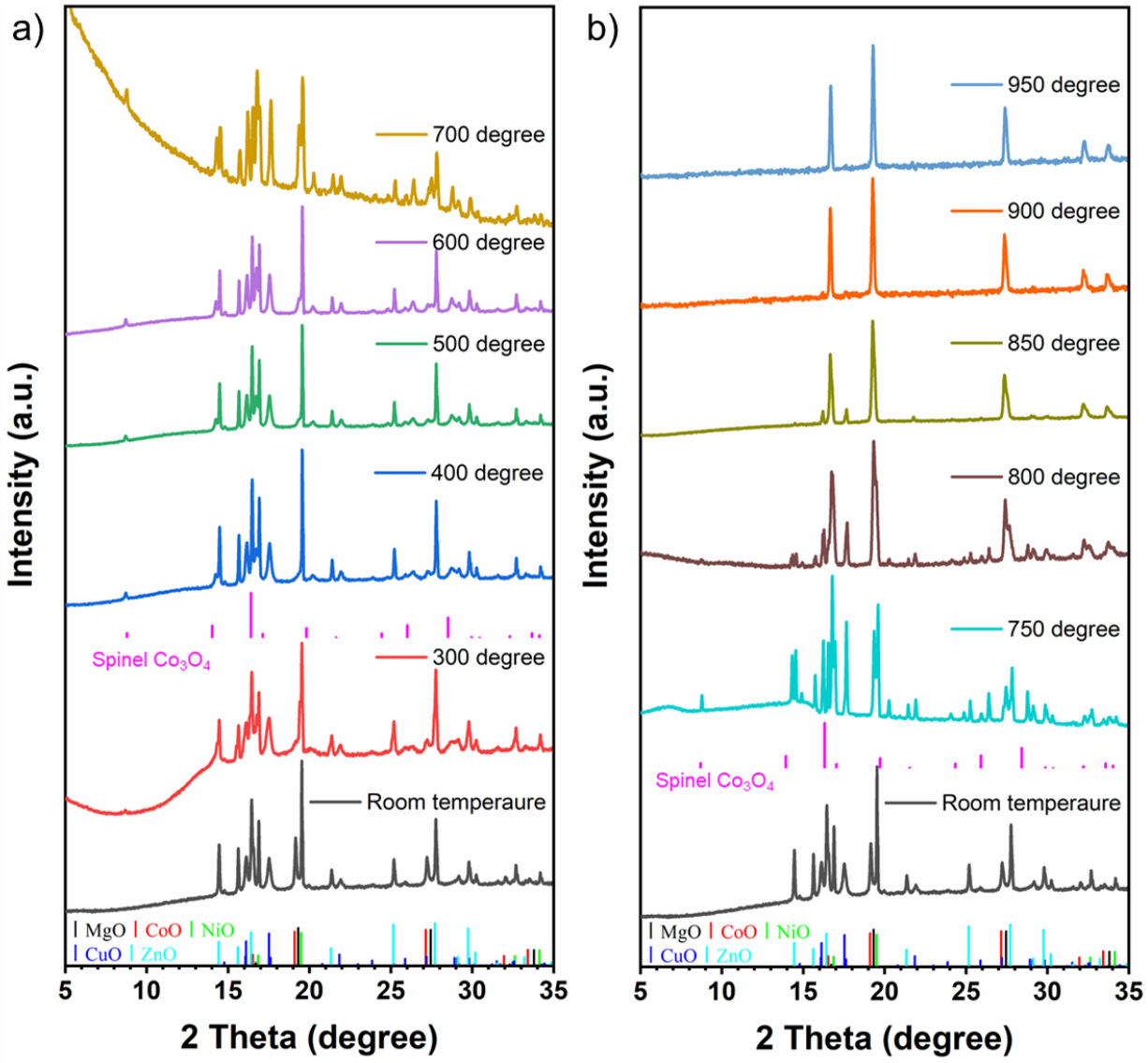

Figure 3-4: structural evolution during calcination observed by *ex-situ* XRD. **a)** *ex-situ* XRD from room temperature to 700 ˚C; **b)** *ex-situ* XRD from 750 ˚C to 950 ˚C. The *ex-situ* XRD patterns were acquired in a diffractometer equipped with a Cu target (λ = 1.540598 Å). For easier comparison with the *in-situ* data shown in Figure 3-3, the XRD patterns here have been plotted after conversion to λ = 0.7093187 Å for a Mo target.

The formation of a Co_3O_4 spinel phase was confirmed by TEM analysis of the *ex-situ* calcined material. The mixed raw materials ware calcined at 400˚C in air for 2 hours followed by quenching in air. Figure 3-5a shows a HAADF image of the calcined sample, in which separated particles can be clearly observed. Figure 3-5b shows the summed EDX spectrum of the area marked in Figure 3-5a (by yellow dash rectangle). The spectrum indicates that the particle marked by the dash yellow box only contains Co, O and C (contamination or supporting carbon) implying that the particle is a pure Co oxide compound. A SAED pattern (Figure 3-5c) was acquired from the same particle (marked with the green circle in Figure 3-5a), which can be indexed as the spinel structure. These results directly demonstrate that the spinel phase formed during calcination is Co_3O_4.

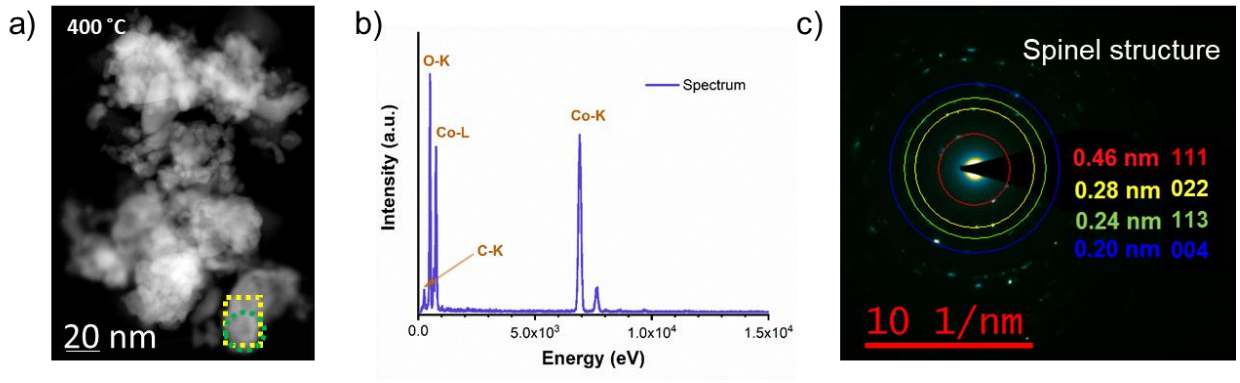

Figure 3-5: structure and composition characterization of the spinel phase. **a)** STEM-HAADF image of the sample heated to 400 ˚C for 2 hours; **b)** summed spectrum from the yellow dash rectangle marked area in **a)**; **c)** SAED pattern acquired from the green circle marked area in **a)**.

The structural transition from the initial rock salt CoO phase to the intermediate Co_3O_4 spinel and finally to the rock salt HEO was demonstrated by the above results. This means that spinel phase Co_3O_4 can be used instead of the rock salt CoO as one of the raw materials to synthesize the $(Co_{0.2}Cu_{0.2}Mg_{0.2}Ni_{0.2}Zn_{0.2})O$ HEO, providing more synthesis routes for HEO preparation. To confirm that, the Co_3O_4 was used to synthesize the HEO in this work. Except for replacing CoO by Co_3O_4 in the mixing process, all other treatment and measurement conditions were identical to the previous synthesis. The *in-situ* XRD patterns of this synthesis are plotted in Figure 3-6. Compared with the XRD patterns shown in Figure 3-3, the small intensity peaks at about 8.8˚ and 14.3˚ in Figure 3-6a prove that the spinel structure of Co_3O_4 is present from room temperature. The contour mode XRD patter shows the peak evolution more clearly and proves that the HEO phase formation follows the same path as in the case of rock salt CoO containing mixture. The spinel associated reflection at 14.3˚ follow the same evolution as the other oxides reflections and can be observed until 750˚C. After 700 ˚C, all structures are starting to change to a single rock salt structure indicating the formation of the $(Co_{0.2}Cu_{0.2}Mg_{0.2}Ni_{0.2}Zn_{0.2})O$ HEO. The reflections corresponding to the HEO appear at about 700 ˚C, the same temperature as in the case of CoO as Co source. In addition, the total disappearance of CuO reflections is delayed here as well due to the higher temperature needed for its incorporation. The perfect matching of the phase transformation in the two experiments that use CoO and Co_3O_4 as Co source implies that the HEO generation is independent of the selected Co source. One should mention that the Co_3O_4 spinel structure can transfer to the rock salt CoO by releasing O_2, which has been widely reported in the literatures.[271–273] N.A. Mayer et al. reported the reaction from Co_3O_4 to CoO to happen between 800 ˚C and 900 ˚C as the pure Co_3O_4 and CoO phases can be found at 800 ˚C to 900 ˚C.[272] In our experiments, the reflections of spinel Co_3O_4 decrease has been observed between 750 ˚C and 800 ˚C (shown in Figure 3-4b) indicating that Co was incorporated into the HEO structure from the spinel Co_3O_4 phase. However, the small temperature difference between our experiment (the decomposing of spinel Co_3O_4 happened around 750 ˚C and 800 ˚C) and the literature (800

˚C to 900 ˚C) could be the results of different experiment conditions. In addition, the reflections of rock salt CoO have close positions with the generated HEO, which introduces the problem that it is difficult to observe if some rock salt CoO phase appears at high temperature (800 ˚C in the Figure 3-4b). Therefore, if Co was incorporated into the HEO from either Co_3O_4 or CoO cannot be fully established in this work.

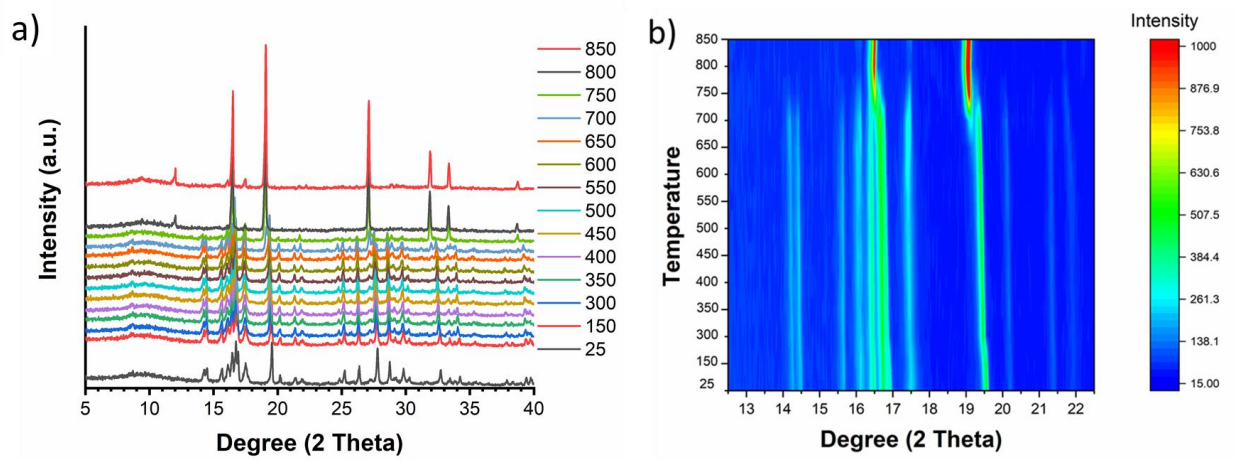

Figure 3-6: structural evolution during HEO synthesizing when using Co_3O_4 as a precursor together with MgO, NiO, CuO and ZnO. **a)** normal mode of *in-situ* XRD; **b)** contour mode of *in-situ* XRD.

The above *in-situ* and *ex-situ* XRD results indicate that the structural change from the oxide phases to the HEO starts in a narrow temperature range for all oxides at around 700˚C. *In-situ* gas and heating TEM was used to track the elemental diffusion progress. EDX maps of the transition metals at 650 ˚C are shown in Figure 3-7. Compared to the elemental maps acquired at 300 ˚C (Figure 3-2a), no obvious differences can be observed in the two sets of elemental maps indicating that there is no significant diffusion detected below 650 ˚C. Despite the fact that no elemental diffusion is observed in the EDX maps below 650 ˚C, the *in-situ* gas STEM-HAADF analysis offers information on the spinel phase formation. This comes from the observation of morphological changes occurring in the oxide phase with increasing temperature. Figure 3-8a presents the overall morphology of the oxide mixture in the TEM lamella at 100 ˚C and 650 ˚C, overlapped with an EDX map of the Co (oxide) distribution. When comparing the STEM-HAADF images at the two temperatures, one can observed that with the exception of Co particles no other oxides exhibit visible morphological changes. Two Co oxide particles are highlighted and their evolution is presented separately in Figure 3-8b and 8c. The main characteristic that changes during the temperature increase is the porosity of the Co oxide particles. As shown in Figure 3-8b and 8c, pores that range from a few tens of nm to a few hundred of nm are not changing below 350 ˚C. At this temperature, the smaller pores are starting to fade, followed by the disappearing of larger pores as the temperature is increased further. Pores smaller than a few hundred nanometers are completely removed at 450 ˚C, while larger pores persist even after 500 ˚C (yellow arrow in Figure 3-8a). Although very small, these morphological changes observed in the STEM-HAADF images imply incorporation of oxygen along with the structural

changes of CoO during calcination in an O_2 containing atmosphere (21% O_2 and 79% Ar). The starting point of this process observed in the TEM at about 350 - 400 ˚C is consistent with the result of *ex-situ* XRD experiment, where the spinel phase was starting to appear at 400 ˚C.

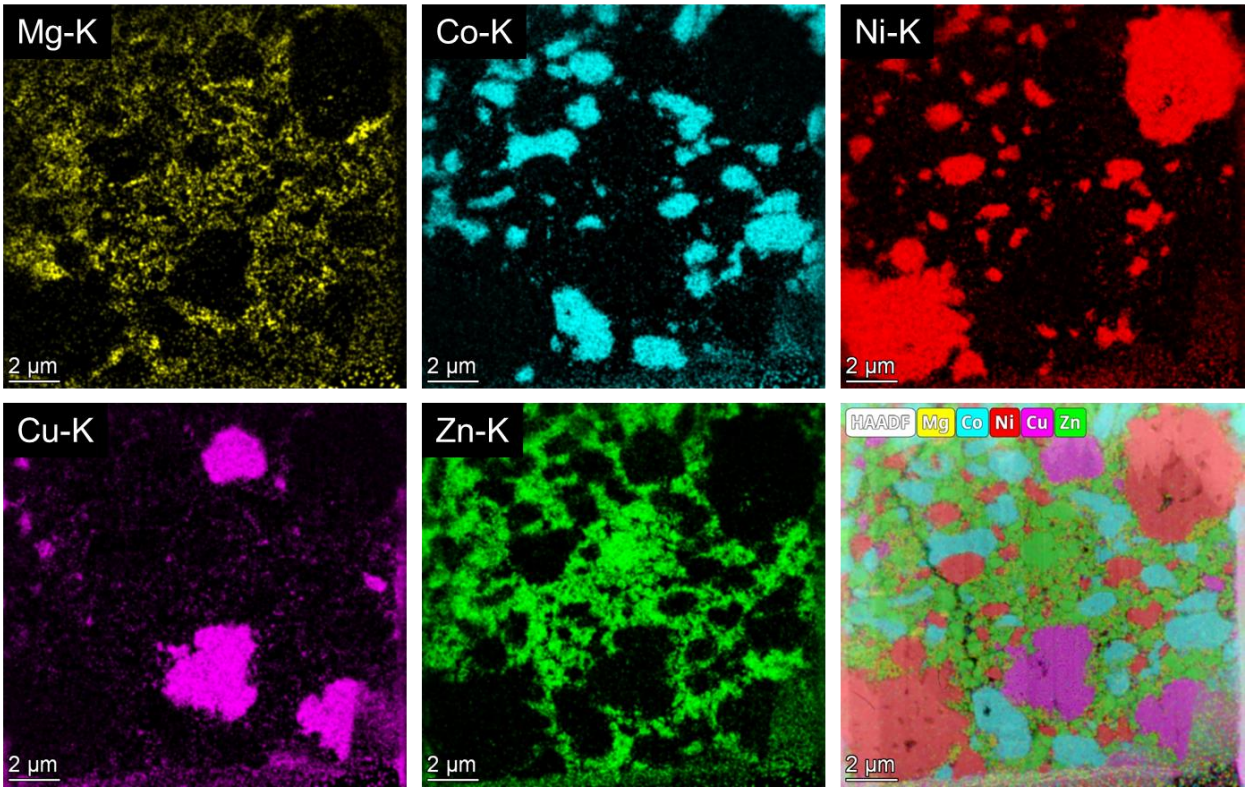

Figure 3-7: elemental distribution maps extracted from STEM EDX data during *in-situ* gas heating at 650 ˚C.

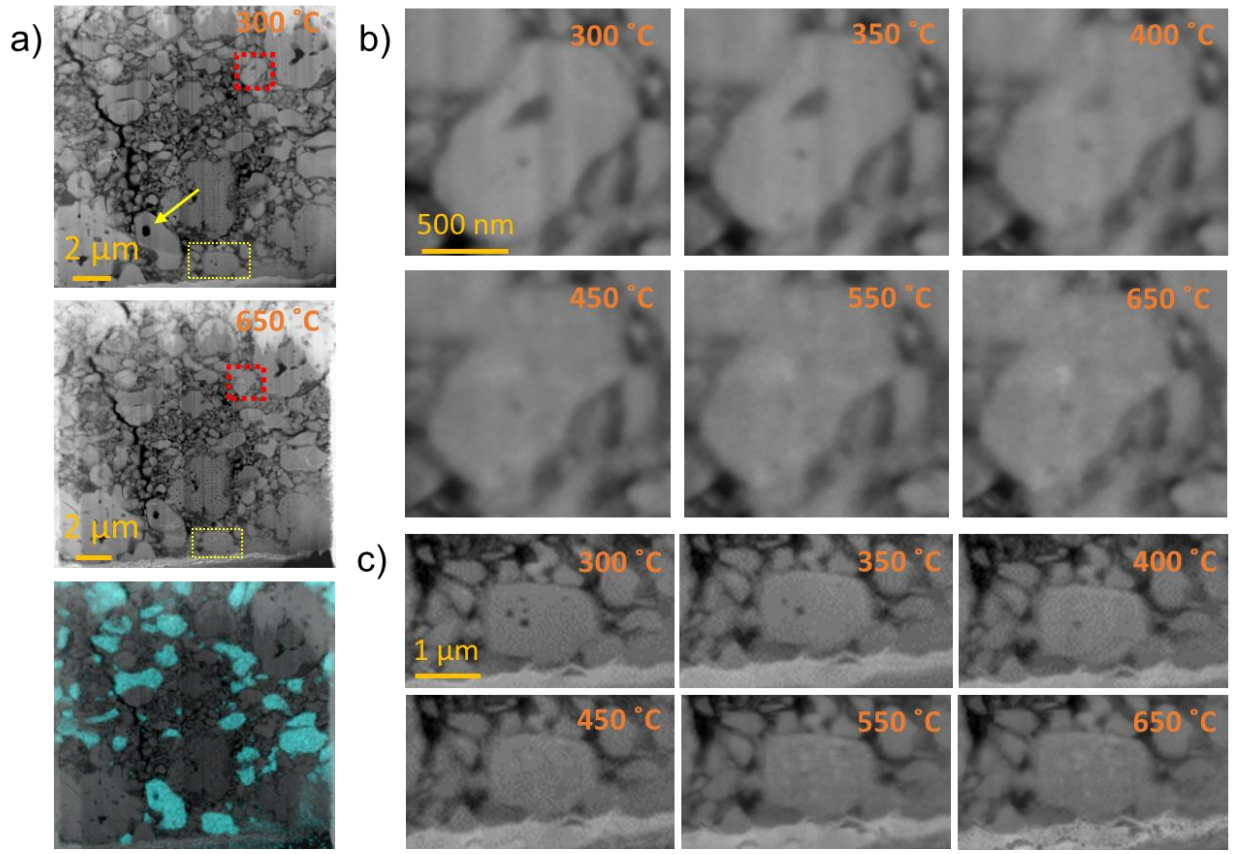

Figure 3-8: morphology changes of CoO particles during calcination. **a)** STEM-HAADF images of the TEM lamella at 100 ˚C (top) and 650 ˚C (middle) and the overlapped image of STEM-HAADF and Co elemental map at 650 ˚C (down); **b)** enlarged images of the red rectangle marked area of **a)**; **c)** enlarged images from the yellow rectangle marked area of **a)**.

STEM-HAADF images and EDX maps of the transition metals from 700 ˚C to 850 ˚C are shown in the Figure 3-9. Whereas no diffusion has been observed below 650 ˚C, the boundaries of the particle are starting to become blurry at 750 ˚C and further shape changes were observed at higher temperatures. Clear particle evolution characterized by elemental diffusion is observed after 750 ˚C that seems to accelerate after 800 ˚C. The elemental distribution maps up to 750 ˚C show minimal variations compared to the oxides distribution in the pristine material (please refer to Figure 3-2a). At 800 ˚C all oxides show extensive redistribution towards a homogenous phase. One can easily observe that smaller particles are more easily redispersed and integrated into the HEO phase, whereas the large CuO and NiO particles are still showing an unreacted core. This fits the observation of the XRD results that the reflections from CuO and NiO disappear at higher temperatures than those of the other oxides. A fully homogenous HEO phase appears at 850 ˚C with all regions now exhibiting a fairly uniform elemental distribution. As seen from the FIB prepared lamella, one can consider the initial oxide mixture as an inhomogeneous phase at the nanometer or even micrometer scale. Despite this, the atomic diffusion reaches all parts of the TEM lamella resulting in a uniform distribution of all elements. Notably, the *in-situ* gas and heating TEM show a slightly different starting point of the HEO generation (750 ˚C) with that observed in XRD experiments

(700 ˚C). This could be due to the 2D morphology of the *in-situ* heating TEM sample, which might limited the diffusion pathways. In the bulk 3D oxide mixture, the distances between oxide particles are reduced and one can expect that diffusion leading to an even elemental dispersion is facilitated. In a 3D oxide mixture, surface diffusion effects can be another factor to decrease starting temperature of the reaction, which was demonstrated to be not negligible in micro powders and provide lower activation energies compared to volume diffusion.[274]

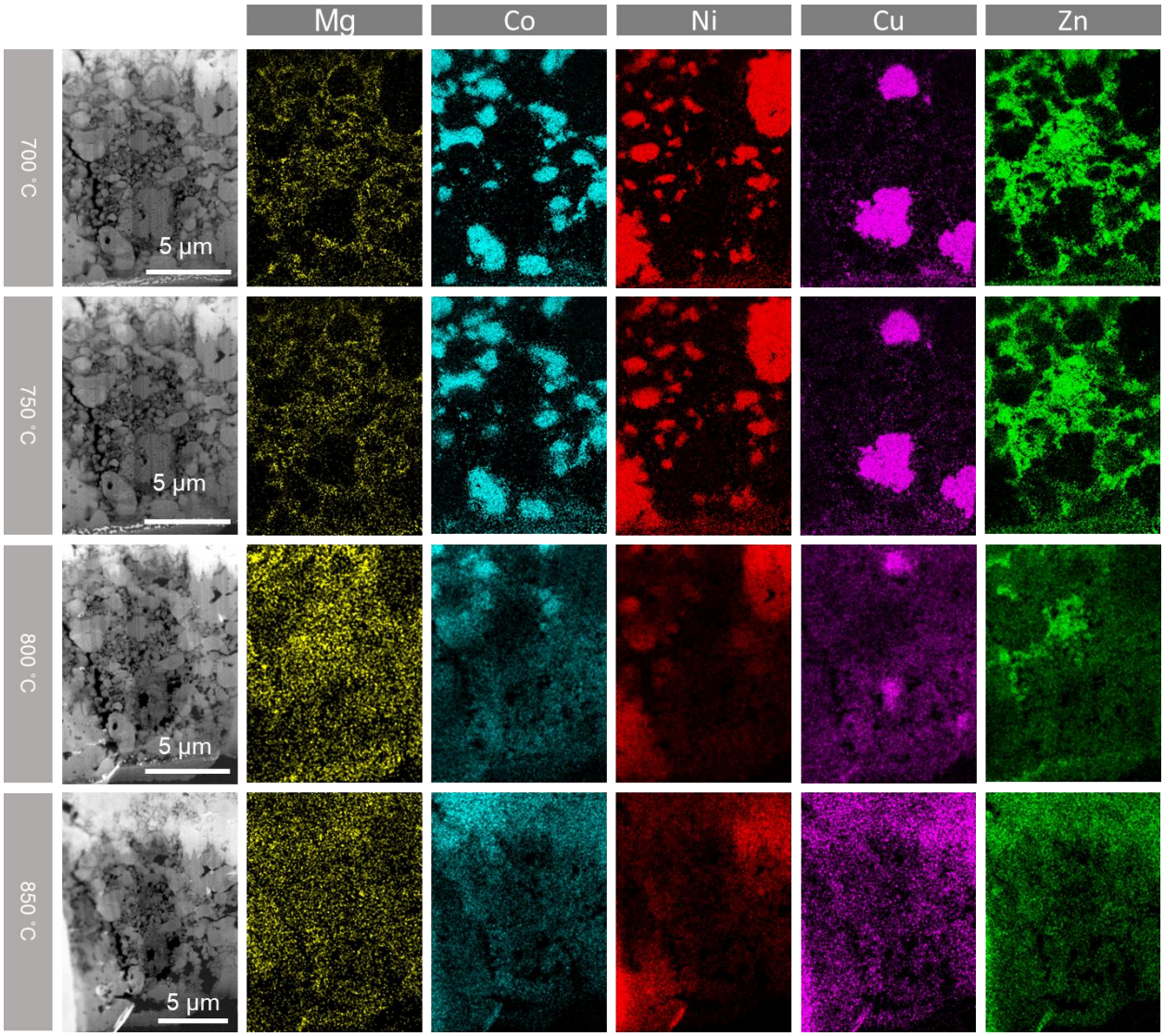

Figure 3-9: morphology and elemental distribution mapping extracted from STEM EDX data during *in-situ* gas heating from 700 ˚C to 850 ˚C.

To more intuitively understand the reaction sequence of the oxides, cross correlation of the elemental maps of different metal elements at different temperatures were carried out and plotted in Figure 3-10. As shown, the cross correlation values between different elements are negative and only show small changes up to 750 ˚C. This indicates that the distribution of the oxides is strongly anti-correlated and with very limited overlap in projection prior to the reaction starting above 750 ˚C. Although

the EDX maps (in Figure 3-9) show that all the elements start to diffuse at 800 ˚C, the calculated correlation values between different elements show significant variations. Several elemental combination, Co-Mg, Zn-Mg, Cu-Co, Zn-Co, Cu-Ni, Cu-Mg, Ni-Co, Zn-Cu, Ni-Mg and Zn-Ni show significant changes compared with those at 750 ˚C, which is an indicator of some phases forming prior to the HEO generation. Among them, Zn-Mg gives the highest positive cross correlation value indicating that Zn and Mg are easily reacting with each other. However, there is no significant correlation changes for Ni-Mg between 750 ˚C and 800 ˚C meaning that they did not react with each other. At 850 ˚C, except for the Zn-Mg, all the correlations show a significant increase demonstrating that all elements diffuse towards a homogenous distribution. The decreasing of the Zn-Mg correlation could be explained by an initial formation of a preferential Mg-Zn-O phase at 800 ˚C prior to the HEO generation. During the HEO generation at higher temperature, the Zn-Mg correlation decrease due to further diffusion of the Zn and Mg from the Mg-Zn-O phase to the HEO phase. The earlier formed phases before HEO generation could be related to the different enthalpy of mixing between individual oxides. However, detailed mixing enthalpy values are not available. In addition, the observed reactions are possibly also related to the particle size and particle distribution. For instance, the Mg-Zn shows the highest correlation at 750 ˚C, which could be caused by the small particle size of MgO and ZnO and their fairly uniform distribution in the observed area. Nevertheless, the formation of a Zn-Mg-O phase prior to the HEO formation and a complete lack of a Ni-Mg-O formation at low temperatures clearly indicates that individual oxide formation mixture has to be considered for the HEO formation, at least during the early stages of the reaction.

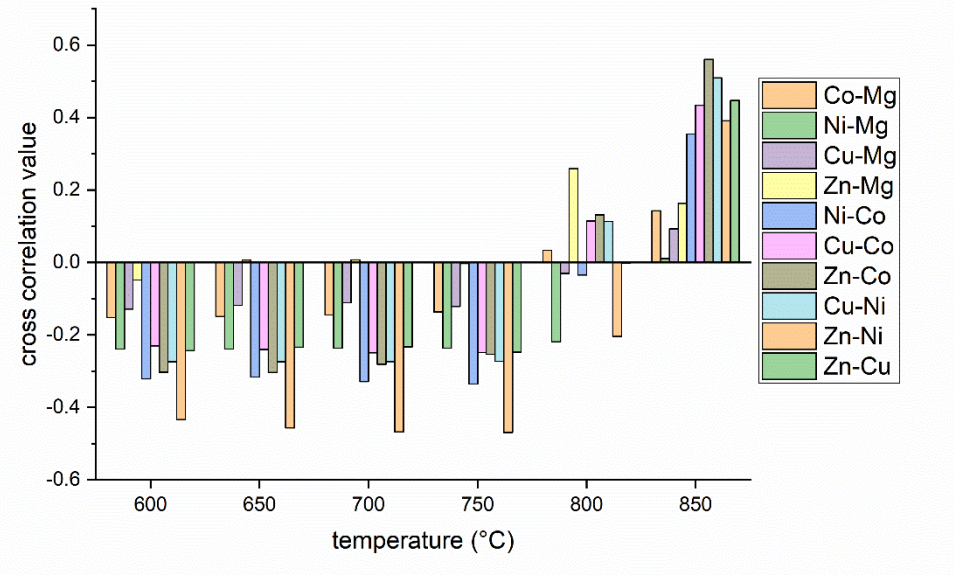

Figure 3-10: cross correlation results between different elemental maps.

3.4. Summary and discussion

In this chapter, we used *in-situ* and *ex-situ* XRD techniques to investigate the structural evolution during the $(Co_{0.2}Cu_{0.2}Mg_{0.2}Ni_{0.2}Zn_{0.2})O$ HEO synthesis starting from the individual oxides. The

morphological changes and elemental distribution at different temperatures at relevant atmosphere conditions (21% O_2) were further characterized by *in-situ* gas TEM using a windowed gas holder. Although the two techniques work at different length scales, the results obtained here correlate reasonably well and offered a unique view of the HEO formation mechanism. The main findings are summarized below:

i. An intermediate phase transformation from the rock salt to a spinel structure by oxygen incorporation of CoO was seen in XRD and confirm by the TEM measurements during the calcination. By showing that a similar phase transformation pathway towards the HEO phase is obtained when starting the synthesis with a spinel Co_3O_4 phase, we provide an alternative Co source for the HEO synthesis.

ii. *In-/ex-situ* results demonstrate that the HEO started forming above 700 ˚C and is fully generated above 850 ˚C. However, the *in-situ* gas and heating TEM results indicate no elemental diffusion below 750 ˚C and the elemental maps show anti-correlations at 750 ˚C. The difference between the XRD and TEM results could be caused by the special 2D geometry of the FIB lamella as only limited connecting boundaries are available and the diffusion is significantly limited by the 2D geometry.

iii. In addition, the cross correlation results imply a multistep reaction for the HEO generation. It shows various changes of the correlation between different elements before the HEO formation. This indicates that some preferential phases are formed prior to the HEO generation. The homogeneous distribution in the elemental maps and the positive correlations of all the metal elements indicate that the HEO is almost completely formed at 850 ˚C.

One should mention, that in a random distribution like the one meet in the pristine powder mixture, the possibility of all elements connecting with each other is quite low. The reaction would most probably happen first at some boundaries, where the elements present in the connected oxides have a lower enthalpy of mixing. After this initial mixing, the generated multi-cation oxide is expected to react with other individual oxides in its vicinity and act as a reaction nucleus. The cross correlation results also indicate that some phases could be formed before the HEO generation. The reaction preference could be affected by the particle size and their distribution. It could be also affected by inherent energetic differences. As another open question, the transformation of Co_3O_4 to CoO at high temperature needs further clarification, which would help to understand the Co incorporation mechanism more clearly and be beneficial for designing similar HEO phases.

4. Self-assembled electric conductive network in multi-cation metal oxides used in lithium ion batteries

4.1. Introduction

The high entropy concept was applied successfully in the energy storage field and exploited as a novel way for designing battery electrode materials. A first example has been the multi-cation HEO $Mg_{0.2}Co_{0.2}Ni_{0.2}Cu_{0.2}Zn_{0.2}O$ where a competitive electrochemical performance in lithium ion batteries was achieved with micron-sized particles.[159] In addition, it was demonstrated that the HEO can show better battery performance than the corresponding medium entropy oxides (oxides with only four transition metals present in equal stoichiometric ratio). The superior performance of the HEO was attributed to the high entropy effect as the entropy drives a stable single solid solution phase that is favorable for ion mobility.[160] It was demonstrated that the disordered arrangement of metal elements in rock salt structure is beneficial for the Li percolation compared with the rock salt oxides with short range ordering.[275] However, the high entropy effect is not enough to explain the excellent stability during electrochemical cycling. The HEO formation is thermodynamically favorable at high temperatures, whereas slow quenching during synthesis results in an oxide mixture. In contrast, the battery cycling is performed at room temperature. Therefore, it is unlikely to reestablish the initial HEO structure after the battery cycling and the high entropy effect cannot be used to explain the stable battery cycling observed. To explain the outstanding performance of HEOs, a 'cocktail effect' has to be considered as discussed in some reports,[164–167,222] implying synergetic effects of the different cations. However, the effects are not fully understood. In this chapter, the reaction mechanisms of the HEO $Mg_{0.2}Co_{0.2}Ni_{0.2}Cu_{0.2}Zn_{0.2}O$ during battery cycling are studied, based on an analysis of the oxidation states of the different elements together with their elemental and phase distribution.

4.2. Experimental

4.2.1. Materials synthesis

The initial HEO ($Mg_{0.2}Co_{0.2}Ni_{0.2}Cu_{0.2}Zn_{0.2}O$) was prepared using Nebulized Spray Pyrolysis (NSP), which has been performed by Mr. Junbo Wang at the Institute of Nanotechnology, Karlsruhe Institute of Technology. Stoichiometric amounts of (($Co(NO_3)_2 \cdot 6H_2O$ (Sigma Aldrich, 99.9%), $Cu(NO_3)_2 \cdot 2.5H_2O$ (Sigma Aldrich, 99.9%), $Mg(NO_3)_2 \cdot 6H_2O$ (Sigma Aldrich, 99.9%), $Ni(NO_3)_2 \cdot 6H_2O$ (Sigma Aldrich, 99.9%), and $Zn(NO_3)2 \cdot 6H_2O$ (Alfa Aesar, 99.9%)) were dissolved in deionized water. Then, the solution was sprayed as a mist and transported by means of a carrier gas into the hot zone of a tubular furnace as described in reference[159]. HEO particles formed from the nebulized phase at 1150 ˚C.

4.2.2. Electrochemical measurements

The HEO was mixed with Super C65 carbon black and polyvinylidene fluoride (PVDF) with a ratio of 7: 2: 1 and dispersed in N-methyl-2-pyrrolidone (NMP). A high-energy dispersion machine (ThinkymixerARE-250, 3min, 2000 rpm) was used to make a uniform slurry. After coating a copper film current collector with the resulting slurry, the electrode was dried in a vacuum oven at 80 °C overnight. The battery was set up in a glove box, where the residual water and oxygen partial pressure was maintained below 0.5 ppm, using glass microfiber filter paper (GF/C, Whatman) and Li metal foil (Gelon LIB Co., Ltd) as separator and counter electrode. The electrolyte was 1 M $LiPF_6$ with a 3: 7 weight mixture of ethylene carbonate/ethyl methyl carbonate (Selectilyte LP57, BASF SE). The mass loading of the electrodes for TEM measurements is about 0.6 mg/cm^2 to obtain comparable conditions with previous studies.[159] 10 mg/cm^2 of the mass loading is used in the batteries for XAS testing to have sufficient signal for the X-ray analysis. Galvanostatic measurements were performed on an Arbin battery test system (BT-2000) at 25°C. The batteries initially underwent a discharging process (lithiation) and were then recharged (delithiation) during cycling.

4.2.3. Characterization

The equipment and setups used for EIS, XAS, and TEM characterizations are described in **section 2.1**. SAED in this chapter was performed using a FEI Titan 80–300 microscope operated at 300 kV. For EELS mapping, 4D-STEM and the HRTEM a probe corrected Thermo Fisher Themis Z was operated at 300 kV. The EELS maps in this chapter were acquired by a K3 IS camera using 7 Å pixel size and 0.01 s exposure time. The 4D-STEM data was acquired by an almost parallel beam (convergence angle 0.85 mrad) in STEM mode using an ADF detector and an OneView camera to acquire the diffraction data. The data was imported into the Automated Crystal Orientation Mapping (ACOM) indexing software to analyze the crystal orientation and phases present.

4.3. Morphology, structure and valence study of HEO during electrochemical cycling

4.3.1. Morphology and structure characterization

The structure of the as-prepared HEO was measured by XRD and SAED, which indicated that the HEO has a pure rock salt structure with lattice parameters similar to NiO (Figure. 4-1a and 1b). Figure. 4-1c shows a TEM image illustrating the micron-sized hollow particles of the as-prepared HEO. This morphology presumably plays a role in eliminating the effect of volume expansion during the lithiation process and thus benefit the stability during battery cycling.

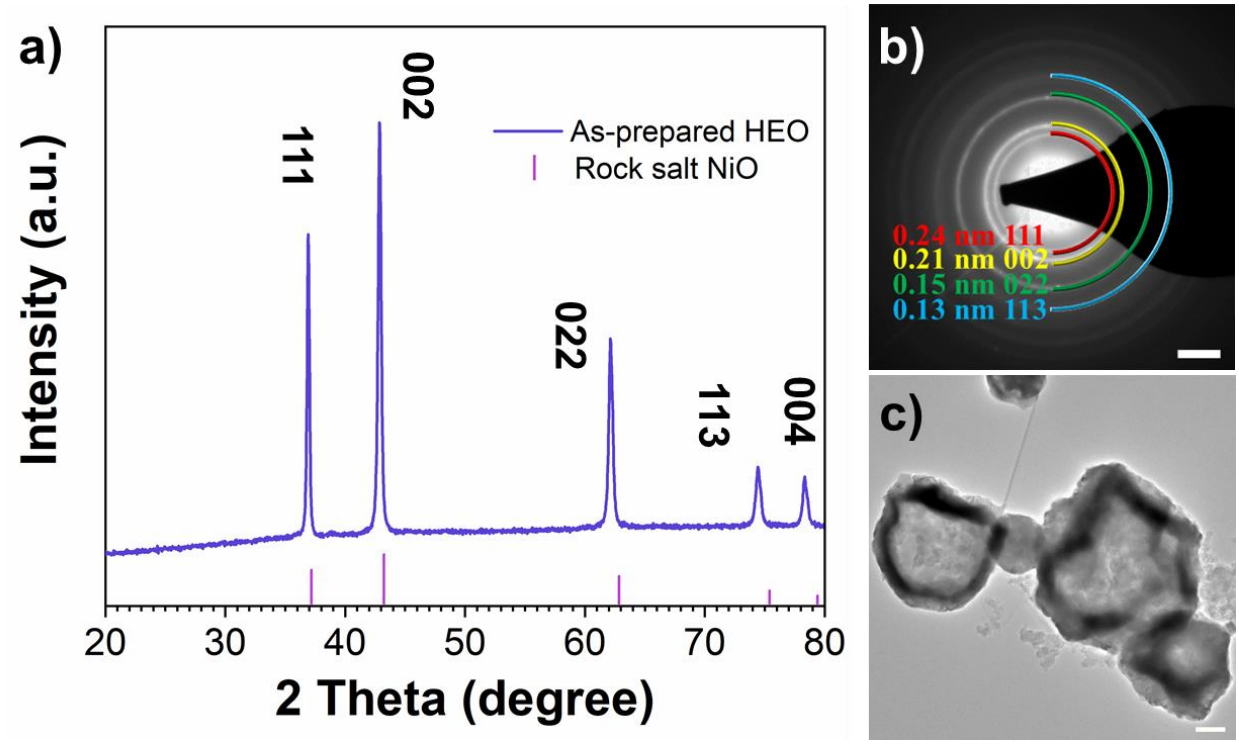

Figure 4-1: morphology and structural characterization of the as-prepared HEO. **a)** XRD pattern comparing with rock salt structure NiO; **b)** SAED pattern; **c)** TEM image, the scale bar in **b)** is 5 1/nm, the scale bar in **c)** is 200nm.

The morphology and structural changes during cycling were studied by TEM. Figure 4-2a/c shows TEM images of samples in the 1st discharged and 1st charged state confirming that the hollow sphere particles are maintained and no obvious dissolution of material into the electrolyte occurred during the electrochemical reaction. However, the limited crystallinity during cycling makes it difficult to index the diffraction patterns in the dis-/charged samples accurately. The SAED of the sample in the 1st discharged state (Figure 4-2b) only exhibits few defined diffraction rings and mostly diffuse scattering is observed. Nevertheless, the Li_2O (111) diffraction ring demonstrates that Li reacted with the oxygen from the HEO during the lithiation process. Ambiguity arises for the major diffraction ring at 2.1 Å, which can be indexed either as the (002) plane of a residual HEO structure or metallic Ni/Co/Cu (111) plane. In the SAED of the 1st recharged state, no clear diffraction planes corresponding to Li_2O are observed. The diffraction ring corresponding to a lattice space of 3.3 Å can be indexed as the (002) reflection of carbon from the conductive carbon. The diffraction ring at 2.1 Å fits to both characteristic MO and M planes and therefore does not allow for an easy interpretation of the structural changes during charging. Therefore, an ePDF analysis was carried out to follow the structural evolution during battery cycling. The ePDF analysis of the as-prepared sample is consistent with a simulated PDF of the rock salt structure in NiO, which is in line with the XRD and SAED results. During discharging, the M-O and M-M peaks in the ePDF at about 2.1 Å and 3.0 Å of HEO structure disappear, meaning that the rock salt HEO decomposes during lithiation. A new peak at about 2.5 Å appeared in the discharged sample, which can be attributed to the nearest M-M distance in an *fcc* metallic structure. The M-O peak at about 2.1 Å in the as-prepared sample shifts to

lower *r* values during the lithiation, which can probably be assigned to a mixture of Mg-O and Li-O bonds as Mg is electrochemically inactive in the given voltage range of 0.01 V to 3.0 V. Unexpectedly, neither the M-O peak at 2.1 Å nor the MO M-M peak at about 3.0 Å increases significantly during the recharging process. In addition, the intense M-M peak at about 2.5 Å remains in the recharged sample indicating that a large amount metallic phases are still present after the delithiation process.

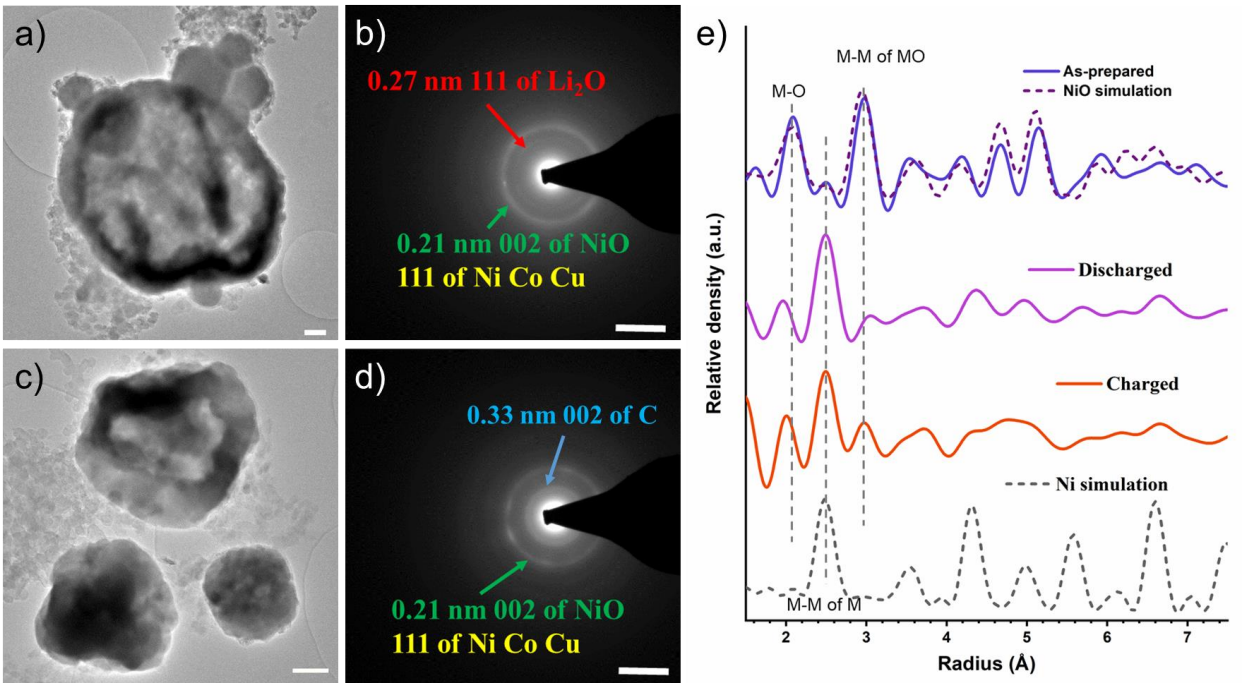

Figure 4-2: structural changes during of cycling. **a)** TEM image of 1st discharged sample; **b)** SAED pattern of the 1st discharged sample; **c)** TEM image of the 1st recharged sample; **d)** SAED pattern of the 1st recharged sample; **e**) ePDFs of the as-prepared and cycled samples with simulated NiO and Ni PDFs for comparison with the experimental data. The scale bar in **a)** and **c)** is 200 nm, the scale bar in **b)** and **d)** is 5 1/nm.

4.3.2. Valence state analysis

The global structural information derived from the ePDF analysis shows that a large amount metallic phases is present in the cycled samples. To understand the behavior of each element, XAS was applied to study the valence state and element specific nearest neighbor distance evolution during cycling. As shown in Figure 4-3, the onset position in the XANES of all metals (Co, Ni, Cu and Zn) in the as-prepared sample is in good agreement with the corresponding standard oxide samples meaning that the four elements exhibit a +2 valence state prior to cycling. Only the near edge spectra of Cu in the as-prepared sample differs from the CuO reference. This is presumably an effect of the different structure/environment in the CuO tenorite used as reference compared to the rock salt environment in the HEO[263]. As expected, the Co, Ni, Cu and Zn spectra in the discharged sample fit to a reduced metallic state, particularly manifested by the spectrum onset position matching the corresponding standard metal or alloy samples. However, the transition metals show a different behavior during the following recharging process. The reduction of

the Co XANES pre-edge (solid red line in Figure 4-3a) demonstrates that some of the Co is reoxidized, but the residue pre-edge clearly indicates that a noticeable amount of Co still is still in a metallic state in the recharged sample. Ni and Cu in recharged sample show almost the same XANES features as in the discharged sample, indicating that they did not take part in the conversion reaction and stayed in a metallic state during delithiation. On the contrary, Zn shows a distinct shift towards the oxidized state, meaning that most of the Zn has been reoxidized back to +2 during the delithiation process.

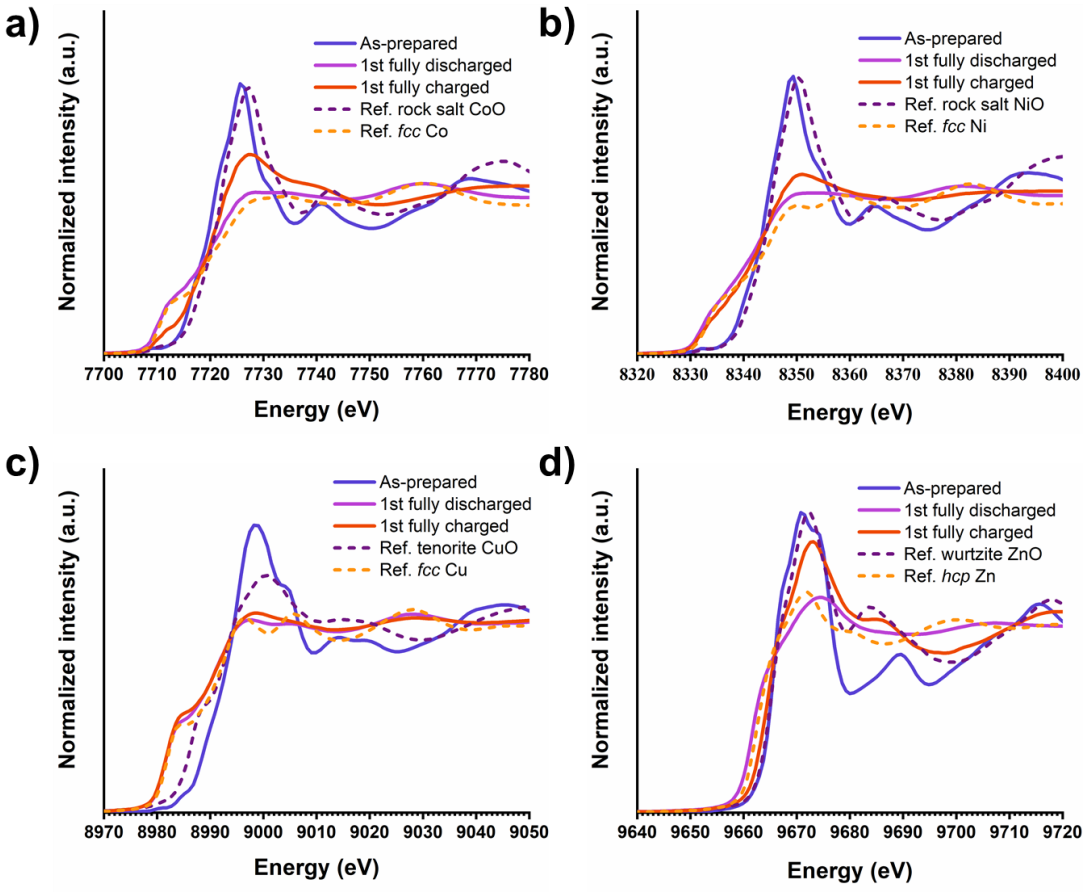

Figure 4-3: XAS state characterization of as-prepared and cycled samples **a)**, **b)**, **c)** and **d)** the normalized XAS spectrum of cobalt, nickel, copper and zinc.

4.3.3. Analysis of the short range order

The Fourier transform of the extended X-ray absorption fine structure (EXAFS-FT) provides an element specific PDF, which contains information on the nearest neighbor environment of that element. This was used to confirm and extend the XANES analysis. As shown in Figure 4-4, the characteristic metal-oxygen (M-O) and metal-oxygen-metal (M-O-M) distances for the HEO are present in the as-prepared state. Due to the difference in crystal symmetry of the HEO (rock salt, as CoO and NiO) and the ZnO reference (wurtzite), the M-O and M-O-M shells of Zn appear at different distances in the ZnO reference. Nevertheless, as the distance of Zn-O-Zn shell is the same as the distance of the other elements (Figure 4-5) all elements are present in a single rock salt phase in agreement with the XRD and SAED analysis. The

increased intensity of the M-O-M shell of Cu in the HEO compared with the reference tenorite can also be ascribe to the structural differences. While the closest Cu-O-Cu distance in tenorite is 2.9 Å equal to the M-O-M distance in the HEO rock salt structure, there is another Cu-Cu distance (3.1 Å) in the tenorite CuO structure. These two Cu-Cu distances make the Cu-O-Cu shell in the CuO reference to be broad and weak. Schematic structures of NiO (to represent HEO), tenorite CuO and wurtzite ZnO are shown in Figure 4-6.

After the first discharging process, the EXAFS-FTs reveal that the M-O distances of all four elements disappeared and metal-metal (M-M) distances appeared, in agreement with all four elements being reduced to the metallic state during the lithiation process. The M-M distances of Co, Ni and Cu (Figure 4-4a to 4c) appear at the same positions as the corresponding metallic references indicating that the metallic Co, Ni and Cu in the discharged state is *fcc* cubic. However, the M-M shell of Zn (Figure 4-4d) does not fit to the hexagonal (*P63/ mmc*) Zn metal structure and is consistent with the metal-metal distances of Co, Ni and Cu. The difference between the experimental data and the hexagonal (*P63/ mmc*) Zn metal structure could be explained by Zn alloying with Li generating an *fcc* ZnLi structure, which has been reported in previous studies.[276–278] Another possibility is that Zn forms an *fcc* alloy with some reduced transition metal elements, Co, Ni and Cu, at the discharged state. However, as shown in Figure 4-5b, Zn shows a weaker and broader shell shape compared with the other three elements. This implies t Zn to be in a different elemental environment than the others, which does not fit to Zn forming an alloy with the other transition metal elements.

After the delithiation during recharging, Co, Ni, Cu and Zn show different behavior echoing the XANES valence state analysis. The Co-O distances (Figure 4-4a) appear in the charged state, which means that some Co has been reoxidized during delithiation. However, the residual M-M shell confirms the XANES result that a noticeable amount of Co is still in the metallic state after recharging. No clear M-O shell is observed in the charged state for Ni and Cu (Figure 4-4b and Figure 4-4c), which means that Ni and Cu do not take part in the conversion reaction and are still in a metallic state in recharged state. As shown in Figure 4-4d, the M-O shell of Zn appears whereas the M-M shell disappears during the recharging process meaning that the +2 state Zn is dominant in charged state. However, the M-O-M shell at 2.X Å was not recovered, indicating a ZnO has low crystallinity and somewhat different short range order compare to ZnO in the wurzite structure.

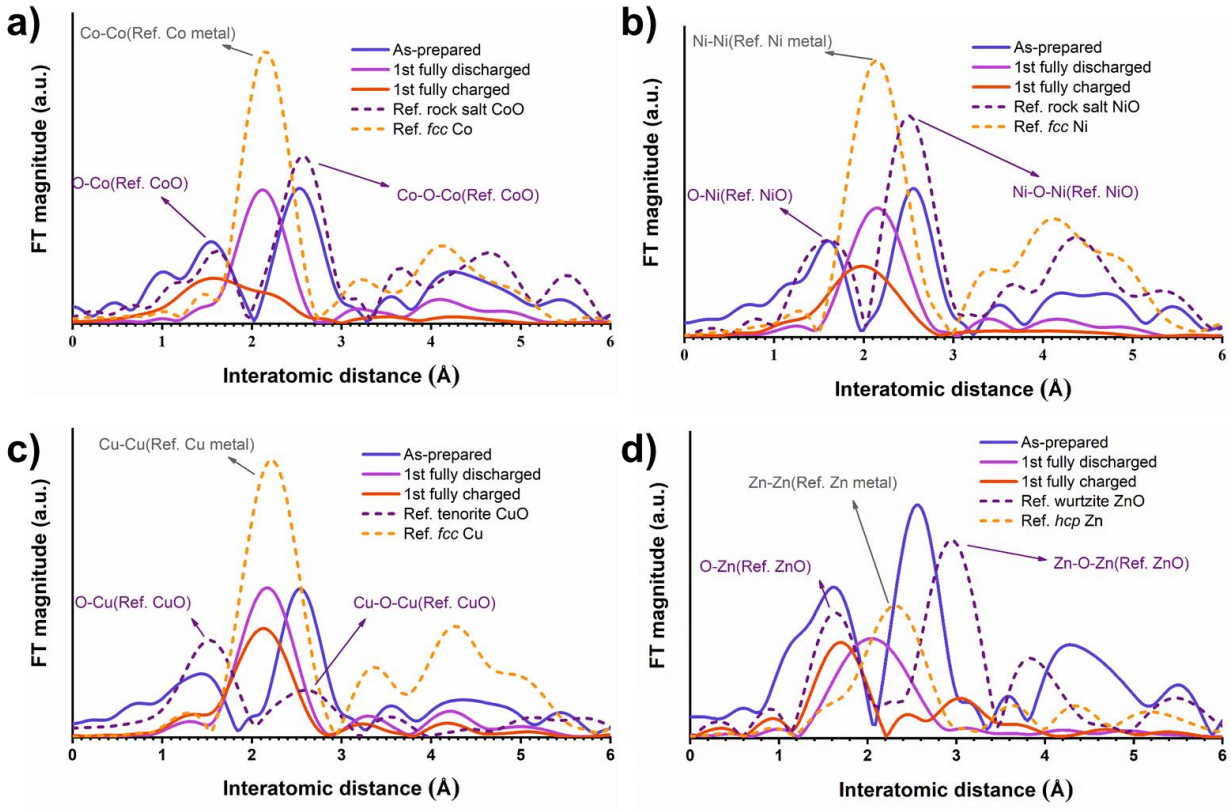

Figure 4-4: EXAFS-FT spectra of **a)** cobalt, **b)** nickel, **c)** copper and **d)** zinc of as-prepared and cycled samples.

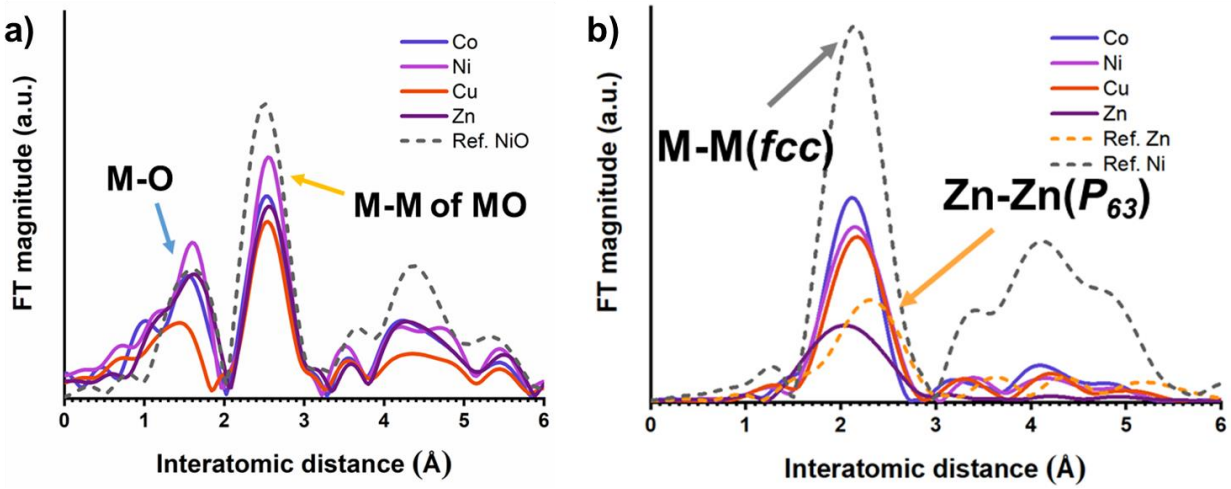

Figure 4-5: **a)** superposition of the EXAFS-FTs of Co, Ni, Cu and Zn in the as-prepared state; **b)** superposition of the EXAFS-FTs of Co, Ni, Cu and Zn in the 1st discharged state.

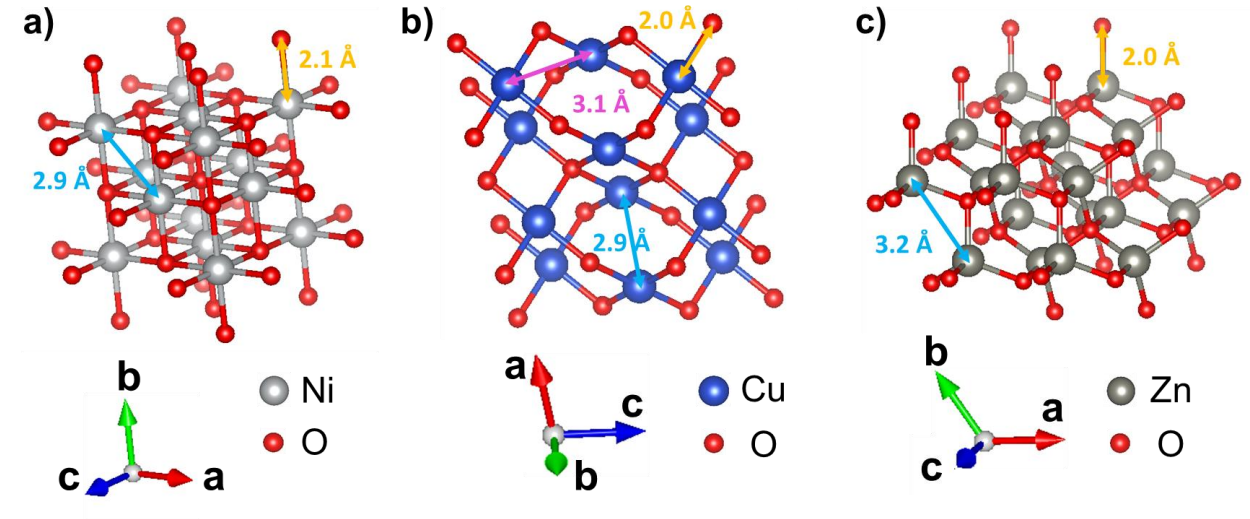

Figure 4-6: schematic structures of **a)** NiO, **b)** CuO and **c)** ZnO.

4.4. Elemental distribution

The ePDF and XAS results reveal that a significant amount of metallic compounds remain in the recharged sample and that the elements exhibit different behavior during cycling. To further analyze the distribution of the transition metals, the elemental distribution was characterized by a series of STEM related techniques. STEM-EDX analysis was conducted to study the elemental distribution in the bulk 1st recharged sample. From the result shown in Figure 4-7, all elements show a homogeneous distribution except for some agglomeration of Cu and Ni in some areas. However, the result here do not deliver accurate elemental distribution information due to serious overlap of the thick particle in projection.

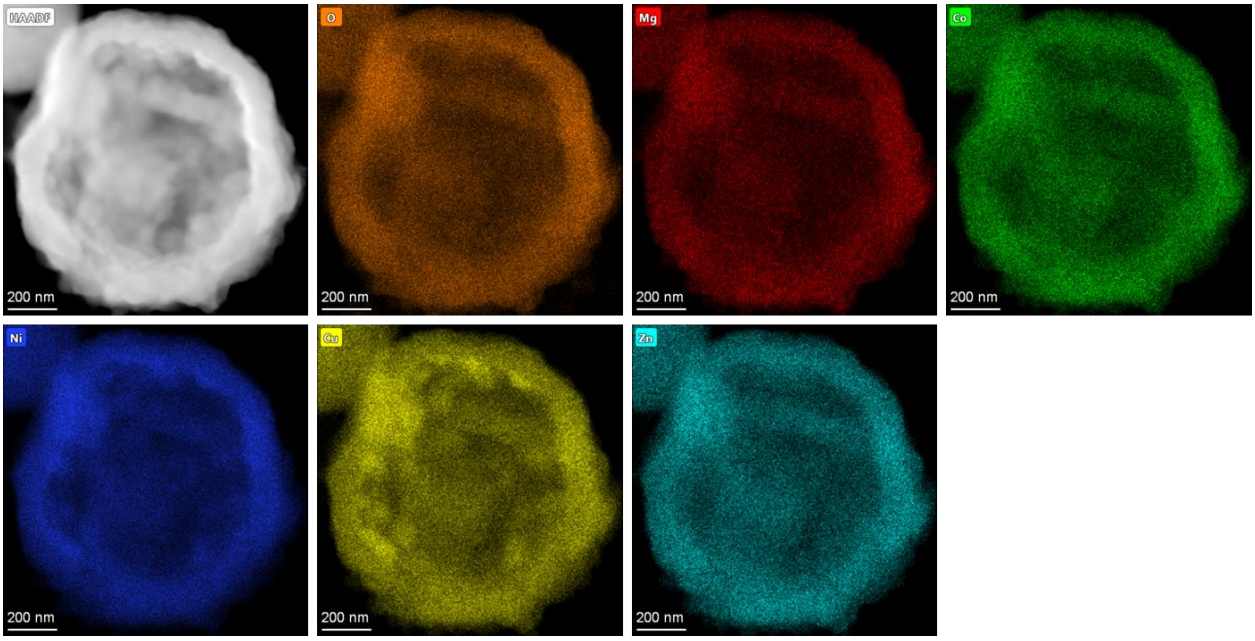

Figure 4-7: STEM-EDX map of the 1st recharged sample.

To avoid the effect of overlap in projection, a focus ion beam (FIB) system was used to prepare thin samples for TEM analysis. Figure 4-8a-c are STEM-HAADF images of the as-prepared, 1st discharged and 1st recharged state. Different from the image of the as-prepared sample that show homogeneous contrast, the cycled samples, both in the discharged and the recharged state, exhibit some dendritic features. The contrast in STEM-HAADF imaging is related to the average atomic weight as the strong scattering from heavier elements results in stronger scattering to the HAADF detector as discussed in **Chapter 2**. Therefore, these features in the cycled samples could be an indicator that different phases separate in the cycled samples. Considering that the particles consist of metal and metal oxide, the higher contrast should be from the metal phase as the oxygen reduces the average atomic number in the oxide phase. To exclude effects due to FIB sample preparation that could possibly damage the sample, the sample was also prepared by ultramicrotomy (Figure 4-8d). Both sample preparation methods revealed the same basic morphology excluding possible artifacts by the FIB sample preparation.

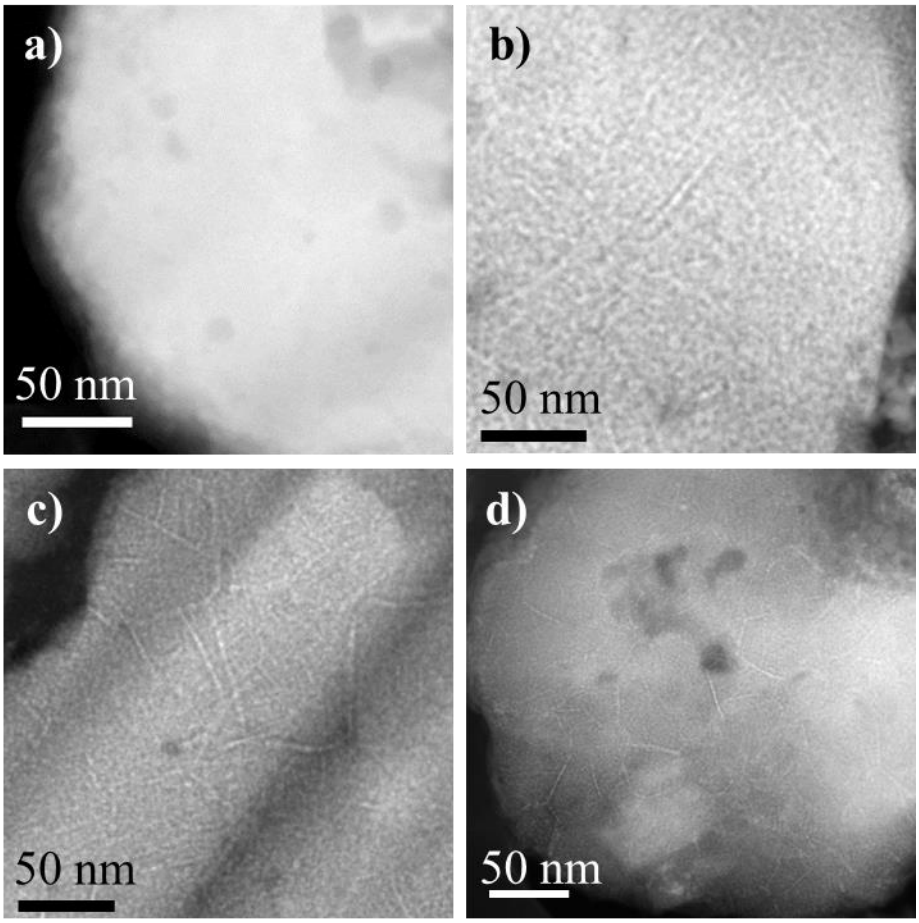

Figure 4-8: STEM-HAADF images of **a)** as-prepared, **b)** 1st discharged and **c)** 1st charged samples prepared by FIB; **d)** STEM-HAADF image of 1st discharged sample prepared by ultramicrotomy.

STEM-EELS maps confirm the conclusions drawn from the STEM-HAADF images. Figure 4-9a shows an STEM-ADF image of the 1st discharged sample. Figure 4-9b shows that Cu and Ni are enriched at the high intensity areas (the dendrites and bright dots) in the STEM-ADF image. At these areas O, Mg and Zn

have low concentration. Mg and O exhibit a high correlation confirming that Mg cannot be reduced by the lithium ions in the given voltage range (0.01V to 3.0V). Zn is enriched at the low intensity areas and show a distribution different from Co, Ni and Cu, which excludes the possibility that Zn is alloying into the *fcc* structure with other transition metals. The Co distribution is relatively homogeneous indicating that Co is present in both the metal and the oxide phase in the discharged state. Figure 4-9d to 9f show the corresponding information for the 1st recharged state. Similar to the discharged state, Cu and Ni are enriched at the high intensity features in the STEM-ADF image. (e.g. the marked areas in Figure 4-9d and 9f). Although the Co map is different from those of Cu and Ni, some overlap at the dendrites means that some metallic Co is with Cu and Ni. The distribution of Co, Ni and Cu indicates that Cu, Ni and partially Co cannot be oxidized after the charging process, which is consistent with the ePDF and the XAS results. At the lower intensity areas, Co is present together with Mg, Zn and O, which indicates the oxidized Co and Zn are incorporated into the MgO structure.

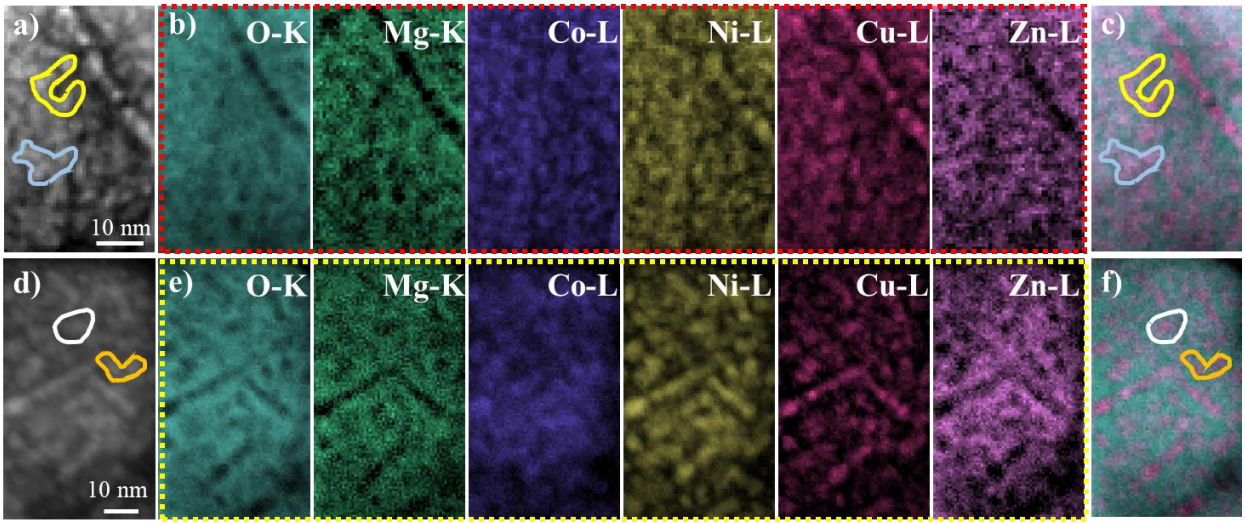

Figure 4-9: EELS characterization of 1st discharged (**a)** to **c)**) and 1st charged (**d)** to **f)**) samples; **a)** and **d)** STEM-ADF images; **b)** and **e)** elements maps; **c)** and **f)** overlapped images of O and Cu.

The Cu L edge in EELS is very sensitive to the bonding state and can be used to analyze the oxidation state fast and efficiently. The white lines (L3 and L2 edges) in Cu are present in the oxidized state due to an electronic transition from the 2p to the incompletely occupied 3d orbital. However, the 3d orbital is completely occupied in metallic Cu leading to an absence of the L3 and L2 peaks. The Cu-L edge EELS spectra of the as-prepared and cycled sample is shown in Figure 4-10. The Cu-L edges of the as-prepared and cycled samples show distinct difference in terms of the L3 and L2 edges presented in the as-prepared sample indicating that the oxidized state present in the as prepared state cannot be found in the cycled samples. This confirms the XAS results that showed Cu in a metallic state in both discharged and recharged samples.

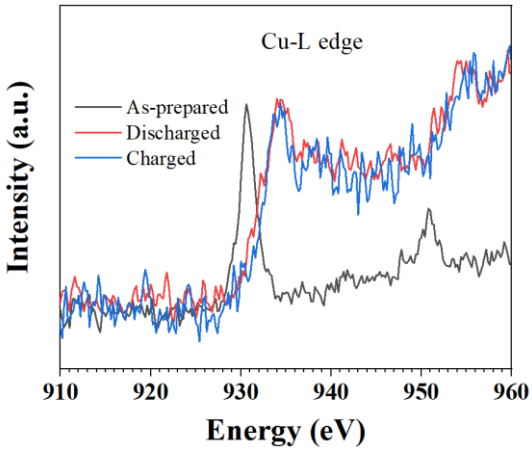

Figure 4-10: Cu-L edge EELS spectra of as-prepared and cycled samples.

4.5. Structure of the metal and metal oxide phases

From the EELS maps it is clear that the metal and metal oxide phases are both present and tightly intermixed in the cycled sample, but no structural information can be extracted from the elemental distribution. Therefore, HRTEM measurement of the 1st recharged sample were preformed (Figure 4-11). The darker dendritic features can be observed easily, corresponding to the Cu, Ni and partially Co enriched area visible in the STEM-HAADF image inset. In the magnified HRTEM image of the area marked in Figure 4-11a the well-defined lattice planes can be clearly observed, which give rise to the features in the corresponding fast Fourier transforms (FFT). The FFT from the dendrite can be indexed as a [101] oriented *fcc* metal structure. Combined with XAS and EELS analysis, it can be concluded that the dendrites in the cycled samples consist of a CuNiCo alloy phase. The *fcc* structure has a lattice parameter of 3.6 Å, which is close to *fcc* Cu (3.62 Å), Ni (3.53 Å) and Co (3.55 Å) single elemental metals. In Figure 4-11d, two sets of diffraction patterns can be identified corresponding to an *fcc* metal structure (outer diffraction pattern) and a rock salt metal oxide structure (inner diffraction pattern). The pattern from the metal phase is consistent with the CuNiCo alloy phase mentioned above. Notably, the metal phase and metal oxide phase in Figure 4-11d have the same orientation. In addition, all the planes in this zone axis for the two structures have the exactly same directions, i.e. the $(\bar{1}\bar{1}1)$, $(\bar{1}11)$ and (020) of metal phase corresponds exactly with the $(\bar{1}\bar{1}1)$, $(\bar{1}11)$ and (020) of the metal oxide phase. This indicates that the metallic (excluding the dendrite at the grain boundary) and the oxide phase have an epitaxial relationship inside the grain. The large difference (16.7%) of the unit cell parameters between the metal (3.6 Å) and the oxide (4.2 Å) in the epitaxial structure observed in this work induces a very large strain energy. However, even larger lattice mismatch has been reported in literature and the maximal allowed lattice mismatch varies for different materials. For instance, a maximum lattice mismatch of 15.7% has been observed in the epitaxial structure of FePt (3.87 Å) and $Zr_{0.70}Ti_{0.30}N$(4.47 Å).[279] In the epitaxial structure of TiN (4.24 Å) and Si (5.43 Å) with a lattice difference of 28.1% was experimentally demonstrated.[280] However, the large lattice mismatch

between the metal and metal oxide structures does not allow for the two phases to form a defined interface over a long distance. Therefore, the sizes of metallic phase and oxide phase are in the range of several nanometer, which agrees with the size of the bright domains (metallic phase) and the dim domains (oxide phase) inside the grain observed in the STEM-ADF images (Figure 4-8 and Figure 4-9).

Figure 4-12e is an enlarged image of the grain boundary (indicated by the white dash box in Figure 4-12b) showing that the ($\bar{1}11$) metal planes and the (020) MO planes are more or less continuous across the boundary. That means the dendrite at the grain boundary has a different crystallographic orientation. As shown in Figure 4-11f (the FFT of Figure 4-11e), the direction of ($\bar{1}11$) of the M dendrite (2.1 Å) is roughly aligned with the (020) direction of the MO (2.1 Å) inside the grain and only tilted by about 7 °. However, the lattice mismatch in the other directions is presumably responsible for the slight disorientation between the dendrite and the grain seen in the HRTEM image (Figure 4-12e) where the dendrite is well aligned along the [101] orientation but grain interior in the vicinity is slightly misaligned from the zone axis.

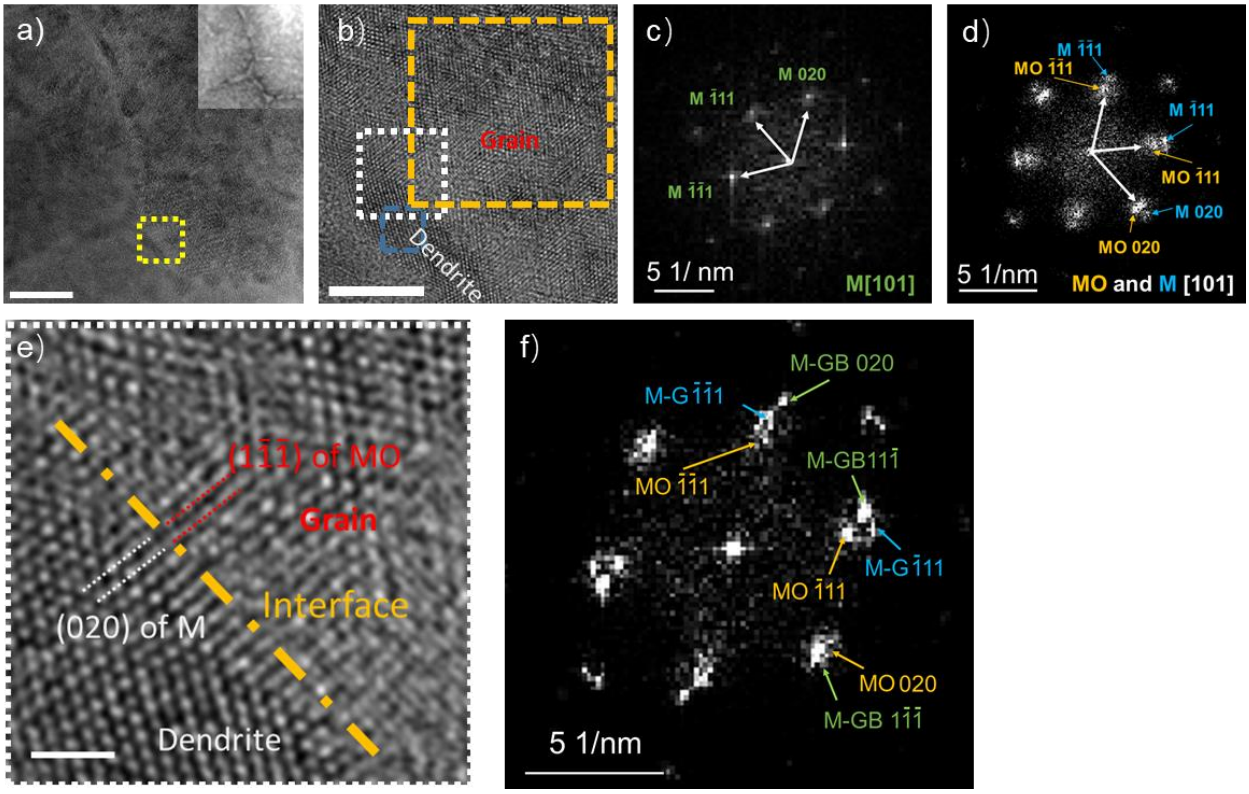

Figure 4-11: Structure characterization of the 1st charged sample. **a)** HRTEM image, inset is the STEM-HAADF image at the same area; **b)** enlarged image of the marked area in **a)**; **c)** FFTs of the blue dash box marked areas in **b)**; **d)** FFTs of the yellow dash box marked areas in **b)**; **e)** enlarged image of the marked area by white dash box in **b)**; **f)** FFT of **e)**. The scale bar in **a)** is 20 nm, in **b)** is 5 nm, in **e)** is 1 nm. The M-GB and M-G in **f)** present the metal phase at grain boundary and inside the grain, respectively.

A similar epitaxial structure between M and MO has been observed in the discharged state as well. Figure 4-12a and 12b are a HRTEM and the corresponding STEM-HAADF image. The dendritic feature can be clearly recognized in the STEM-HAADF image is rather diffuse in the HRTEM image, due to the low crystallinity of the discharged sample. This low crystallinity is directly noticeable by the FFT shown in the insert in Figure 4-12a, which exhibits only streaky diffraction spots. Nevertheless, two sets diffraction patterns for M and MO with the same orientation can be seen in the FFT, meaning that inside the grain of the discharged sample the epitaxial structural relationship between the M and MO phases has already developed during the lithiation process. However, a clear interface at the grain boundary cannot be directly observed here due to the low crystallinity.

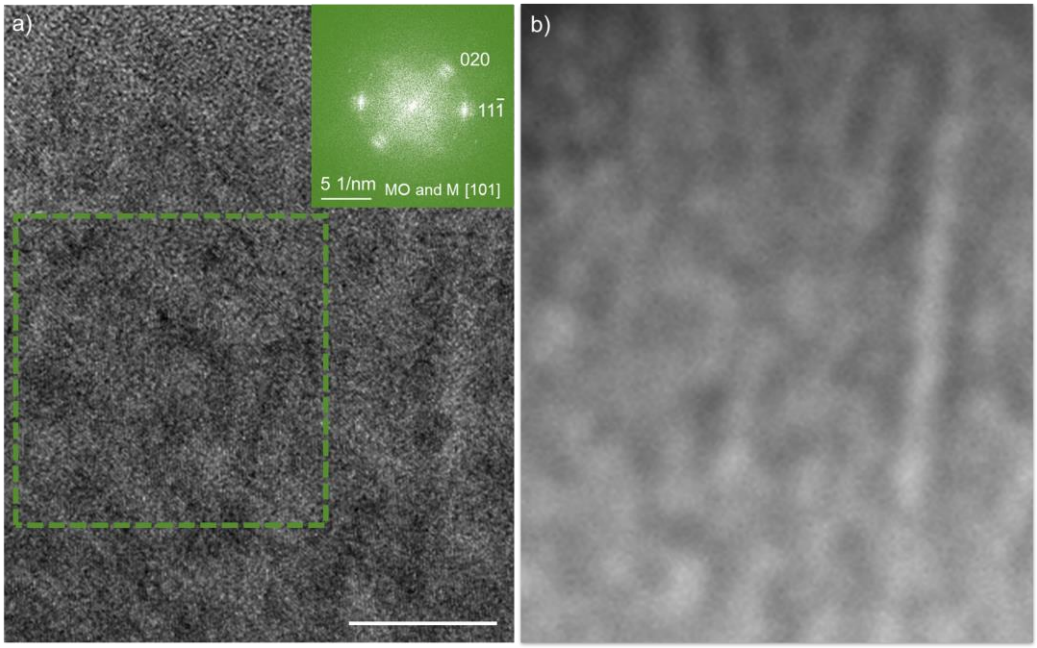

Figure 4-12: Structure characterization of the 1st discharged sample. **a)** HRTEM image of 1st discharged sample, insert is FFT from the marked area; **b)** STEM-HAADF image at the same area with **a).** The scale bar is in **a)** is 10 nm.

4.6. Orientation and phase distribution

4D-STEM with an almost parallel beam was used to confirm the phase and orientation information over a larger area. Figure 4-13a displays the STEM image corresponding to the 4D-STEM data set at the 1st discharged state, where some dendrites can be easily observed. Figure 4-13b is the corresponding orientation map obtained by indexing the zone axis of each local diffraction pattern in the 4D-STEM data. *Fcc* Cu and rock salt MgO were used as representative structures for M and MO to index the diffraction patterns of the 4D-STEM data set as their lattice parameters are very similar to the experimental data (obtained in HRTEM). It is clear that the particle has a polycrystalline structure with a grain size of a few hundred nanometer. Comparing the STEM-HAADF image and the orientation map, it is clear that the dendrites preferentially develop at the grain boundary, e.g. the areas indicated by arrows in Figure 4-13a

and 13b. This means that Cu, Ni and some Co diffuse from the rock salt structure to the grain boundary and form an alloy, which could provide a fast electron transfer path during the following cycles.

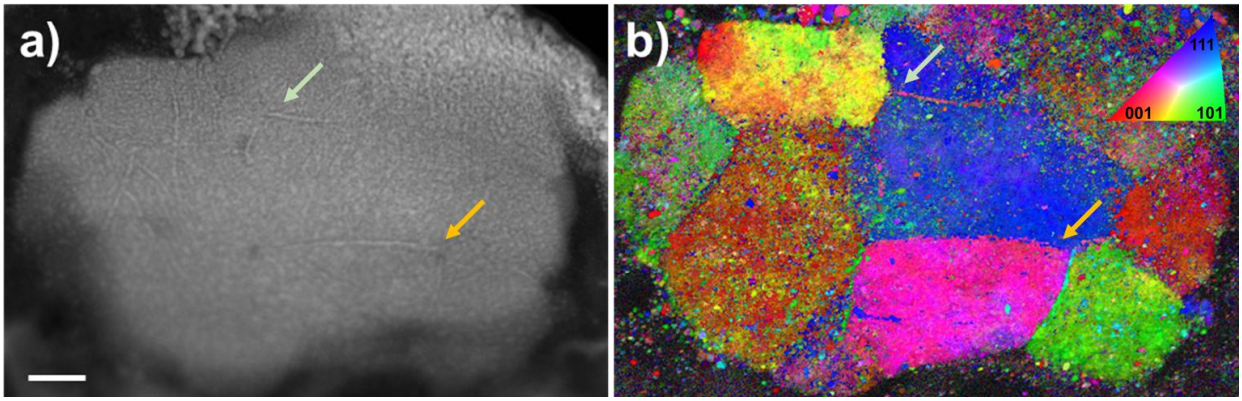

Figure 4-13: **a)** STEM-HAADF image of the 4D STEM data acquiring area of the 1st discharged sample, the scale bar is 50 nm; **b)** orientation map of the corresponding area in **a)**.

Figure 4-14a is the phase map acquired by analyzing the 4D -STEM data that shows the M (green) and MO (red) mixed homogenously at the nanometer level within the grain, while the dendrites dominated by the metal structure are present at the grain boundaries. Figure 4-14c/d are the summed diffraction patterns from the yellow and blue areas in Figure 4-14b. Although the M and MO structure contribute more to one diffraction pattern than to the other in Figure 4-14c/d, both sets of diffraction spots can be found in each pattern, indicating a significant mixture of both structures in projection. The colors shown in the phase map are assigned based on the phase which dominates the diffraction pattern, but the overall reliability of this ACOM analysis is low because of the serious overlapping of the metal and oxide phases. In addition, the *fcc* ZnLi alloy was also found in the diffraction pattern in Figure 4-14e, which shows the integrated signal from the area marked by the yellow dash box in Figure 4-14a. Figure 4-14f and 14g are line profiles along the arrows at the green and blue rectangle areas in Figure 4-14e, in which three sets diffraction patterns can be indexed including *fcc* M, rock salt MO and ZnLi alloy. Considering that Mg^{2+} cannot be reduced during the lithiation in the given voltage range and the metallic state of all the other four elements has been confirmed by XAS, the MO here should be MgO. Although a large amount Li_2O should be present at the discharged state, it was not detected in the TEM measurements, which could be caused by the beam sensitivity of Li_2O or due to an incorporation with the other oxides. The lattice spacing of the {004} and {022} planes in ZnLi are very close to the d-values of {022} and {002} in MgO. In the ACOM analysis, this cannot be properly separated and with the thus enhanced MO signal (red) viewed along the [001] direction this results in Figure 4-14a showing more intense red color this grain in the left-top corner. The shift of the (002) peaks of M and MO (MgO) and (022) of ZnLi in the reciprocal space are aligned suggesting a defined orientation relationship among the three compounds.

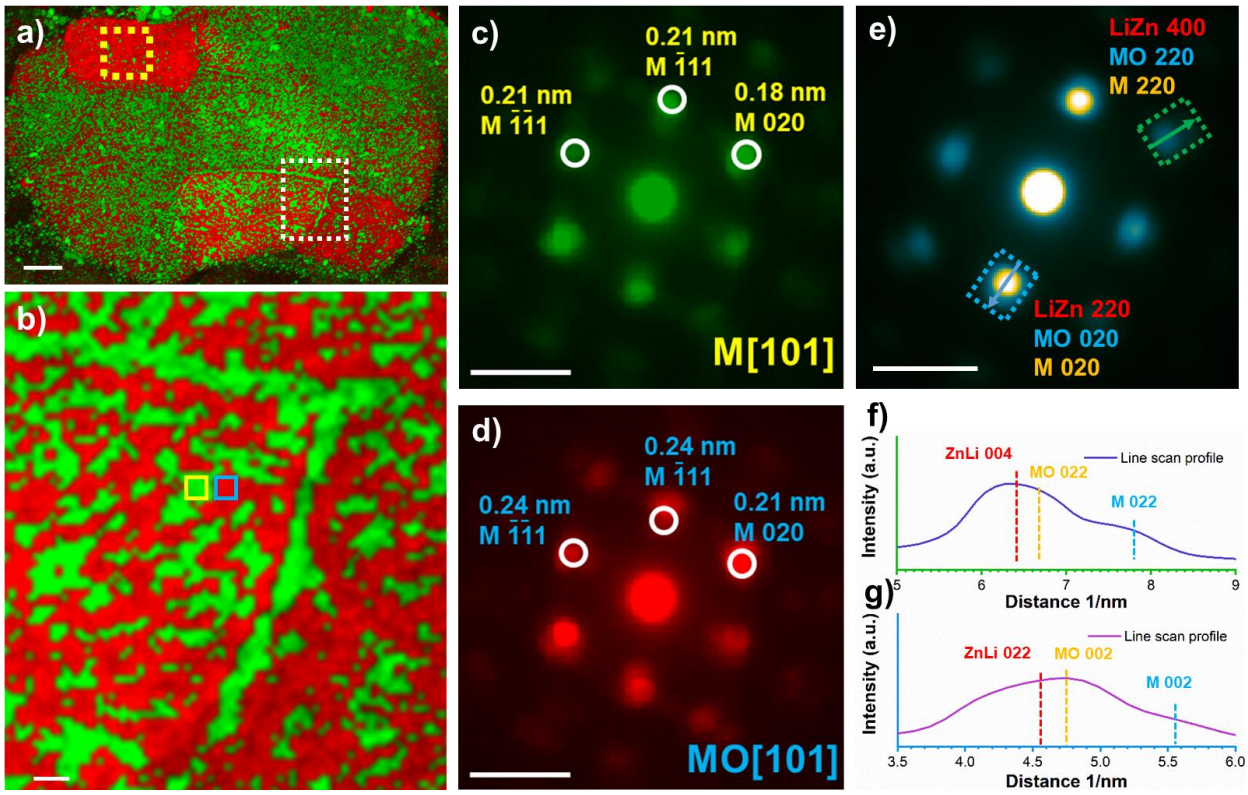

Figure 4-14: **a)** phase map processed from the 4D-STEM data in Figure 4-13; **b)** local phase map at the area marked in a by white rectangle in **a)**; **c)** and **d)** summed diffraction of the yellow and blue rectangle areas in **b)**; **e)** summed diffraction at the yellow rectangle marked area in **a)**; **f)** and **g)** line scan profiles of the green and blue rectangle areas in **e)** along the arrows directions. The scale bar in **a)** is 50 nm, in **b)** is 5nm, in **c)** and **d)** is 5 1/nm, in **e)** is 5 1/nm.

Based on the results from the HRTEM and 4D-STEM, the complex structure relationships of the different phases in cycled materials, at the discharged and recharged state, could be drawn. The initial HEO has a polycrystalline rock salt structure. During the lithiation process, during discharging, except for Mg all metal elements are reduced to a metallic state from the oxide. Some amount of Co, Ni and Cu separated out of the grain and alloyed into an *fcc* structure at the grain boundary as confirmed by the EELS, HRTEM and 4D-STEM data. Co, Ni and Cu still presented within the grain form an *fcc* alloy inside the grain. A schematic of the structure is shown in Figure 4-15a. In the discharged sample, a rock salt oxide phase was confirmed by both HRTEM and 4D-STEM data. As the XAS data confirms except for Mg that all metal elements are in a metallic state and Mg should be the only elements from the initial HEO in the oxide phase. During the discharging, the other metal elements were driven out of the HEO structure and the vacancies left by the transition metal elements (Co, Ni Cu and Zn) could be filled by Li^+ and form a continuous rock salt structure Mg-Li-O network. The large grain size (hundreds nm) visible in Figure 4-13b could be an indicator for this speculation: if Li^+ did not occupy a large amount of vacancies left by the transition metals (80% of metal sites in the initial HEO) the orientation of oxide phase would be expected to vary locally. A schematic of the structure of the Mg-Li-O phase is shown in Figure 4-15b. The 4D-STEM data in Figure 4-14 indicates that the alloy and oxide phases have an epitaxial relationship as the planes

in the two structures have exactly the same orientation in both [101] (Figure4-14c and 14d) and [100] (Figure 4-14e) direction in one grain. The ZnLi alloy formation was confirmed to be another phase in the discharged sample. XAS data of Zn in the discharged state showed that Zn has an *fcc* metallic environment. The EELS maps exclude the possibility of Zn alloying with other transition metals as they show different distributions. Various literature references confirm that Zn can alloy with Li forming an *fcc* alloy during lithiation process[276–278], which is a consistent conclusion from our work about the Zn environment in the discharged state. Besides the CoNiCu alloy and Mg-Li-O, a third phase detected in the 4D-STEM data can be indexed using the ZnLi structure. A schematic of the ZnLi alloy is shown in Figure 3-15c. The 4D-STEM data indicates the ZnLi showing an epitaxial structure relationship with the Mg-Li-O phase as the (004) and (022) planes of ZnLi have the same orientation with the (022) and (002) planes of the Mg-Li-O phase. These planes have similar d-space values as well. The assumed schematic of the epitaxial structure between ZnLi and Mg-Li-O is shown in Figure 4-15-right. An overall structure relationship inside the grain can be concluded based on the above discussion that all the phases formed, CoNiCu alloy, ZnLi alloy and Mg-Li-O, have an epitaxial relationships and randomly distribute inside the grain with small domain sizes of several nm. Unfortunately, the structure relationship of the CoNiCu alloy and Mg-Li-O was not been directly observed in the discharged state due to the low crystallinity (as shown in the Figure 4-12). However, we assume the structure relationship between the CoNiCu alloy and Mg-Li-O is consistent with that at the recharged state because the CoNiCu alloy was already formed (demonstrated by the HRTEM and 4D-STEM data) and it can be clearly observed in the dendrites located at the grain boundary in the lithiated sample. HRTEM in the delithiated state (Figure 4-11e) shows that the (111) reflection of the formed *fcc* alloy and the (002) of the oxide phase are continuous across the grain boundary indicating that the two structure could intergrown along this direction. However, in another direction the lattice distance of the two phase, (022) of metal phase (1.3 Å) and (022) of oxide phase (1.5 Å), cannot match with each other. Therefore, a titled angle could be need between the two phases to compensate part of the mismatch. A basis for this speculation is that the dendrite is well aligned along the [101] orientation but the grain interior in the vicinity is slightly misaligned from the zone axis as shown in the HRTEM in Figure 4-11e. A possible schematic of the structure relationship of CoNiCu alloy and Mg-Li-O at the grain boundary is shown in Figure 4-15d (left). The overall relationship among the different phases at the lithiated state is shown by the diagram in Figure 4-15e based on the experimental results and uncertainties mentioned above. During the following delithiation process, the Zn and partial Co can be reoxidized back to 2^+. They could be incorporated into the Mg-Li-O phase and replace some Li^+ as the EELS maps show quite similar distribution for Mg, Co, Zn and O (Figure 4-9e). The released Li^+ was transferred towards to the counter electrode. The CoNiCu alloy formed at the grain boundary and inside the grain cannot be reoxidized and kept the structural relationship with the oxide phase that at the lithiated state.

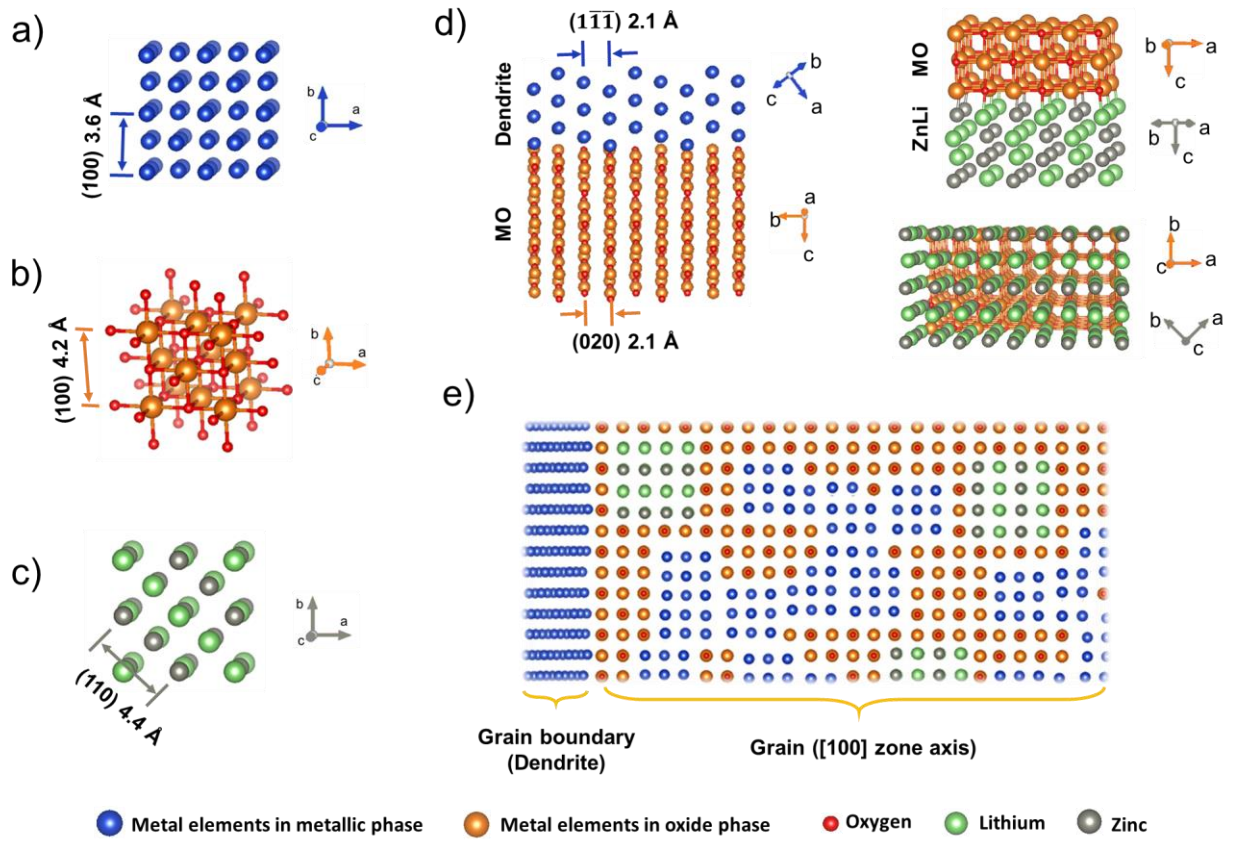

Figure 4-15: diagram of structures and epitaxial phase relationship. Sketches of the phase structure of **a)** M phase, **b)** MO phase and **c)** ZnLi phase; **d)** relationship of the dendrite and the oxide phase (left) at the grain boundary as well as of the oxide phase and ZnLi (right) in the grain; **e)** an exemplary overview structure schematic in the discharged state.

4.7. Study of the 3D electric conductive network

4D-STEM data revealed the presence of metal alloy dendrites at the grain boundaries. However, no 3D information on the connectivity of these conductive paths is available from the 4D-STEM data. Therefore, STEM based electron tomography at the discharged state was performed to analyze the 3D structure. Figure 4-16a shows a volume rendering of a part of the complete reconstructed particle, in which denser, thin layers can be observed. After segmentation, surface rendering of the alloy at the grain boundary was conducted (inset Figure 4-16a), which reveals that the alloy forms a connected 2D sheet-like morphology. Figure 4-16b to 16f show different cross sections of the selected volume revealing the interconnected high intensity alloy present throughout the thickness. Combining the 4D-STEM and the 3D tomography information of the discharged sample, the reduced Cu, Ni and Co alloy generate this highly interconnected sheet-like alloy network at the grain boundaries of the particles. This 3D alloy network provides a fast electron transfer path in the otherwise insulating oxide particles and thus eliminates the particle/aggregate size effects in MOs serving as electrode material. Inside the grain, the metal phase intermixed with the oxide phase at the nanometer level provides a short electron transfer path further

enhancing the electronic conductivity of the grain. These observation lead to the conclusion that the electric conductivity of the cycled sample should be enhanced dramatically compared with the initial HEO.

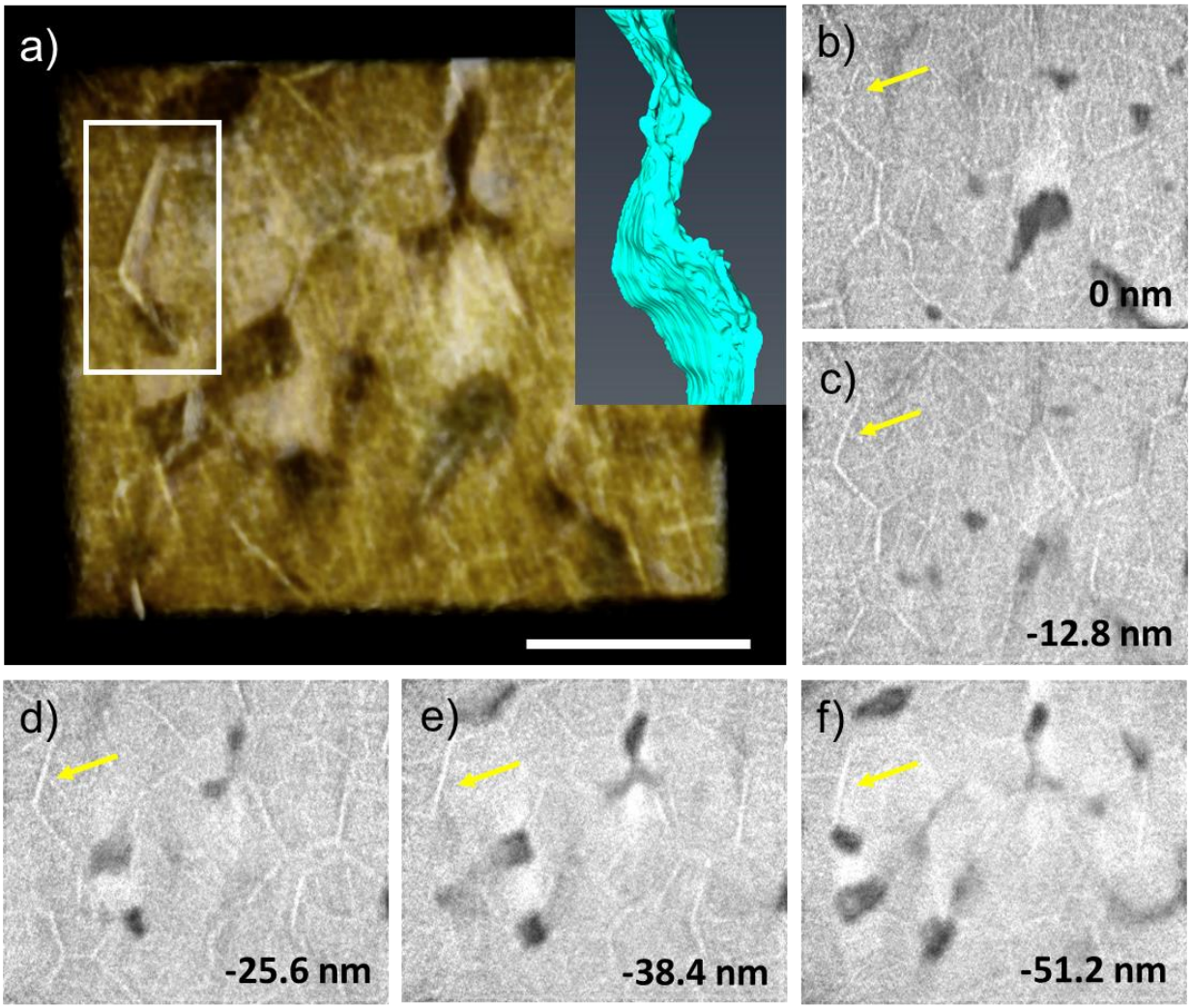

Figure 4-16: **a)** visualization of 3D tomographic reconstruction of the sample at 1st discharge state, the insertion is a surface rendering of the alloy phase at the grain boundary in the white box marked area; **b)** to **f)** slices of the reconstruction along the view direction in the depth denoted at the bottom right corner in the images.

To experimentally confirm the improved conductivity, a STEM-STM holder was used to measure the electrical conductivity of the as-prepared and 1st recharged sample. As shown in Figure 4-17a, the recharged sample shows a dramatically enhanced electric conductivity compared with the as-prepared sample. The as-prepared sample behaves as an insulator where almost no current could be detected in the voltage range of -15 to 15 V. However, the current intensity of the cycled sample reached 0.1 µA at 15 V. The fact that almost no current was measured in the range from -5 to 5 V can be assigned to the contact resistance between the W tip and analyzed particle.

Electrochemical impedance spectroscopy (EIS) was conducted to separate the effect of ion transfer on the conductivity and to obtain a statistically relevant analysis at the macroscopic level to study charge

transfer and mass transfer resistance in the entire battery system. The EIS spectra from as-prepared (black) and recharged (red) samples are shown in Figure 4-17b. In the EIS spectrum, the x axis and y axis present the real part (Z') and imaginary part (Z'') of the impedance. The frequency decreases with an increasing real part (Z') of the impedance. As shown in Figure 4-17b, the EIS of the as-prepare sample consists of a semicircle at high and medium frequency and a straight line in the low frequency region, which are dominated by the charge transfer and mass transfer.[281,282] In the spectrum of the 1st charged sample, two flattened semicircles (as marked by the arrows in Figure 4-17b) are observed in the high and middle frequency region. The appearance of the first high-frequency semicircle is caused by the solid electrolyte interface (SEI) formation at the cathode surface during the lithiation process, which is a common phenomenon that can be observed in cycled batteries[283–286]. The second semicircle in the medium frequency region is caused by the charge transfer resistance of the anode/electrolyte interface. As expected, the charge transfer resistance (R_{ct}, the diameter of the second semicircle at medium frequency) of the 1st recharged sample is much smaller than the diameter of the semicircle in the as-prepared sample indicating that the the electronic resistance was reduced after cycling. The results shown here confirm the hypothesis presented above and prove that the 3D alloy network at the grain boundaries and inside the grain can reduce the electron resistance of the cycled samples.

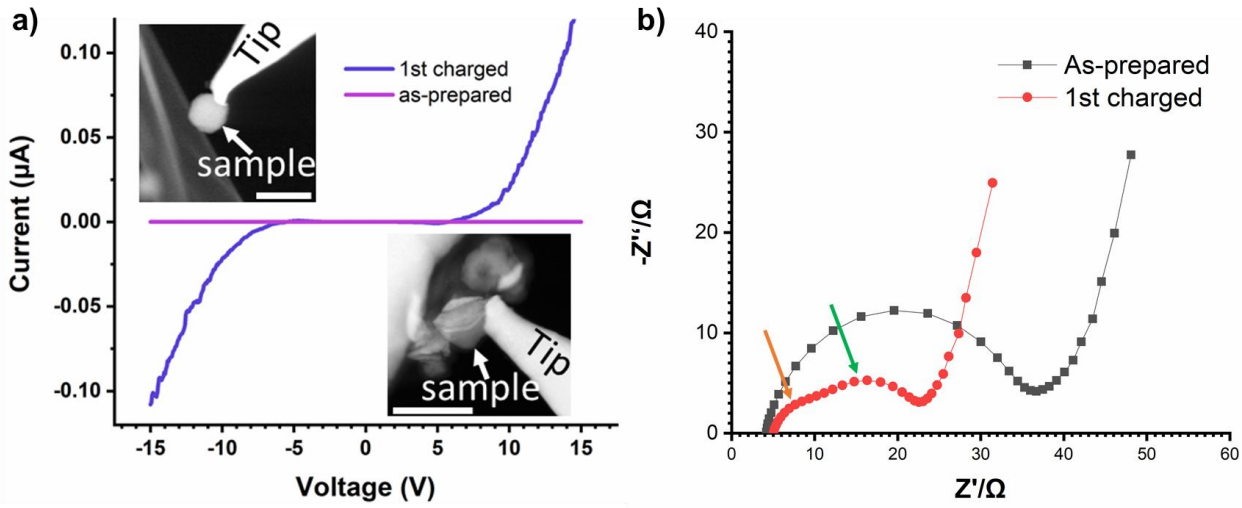

Figure 4-17: **a)** current-voltage curve of the as-prepared and 1st charged samples, the insets at the top-left and bottom-right show the situation of the as-prepared and the 1st charged sample respectively, the scale bars are 500 nm; **b)** electrochemical impedance spectroscopy (EIS) of the as-prepared and 1st charged samples.

4.8. Summary and discussion

4.8.1. Summary

In this chapter, we investigated the reaction mechanisms of the HEO $(Co_{0.2}Cu_{0.2}Mg_{0.2}Ni_{0.2}Zn_{0.2})O$ used as anode in lithium batteries. Samples in the as-prepared, delithiated and delithiated states have been characterized by various techniques in order to understand the electrochemical reactions. The results

show that the initial HEO consists of micro-size hollow particles exhibiting a pure rock salt structure. In the lithiated state Co, Ni, Cu and Zn were reduced to a metallic state with Zn further forming an *fcc* ZnLi phase. The reduced Co, Ni and Cu formed an *fcc* alloy at the grain boundary and inside the grain. Mg cannot be reduced by Li in the given voltage window due to its higher reducibility compared with Li. This was confirmed by EELS maps where the Mg distribution showed a high correlation with O. HRTEM and 4D-STEM results also confirm a continuous rock salt structure in the lithiated sample even though all the Co, Ni, Cu and Zn were demonstrated by XAS to be in a metallic state in the lithiated sample. During the lithiation the Co, Ni, Cu and Zn are extracted from the rock salt structure of the initial HEO, which leaves a large amount of vacancies. The vacancies might be filled by the Li^+ transferred from the electrolyte and an Mg-Li-O frame is supposedly produced in the lithiated sample. Evidence for this speculation is the continuous rock salt oxide network present in the lithiated sample although 80% of metal elements in the HEO have been removed from the metal sites of the initial structure. The Mg-Li-O frame probably plays a critical role in stabilizing the material by forming an epitaxial structure with the metallic phase (CoNiCu alloy inside the grain) and the ZnLi alloy during battery cycling. A large lattice mismatch is present between the CoNiCu alloy (3.6 Å) and Mg-Li-O (4.2 Å) and the strain energy is partially released by forming misfit dislocation. This is consistent with the small domain size of the metal and oxide phases observed by STEM-HAADF imaging. Moreover, the CoNiCu alloy at the grain boundaries leads to the formation of a 3D electrically conductive network, which has been confirmed by both the 4D-STEM and 3D tomography results. During the following delithiation process, after dealloying of ZnLi, Zn and partially Co were reoxidized back to 2^+. Due to the strong correlation of the Mg, Co, Zn and O elemental distribution maps at the delithiated state, we speculate that the reoxidized Co and Zn is incorporated into the oxide phase and forms a Mg-Co-Zn-Li-O network in the delithiated sample. The CoNiCu alloy network is not reoxidized during recharging and is still present in the delithiated sample. This could be due to the strong oxidation potential of Cu that cannot be oxidized in the given voltage window.[287] The 3D alloy distribution provides a good electron transport path and is of great advantage for metal oxides that are intrinsically electronically insulating. During battery cycling, the 3D alloy network can thus provide a fast electron transfer path through the grain boundaries. The nanoscale CoNiCu alloy intermixed with Mg-Li-O/ Mg-Co-Zn-Li-O result in short electron transport paths within the grain. At the same time, the Mg-Li-O/ Mg-Co-Zn-Li-O frame could be a good conductor for Li ions and one can speculate that the Li ions can migrate using the Li sites in the Mg-Li-O/ Mg-Co-Zn-Li-O network. M. Mozdzierz et al. reported that in a series of rock salt $(Co,Cu,Mg,Ni,Zn)_{1-x}Li_xO$ oxides ($x < 0.30$) the ionic conductivity of the material increases with increasing Li amount.[288] In addition, the Mg-Li-O/ Mg-Co-Zn-Li-O network seems to stabilize the structure and avoids strong volume changes and crushing of the initial particles (the hollow morphology of initial HEO was intact after the 1st cycle) and thus prevents dead volume generation and leads to a stable battery cycling.

In this work, the self-assembled 3D electron and ion conductive networks were revealed in the HEO ($Co_{0.2}Cu_{0.2}Mg_{0.2}Ni_{0.2}Zn_{0.2}$)O during battery cycling. The results shade light on the mechanism allowing HEO to avoid the 'size effect' when serving as anode in LIBs. This could open new perspective in the designing of metal oxides used for anode materials and the possibility of employing large particle size multi-cations metal oxides as next generation lithium ion electrode materials. Compared with the nanoscale metal oxides, the micro-size HEO could provide higher volumetric energy density and avoid the higher industrial production cost of the nanoscale manufacturing.

4.8.2. Discussion

The cyclic voltammetry (CV) curve of the HEO ($Co_{0.2}Cu_{0.2}Mg_{0.2}Ni_{0.2}Zn_{0.2}$)O during first five cycles is shown in Figure 4-18. In the first cathodic process, a broad peak appeared at about 0.5 V due to the reduction of the metal oxides, Co, Ni, Cu, Zn and ZnLi generation[111]. In addition, a SEI formation process is presumably also incorporated in this broad peak as the Li ions can react with a small amount of polar aprotic solvent in the electrolyte and form an organic solid electrolyte film on the particle surface.[289] In the following anodic scan, two weak, broad peaks can be observed. The first peak has a maximum at about 0.7 V and can be attributed to the dealloying of ZnLi.[111] The second peak has a maximum at about 1.8 V and corresponds to the oxidization of the metal elements. The wide voltage window, from about 1.3 V to 2.5 V, in principle includes the oxidization range for Co, Ni and Zn. However, the XAS results in this work show Ni not to be reoxidized during the delithiation process. Therefore, the second peak at about 1.8 V in the delithiation process corresponds only to the oxidization of Zn and Co. The overlapping of the reduction peaks of Co, Ni, Cu, Zn and the oxidization peaks of Co and Zn in the cathodic and anodic processes could be caused by the closed reaction potentials of the active metal elements in the HEO. Another explanation is that the electrochemical reaction of the HEO during lithiation and delithiation is a solid solution process where different metal elements (Co, Ni, Cu and Zn in first lithiation process, Co and Zn in delithiation process) react simultaneously. The simultaneous reaction of different metal elements during the lithiation and delithiation processes could be beneficial for the fast CoNiCu alloy formation and the incorporation of the Co and Zn into the Mg-Co-Zn-Li-O network. In addition, the solid solution reaction would provide a smooth voltage-capacity curve that can be easily incorporated in battery management systems. However, to confirm the solid solution reaction and the detailed sequence of the active metal elements transformation, more *in-situ* experiments, such as *in-situ* XAS, would be needed. During the following cycles, the cathodic peak shifts to higher energy compared to the first cycle, which could be caused by a suppressed SEI formation. The intensity of all the cathodic and anodic peaks decrease with increasing number of electrochemical cycles showing a capacity fading of the battery during cycling.

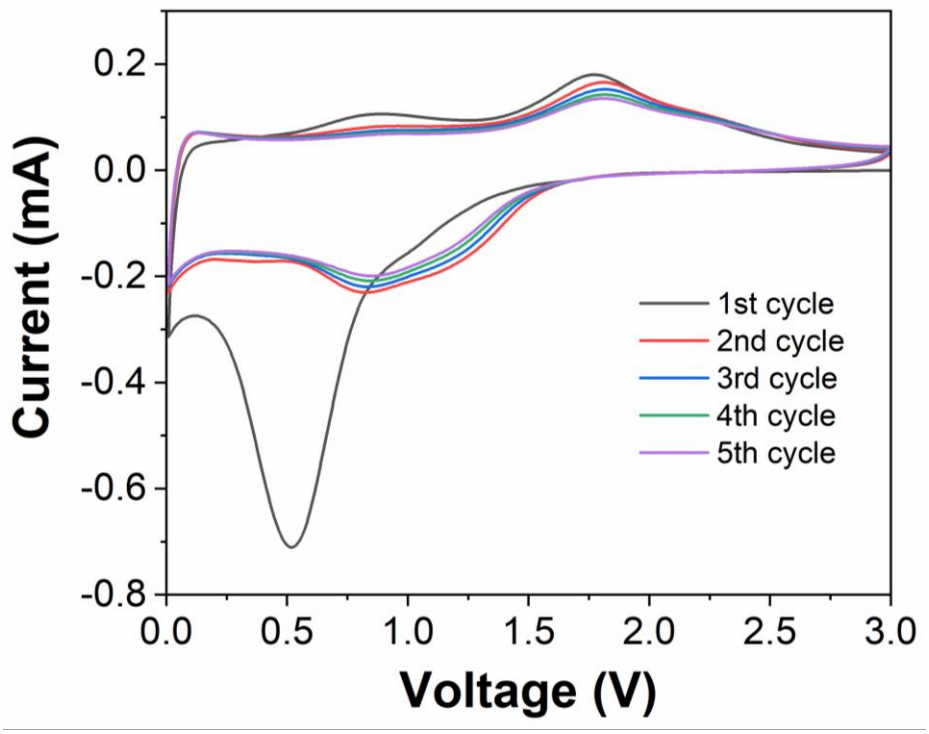

Figure 4-18: CV curve of HEO during the first five cycles in the voltage window between 0.01 and 3 V.

This work shows that the capacity of HEO ($Co_{0.2}Cu_{0.2}Mg_{0.2}Ni_{0.2}Zn_{0.2}$)O is given by the contribution of Zn and the partial contribution of Co. During the 1st lithiation process, Co, Ni, Cu and Zn were reduced to the metallic state using the electrons transferred from the external circuit. Zn further alloys with Li forming ZnLi. During the following delithiation process, the dealloying of ZnLi at about 0.7 V could provide about 70 mAh/g capacity. Then, Zn and partially Co were oxidized back to 2^+. During the oxidization of Zn, the state change from Zn to Zn^{2+} after the dealloying reaction could provide about 153 mAh/g capacity. If we assume all the Co can be reoxidized back to 2^+ (which it actually cannot), it would also provide a capacity of 153 mAh/g. Therefore, following the electrochemical reactions identified in this work, the HEO could only exhibit a total capacity of about 376 mAh/g (the summed value of the above mentioned processes). However, an experimental capacity of about 500 mAh/g was measured, much higher than the calculated capacity.[159] One explanation for this could be that the CuNiCo phase might also be able to alloy with lithium and thereby contribute to the capacity. The crystallinity changes in the discharged and charged material could be considered as evidence for the CuNiCo alloy to react during cycling, thereby adding to the capacity. As described in the results section, the discharged sample exhibits a lower crystallinity than the charged one, which could be caused by lithium insertion leading to the formation of a distorted structure in a CuNiCoLi alloy. Local EELS analysis of Li K-edge might in principle be able provide the answer. However, practically this was not possible for our samples due to the overlap of the very small metal and metal oxide phases in projection and the significant overlap of the Li-K edge and the M-edges of the transition metals, Co, Ni, Cu and Zn. In addition, the decomposition of SEI during delithiation and the pseudocapacitance could be other reasons for the higher experimental capacity.

This study has helped to reveal the behavior and the contribution of each of the five metal elements in the HEO during battery cycling. It has been shown that the function of each element cannot be considered isolated from each other, but they show synergetic effects in the battery. In a previous study it has been shown that the five metal element HEO exhibits better battery performance than any of the related four transition metal element MEOs (removal of single transition metal from the HEO).[159] The electrochemical performance comparison between the HEO and the MEOs (the pure phase MEO-Ni and MEO-Mg cannot be prepared experimentally) can be found in Figure 4-19. These results confirm that for achieving the high capacity and the stable cycling, the contribution of all metal elements in the HEO is indispensable for this synergic effect. The MEO without Co (MEO-Co) delivered a lower initial capacity compared with the HEO and completely lost the lithium storage ability after 11 cycles. This suggests that Co is a critical element in the HEO. During the battery cycling of HEO, the Co is present in both metallic and oxide phases. One possible reason for the inferior battery performance of MEO-Co could be that Co is essential for the formation of either CoNiCu alloy or Mg-Co-Zn-Li-O (at charged state) phases. However, we should mention that the success of HEO is based on the synergetic effect and not a simple summing of the behaviors of different elements. Therefore, only considering the function of each single element isolated from the other HEO cations might not be enough to illustrate the battery performance of the MEOs. Zn was demonstrated to be one of the main elements contributing actively to the capacity using the conversion reaction and alloy reaction. However, after removing Zn from the HEO, the MEO-Zn shows higher initial capacity than the HEO. In addition, while Cu and Zn have significant different roles in the HEO, the MEO-Cu and MEO-Zn show similar electrochemical performance. Although they have a higher initial capacity than the HEO, the capacity fades continuously after 20 cycles and reaches a lower capacity than the HEO after 30 cycles. The high initial capacity suggests that without Cu or Zn, more metal elements take part in the redox reactions meaning that fewer elements (or no metal elements at all) contribute to the alloy formation, which is a stable phase during the de/lithiation process (electrochemically inert like the CoNiCu alloy in HEO). The missing of the 3D network of CoNiCu alloy at the grain boundary and inside the grain could be one reason for the inferior battery cycling stability of MEO-Cu and MEO-Zn. Further experiments including *ex-situ* XAS and TEM measurements would need to be carried out for the MEOs at different cycling stages to better understand how the lack of the different transition metals affects their battery performance.

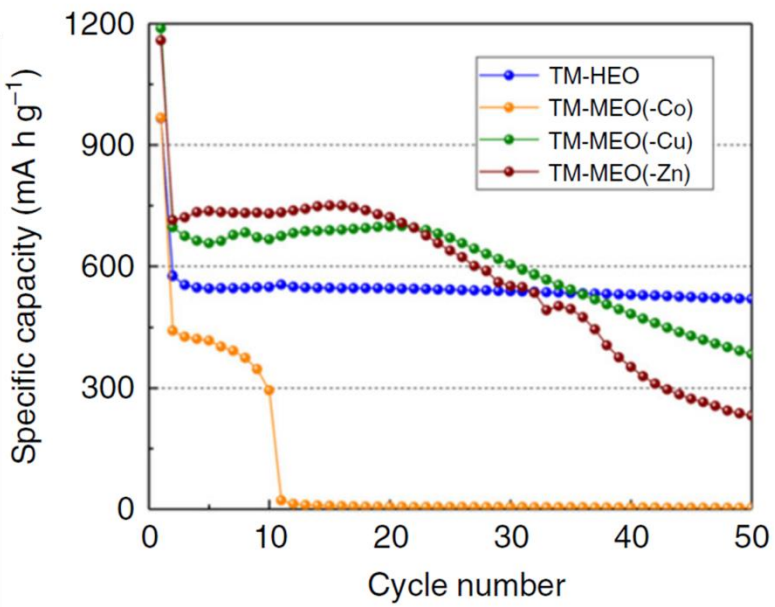

Figure 4-19: comparison of the battery performance among the HEO and MEOs using a current density of 50 mA/g, adopted from reference[159]. TM-HEO, TM-MEO(-Co), TM-MEO(-Cu) TM-MEO(-Zn) present $(Co_{0.2}Cu_{0.2}Mg_{0.2}Ni_{0.2}Zn_{0.2})O$, $(Cu_{0.25}Mg_{0.25}Ni_{0.25}Zn_{0.25})O$, $(Co_{0.25}Mg_{0.25}Ni_{0.25}Zn_{0.25})O$ and $(Co_{0.25}Cu_{0.25}Mg_{0.25}Ni_{0.25})O$, respectively. The battery performance of TM-MEO(-Ni) and TM-MEO(-Mg) are not shown here due to the pure phase TM-MEO(-Ni) and TM-MEO(-Mg) cannot be obtained in the same preparing condition with HEO.

5. New insight of de-/sodiation mechanism of MoS_2: sodium insertion in amorphous Mo-S clusters

5.1. Introduction

Beside metal oxides, molybdenum disulfide (MoS_2) is also a promising anode material for LIBs and SIBs with the advantage of a high theoretical capacity and excellent rate performance.[45,86,290] These advantages are especially useful for SIBs, where the traditional commercial graphite anode in LIBs is thermodynamically not feasible.[119] In LIBs, the lithiation mechanism is considered to be an intercalation reaction following a conversion reaction, which has been demonstrated by TEM and XAS analysis.[194,195] Mo cluster formation was observed directly by TEM and STEM imaging in work reported by S. Yu et al. and Q. Su et al.[194,195] W. Choi et al. demonstrated a conversion reaction mechanism by the disappearance of a defined Mo-S shell in the fully discharged state using XAS measurements.[196] An intercalation reaction during de/sodiation along with a phase change of MoS_2 from 2H to 1T was further confirmed by TEM and Raman studies.[190,191,291] However, the next reaction following the initial intercalation during further sodiation is still unclear. Considering the similarities of the alkali metal ions, further sodiation after the initial intercalation reaction of MoS_2 was believed to similar to that in LIBs. Therefore, it was expected that MoS_2 converts to Mo and Na_2S in the fully sodiated state.[191,291–293] This hypothesis was mainly supported by Raman analysis and (S)TEM studies. However, as discussed in chapter 1, both of them are not able to provide direct bond information of the amorphous structure in the complicated environment after the battery reaction. The ePDF and XAS measurements used in the previous chapter are powerful tools to identify bonding information including atomic distances, bound angles and valence state, and were applied in this chapter to study the de/sodiation mechanism of MoS_2. A state-of-art MoS_2/C composite (noted as MoS_2-C@C in this thesis), in which carbon is inserted between the MoS_2 layers and with carbon as additional conductive backbone, was chosen to study the reaction mechanism of MoS_2 in SIBs. This material exhibited a high capacity and good cyclic stability in SIBs in a previous study. [145] To separate the effect of carbon on the reaction mechanism, bare MoS_2 (without carbon) was also investigated and compared to MoS_2-C@C. Moreover, the effect of the carbon support structures on battery cycling was investigated using S/TEM imaging and 4D-STEM.

5.2. Experimental

5.2.1. Materials synthesis

Hierarchically structured MoS_2 (denoted as MoS_2–C@C) and bare MoS_2 were synthesized by Dr. Zhenyou Li in the group of Prof. Dr. Maximilian Fichtner using an interfacial engineering approach developed. A schematic of the synthesis is shown in Figure 5-1. α-MoO3 was dispersed in a 2 mg/mL

dopamine hydrochloride/ tris-aminomethane buffer solution (pH= 8.5) with a molar ratio of 1:3 of α-MoO_3:dopamine. During ripening for more than 12 h, a polydopamine (PDA)-MoO_3 complex was generated and separated from the suspension. The PDA-MoO_3 complex was cleaned by washing with H_2O and ethanol 5 times. Afterwards, the complex was dispersed in an aqueous thiourea solution, with a molar ratio of 1:5 of Mo:S. The solution was transferred into a Teflon coated autoclave after stirring for 1 h. After heating for 24h to 200 ˚C, the product was obtained from the hydrothermal reaction. The final product was obtained by calcining the powder at 350 ˚C for 1 h an 800 ˚C for 3 h. Bare MoS_2 (denoted as m-MoS_2) was also synthesized for comparison following the same approach, but without the addition of dopamine.

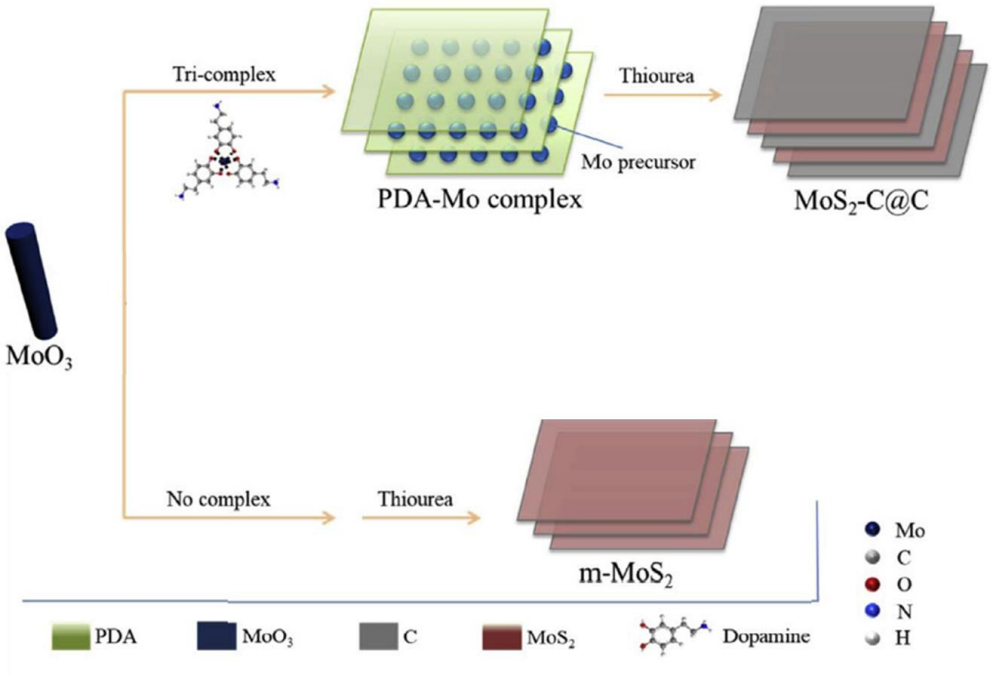

Figure 5-1: schematic of the synthesis strategies for the MoS_2-C@C and m-MoS_2 composites, modified from[145].

5.2.2. Electrochemical measurement

A two-electrode Swagelok cell configuration was used for all electrochemical studies. The electrodes were made by coating a copper foil with a slurry containing 70% active material, 20% Super P and 10% carboxymethyl cellulose (CMC) in N-methyl-2-pyrrolidone (NMP), followed by drying in vacuum at 80 ˚C for 15 h. Except for the cells for *in-situ* XAS measurements, a typical mass loading of the active material of 1.0-1.5 mg cm^{-2} was used for all electrodes. The mass loading of the electrodes for XAS was about 5 mg cm^{-2}. The cells were assembled in an Ar-filled glovebox (both H_2O and O_2 < 0.5 ppm) using 1 M $NaClO_4$ in propylene carbonate (PC) with 5 wt. % fluoroethylene carbonate (FEC) as electrolyte. Na foil and glass fiber were selected as counter electrode and separator.

5.2.3. Characterization

S/TEM imaging, SAED and EDX measurements were performed using an aberration (image) corrected FEI Titan 80–300 microscope operated at 300 kV. The STEM-EELS data was acquired using an image and probe double corrected ThermoFisher Themis Z operated at 300 kV. Cycled samples were transferred under inert gas condition from a glove box to the microscope using a Gatan 648 vacuum transfer holder to minimize air exposure. 4D-STEM data sets was acquired using a quasi-parallel beam in STEM mode in the Titan 80-300. A Medipix 4s detector was used to obtain the diffraction patterns.

5.3. Morphological and structural characterization of as-prepared MoS_2-C@C

The morphology and structure of the as-prepared MoS_2-C@C were examined by TEM and XRD (Figure 5-2). The as-prepared MoS_2–C@C has a sheet-like morphology as shown in S/TEM images in Figure 5-2a and 2b. The distance between the sheets is inherited from the (002) d-spacing of 0.62 nm in the MoS_2 crystalline structure, but increased varying between 0.79 nm to 1.14 nm, indicating that carbon was inserted between the MoS_2 layers. XRD measurements were carried out to confirm the structure of the as-prepared MoS_2-C@C (Figure 5-3c). However, only two peaks were observed in the XRD pattern due to the low crystallinity of the as prepared sample, which could be indexed to the $(\bar{1}20)$ and (010) planes of MoS_2 (JCPDS #37-1492). The inserted picture in Figure 5-3c shows the SAED pattern. Consistently, there are two crystal plans visible in the SAED pattern corresponding to the $(\bar{1}20)$ and (010) planes. Between them, a broad halo is observed, which suggests that the MoS_2–C@C material has low crystallinity due to the carbon insertion between the MoS_2 layers. An ePDF was calculated based on the SAED pattern. Figure 5-2d shows a comparison of the experimentally determined MoS_2–C@C PDF and simulated PDFs for the 2H and 1T type MoS_2 and graphene. All of the peaks in the experimental PDF can be explained by the crystalline 2H MoS_2 and graphene structures meaning that the short- and medium-range order of the MoS_2–C@C is the same as in the crystalline material. The simulated partial PDFs of 2H and 1T type MoS_2 are shown in Figure 5-3, which clearly illustrate that the first peak (2.38 Å) and second peak (3.12 Å) in the PDFs of the 2H and the 1T type MoS_2 can be attributed to the Mo-S and Mo-Mo/S-S distance. The two peaks correspond to the second and third peak in the experimental ePDF of the as-prepared MoS_2–C@C in Figure 5-2d. The first peak in the experimental PDF corresponds to the C–C bond distance in graphene.

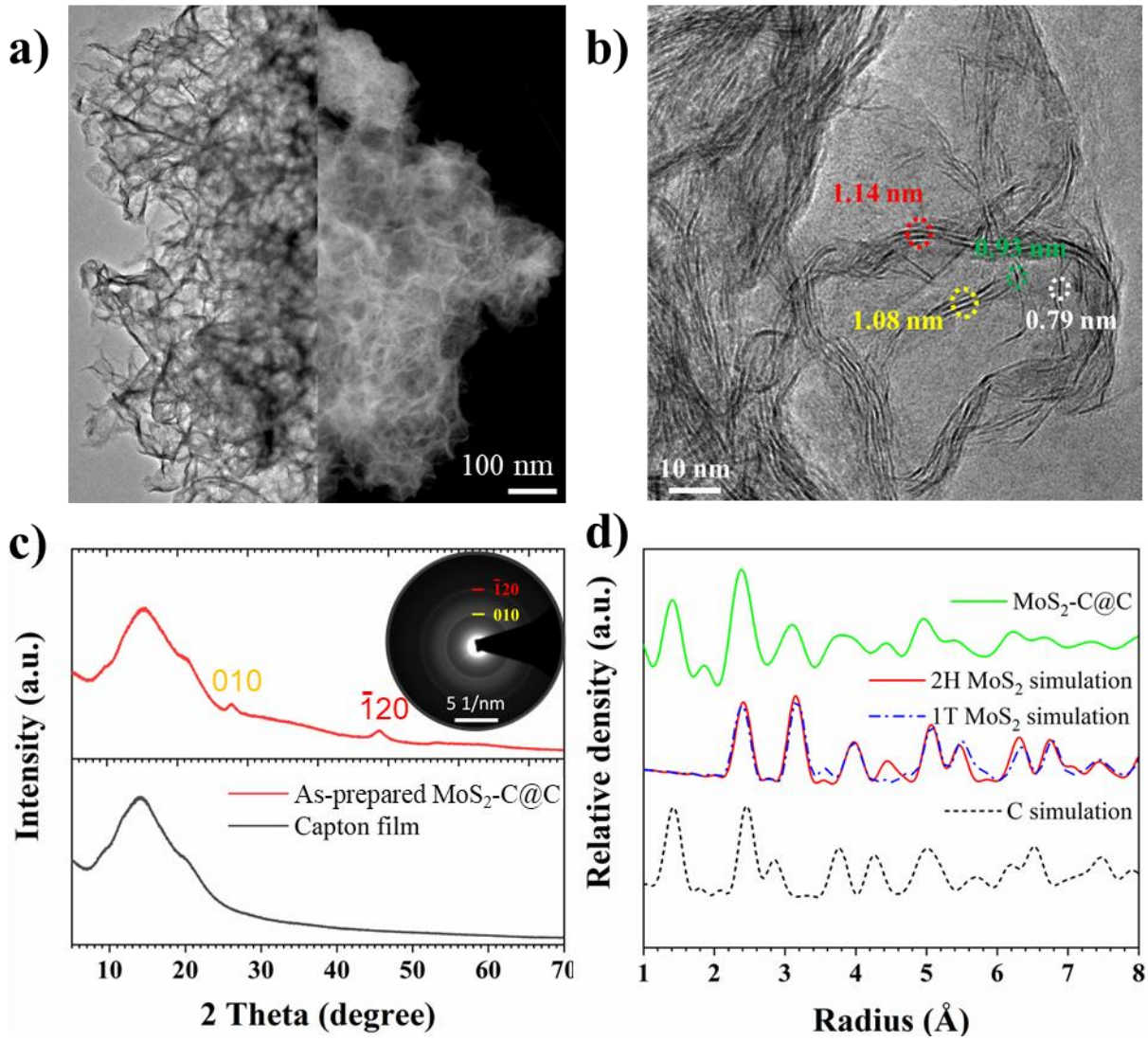

Figure 5-2: **a)** TEM (left) and STEM-HAADF (right) images of as-prepared MoS_2-C@C; **b)** HRTEM image of as-prepared MoS_2-C@C; **c)** XRD pattern of as-prepared MoS_2-C@C, inset is the SAED; **d)** PDF of as-prepared MoS_2-C@C and simulated PDFs of 2H MoS_2, 1T MoS_2 and graphene.

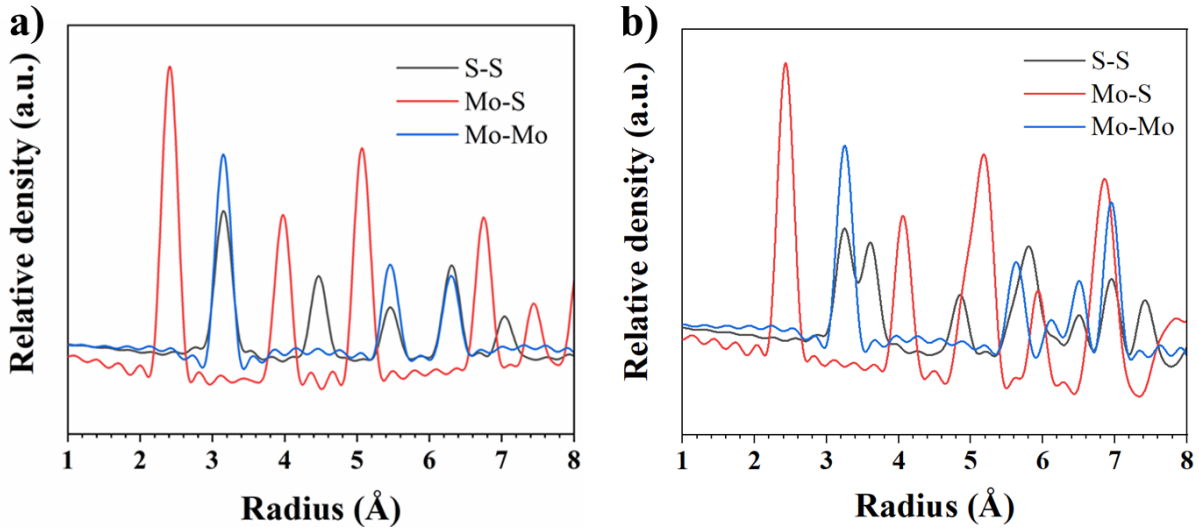

Figure 5-3: partial PDF simulated of 2H (**a)**) and 1T (**b)**) type MoS_2.

5.4. Structural changes during cycling of MoS_2-C@C

To reveal the de/sodiation mechanisms of MoS_2-C@C, XRD and ePDF analysis were performed for samples at different charging states. As shown in Figure 5-4a, batteries were stopped at the various states marked by the red points on the voltage-capacity curve of the first cycle and the electrode materials recovered. Figure 5-4b shows XRD patterns of the samples at the different states where the intensity of the $(\bar{1}20)$ and (010) reflections at about 26 and 46 ° gradually decreases and totally disappears at the fully discharged state. The presence of the two reflections from as-prepared to the 'discharge 3' state means that in this discharging interval the crystal structure is still (partially) present during sodiation, which can be explained an initial intercalation of sodium ions in between the MoS_2/C layers.[191,294] Significant structural alterations are starting to happen between the 'discharge 3' point and the fully discharged state, where the crystalline reflections disappear. In addition, two new reflections at about 30 and 43 ° appear in the 'discharge 1' sample and are present throughout the discharge cycle, which can be indexed as (002) and (022) planes in NaF. The formation of NaF could be the result of a decomposition of electrolyte along with the generation of an SEI layer during discharging. SAED patterns were also acquired at the fully recharged state for comparison with the XRD results (Figure 5-5). Compared to the SAED of the as-prepared sample, the two diffraction rings corresponding to the $(\bar{1}20)$ and (010) planes disappeared and only broad amorphous halos were observed for the cycled samples, confirming the loss of long-range order in the cycled samples. After integrating the diffraction signal in radial direction and removing the background corresponding to single atom scattering, the structure factor of the samples was calculated (Figure 5-5b). The structure factors of cycled sample are quite similar, whereas, they are clearly different from the as-prepared sample. It means that the as-prepared sample undergoes a structure/phase evolution during sodiation, and the structural evolution is irreversible in the following desodiation process.

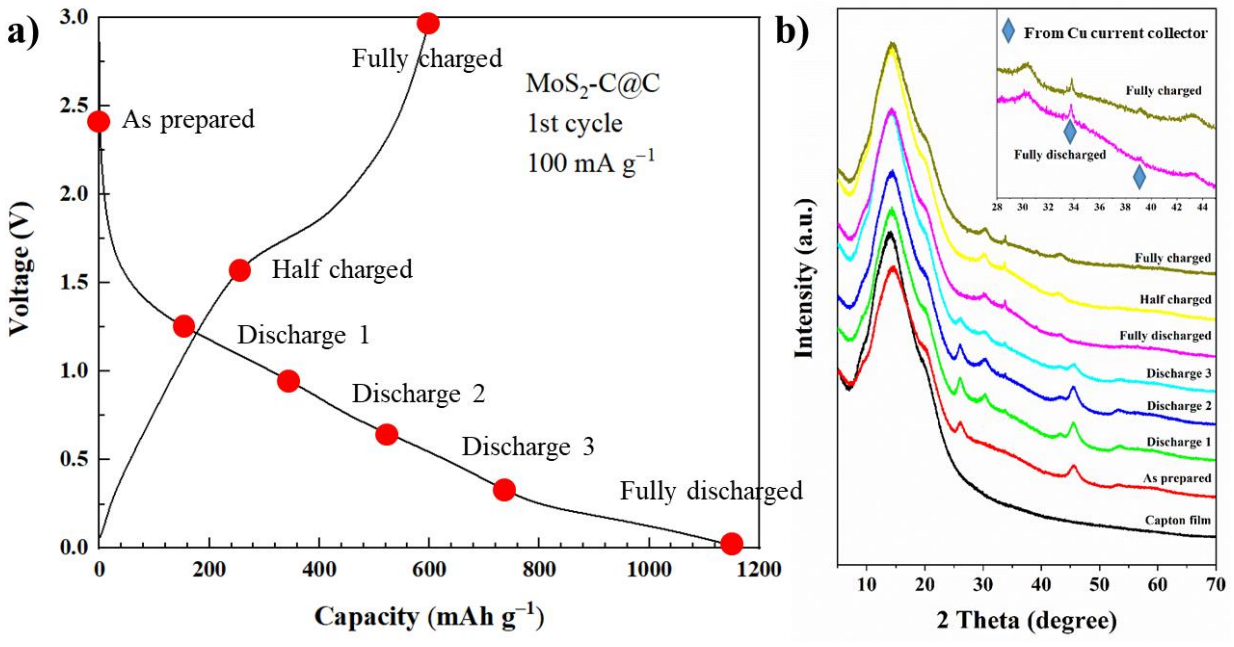

Figure 5-4: **a)** voltage-capacity curve of first discharge and charge process of MoS_2-C@C, the marked points present the state of *ex-situ* XRD and PDF samples; **b)** *ex-situ* XRD of MoS_2-C@C during 1st cycle.

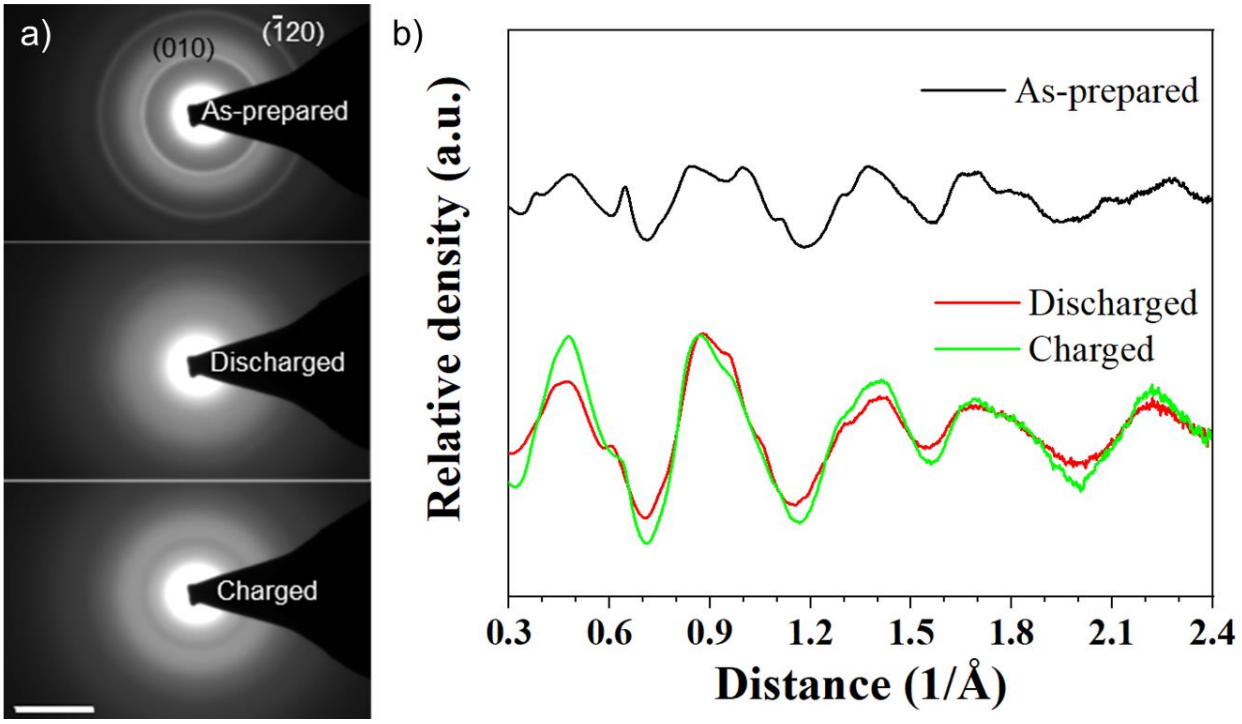

Figure 5-5: **a)** SAED of as-prepared and cycled MoS_2-C@C; **b)** structure factors of as-prepared and cycled MoS_2-C@C samples, the scale bar in **a)** is 5 1/nm.

For a more intuitive interpretation of the amorphous structure using atomic distances and bond information in real space, ePDFs were calculated based on the structure factors (Figure 5-6a). In the ePDF of the as-prepared sample, several pronounced peaks can be observed fitting to the structure of MoS_2 and graphene. As previously explained, the second peak at about 2.4 Å and the third peak at about 3.1Å in the PDF of the as-prepared sample correspond to the Mo-S and Mo-Mo/S-S distances. For a conversion reaction, it would be expected that the 2nd peak at 2.4 Å corresponding to the Mo–S bonds disappears during the discharging process. However, a strong peak at 2.4 Å can be clearly observed in the fully discharged sample as the dominate peak. This indicates that a large fraction of the Mo-S bonds persist throughout the sodiation process. In the contrast, the Mo-Mo/S-S peak at 3.1 Å disappears revealing that most Mo-Mo/S-S nearest correlations are lost, which is in line with a loss in crystallinity during discharging. This indicates that the MoS_2 sheets break up into Mo-S_x polyhedral clusters during the discharge process and the Mo-S_x clusters randomly arrange without any long-range order. The result reported here is different from previous reports about the conversion reaction mechanism of MoS_2 in sodium ion batteries, where MoS_2 was believed to be converted into metallic Mo and Na_2S.[191,291–293] To further confirm the reaction mechanism, simulated PDFs of Na_2S and Mo are shown in Figure 5-6a. The Na–S bond length in Na_2S is at about 2.8 Å, and the Mo–Mo bond length in metallic Mo is about 2.7 Å. Neither Na_2S nor Mo signatures can be observed in the ePDF of the discharged sample, meaning that Na_2S and Mo are not the

main products during sodiation. Furthermore, the ePDF of the recharged sample is mostly identical to the discharged state where the Mo-Mo/S-S distances at about 3.1 Å remain weak. A comparison of the ePDFs in the discharged and charged state illustrates that the majority of the MoS_2 structure does not recover after the desodiation process.

To obtain bulk information on the whole electrode, XAS analysis was carried out to get valence state and short range order information to follow the evolution of MoS_2-C@C. As shown in Figure 5-6b, the Mo XANES of the as-prepared and the cycled samples show identical onset positions, which are different from metallic Mo. This XANES result is in agreement with the previous PDF analysis, that Mo cannot be reduced to a metallic state during sodiation and desodiation. Notably, a clear pre-edge appears in the XANES of the discharged sample, which cannot be observed in the as-prepared and charged samples. The pre-edge of XANES is related to the atomic environment and affected by the coordination symmetry. The change in symmetry could be caused by a large amount of sodium in the electrodes in the discharged sample. For instance, a similar pre-edge appears in monoclinic MoO_3 (shown in Figure 5-6b), which is due to a distorted coordination of the Mo atoms.[295] However, the onset positions in the discharged sample and MoO_3 are obviously different, which exclude the possibility that the spectrum of the discharged sample is due to MoO_3. EXAFS-FT (Figure 5-6c) shows element specific PDFs bringing information on the atomic nearest neighbors. It confirms the structure of the as-prepared sample with the two characteristic distances corresponding to Mo–S and Mo-Mo distances in a single layer of MoS_2 (2H and 1T type). As expect, the EXAFS-FT is consistent with the ePDF data. In the discharged sample, the Mo-Mo distances are not observed any more. In addition, the Mo-Mo distance does not reappear after the recharging process, which means that the Mo-S_x clusters replace the initial MoS_2 to store sodium ions in following cycles. Furthermore, the shape of Mo-S peak in the discharged and recharged EXAFS-FT are slightly different, which indicates a different coordination symmetry of the MoS_x polyhedral clusters caused by the sodiation and desodiation. EELS spectra of the S-K edge in the discharged and charged state are shown in Figure 5-6d. The spectra were obtained by averaging the signal acquired from different locations to get more statistics and a better signal to noise ratio. It is clear that S in the sodiated sample shows a reduced pre-edge compared with the desodiated sample, which could be caused by Na-S bonding. The formation of Na-S bounds would explain the change in symmetry of the Mo-S clusters in the discharged state.

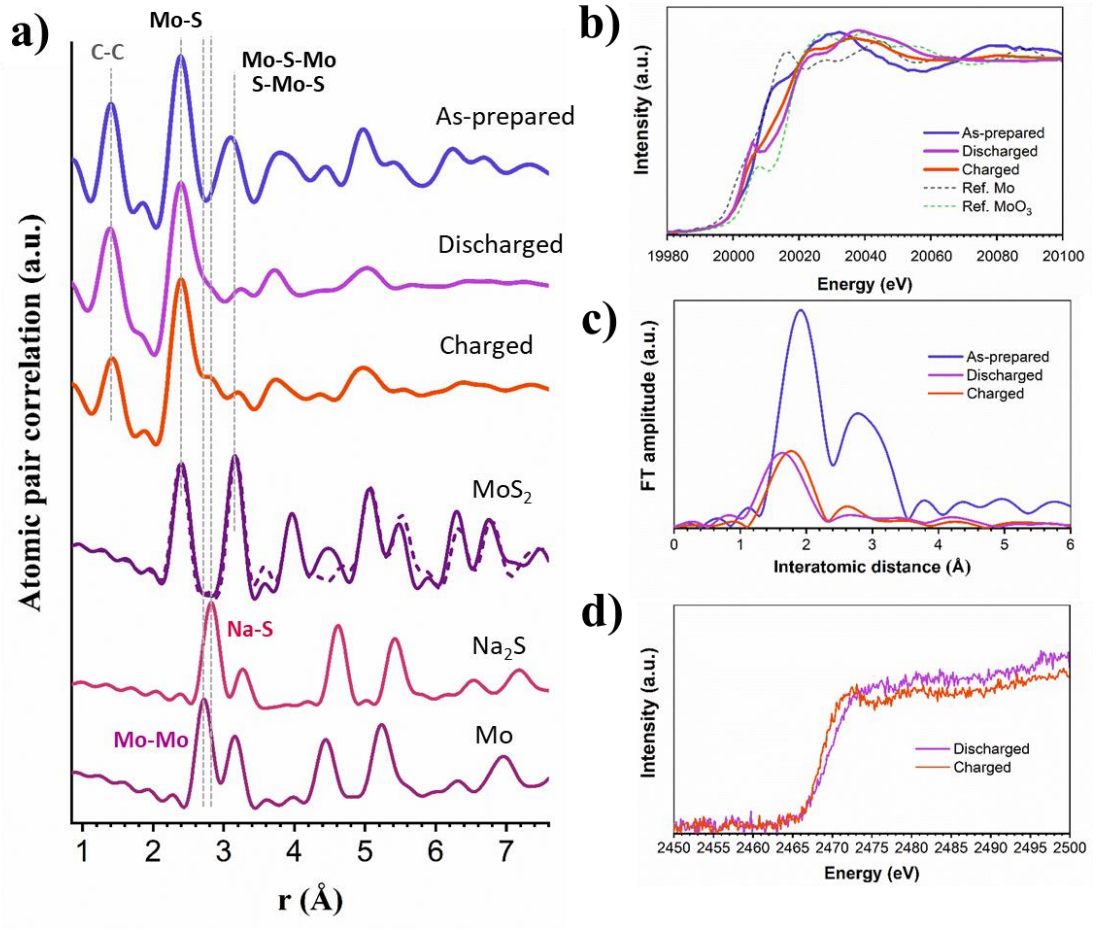

Figure 5-6: **a)** PDFs of as-prepared, discharged and charged samples with the simulated PDFs of MoS_2 (solid line and dash line presents the 2H type and 1 T type MoS_2, respectively), Na_2S and metal Mo; **b)** and **c)** XANES and FT-EXAFS characterization of as-prepared and cycled samples; **d)** EELS spectrum of S K-edge at discharged and charged states.

Based on the consistent observations of ePDF and XAS analysis, the following scenario has been identified: during insertion of sodium ions into the MoS_2-C@C composite, the initial crystalline MoS_2 is reacting to form Mo-S_x clusters in the fully discharged state. The Mo-S_x clusters show different symmetry compared to the initial MoS_2 structure, because of bonding to the surrounding sodium ions. After removal of the sodium ions from the Mo-S_x clusters and the carbon composite, the symmetry of the Mo-S_x clusters in recharged state is recovered (fitting to the symmetry in the as-prepared sample). However, the long-range order of the crystalline MoS_2 cannot be recovered during the desodiation process.

For a better understanding the cycled products, STEM-EELS (Figure 5-7) was used to analyze the fully discharged sample. It should be noted that S and Mo show the same distribution at the nanoscale (the pixel size is 1.5 nm). There are no agglomerated Mo areas observed in the STEM-EELS map, which is consistent with the previous structural analysis that Mo cannot be reduced to the metallic state in the fully discharged state. However, sodium shows a different distribution from Mo/S with more sodium

appearing in the thick region. This can be due to the higher amount of active materials and carbon matrix locate at the thick area that could store more sodium and generate more SEI.

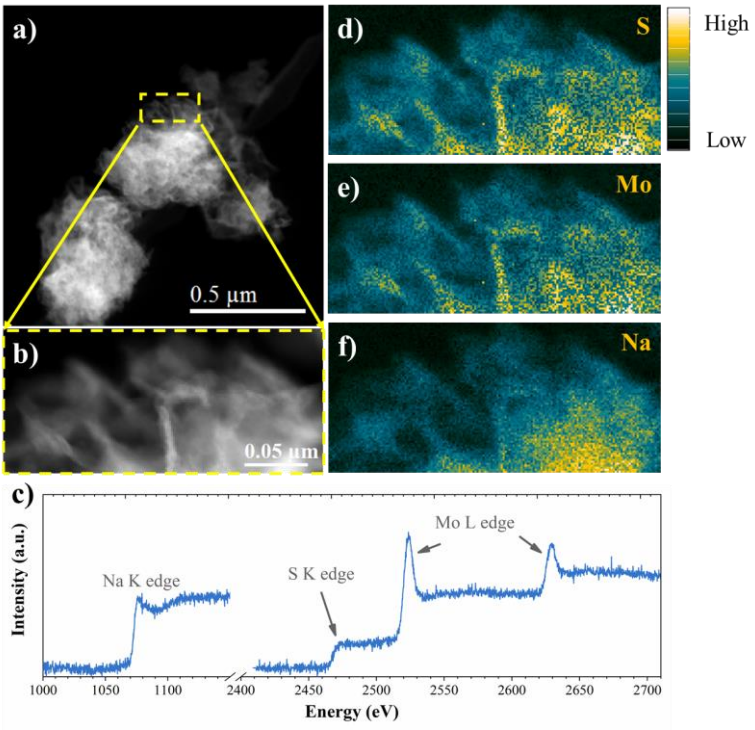

Figure 5-7: **a)** STEM-HAADF image; **b)** enlarged image of the area marked in **a)**; **c)** sum spectrum from the whole EELS data cube; **d)** to **f)** elemental maps (integrated single) of S, Mo and Na.

5.5. De/sodiation mechanism of bare MoS_2

To understand if the carbon in the MoS_2-C@C composite affects the de/sodiation mechanism, the reaction mechanism of bare MoS_2 (without carbon) was studied. Figure 5-8a and 8b show the morphology and HRTEM images of bare MoS_2. The bare MoS_2 shows a sheet-like morphology, which is similar to that of the MoS_2-C@C composite. However, the bare MoS_2 exhibits much higher crystallinity than the MoS_2-C@C composite. In the insert in Figure 5-8b, it is clear that the (002) planes exhibit good crystallinity with the regular 0.65 nm lattice spacing. In the inserted SAED on the right side of Figure 5-8, the as-prepared MoS_2 show strong diffraction rings that can be indexed as 2H MoS_2. Similar to the MoS_2-C@C composite, the cycled bare MoS_2 exhibits a low crystallinity without any clear diffraction rings in the SAED pattern. ePDF analysis (Figure 5-8c) demonstrates that the Mo-S bonding in the bare MoS_2 does not disappear during the first discharging cycle, similar to the MoS_2-C@C composite. In addition, the initial structure of MoS_2 cannot be fully recovered after the recharging process analogous to the MoS_2-C@C composite. The consistent results for the bare MoS_2 and MoS_2-C@C indicates that the de/sodiation mechanism of MoS_2 is independent of the carbon composite.

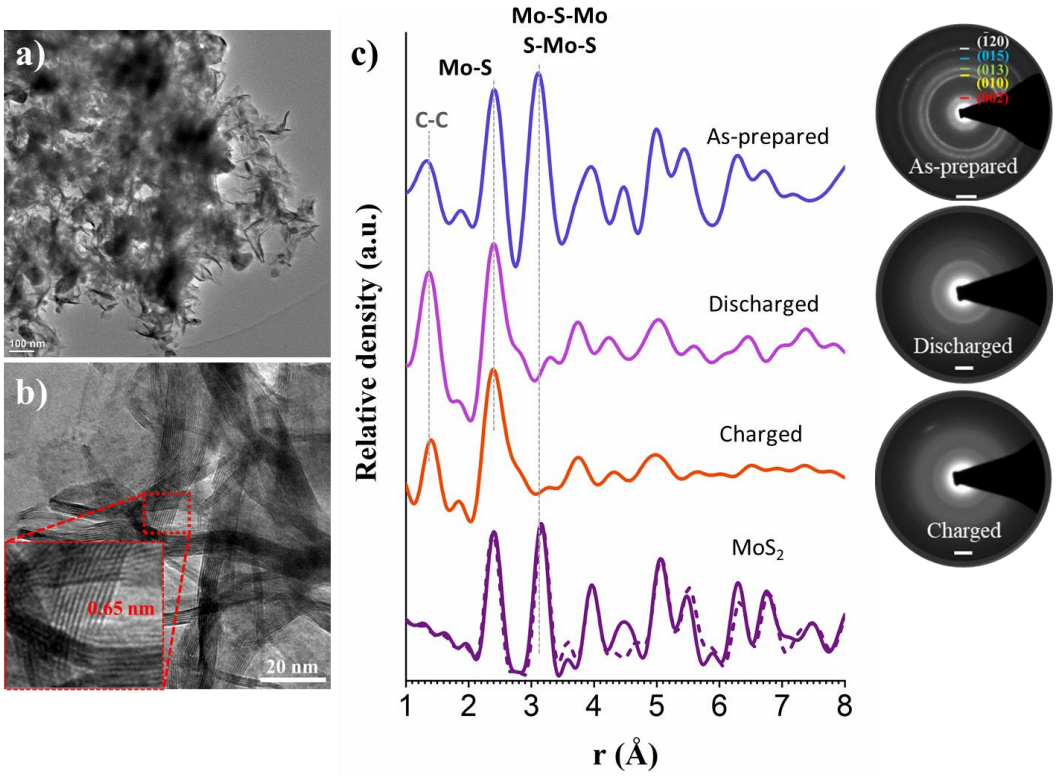

Figure 5-8: **a)** TEM image of as-prepared bare MoS_2; **b)** HRTEM image of as-prepared bare MoS_2; **c)** the PDFs of as-prepared, discharged and charged bare MoS_2 samples, the right inserted pictures are SAED patterns, the scale bars in the SAED patterns are 5 1/nm.

5.6. The role of carbon in MoS_2-C@C.

In the above sections, it was already demonstrated that the presence of carbon does not change the reaction mechanism of MoS_2 in SIBs. However, MoS_2 with carbon always show a much better battery performance than the bare MoS_2.[39,181,296–298] This implies that carbon has a vital role during battery cycling of this material. Figure 5-9 shows STEM and TEM images of the as-prepared (a, d), discharged (b, e) and recharged samples (c, f). Both STEM and TEM images show a better crystallinity of the as-prepared sample than the cycled ones. The STEM images demonstrates that the discharged and charged samples still have a sheet-like morphology similar to the pristine sample. However, almost no crystalline lattice could be observed in HRTEM except for a few short (002) planes marked in the images. The fact that the morphology is maintained while the crystallinity is lost during cycling indicates the crucial role of the carbon outside the MoS_2–C@C: carbon helps to maintain the overall morphology and thus the integrity of the sample during cycling.

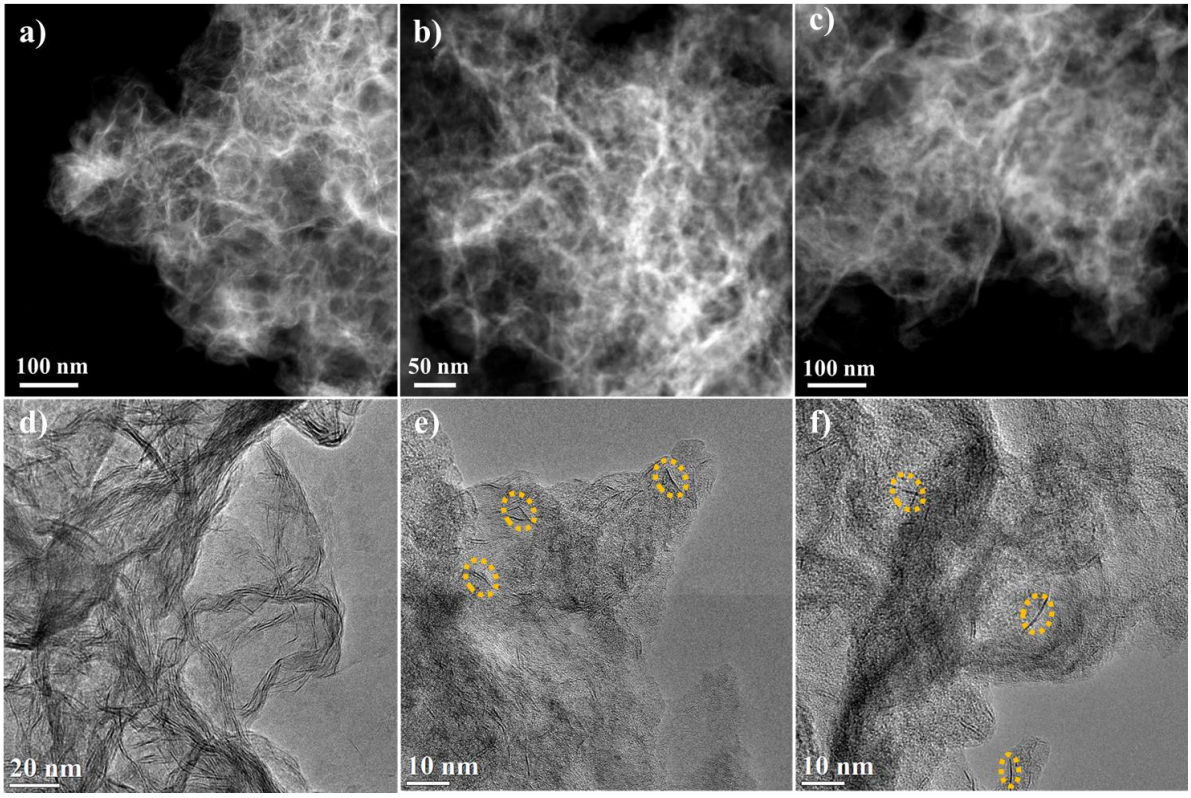

Figure 5-9: STEM (**a)**, **b)** and **c)**) and TEM (**d)**, **e)**, **f)**) images of as-prepared (**a)** and **d)**), 1st discharged (**b)** and **e)**) and 1st charged (**c)** and **f)**) MoS_2-C@C samples.

4D-STEM PDF mapping was used to obtain local structure/phase information in the recharged sample of the MoS_2–C@C composite (Figure 5-10). Manual analysis of the ePDF array revealed three different characteristic ePDFs. The three PDFs are displayed in Figure 5-9b with simulated PDFs for the corresponding references. The blue curve includes characteristic C-C and Mo-S peaks, which can be ascribed to the MoS_x-C@C composite. The green PDF contains almost no C-C bonding, which is assigned to detached MoS_x clusters. The red curve shows characteristic graphitic distances and is considered to be carbon. In the SAED profile in Figure 5-11, a clear peak appears at about 0.3 1/Å corresponding to the characteristic interlayer distance in graphite; the carbon observed here, probably comes from the conductive carbon used in the battery. Using the diffraction profiles shown in Figure 5-11 as reference in multiple linear least squares (MLLS) fitting, maps of the three components were obtained (Figure 5-10a). An overlay of the three compound maps clearly reveals that detached MoS_x clusters are mainly locate on the surface of MoS_2–C composite, which is presumably the first step in leaching into the electrolyte. Leaching of MoS_x clusters is presumably responsible for the capacity fading during the following cycles. However, the MoS_x clusters, which are still embedded in the carbon composite (blue area), will contribute to a stable cycling. It should be mentioned here, that most particles in the cycled MoS_2-C@C composite only show very limited amount of leached MoS_x clusters on the surface. The extreme example (shown in Figure 5-10) is chosen to explain the function of carbon in the MoS_2-C@C composite.

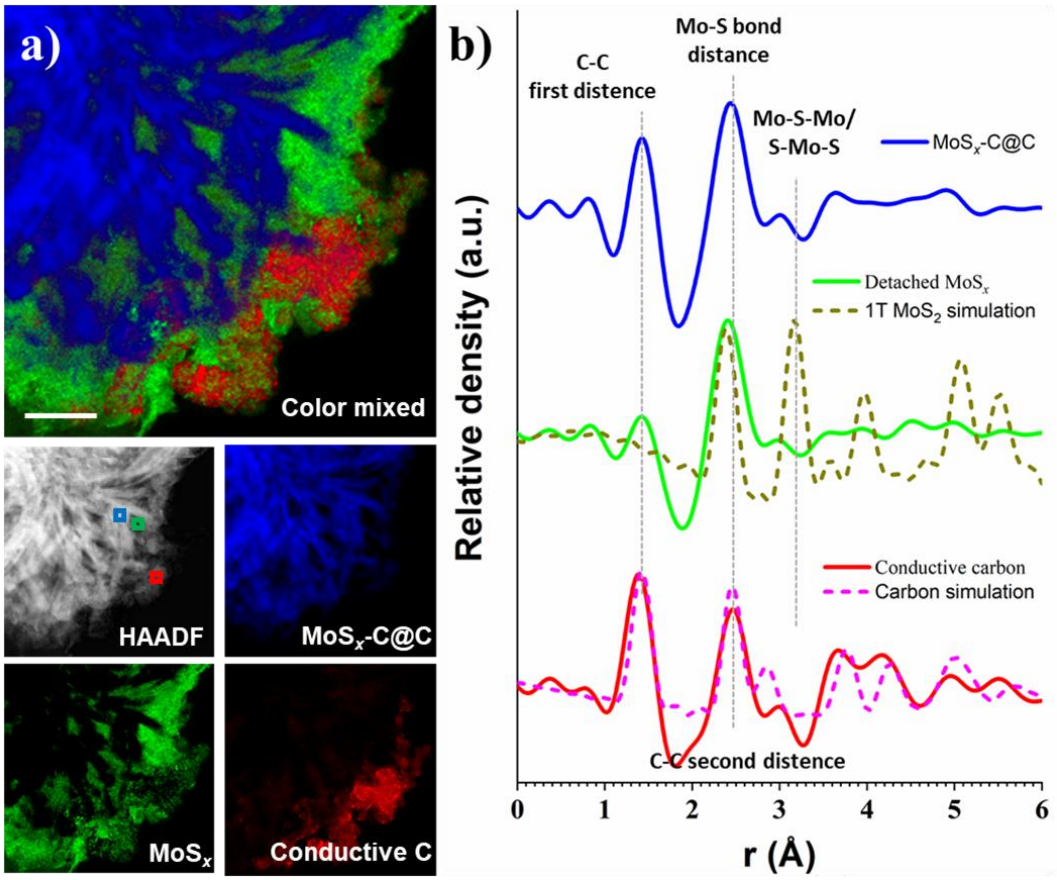

Figure 5-10: **a)** STEM-PDF map of the 1st charged MoS_2–C@C composite, the scale bar is 100 nm; **b)** PDF curves from different areas and simulated PDFs of reference compounds, the pixel size in **a)** is 2.4 nm.

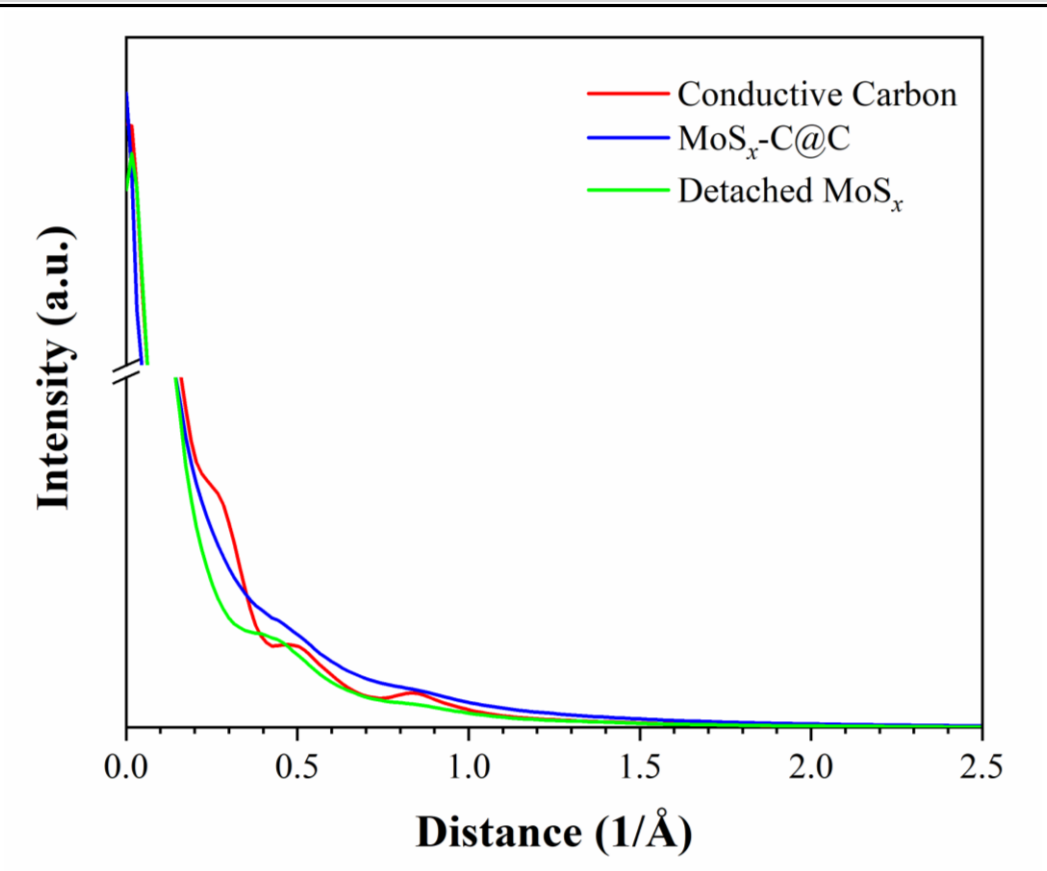

Figure 5-11: Diffraction profile used for the multiple linear least squares (MLLS) fitting in Figure 5-10.

5.7. Conclusion

A thorough investigation of the de-/sodiation mechanism of MoS_2–based materials has been conducted using electron diffraction and XAS based PDF analysis together with comprehensive (S)TEM characterization. The PDF data from both electron diffraction and x-ray absorption reveals a loss of long-range order of the MoS_2 during the first discharge process. However, well-preserved Mo-S bonding is maintained throughout the battery cycling. EELS elemental mapping is in agreement with the PDF analysis as Mo and S exhibit a similar spatial distribution. As a result, we propose that even in the highly sodiated state, MoS_2 does not react during the conversion to metallic Mo and Na_2S. Instead, MoS_2 nano-/crystals fragment into disordered Mo-S_x clusters, which serve as new active species for the following recharging and discharging processes. The long-range order of MoS_2 has been demonstrated to be irreversibly lost during cycling. In addition, the 4D-STEM analysis used in this work reveals a confinement effect of carbon in the MoS_2/C composite. Although carbon is not participating in the de/sodiation, it can alleviate diffusion of Mo-S_x cluster from the electrode into the electrolyte. Thereby, the carbon matrix enhances the stability and thus the battery performance significantly. In this scenario (shown in Figure 5-12), the structural and morphological engineering of the MoS_2/C composite could be an effective strategy towards fast-charging and long-term stability. This work not only provides an atomic scale understanding of the sodium storage mechanism in MoS_2–based materials, but could be also helpful as a methodological reference for studying

the reaction mechanism in similar types of transition-metal dichalcogenides materials used in lithium or sodium battery systems.

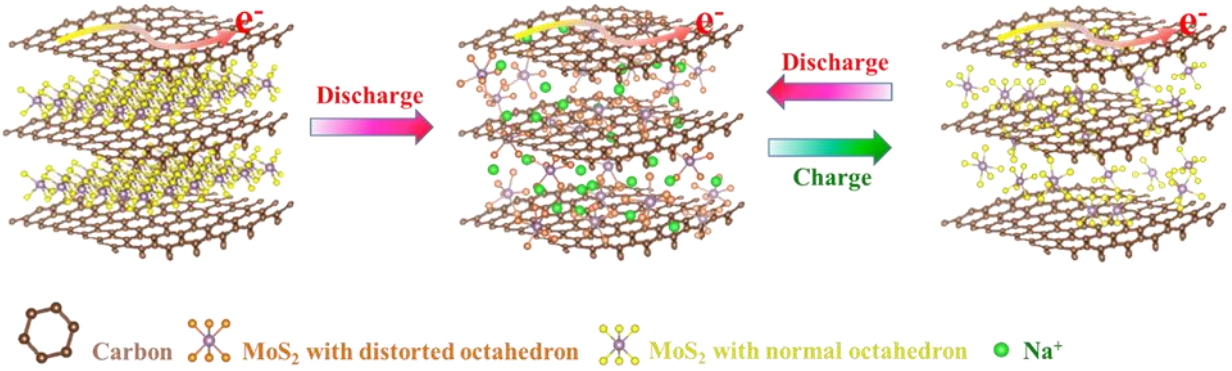

Figure 5-12: schematic of the proposed de-/sodiation mechanism of the MoS_2–C@C composite.

6. Summary and outlook

6.1. Summary

Revealing the reaction processes accompanying the structural, morphological and chemical evolution during electrochemical cycling, is a key point in investigating battery materials as it allows to develop a fundamental understanding of the reaction mechanisms and material properties. A deeper understanding of these mechanism is critical for a targeted optimization and development of new battery materials. Conversion reaction anodes with high theoretical capacity, energy density and excellent battery cycling stability are regarded as promising candidates for the next generation of electrode materials. MOs[38,203] and TMDs[299,300] are two classes of conversion materials that have been intensely investigated over last two decades. However, complex reaction mechanisms combined with a complicated mixture of amorphous products after battery cycling limits the full understanding and further development of these materials. In this thesis, a series of TEM related techniques including S/TEM imaging, electron diffraction, EDX, EELS, ePDF and 4D-STEM were applied to characterize the morphology, structure and chemical compositions of battery materials at different charging states. XAS, XRD, and electrochemical testing have been carried out to complement the TEM based investigations, connecting structural and electrochemical features. This thesis focuses on the investigation of a HEO and MoS_2/carbon composites as the representative examples for MOs and TMDs materials. The reaction mechanisms have been investigated in great detail when used in LIBs (HEO) and SIBs systems (MoS_2/carbon composite). In addition, the synthesis process of the HEO during calcination has been studied. The main achievements and insights are summarized below.

6.1.1. Methodology used in this thesis for studying the reaction mechanism during calcination and battery reaction

Although *in-situ* heating experiments in a TEM in a defined gas atmosphere is a well establish approach[301,302], its application to study the processes during synthesis of multi-cation oxides has been rarely reported. For multi-cation oxides that require more than one raw material as precursor, forming a stable and connected sample is problematic in traditional *in-situ* heating experiments in a TEM. In this thesis, we used a FIB preparation method starting from a highly compressed mixture of the raw oxides for the HEO formation. The FIB lamella was transferred to a MEMS based heating chip of an atmosphere holder for *in-situ* heating experiments inside the TEM. Furthermore, bulk information on the structural evolution was obtained by *in-situ* and *ex-situ* XRD measurements. The combination of these approaches including FIB preparation, *in-situ* heating in the TEM and XRD measurements allowed to investigate the structural evolution and elemental diffusion during HEO formation, both locally with nanometer spatial resolution as well as in the bulk.

Conversion reactions produce a complex array of amorphous products during electrochemical cycling. Studying the reaction mechanisms and reaction products after conversion is therefore experimentally challenging. In this thesis, we used ePDF and 4D STEM techniques, which offer significant advantages compared to the more common characterization methods, i.e. XRD, SAED and Raman. The advantages arise from the high spatial resolution and the information that can be obtained on the local chemical bounding both for low crystallinity and amorphous materials. Combined with bulk characterization methods, such as XAS and electrochemical testing, this methodology shows excellent prospects for studying reaction mechanisms of conversion materials.

6.1.2. Scientific questions answered in this thesis

In **chapter 3** of this thesis, *in-situ* heating experiments in a TEM in an air-like atmosphere have been conducted and revealed information on the elemental diffusion processes during synthesis of the HEO $(Co_{0.2}Cu_{0.2}Mg_{0.2}Ni_{0.2}Zn_{0.2})O$. Combined with *in-situ* and *ex-situ* XRD measurements, the structural evolution corresponding to the elemental migration has been clarified to a certain level. The starting temperature for the HEO formation has been determined to be around 700 ˚C and the pure rock salt phase HEO $(Co_{0.2}Cu_{0.2}Mg_{0.2}Ni_{0.2}Zn_{0.2})O$ has been confirmed at about 900 ˚C. The results presented here can be used to guide for the industrial HEO production. In addition, the temperature difference between the starting point of the HEO generation and the full HEO transformation implies multi-step phase evolution towards the final HEO. This is further supported by cross-correlation data derived from STEM-EDX mapping during HEO formation showing significant changes in the correlation of selected elements, which is an indication for the formation of intermediate oxide phases prior to the final HEO generation, whereas, in particular, Ni-Mg are not forming any binary oxides during the HEO synthesis. Furthermore, the transient observation of the transformation of CoO to Co_3O_4 prior to the final HEO formation, shows that the generation of the single phase HEO is not directly related to the structure and the valence state of the transition metal in raw material.

In **chapter 4**, the reaction mechanism of the HEO $(Co_{0.2}Cu_{0.2}Mg_{0.2}Ni_{0.2}Zn_{0.2})O$ in LIBs has been investigated in detail. XAS and TEM results consistently supported the hypothesis of beneficial synergistic effects of the different cations in the HEO. It was found that as Mg^{2+} cannot be reduced by Li and persists in an oxide phase at all cycled states, this helps to maintain a stable structure with all other phases formed during cycling, which are growing epitaxially on the HEO/MgO. A Mg-Li-O and a Mg-Co-Zn-Li-O network were identified in the lithiated and delithiated state. They provide a good lithium ion diffusion pathway inside the grains in the cycled anode. Moreover, this study showed that the capacity of the system during cycling is dominated partial by Co oxidation/reduction and Zn contributing both by conversion and alloying reactions (generation of ZnLi alloy in the discharged state). During the first discharge, some amount of Cu, Ni and Co segregate to the grain boundary and form an alloy resulting in a metallic 3D

network for electron transfer. Furthermore, Cu, Ni and Co that did not segregate to the grain boundary form a nanoscale alloy phase inside the grain, which inherits its orientation from the initial HEO and shows an epitaxial orientation relationship with the oxide phase. The combination of mixed metal and oxide phases result in good ion and electron diffusion paths in the grain.

Electron conductivity is well known to limit the application of oxides with large particle sizes and has been a long standing topic of discussion in battery research. To avoid these limitations, typically nanoscale metal oxides have to be combined with a specially designed conductive network. However, these approaches decrease the tap density (volumetric energy density) and increase the production cost. The findings presented in **Chapter 4** provide a new idea for designing optimized materials that spontaneously self-assemble to form a 3D electron and ion conducting network during battery cycling. The 3D electron conductive network allows materials with large particle sizes to contribute to the electrochemical performance in a similar way to those with small particle sizes as the electrons can be transferred fast along the metallic grain boundaries during battery cycling as well as inside the grain with the finely dispersed metal phase.

While the reaction mechanism of MoS_2 in LIBs is well studied in literature, the de/sodiation process was still not fully understood due to the limitations of traditional structural characterization methods for amorphous materials. In **Chapter 5** we therefore investigated the de/sodiation mechanism of MoS_2 based on the ePDF and XAS analysis approaches established in **Chapter 4**. It was shown that Mo-S_x clusters are the main product after complete sodiation, rather than the originally expected metallic Mo and Na_2S phases. The long range ordering MoS_2 is irreversible after battery cycling. Moreover, this reaction mechanism was demonstrated to be independent of the presence of carbon in the MoS_2-C composite. However, the carbon is beneficial by limiting leaching of MoS_x clusters into the electrolyte.

6.2. Outlook

The microstructural evolution and elemental diffusion during HEO synthesis have been studied in **Chapter 3**. However, some aspects presented in this chapter are still not been fully understood and are worth a deeper investigation. Although the analysis of the EDX elemental distribution maps by cross-correlation indicates the formation of intermediate phases formed prior to the HEO formation, the factors influencing the formation of the intermediate oxide structures (enthalpy of mixing, particle connection or particle size) are still unclear. This could be clarified in combination with theoretical calculations of the enthalpy of mixing of the different metal oxides and reference experiments with different oxide distributions with similar particle size in the as-prepared FIB lamella. Understanding the influence of the different parameters might help to optimize the synthesis conditions of further high entropy oxides. In addition, more details about the phase transformation of Co_3O_4 prior to HEO generation can be obtained by reference experiments, e.g. calcining pure Co_3O_4 to check if it decomposes into CoO at the temperature

range of HEO generation, which would be helpful to understand if Co can be incorporated in the HEO from a spinel structure as well.

In **chapter 4**, the reaction mechanism of the HEO $(Co_{0.2}Cu_{0.2}Mg_{0.2}Ni_{0.2}Zn_{0.2})O$ in LIBs was clarified and revealed that the outstanding battery performance can be attributed to the synergy among the cations instead of the configuration entropy in the initial HEO. One can imagine that a stoichiometric ratio of the cations is not essential for multi-cation metal oxides to be used as battery anodes. Therefore, the ratio of the transition metals can be further optimized, e.g. increasing the Co and Zn ratio to obtain higher capacity. However, any limitation for the elemental ratio in the multi-cation oxide has not been determined. In addition, not reported in this thesis, we saw that the HEO $(Co_{0.2}Cu_{0.2}Mg_{0.2}Ni_{0.2}Zn_{0.2})O$ only delivers a very limited capacity when used in SIBs. Investigation of the reaction mechanism of this HEO in SIBs could result in a more clear understanding of the material properties and give further guidance for designing anode materials for SIBs. Based on the understanding developed in the current thesis, the Mg containing oxide phase plays an important role in stabilizing the overall structure. In SIBs, it is expected that Mg^{2+} is reduced by Na resulting in a loss of this stabilizing network. This could be one of the reasons for the failure of this HEO in SIBs. The more reductive Ca could replace Mg in the HEO and would presumably stay in an oxidized state throughout the electrochemical cycling and might thus stabilize a HEO in SIBs. Although the idea of a Ca containing HEO was already introduced, theoretical calculation showed that the synthesis would require a very high temperature to form a uniform single phase.[270] However, W. Li et al. successfully prepared this HEO using reactive flash sintering method.[303]

All of these findings will help us to unravel the fundamental processes and the structural evolution during synthesis and battery cycling more clearly. They could provide guidance for further materials design and optimization. The methodology used in this thesis for studying the reaction mechanism during battery cycling could also shine light on reaction mechanisms of other conversion reaction materials in LIBs and SIBs.

Reference

[1] M.C. Argyrou, P. Christodoulides, S.A. Kalogirou, Energy storage for electricity generation and related processes: Technologies appraisal and grid scale applications, Renewable and Sustainable Energy Reviews. 94 (2018) 804–821.

[2] E. Kabir, P. Kumar, S. Kumar, A.A. Adelodun, K. Kim, Solar energy : Potential and future prospects, Renewable and Sustainable Energy Reviews. 82 (2018) 894–900.

[3] B.K. Sahu, Wind energy developments and policies in China : A short review, Renewable and Sustainable Energy Reviews. 81 (2018) 1393–1405.

[4] A.P. Marugán, F. Pedro, G. Márquez, J. María, P. Perez, D. Ruiz-hernández, A survey of arti fi cial neural network in wind energy systems, Applied Energy. 228 (2018) 1822–1836.

[5] Y. Noorollahi, M. Salman, A.F. Siddiqi, L.K. Ilyashenko, Geothermics Review of two decade geothermal energy development in Iran , bene fi ts , challenges , and future policy, Geothermics. 77 (2019) 257–266.

[6] D. Moya, C. Aldás, P. Kaparaju, Geothermal energy : Power plant technology and direct heat applications, Renewable and Sustainable Energy Reviews. 94 (2018) 889–901.

[7] B. Lu, M. Stocks, A. Blakers, K. Anderson, Geographic information system algorithms to locate prospective sites for pumped hydro energy storage, Applied Energy. 222 (2018) 300–312.

[8] F. Jinyang, X. Heping, C. Jie, J. Deyi, L. Cunbao, W. Ngaha, Preliminary feasibility analysis of a hybrid pumped-hydro energy storage system using abandoned coal mine goafs, Applied Energy. 258 (2020) 114007.

[9] J. Wang, K. Lu, L. Ma, J. Wang, J. Li, D. Wang, S.- Min, E. Com, E. Com, Overview of Compressed Air Energy Storage and Technology Development, Energies. 991 (2017) 1–22.

[10] M. Zeynalian, A.H. Hajialirezaei, A.R. Razmi, M. Torabi, Carbon Dioxide Capture from a Compressed Air Energy Storage (CAES) System, Applied Thermal Engineering. 178 (2020) 115593.

[11] M. Ghanaatian, S. Lotfifard, Control of Flywheel Energy Storage Systems in the Presence of Uncertainties, IEEE Transactions on Sustainable Energy. 10 (2019) 36–45.

[12] S.M.G. Mousavi, F. Faraji, A. Majazi, K. Al-haddad, A comprehensive review of Flywheel Energy Storage System technology, Renewable and Sustainable Energy Reviews. 67 (2017) 477–490.

[13] B. Wang, T. Ruan, Y. Chen, F. Jin, L. Peng, Y. Zhou, D. Wang, S. Dou, Graphene-based composites for electrochemical energy storage, Energy Storage Materials. 24 (2019) 22–51.

[14] T.S. Mathis, N. Kurra, X. Wang, D. Pinto, P. Simon, Energy Storage Data Reporting in Perspective - Guidelines for Interpreting the Performance of Electrochemical Energy Storage Systems, Adv. Energy Mater. 1902007 (2019) 1–13.

[15] D.G. Mackanic, T. Chang, Stretchable electrochemical energy storage devices, Chem. Soc. Rev. 49 (2020) 4466–4495.

[16] H. Sun, Hierarchical 3D electrodes for electrochemical energy storage, Nat Rev Mater. 4 (2019) 45–60.

[17] S. Chen, L. Qiu, H. Cheng, Carbon-Based Fibers for Advanced Electrochemical Energy Storage Devices, Chem. Rev. 120 (2020) 2811–2878.

[18] R. Hou, G.S. Gund, K. Qi, P. Nakhanivej, H. Liu, F. Li, B.Y. Xia, H.S. Park, Hybridization design of materials and devices for flexible electrochemical energy storage, Energy Storage Materials. 19 (2019) 212–241.

[19] K. Zhang, M. Liu, T. Zhang, X. Min, Z. Wang, L. Chaia, Y. Shi, High-performance supercapacitor energy storage using carbon material derived from lignin by bacterial activation before carbonization, J. Mater. Chem. A. 7 (2019) 26838–26848.

[20] D.A. Bridge, Hybrid Model Predictive Control Strategy of Supercapacitor Energy Storage System Based on Double Active Bridge, Energies. 2134 (2019) 1–20.

[21] Y. Liao, H. Wang, M. Zhu, A. Thomas, Efficient Supercapacitor Energy Storage Using Conjugated Microporous Polymer Networks Synthesized from Buchwald – Hartwig Coupling, Adv. Mater. 1705710 (2018) 1–10.

[22] K. Mensah-darkwa, C. Zequine, P.K. Kahol, R.K. Gupta, Supercapacitor Energy Storage Device Using Biowastes : A Sustainable Approach to Green Energy, Sustainability. 11 (2019) 1–22.

[23] R. Dubey, V. Guruviah, Review of carbon-based electrode materials for supercapacitor energy storage, Ionics. 25 (2019) 1419–1445.

[24] L. Kouchachvili, W. Yaïci, E. Entchev, Hybrid battery / supercapacitor energy storage system for the electric vehicles, Journal of Power Sources. 374 (2018) 237–248.

[25] A. Colmenar-santos, E. Luis-molina, E. Rosales-asensio, Á. Lopez-Rey, Technical approach for the inclusion of superconducting magnetic energy storage in a smart city, Energy. 158 (2018) 1080–1091.

[26] J. Shi, Y. Xu, M. Liao, S. Guo, Y. Li, L. Ren, R. Su, S. Li, X. Zhou, Y. Tang, Integrated design method for superconducting magnetic energy storage considering the high frequency pulse width modulation pulse voltage on magnet, Applied Energy. 248 (2019) 1–17.

[27] Y. Miyazaki, K. Mizuno, T. Yamashita, M. Ogata, H. Hasegawa, Development of superconducting magnetic bearing for flywheel energy storage system, Cryogenics. 80 (2016) 234–237.

[28] P. Mukherjee, Design and Development of High Temperature Superconducting Magnetic Energy Storage for Power Applications - A Review, Physica C: Superconductivity and Its Applications. 563 (2019) 67–73.

[29] P. Mukherjee, V. V Rao, Superconducting magnetic energy storage for stabilizing grid integrated with wind power generation systems, Journal of Modern Power Systems and Clean Energy. 7 (2018) 400–411.

[30] V.S.V. G, S. Madichetty, Application of superconducting magnetic energy storage in electrical

power and energy systems : a review, Int. J. Energy Res. 42 (2017) 358–368.

[31] C. Chen, L. Hu, Nanocellulose toward Advanced Energy Storage Devices : Structure and Electrochemistry, Acc. Chem. Res. 51 (2018) 3154–3165.

[32] B.Y. Guan, X.Y. Yu, H. Bin Wu, X. Wen, D. Lou, Complex Nanostructures from Materials based on Metal – Organic Frameworks for Electrochemical Energy Storage and Conversion, Adv. Mater. 1703614 (2017) 1–20.

[33] Q. Deng, Y. Fu, C. Zhu, Y. Yu, Niobium-Based Oxides Toward Advanced Electrochemical Energy Storage : Recent Advances and Challenges, Small. 1804884 (2019) 1–26.

[34] B. Scrosati, Lithium Rocking Chair Batteries: An Old Concept?, Journal of The Electrochemical Society. 139 (1992) 2776.

[35] S. Yan, K.P. Abhilash, L. Tang, M. Yang, Y. Ma, Q. Xia, Q. Guo, Research Advances of Amorphous Metal Oxides in Electrochemical Energy Storage and Conversion, Small. 15 (2019) 1804371.

[36] X. Sun, G. Hao, X. Lu, L. Xi, B. Liu, W. Si, C. Ma, Q. Liu, Q. Zhang, S. Kaskel, O.G. Schmidt, High-defect hydrophilic carbon cuboids anchored with Co/CoO nanoparticles as highly efficient and ultra-stable lithium-ion battery anodes, J. Mater. Chem. A. (2016) 10166–10173.

[37] X. Zhao, Z. Liu, W. Xiao, H. Huang, L. Zhang, Y. Cheng, J. Zhang, Low Crystalline MoS_2 Nanotubes from MoS_2 Nanomasks for Lithium Ion Battery Applications, ACS Appl. Nano Mater. 3 (2020) 7580−7586.

[38] Y. Sun, X. Hu, W. Luo, Y. Huang, Self-assembled mesoporous CoO nanodisks as a long-life anode material for, J. Mater. Chem. 22 (2012) 13826–13831.

[39] P. Li, J.Y. Jeong, B. Jin, K. Zhang, J.H. Park, Vertically Oriented MoS_2 with Spatially Controlled Geometry on Nitrogenous Graphene Sheets for High-Performance Sodium-Ion Batteries, Adv. Energy Mater. 8 (2018) 1703300.

[40] A. Manthiram, Y. Fu, Y.-S. Su, Challenges and Prospects of Lithium–Sulfur Batteries, Accounts of Chemical Research. 46 (2013) 1125–1134.

[41] C.H. Shen, L. Huang, Z. Lin, S.Y. Shen, Q. Wang, H. Su, F. Fu, X.M. Zheng, Kinetics and structural changes of Li-Rich layered oxide $0.5Li_2MnO_3{\cdot}0.5LiNi_{0.292}Co_{0.375}Mn_{0.333}O_2$ material investigated by a novel technique combining in situ XRD and a multipotential step, ACS Applied Materials and Interfaces. 6 (2014) 13271–13279.

[42] G.Z. Wei, X. Lu, F.S. Ke, L. Huang, J.T. Li, Z.X. Wang, Z.Y. Zhou, S.G. Sun, Crystal habit-tuned nanoplate material of $Li[Li_{1/3-2x/3}Ni_xMn_{2/3-x/3}]O_2$ for high-rate performance lithium-ion batteries, Advanced Materials. 22 (2010) 4364–4367.

[43] Z. Zheng, Y. Zao, Q. Zhang, Y. Cheng, H. Chen, K. Zhang, M. Wang, D. Peng, Robust Erythrocyte-like Fe_2O_3@carbon with Yolk-shell Structures as High-performance Anode for Lithium Ion Batteries, Chemical Engineering Journal. 347 (2018) 563–573.

[44] K.H. Jeong, H.W. Ha, N.J. Yun, M.Z. Hong, K. Kim, Zr-doped $Li[Ni_{0.5-x}Mn_{0.5-x}Zr_{2x}]O_2$ (x = 0, 0.025) as

cathode material for lithium ion batteries, Electrochimica Acta. 50 (2005) 5349–5353.

[45] G. Ali, J.-H. Lee, D. Susanto, S.-W. Choi, B.W. Cho, K.-W. Nam, K.Y. Chung, Polythiophene-Wrapped Olivine $NaFePO_4$ as a Cathode for Na-Ion Batteries, ACS Applied Materials & Interfaces. 8 (2016) 15422–15429.

[46] D. Li, J. Zhou, X. Chen, H. Song, Amorphous Fe_2O_3/Graphene Composite Nanosheets with Enhanced Electrochemical Performance for Sodium-Ion Battery, ACS Applied Materials and Interfaces. 8 (2016) 30899–30907.

[47] X.H. Zhang, W.L. Pang, F. Wan, J.Z. Guo, H.Y. Lü, J.Y. Li, Y.M. Xing, J.P. Zhang, X.L. Wu, P2-$Na_{2/3}Ni_{1/3}Mn_{5/9}Al_{1/9}O_2$ Microparticles as Superior Cathode Material for Sodium-Ion Batteries: Enhanced Properties and Mechanisam via Graphene Connection, ACS Applied Materials and Interfaces. 8 (2016) 20650–20659.

[48] M. Palanisamy, H.W. Kim, S. Heo, E. Lee, Y. Kim, Insights into the Dual-Electrode Characteristics of Layered $Na_{0.5}Ni_{0.25}Mn_{0.75}O_2$ Materials for Sodium-Ion Batteries, ACS Applied Materials and Interfaces. 9 (2017) 10618–10625.

[49] K.H. Ha, S.H. Woo, D. Mok, N.S. Choi, Y. Park, S.M. Oh, Y. Kim, J. Kim, J. Lee, L.F. Nazar, K.T. Lee, $Na_{4-\alpha}M_{2+\alpha/2}(P_2O_7)_2$ ($2/3 \leq \alpha \leq 7/8$, M = Fe, $Fe_{0.5}Mn_{0.5}$, Mn): A promising sodium ion cathode for na-ion batteries, Advanced Energy Materials. 3 (2013) 770–776.

[50] R. Rajagopalan, Y. Tang, X. Ji, C. Jia, H. Wang, Advancements and Challenges in Potassium Ion Batteries : A Comprehensive Review, Adv. Funct. Mater. 1909486 (2020) 1–35.

[51] W. Zhang, Y. Liu, Z. Guo, Approaching high-performance potassium-ion batteries via advanced design strategies and engineering, Science. Adv. 5 (2019) 1–13.

[52] J.C. Pramudita, D. Sehrawat, D. Goonetilleke, N. Sharma, An Initial Review of the Status of Electrode Materials for Potassium-Ion Batteries, Adv. Energy Mater. 1602911 (2017) 1–21.

[53] J. Wang, B. Wang, B. Lu, Nature of Novel 2D van der Waals Heterostructures for Superior Potassium Ion Batteries, Adv. Energy Mater. 2000884 (2020) 1–10.

[54] B. Ji, W. Yao, Y. Zheng, P. Kidkhunthod, X. Zhou, S. Tunmee, S. Sattayaporn, H. Cheng, H. He, Y. Tang, batteries with ultra-long cyclability, Nature Communications. 1225 (2020) 1–10.

[55] Y. Zhang, S. Liu, Y. Ji, J. Ma, H. Yu, Emerging Nonaqueous Aluminum-Ion Batteries : Challenges , Status , and Perspectives, Adv. Mater. 1706310 (2018) 1–23.

[56] F. Wu, H. Yang, Y. Bai, C. Wu, Paving the Path toward Reliable Cathode Materials for Aluminum-Ion Batteries, Adv. Mater. 1806510 (2019) 1–18.

[57] I. Edition, Graphene: A Cathode Material of Choice for Aluminum-ion Battery, Angew.Chem.Int.Ed. 57 (2018) 16606–16617.

[58] H. Li, H. Yang, Z. Sun, Y. Shi, H. Cheng, F. Li, A Highly Reversible Co_3S_4 Microsphere Cathode Material for Aluminum-Ion Batteries, Nano Energy. 56 (2019) 100–108.

[59] F. Wang, X. Fan, T. Gao, W. Sun, Z. Ma, C. Yang, F. Han, K. Xu, C. Wang, High-Voltage Aqueous

Magnesium Ion Batteries, ACS Cent. Sci. 3 (2017) 1121–1128.

[60] X. Ji, J. Chen, F. Wang, W. Sun, Y. Ruan, L. Miao, J. Jiang, C. Wang, Water activated VOPO4 for magnesium ion batteries, Nano Lett. 18 (2018) 6441–6448.

[61] D. Kim, S.C. Jung, S. Ha, Y. Kim, Y. Park, J.H. Ryu, Y. Han, K.T. Lee, D.M. Kim, S.C. Jung, S. Ha, Y. Kim, Y. Park, J. Heon, Co-Intercalation of Mg Ions into Graphite for Magnesium-Ion Batteries Co-Intercalation of Mg^{2+} Ions into Graphite for Magnesium-Ion Batteries, Chem. Mater. 30 (2018) 3199–3203.

[62] X. Lei, Y. Zheng, F. Zhang, Y. Wang, Y. Tang, Highly stable magnesium-ion-based dual-ion batteries based on insoluble small-molecule organic anode material, Energy Storage Materials. 30 (2020) 34–41.

[63] B. Li, R. Masse, C. Liu, Y. Hu, W. Li, G. Zhang, G. Cao, Technology on Energy Storage and Power Generation of Guangdong Higher, Energy Storage Materials. 22 (2019) 96–104.

[64] G.-L. Xu, Tuning the structure and property of nanostructured cathode materials of lithium ion and lithium sulfur batteries, Journal of Materials Chemistry A. 2 (2014) 19941–19962.

[65] W. Hua, Lithium- and oxygen-driven structural evolution in Co-free Li-Mn-rich oxides as cathodes for lithium ion batteries, 2019.

[66] Y. Huang, J.B. Goodenough, High-Rate $LiFePO_4$ Lithium Rechargeable Battery Promoted by Electrochemically Active Polymers, Chem. Mater. (2008) 7237–7241.

[67] S. Yang, Y. Song, K. Ngala, P.Y. Zavalij, M.S. Whittingham, Performance of $LiFePO_4$ as lithium battery cathode and comparison with manganese and vanadium oxides, Journal of Power Sources. 121 (2003) 239–246.

[68] A. Yamada, S.C. Chung, K. Hinokuma, Optimized LiFePO 4 for Lithium Battery Cathodes, Journal of The Electrochemical Society. 148 (2001) A224–A229.

[69] F. Croce, A.D. Epifanio, J. Hassoun, A. Deptula, T. Olczac, A Novel Concept for the Synthesis of an Improved $LiFePO_4$ Lithium Battery Cathode, Electrochemical and Solid-State Letters. 5 (2002) A47–A50.

[70] Y. Wu, L. Zhou, G. Xu, J. Huang, X. Fang, Y. Wang, Y. Jin, X. Tang, Preparation of High Tap Density $LiFePO_4$/C through Carbothermal Reduction Process Using Beta-Cyclodextrin as Carbon Source, Int. J. Electrochem. Sci. 13 (2018) 2958–2968.

[71] T. Wang, K. Ren, M. He, W. Dong, W. Xiao, H. Pan, Synthesis and Manipulation of Single-Crystalline Lithium Nickel Manganese Cobalt Oxide Cathodes : A Review of Growth Mechanism, Frontiers in Chemistry. 8 (2020) 1–8.

[72] X. Yang, T. Liu, C. Wang, Thermally modulated lithium iron phosphate batteries for mass-market electric vehicles, Nature Energy. 6 (2021) 176–185.

[73] M. Ni, Q. Li, G. Li, C. Fu, D. Luo, J. Fan, D. Xie, L. Li, Balancing stability and speci fi c energy in Li-rich cathodes for lithium ion batteries : a case study of a, J. Mater. Chem. A. 3 (2015) 10592–10602.

[74] J. Wei, S. Zhao, L. Ji, T. Zhou, Y. Miao, K. Scott, Resources , Conservation & Recycling Reuse of Ni-Co-Mn oxides from spent Li-ion batteries to prepare bifunctional air electrodes, Resources, Conservation & Recycling. 129 (2018) 135–142.

[75] W. Hua, B. Schwarz, R. Azmi, M. Müller, M.S. Dewi, M. Knapp, A. Senyshyn, M. Heere, A. Missiul, J.R. Binder, S. Indris, H. Ehrenberg, Lithium-ion (de)intercalation mechanism in core-shell layered Li(Ni,Co,Mn)O_2 cathode materials, Nano Energy. 78 (2020) 105231.

[76] H. Kitaura, A. Hayashi, K. Tadanaga, M. Tatsumisago, Electrochemical performance of all-solid-state lithium secondary batteries with Li -Ni-Co-Mn oxide positive electrodes, Electrochimica Acta. 55 (2010) 8821–8828.

[77] J.U. Choi, N. Voronina, Y. Sun, S. Myung, Recent Progress and Perspective of Advanced High-Energy Co-Less Ni-Rich Cathodes for Li-Ion Batteries : Yesterday, Today, and Tomorrow, Adv. Energy Mater. 10 (2020) 1–31.

[78] A. Devaraj, M. Gu, R. Colby, P. Yan, C.M. Wang, J.M. Zheng, J. Xiao, A. Genc, J.G. Zhang, I. Belharouak, D. Wang, K. Amine, S. Thevuthasan, Visualizing nanoscale 3D compositional fluctuation of lithium in advanced lithium-ion battery cathodes, Nat Commun. (2015).

[79] M. Lee, S. Lee, P. Oh, Y. Kim, J. Cho, High Performance $LiMn_2O_4$ Cathode Materials Grown with Epitaxial Layered Nanostructure for Li-Ion Batteries, Nano Lett. 14 (2014) 993−999.

[80] J.-L. Shi, J.-N. Zhang, M. He, X.-D. Zhang, L.-J. Wan, Mitigating Voltage Decay of Li-Rich Cathode Material via Increasing Ni-Content for Lithium-Ion Batteries, ACS Appl. Mater. Interfaces. 2 (2016) 20138–20146.

[81] F. Fu, Y. Yao, H. Wang, G. Xu, Structure dependent electrochemical performance of Li-rich layered oxides in lithium-ion batteries, Nano Energy. 35 (2017) 370–378.

[82] J. Fan, G. Li, B. Li, D. Zhang, D. Chen, L. Li, Reconstructing the Surface Structure of Li-Rich Cathode for High-Energy Lithium-Ion Batteries, ACS Appl. Mater. Interfaces. 11 (2019) 19950–19958.

[83] M. Ellwanger, M. Daub, A. Hoffmann, Fluorination of Li-rich Lithium Ion Battery Cathode Materials by Fluorine Gas: Chemistry, Characterization, and Electrochemical Performance in Half Cells, ChemElectroChem. 6 (2019) 3337–3349.

[84] C.M. Julien, A. Mauger, K. Zaghib, H. Groult, Comparative Issues of Cathode Materials for Li-Ion Batteries, Inorganics. (2014) 132–154.

[85] J.-L. Yue, W.-W. Yin, M.-H. Cao, S. Zulipiya, Y.-N. Zhou, Z.-W. Fu, A quinary layer transition metal oxide of $NaNi_{1/4}Co_{1/4}Fe_{1/4}Mn_{1/8}Ti_{1/8}O_2$ as a high-rate-capability and long-cycle-life cathode material for rechargeable sodium ion batteries, Chem. Commun. 51 (2015) 15712–15715.

[86] J. Deng, W. Bin Luo, X. Lu, Q. Yao, Z. Wang, H.K. Liu, H. Zhou, S.X. Dou, High Energy Density Sodium-Ion Battery with Industrially Feasible and Air-Stable O3-Type Layered Oxide Cathode, Advanced Energy Materials. 8 (2018) 1–9.

[87] M. Kalapsazova, G.F. Ortiz, J.L. Tirado, O. Dolotko, E. Zhecheva, D. Nihtianova, L. Mihaylov, R.

Stoyanova, P3-Type Layered Sodium-Deficient Nickel-Manganese Oxides: A Flexible Structural Matrix for Reversible Sodium and Lithium Intercalation, ChemPlusChem. 80 (2015) 1642–1656.

[88] J.-L. Yue, Y.-N. Zhou, X. Yu, S.-M. Bak, X.-Q. Yang, Z.-W. Fu, O3-type layered transition metal oxide Na(NiCoFeTi) $_{1/4}$ O $_{2}$ as a high rate and long cycle life cathode material for sodium ion batteries, J. Mater. Chem. A. 3 (2015) 23261–23267.

[89] M.H. Han, E. Gonzalo, N. Sharma, J.M. López Del Amo, M. Armand, M. Avdeev, J.J. Saiz Garitaonandia, T. Rojo, High-Performance P2-Phase $Na_{2/3}Mn_{0.8}Fe_{0.1}Ti_{0.1}O_2$ Cathode Material for Ambient-Temperature Sodium-Ion Batteries, Chemistry of Materials. 28 (2016) 106–116.

[90] T. Huang, G. Du, Y. Qi, J. Li, W. Zhong, Q. Yang, X. Zhang, M. Xu, A Prussian blue analogue as a long-life cathode for liquid-state and solid-state sodium-ion batteries, Inorg. Chem. Front. 7 (2020) 3938–3944.

[91] J. Qian, C. Wu, Y. Cao, Z. Ma, Y. Huang, X. Ai, Prussian Blue Cathode Materials for Sodium-Ion Batteries and Other Ion Batteries, Adv. Energy Mater. 8 (2018) 1–24.

[92] Y. Zhu, Z. Zhang, J. Bao, S. Zeng, Multi-metal doped high capacity and stable Prussian blue analogue for sodium ion batteries, Int J Energy Res. (2020) 9205–9212.

[93] Q. Liu, Z. Hu, M. Chen, C. Zou, H. Jin, S. Wang, The Cathode Choice for Commercialization of Sodium-Ion Batteries : Layered Transition Metal Oxides versus Prussian Blue Analogs, Adv. Funct. Mater. 30 (2020) 1–15.

[94] S. Guo, Q. Li, P. Liu, M. Chen, H. Zhou, Environmentally stable interface of layered oxide cathodes for sodium-ion batteries, Nature Communications. 8 (2017) 1–9.

[95] J. Hwang, J. Kim, T. Yu, Y. Sun, A New P2-Type Layered Oxide Cathode with Extremely High Energy Density for Sodium-Ion Batteries, Adv. Energy Mater. 9 (2019) 1803346.

[96] Y. Xiao, Y. Zhu, H. Yao, P. Wang, X. Zhang, H. Li, X. Yang, L. Gu, Y. Li, T. Wang, Y. Yin, X. Guo, A Stable Layered Oxide Cathode Material for High-Performance Sodium-Ion Battery, Adv. Energy Mater. 9 (2019) 1803978.

[97] K. Zhang, D. Kim, Z. Hu, M. Park, G. Noh, Y. Yang, J. Zhang, V.W. Lau, S. Chou, M. Cho, S. Choi, Y. Kang, Manganese based layered oxides with modulated electronic and thermodynamic properties for sodium ion batteries, Nature Communications. 10 (2019) 5203.

[98] E. Lee, J. Lu, Y. Ren, X. Luo, X. Zhang, J. Wen, D. Miller, A. Dewahl, S. Hackney, B. Key, D. Kim, M.D. Slater, C.S. Johnson, Layered P2/O3 Intergrowth Cathode: Toward High Power Na-Ion Batteries, Adv. Energy Mater. 4 (2014) 1400458.

[99] S. Guo, P. Liu, H. Yu, Y. Zhu, M. Chen, M. Ishida, A Layered P2- and O3-Type Composite as a High-Energy Cathode for Rechargeable Sodium-Ion Batteries, Angew. Chem. 127 (2015) 5992–5997.

[100] W. Li, C. Han, G. Cheng, S. Chou, H. Liu, S. Dou, Chemical Properties , Structural Properties , and Energy Storage Applications of Prussian Blue Analogues, Small. 1900470 (2019) 1–21.

[101] S.H. Ng, J. Wang, Z.P. Guo, J. Chen, G.X. Wang, H.K. Liu, Single wall carbon nanotube paper as anode

for lithium-ion battery, 51 (2005) 23–28.

[102] S.H. Moo, G. Nanoarchitectures, T. Application, H.A. Material, L. Batteries, Self-Assembled Hierarchical MoO_2/Graphene Nanoarchitectures and Their Application as a High-Performance Anode Material for Lithium-Ion, (2011) 7100–7107.

[103] C. De Casas, W. Li, A review of application of carbon nanotubes for lithium ion battery anode material, Journal of Power Sources. 208 (2012) 74–85.

[104] H. Liu, W. Li, D. Shen, D. Zhao, G. Wang, Graphitic Carbon Conformal Coating of Mesoporous TiO 2 Hollow Spheres for High-Performance Lithium Ion Battery Anodes, (2015).

[105] L. Fang, B.V.R. Chowdari, Sn-Ca amorphous alloy as anode for lithium ion battery, Journal of Power Sources. 98 (2001) 181–184.

[106] X. Cheng, P. Shi, Electroless Cu-plated Ni_3Sn_4 alloy used as anode material for lithium ion battery, Journal of Alloys and Compounds. 391 (2005) 241–244.

[107] B.G. Derrien, J. Hassoun, S. Panero, B. Scrosati, Nanostructured Sn-C Composite as an Advanced Anode Material in High-Performance Lithium-Ion Batteries, Adv. Mater. 19 (2007) 2336–2340.

[108] H. Wu, G. Zheng, N. Liu, T.J. Carney, Y. Yang, Y. Cui, Engineering Empty Space between Si Nanoparticles for Lithium-Ion Battery Anodes, Nano Lett. 12 (2012) 904–909.

[109] B. Varghese, M. V Reddy, Z. Yanwu, C.S. Lit, T.C. Hoong, G.V.S. Rao, B.V.R. Chowdari, A. Thye, S. Wee, C.T. Lim, Fabrication of NiO Nanowall Electrodes for High Performance Lithium Ion Battery, Chem. Mater. 20 (2008) 3360–3367.

[110] K. Zhong, X. Xia, B. Zhang, H. Li, Z. Wang, L. Chen, MnO powder as anode active materials for lithium ion batteries, Journal of Power Sources. 195 (2010) 3300–3308.

[111] X.H. Huang, X.H. Xia, Y.F. Yuan, F. Zhou, Porous ZnO nanosheets grown on copper substrates as anodes for lithium ion batteries, Electrochimica Acta. 56 (2011) 4960–4965.

[112] J.M. Chem, X. Li, D. Li, L. Qiao, X. Wang, X. Sun, P. Wang, D. He, Interconnected porous MnO nanoflakes for high-performance lithium ion battery anodes, J. Mater. Chem. 22 (2012) 9189–9194.

[113] Y. Shi, Q. Wang, Carbon materials from melamine sponges for supercapacitors and lithium battery electrode materials : A review, Carbon Energy. (2019) 1–23.

[114] C.M. Subramaniyam, N.R. Srinivasan, Z. Tai, H.K. Liu, J.B. Goodenough, S.X. Dou, Self-assembled porous carbon microparticles derived from halloysite clay as a lithium battery, J. Mater. Chem. A. 5 (2017) 1–10.

[115] B.J. Landi, Carbon nanotubes for lithium ion batteries, Energy Environ. Sci. 2 (2009) 638–654.

[116] M. Mohri, N. Yanagisawa, Y. Tajima, H. Tanaka, T. Mitate, S. Nakajima, M. Yoshida, Y. Yoshimoto, T. Suzuki, H. Wada, S. Corpomtion, rechargeable lithium battery based on pyrolytic, Journal of Power Sources. 26 (1989) 545–551.

[117] Y. Matsumura, S. Wang, J. Mondori, Interaction between disordered carbon and lithium in lithium

ion rechargeable batteries, Carbon. 33 (1995) 1457–1462.

[118] A.R. Kamali, D.J. Fray, Review on Carbon and Silicon Based Materials as Anode Materials for Lithium Ion Batteries, J. New Mat. Electrochem. Systems. 160 (2010) 147–160.

[119] M. Balogun, Y. Luo, W. Qiu, P. Liu, Y. Tong, A review of carbon materials and their composites with alloy metals for sodium ion battery anodes, Carbon. 98 (2016) 162–178.

[120] D. Li, H. Chen, G. Liu, M. Wei, L. Ding, S. Wang, H. Wang, Porous nitrogen doped carbon sphere as high performance anode of sodium-ion battery, CARBON. 94 (2015) 888–894.

[121] J. Ding, H. Wang, Z. Li, A. Kohandehghan, K. Cui, Z. Xu, B. Zahiri, X. Tan, E.M. Lotfabad, B.C. Olsen, D. Mitlin, Carbon nanosheet frameworks derived from peat moss as high performance sodium ion battery anodes, ACS Nano. 7 (2013) 11004–11015.

[122] Y. Cao, L. Xiao, M.L. Sushko, W. Wang, B. Schwenzer, J. Xiao, Z. Nie, L. V Saraf, Z. Yang, J. Liu, Sodium Ion Insertion in Hollow Carbon Nanowires for Battery Applications, Nano Lett. 12 (2012) 3783−3787.

[123] J. Park, Z. Xu, K. Kang, Solvated Ion Intercalation in Graphite: Sodium and Beyond, Front. Chem. 8 (2020) 1–14.

[124] K. Volgmann, V. Epp, J. Langer, B. Stanje, S. Nakhal, M. Lerch, M. Wilkening, P. Heitjans, Solid-State NMR to Study Translational Li Ion Dynamics in Solids with Low- Solid-State NMR to Study Translational Li Ion Dynamics in Solids with Low-Dimensional Diffusion Pathways, Z. Phys. Chem. 231 (2017) 1215–1241.

[125] U.K. Sen, A. Shaligram, S. Mitra, Intercalation Anode Material for Lithium Ion Battery Based on Molybdenum Dioxide, ACS Appl. Mater. Interfaces. 6 (2014) 14311−14319.

[126] S.H. Moo, G. Nanoarchitectures, T. Application, H.A. Material, L. Batteries, Self-Assembled Hierarchical MoO_2/Graphene Nanoarchitectures and Their Application as a High-Performance Anode Material for Lithium-Ion, ACS Nano. (2011) 7100–7107.

[127] J. Ni, S. Fu, Y. Yuan, L. Ma, Y. Jiang, L. Li, J. Lu, Boosting Sodium Storage in TiO_2 Nanotube Arrays through Surface Phosphorylation, Adv. Mater. 30 (2018) 1–7.

[128] N. Wu, X. Qiao, J. Shen, G. Liu, T. Sun, H. Wu, H. Hou, X. Liu, Y. Zhang, X. Ji, Anatase inverse opal TiO_{2-x}@N-doped C induced the dominant pseudocapacitive effect for durable and fast lithium/sodium storage, Electrochimica Acta. 299 (2019) 540–548.

[129] K. Cao, T. Jin, L. Jiao, Recent progress in conversion reaction metal oxide anodes for Li-ion batteries, Mater. Chem. Front. 1 (2017) 2213–2242.

[130] X. Li, M. Zhang, S. Yuan, C. Lu, Research Progress of Silicon/Carbon Anode Materials for Lithium-Ion Batteries : Structure Design and Synthesis Method, ChemElectroChem. 7 (2020) 4289–4302.

[131] N. Liu, H. Wu, M.T. Mcdowell, Y. Yao, C. Wang, Y. Cui, A Yolk-Shell Design for Stabilized and Scalable Li-Ion Battery Alloy Anodes, Nano Lett. 12 (2012) 3315−3321.

[132] Y. Zhao, L.P. Wang, M.T. Sougrati, Z. Feng, Y. Leconte, A Review on Design Strategies for Carbon

Based Metal Oxides and Sulfides Nanocomposites for High Performance Li and Na Ion Battery Anodes, Adv. Energy Mater. 7 (2017) 1601424.

[133] M. Zheng, H. Tang, L. Li, Q. Hu, L. Zhang, H. Xue, H. Pang, Hierarchically Nanostructured Transition Metal Oxides for Lithium-Ion Batteries, Adv. Sci. 5 (2018) 1700592.

[134] G. Wang, X. Leng, S. Han, Y. Shao, How to improve the stability and rate performance of lithium-ion batteries with transition metal oxide anodes, J. Mater. Res. 32 (2017) 16–36.

[135] K. Bindumadhavan, P.-Y. Chang, M.-H. Yeh, R. Doong, Ultra-small CoO nanocrystals anchored on reduced graphene oxide for enhanced lithium storage in lithium ion batteries, MRS Communications. 7 (2017) 236–244.

[136] G. Li, Y. Li, J. Chen, P. Zhao, D. Li, Y. Dong, L. Zhang, Electrochimica Acta Synthesis and Research of Egg shell-yolk NiO / C porous composites as Lithium-ion Battery Anode Material, Electrochimica Acta. 245 (2017) 941–948.

[137] H. Chen, N. Qiu, B. Wu, Z. Yang, S. Sun, Y. Wang, A new spinel high-entropy oxide (Mg0.2Ti0.2Zn0.2Cu0.2Fe0.2)3O4 with fast reaction kinetics and excellent stability as an anode material for lithium ion batteries†, RSC Adv. (2020) 9736–9744.

[138] N. Qiu, H. Chen, Z. Yang, S. Sun, Y. Wang, Y. Cui, A high entropy oxide ($Mg_{0.2}Co_{0.2}Ni_{0.2}Cu_{0.2}Zn_{0.2}O$) with superior lithium storage performance, Journal of Alloys and Compounds. 777 (2018) 767-774.

[139] D. Wang, S. Jiang, C. Duan, J. Mao, Y. Dong, K. Dong, Z. Wang, S. Luo, Y. Liu, X. Qi, Spinel-structured high entropy oxide $(FeCoNiCrMn)_3O_4$ as anode towards superior lithium storage performance, Journal of Alloys and Compounds. 844 (2020) 156158.

[140] Q. Wang, A. Sarkar, Z. Li, Y. Lu, L. Velasco, Electrochemistry Communications High entropy oxides as anode material for Li-ion battery applications : A practical approach, Electrochemistry Communications. 100 (2019) 121–125.

[141] W. Zhao, J. Pan, Y. Fang, X. Che, D. Wang, K. Bu, Metastable MoS_2: Crystal Structure , Electronic Band Structure , Synthetic Approach and Intriguing Physical Properties, Chem. Eur. J. 24 (2018) 15942–15954.

[142] X. Zheng, Z. Guo, G. Zhang, H. Li, J. Zhang, Q. Xu, Building a lateral/vertical 1T-2H MoS_2/Au heterostructure for enhanced photoelectrocatalysis and surface enhanced Raman scattering†, J. Mater. Chem. A,. 7 (2019) 19922–19928.

[143] C.D. Quilty, L.M. Housel, D.C. Bock, M.R. Dunkin, L. Wang, D.M. Lutz, A. Abraham, A.M. Bruck, E.S. Takeuchi, K.J. Takeuchi, A.C. Marschilok, Ex-Situ and Operando XRD and XAS Analysis of MoS_2: A Lithiation Study of Bulk and Nanosheet Materials, ACS Appl. Energy Mater. 2 (2019) 7635–7646.

[144] D. Chen, G. Ji, B. Ding, Y. Ma, B. Qu, W. Chen, J.Y. Lee, Double Transition-Metal Chalcogenide as a High-Performance Lithium-Ion Battery Anode Material, Ind. Eng. Chem. Res. 53 (2014) 17901−17908.

[145] Z. Li, S. Liu, B.P. Vinayan, Z. Zhao-karger, T. Diemant, K. Wang, R.J. Behm, C. Kübel, R. Klingeler, M.

Fichtner, Hetero-layered MoS2/C composites enabling ultrafast and durable Na storage, Energy Storage Materials. 21 (2019) 115–123.

[146] B.J. Yeh, S. Chen, S. Lin, J. Gan, T. Chin, T. Shun, C. Tsau, Nanostructured High-Entropy Alloys with Multiple Principal Elements : Novel Alloy Design Concepts and Outcomes, ADVANCED ENGINEERING MATERIALS. 6 (2004) 299–303.

[147] C.M. Rost, E. Sachet, T. Borman, A. Moballegh, E.C. Dickey, D. Hou, J.L. Jones, S. Curtarolo, J.P. Maria, Entropy-stabilized oxides, Nature Communications. 6 (2015) 1–8.

[148] B.N. Dragoe, Order emerging from disorder, Science. 366 (2019) 573–574.

[149] S.H. Albedwawi, A. Aljaberi, G.N. Haidemenopoulos, K. Polychronopoulou, High entropy oxides-exploring a paradigm of promising catalysts: A review, Materials & Design. 202 (2021) 109534.

[150] High Entropy Oxides, https://www.int.kit.edu/7190.php.

[151] X. Yan, Y. Zhang, Functional properties and promising applications of high entropy alloys Scripta Materialia Functional properties and promising applications of high entropy alloys, Scripta Materialia. 187 (2020) 188–193.

[152] D.B. Miracle, O.N. Senkov, A critical review of high entropy alloys and related concepts, Acta Materialia. 122 (2017) 448–511.

[153] M.C. Gao, J.A. Hawk, X.H.Yan, Y. Zhang, J.A. Hawk, High-entropy functional materials, J. Mater. Res. 33 (2018) 3138-3155.

[154] H. Chen, N. Qiu, A new spinel high-entropy oxide $(Mg_{0.2}Ti_{0.2}Zn_{0.2}Cu_{0.2}Fe_{0.2})_3O_4$ with fast reaction kinetics and excellent stability as an anode materialfor lithium ion batteries, RSC Adv. 10 (2020) 9736–9744.

[155] C. Zhao, F. Ding, Y. Lu, L. Chen, Y. Hu, High-Entropy Layered Oxide Cathodes for Sodium-Ion Batteries, Angew. Chem. Int. Ed. 213300 (2020) 264–269.

[156] M. Anik, Electrochemical Performance of $(MgCoNiZn)_{1-x}Li_xO$ High-Entropy Oxides in Lithium-Ion Batteries, ACS Appl. Mater. Interfaces. 12 (2020) 23860−23866.

[157] S. Franger, A.K. Meena, N. Dragoe, Room temperature lithium superionic conductivity in high entropy oxides, Journal of Materials Chemistry A. 4 (2016) 9536–9541.

[158] V.A. Online, S. Franger, A.K. Meena, N. Dragoe, Room temperature lithium superionic conductivity in high entropy oxides, J. Mater. Chem. A. 4 (2016) 9536–9541.

[159] A. Sarkar, L. Velasco, D. Wang, Q. Wang, G. Talasila, L. De Biasi, C. Kübel, T. Brezesinski, S.S. Bhattacharya, H. Hahn, B. Breitung, High entropy oxides for reversible energy storage, Nat Commun. 9 (2018) 3400.

[160] Z. Lun, B. Ouyang, D. Kwon, Y. Ha, E.E. Foley, T. Huang, Z. Cai, H. Kim, M. Balasubramanian, Y. Sun, J. Huang, Y. Tian, H. Kim, B.D. Mccloskey, W. Yang, R.J. Clément, H. Ji, G. Ceder, Cation-disordered rocksalt-type high-entropy cathodes for Li-ion batteries, Nature Materials. 20 (2021) 214–221.

[161] R. J. Cle´ment, Z. Lun, G. Ceder, Cation-disordered rocksalt transition metal oxides and oxyfluorides

for high energy lithium-ion cathodes, Energy Environ. Sci. 13 (2020) 345–373.

[162] B. Breitung, Q. Wang, A. Schiele, Đ. Tripković, Gassing Behavior of High-Entropy Oxide Anode and Oxyfluoride Cathode Probed Using Differential Electrochemical Mass Spectrometry, Batteries & Supercaps. 3 (2020) 361–369.

[163] S.Q. Wang, H. Hahn, B. Breitung, A. Du, P. Heitjans, T. Brezesinski, Multi-anionic and -cationic compounds: new high entropy materials for advanced Li-ion batteries, Energy Environ. Sci. 12 (2019) 2433.

[164] Y. Ma, Y. Ma, Q. Wang, B. Breitung, High-entropy energy materials: challenges and new opportunities, Energy Environ. Sci. 14 (2021) 2883–2905.

[165] B. Xiao, G. Wu, T. Wang, Z. Wei, Y. Sui, B. Shen, High entropy oxides $(FeNiCrMn_X)_3O_4$ (X = Zn , Mg) as anode materials for lithium ion batteries, Ceramics International. 4 (2021).

[166] A. Amiri, R. Shahbazian-yassar, Recent progress of high-entropy materials for energy storage and conversion, J. Mater. Chem. A. 9 (2021) 782–823.

[167] Y. Chen, H. Fu, Y. Huang, L. Huang, X. Zheng, Y. Dai, Y. Huang, W. Luo, Opportunities for High-Entropy Materials in Rechargeable Batteries, ACS Materials Lett. 3 (2021) 160−170.

[168] B.T. Wei, C. Chen, H. Chien, S. Lu, C. Hu, A Cost-Effective Supercapacitor Material of Ultrahigh Specific Capacitances: Spinel Nickel Cobaltite Aerogels from an Epoxide-Driven Sol-Gel Process, Adv. Mater. 30013 (2010) 347–351.

[169] L. Hu, L. Wu, M. Liao, X. Hu, X. Fang, Electrical Transport Properties of Large, Individual $NiCo_2O_4$ Nanoplates, Adv. Funct. Mater. 22 (2012) 998–1004.

[170] Y. Zhao, X. Li, B. Yan, D. Xiong, D. Li, S. Lawes, Recent Developments and Understanding of Novel Mixed Transition-Metal Oxides as Anodes in Lithium Ion Batteries, Adv. Energy Mater. 6 (2016) 1502175.

[171] P.A. Connor, J.T.S. Ir, Combined X-ray study of lithium (tin) cobalt oxide matrix negative electrodes for Li-ion batteries, Electrochimica Acta. 47 (2002) 2885–2892.

[172] P.A. Connor, J.T.S. Irvine, Novel tin oxide spinel-based anodes for Li-ion batteries, Journal of Power Sources. 98 (2001) 223–225.

[173] F. Belliard, P.A. Connor, J.T.S. Irvine, Novel tin oxide-based anodes for Li-ion batteries, Solid State Ionics. 135 (2000) 163–167.

[174] G. Huang, X. Guo, X. Cao, Q. Tian, H. Sun, 3D networksingle-phase$Ni_{0.9}Zn_{0.1}O$ as anode materials for lithium-ion batteries, Nano Energy. 28 (2016) 338–345.

[175] X. Li, C. Wang, Significantly increased cycling performance of novel "'self-matrix'" $NiSnO_3$ anode in lithium ion battery application, RSC Advances. 2 (2012) 6150–6154.

[176] J. Zhao, L. Zhao, N. Dimov, S. Okada, T. Nishida, Electrochemical and Thermal Properties of α - $NaFeO_2$ Cathode for Na-Ion Batteries, 160 (2013) 3077–3081.

[177] A. Rudola, K. Saravanan, C.W. Mason, P. Balaya, $Na_2Ti_3O_7$: an intercalation based anode for sodium-

ion battery applications, J. Mater. Chem. A. 1 (2013) 2653–2662.

[178] S. Il Park, I. Gocheva, S. Okada, J. Yamaki, Electrochemical Properties of $NaTi_2(PO_4)_3$ Anode for Rechargeable Aqueous Sodium-Ion Batteries, 158 (2011) 1067–1070.

[179] Y. Zhu, X. Han, Y. Xu, Y. Liu, S. Zheng, K. Xu, L. Hu, Electrospun Sb/C Fibers for a Stable and Fast Sodium-Ion Battery Anode, ACS Nano. 7 (2013) 6378–6386.

[180] D.A. Links, In situ synthesis of MoS_2/graphene nanosheet composites with extraordinarily high electrochemical performance for lithium ion batteries, Chem. Commun. 47 (2011) 4252–4254.

[181] X. Hu, Y. Li, G. Zeng, J. Jia, H. Zhan, Z. Wen, Three-Dimensional Network Architecture with Hybrid Nanocarbon Composites Supporting Few-Layer MoS 2 for Lithium and Sodium Storage, ACS Nano. 12 (2018) 1592–1602.

[182] Y. Fang, X. Hu, W. Zhao, J. Pan, D. Wang, K. Bu, Y. Mao, S. Chu, P. Liu, T. Zhai, F. Huang, Structural Determination and Nonlinear Optical Properties of New 1T‴-Type MoS_2 Compound, J. Am. Chem. Soc. 141 (2019) 790–793.

[183] B. Mos, Y. Fang, J. Pan, J. He, R. Luo, D. Wang, X. Che, K. Bu, W. Zhao, P. Liu, G. Mu, H. Zhang, T. Lin, F. Huang, Superconductivity Structure Re-determination and Superconductivity Observation of 1T MoS_2, Angew. Chem. Int. Ed. 130 (2018) 1246–1249.

[184] T. Stephenson, Z. Li, D. Mitlin, Lithium ion battery applications of molybdenum disulfide (MoS_2) nanocomposites, Energy Environ. Sci. 7 (2014) 209–231.

[185] K. Kobayashi, J. Yamauchi, Electronic structure and scanning-tunneling-microscopy image of molybdenum dichalcogenide surfaces, PHYSICAL REVIEW B. 51 (1995) 17085–17095.

[186] B. Mos, Y. Fang, J. Pan, J. He, R. Luo, D. Wang, X. Che, K. Bu, W. Zhao, P. Liu, G. Mu, H. Zhang, T. Lin, F. Huang, Superconductivity Structure Re-determination and Superconductivity Observation of Bulk 1T MoS_2, Angew. Chem. Int. Ed. 130 (2018) 1246–1249.

[187] K.S. Novoselov, D. Jiang, F. Schedin, T.J. Booth, V. V Khotkevich, S. V Morozov, A.K. Geim, Two-dimensional atomic crystals, PNAS. 102 (2005) 10451–10453.

[188] T. Stephenson, Z. Li, D. Mitlin, Lithium ion battery applications of molybdenum disulfide (MoS_2) nanocomposites†, Energy Environ. Sci. 7 (2014) 209–231.

[189] Y. Hu, Y. Bai, X. Wu, X. Wei, K. Wang, J. Chen, MoS2 nanoflakes integrated in a 3D carbon framework for high- performance sodium-ion batteries, Journal of Alloys and Compounds. 797 (2019) 1126–1132.

[190] X. Xie, T. Makaryan, M. Zhao, K.L. Van Aken, Y. Gogotsi, G. Wang, MoS_2 Nanosheets Vertically Aligned on Carbon Paper : A Freestanding Electrode for Highly Reversible Sodium-Ion Batteries, Adv. Energy Mater. 6 (2016) 1502161.

[191] Q. Li, Z. Yao, J. Wu, S. Mitra, S. Hao, Nano Energy Intermediate phases in sodium intercalation into MoS_2 nanosheets and their implications for sodium-ion batteries, Nano Energy. 38 (2017) 342–349.

[192] D. Sun, D. Ye, P. Liu, Y. Tang, J. Guo, L. Wang, H. Wang, MoS_2/Graphene Nanosheets from Commercial Bulky MoS_2 and Graphite as Anode Materials for High Rate Sodium-Ion Batteries, Adv. Energy Mater. 8 (2018) 1702383.

[193] Z. Li, S. Liu, B.P. Vinayan, Z. Zhao-karger, K. Wang, R.J. Behm, C. Kübel, R. Klingeler, Hetero-layered MoS2 /C composites enabling ultrafast and durable Na storage, Energy Storage Materials. 21 (2019) 115–123.

[194] S. Yu, M.J. Zachman, K. Kang, H. Gao, X. Huang, F.J. Disalvo, J. Park, L.F. Kourkoutis, H.D. Abruña, Atomic-Scale Visualization of Electrochemical Lithiation Processes in Monolayer MoS_2 by Cryogenic Electron Microscopy, Adv. Energy Mater. 9 (2019)

[195] Q. Su, S. Wang, M. Feng, G. Du, B. Xu, Direct Studies on the Lithium-Storage Mechanism of Molybdenum Disulfide, Sci Rep. 7 (2017) 7275.

[196] W. Choi, Y.S. Choi, H. Kim, J. Yoon, Y. Kwon, T. Kim, J. Ryu, J.H. Lee, W. Lee, J. Huh, J.M. Kim, W. Yoon, Evidence for the Coexistence of Polysul fi de and Conversion Reactions in the Lithium Storage Mechanism of MoS_2 Anode Material, Chem. Mater. 33 (2021) 1935–1945.

[197] X. Xie, Z. Ao, D. Su, J. Zhang, G. Wang, MoS2/Graphene Composite Anodes with Enhanced Performance for Sodium-Ion Batteries : The Role of the Two-Dimensional Heterointerface, Adv. Funct. Mater. 25 (2015) 1393–1403.

[198] R. Jung, J.E. Soc, R. Jung, M. Metzger, F. Maglia, C. Stinner, Oxygen Release and Its Effect on the Cycling Stability of LiNixMnyCozO 2 (NMC) Cathode Materials for Li-Ion Batteries, Journal of The Electrochemical Society. 2 (2017) A1361–A1377.

[199] D.J. Xiong, J. Electrochem, A. Soc, D.J. Xiong, L.D. Ellis, J. Li, H. Li, T. Hynes, J.P. Allen, J. Xia, D.S. Hall, I.G. Hill, J.R. Dahn, Measuring Oxygen Release from Delithiated $LiNixMnyCo_{1-x-y}O_2$ and Its Effects on the Performance of High Voltage Li-Ion Cells, Journal of The Electrochemical Society. 13 (2017) A3025–A3037.

[200] P. Vassilaras, D. Kwon, S.T. Dacek, T. Shi, D. Seo, J. Chul, Electrochemical properties and structural evolution of O3-type layered sodium mixed transition metal oxides with trivalent nickel, J. Mater. Chem. A. 5 (2017) 4596–4606.

[201] Y. Jiang, X. Yan, W. Xiao, M. Tian, L. Gao, D. Qu, H. Tang, Co_3O_4-graphene nanoflowers as anode for advanced lithium ion batteries with enhanced rate capability, Journal of Alloys and Compounds. 710 (2017) 114–120.

[202] E.R. Adkins, T. Jiang, L. Luo, C. Wang, B.A. Korgel, In Situ Transmission Electron Microsopy of Oxide Shell-Induced Pore Formation in (De)lithiated Silicon Nanowires, ACS Energy Lett. 3 (2018) 2829–2834.

[203] H. Liu, L. Shi, D. Li, J. Yu, H. Zhang, S. Ullah, B. Yang, C. Li, C. Zhu, J. Xu, Rational design of hierarchical ZnO@Carbon nano flower for high performance lithium ion battery anodes, Journal of Power Sources. 387 (2018) 64–71.

[204] D.D.V. Ii, O.D. Hentz, S. Chen, R.E. Schaak, Formation of SnS nanoflowers for lithium ion batteries, Chem. Commun. (2012) 5608–5610.

[205] N. Spinner, L. Zhang, W.E. Mustain, Investigation of metal oxide anode degradation in lithium-ion batteries via identical-location TEM, J. Mater. Chem. A. 2 (2014) 1627–1630.

[206] G. Xu, R. Amine, Y. Xu, J. Liu, J. Gim, T. Ma, Y. Ren, C. Sun, Y. Liu, X. Zhang, S.M. Heald, A. Solhy, I. Saadoune, W.L. Mattis, S. Sun, Z. Chen, K. Amine, Environmental Science materials for high voltage sodium-ion batteries †, Energy Environ. Sci. 10 (2017) 1677–1693.

[207] Z. Yan, L. Tang, Y. Huang, W. Hua, Y. Wang, R. Liu, Q. Gu, S. Indris, S. Chou, Y. Huang, M. Wu, S. Dou, A Hydrostable Cathode Material Based on the Layered P2@P3 Composite that Shows Redox Behavior for Copper in High-Rate and Long-Cycling Sodium-Ion Batteries, Angew. Chem. Int. Ed. 200444 (2019) 1412–1416.

[208] Y. Nomura, K. Yamamoto, T. Hirayama, E. Igaki, K. Saitoh, Visualization of Lithium Transfer Resistance in Secondary Particle Cathodes of Bulk-Type Solid-State Batteries, ACS Energy Lett. 5 (2020) 2098–2015.

[209] H. Dai, C. Yang, X. Ou, X. Liang, H. Xue, W. Wang, Unravelling the electrochemical properties and thermal behavior of NaNi2/3Sb1/3O2 cathode for sodium-ion batteries by in situ X-ray diffraction investigation, Electrochimica Acta. 257 (2017) 146–154.

[210] Z. Li, X. Mu, Z. Zhao-karger, T. Diemant, R.J. Behm, C. Kübel, M. Fichtner, Fast kinetics of multivalent intercalation chemistry enabled by solvated magnesium-ions into selfestablished metallic layered materials, Nat Commun. 9 (2018) 5115.

[211] P.A. Sukkurji, Y. Cui, S. Lee, K. Wang, R. Azmi, A. Sarkar, S. Indris, S.S. Bhattacharya, R. Kruk, H. Hahn, Q. Wang, B. Breitung, Mechanochemical synthesis of novel rutile-type high entropy fluorides for electrocatalysis, J. Mater. Chem. A. 9 (2021) 8998–9009.

[212] L. Lin, K. Wang, R. Azmi, J. Wang, A. Sarkar, M. Botros, S. Najib, Y. Cui, D. Stenzel, P.A. Sukkurji, Q. Wang, H. Hahn, S. Schweidler, B. Breitung, Mechanochemical synthesis : route to novel rock-salt-structured high-entropy oxides and oxyfluorides, J Mater Sci. 55 (2020) 16879–16889.

[213] D. Stenzel, I. Issac, K. Wang, R. Azmi, R. Singh, J. Jeong, S. Najib, S.S. Bhattacharya, H. Hahn, T. Brezesinski, S. Schweidler, B. Breitung, High Entropy and Low Symmetry: Triclinic High-Entropy Molybdates, Inorg. Chem. 60 (2021) 115–123.

[214] J. Wang, Y. Cui, Q. Wang, K. Wang, X. Wang, D. Stenzel, A. Sarkar, S.S. Bhattacharya, R. Kruk, H. Hahn, T. Brezesinski, B. Breitung, C. Wang, J. Wang, Y. Cui, Q. Wang, K. Wang, X. Huang, D. Stenzel, A. Sarkar, S. Subramshu, Layered High-Entropy Oxide Structures for Reversible Energy Storage Layered High-Entropy Oxide Structures for Reversible Energy Storage, ChemRxiv. 2 (2020) 1–13.

[215] P. Yan, J. Zheng, J. Liu, B. Wang, X. Cheng, Y. Zhang, X. Sun, C. Wang, J. Zhang, Tailoring grain boundary structures and chemistry of Ni-rich layered cathodes for enhanced cycle stability of lithium-ion batteries, Nature Energy. 3 (2018) 600–605.

[216] Y. Sun, L. Zhao, H. Pan, X. Lu, L. Gu, Y. Hu, H. Li, M. Armand, Y. Ikuhara, L. Chen, X. Huang, Direct atomic-scale confirmation of three-phase storage mechanism in $Li_4Ti_5O_{12}$ anodes for room-temperature sodium-ion batteries, Nature Communications. 1870 (2013).

[217] B.D.A. Levin, M.J. Zachman, J.G. Werner, R. Sahore, K.X. Nguyen, Y. Han, B. Xie, L. Ma, L.A. Archer, E.P. Giannelis, U. Wiesner, L.F. Kourkoutis, D.A. Muller, Characterization of Sulfur and Nanostructured Sulfur Battery Cathodes in Electron Microscopy Without Sublimation Artifacts, Microsc. Microanal. 23 (2017) 155–162.

[218] J. Yoshida, M. Stark, J. Holzbock, N. Hüsing, S. Nakanishi, H. Iba, H. Abe, M. Naito, Analysis of the size effect of $LiMnPO_4$ particles on the battery properties by using STEM-EELS, Journal of Power Sources. 226 (2013) 122–126.

[219] X. Li, Z. Ren, M.N. Banis, S. Deng, Y. Zhao, Q. Sun, C. Wang, X. Yang, W. Li, J. Liang, X. Li, Y. Sun, K. Adair, R. Li, Y. Hu, T. Sham, H. Huang, L. Zhang, S. Lu, J. Luo, X. Sun, Unravelling the Chemistry and Microstructure Evolution of a Cathodic Interface in Sulfide-Based All-Solid-State Li-Ion Batteries, ACS Energy Lett. 4 (2019) 2480–2488.

[220] H. Liu, M. Bugnet, M.Z. Tessaro, K.J. Harris, M.J.R. Dunham, M. Jiang, G.R. Goward, G.A. Botton, Spatially resolved surface valence gradient and structural transformation of lithium transition metal oxides in lithium-ion batteries, Phys. Chem. Chem. Phys. 18 (2016) 29064--29075.

[221] F.C. Castro, V.P. Dravid, Characterization of Lithium Ion Battery Materials with Valence Electron Energy-Loss Spectroscopy, Microscopy and Microanalysis. 24 (2017) 214–220.

[222] C. Oses, C. Toher, S. Curtarolo, High-entropy ceramics, Nature Reviews Materials. 5 (2020) 295–309.

[223] I. Protochips, Atmosphere 210 User Manual v1.5 M-00002, 2018.

[224] Y. Tang, L. Zhang, Y. Tang, X. Wang, T. Zhang, R. Yang, C. Ma, N. Li, Y. Liu, X. Zhao, X. Zhang, Z. Wang, B. Guo, Y. Li, J. Huang, In situ imaging of electrocatalysis in a $K–O_2$ battery with a hollandite a -MnO 2 nanowire air cathode, Chem. Commun. 55 (2019) 10880–10883.

[225] D.B. Williams, C.B. Carter, Transmission Electron Microscopy.

[226] J.M. Zuo, J.C.H. Spence, Advanced Transmission Electron Microscopy.

[227] R. Egerton, Electron Energy Loss Spectroscopy in the Electron Microscope.

[228] G.P. Summers, E.A. Burkej, M.A. Xapsos, Displacement damage analogs to ionizaing Radiation effects, Radiation Measurements. 24 (1995) 1–8.

[229] X. Mu, A. Kobler, D. Wang, V.S.K. Chakravadhanula, S. Schlabach, D. V. Szabó, P. Norby, C. Kübel, Comprehensive analysis of TEM methods for $LiFePO_4/FePO_4$ phase mapping: spectroscopic techniques (EFTEM, STEM-EELS) and STEM diffraction techniques (ACOM-TEM), Ultramicroscopy. 170 (2016) 10–18.

[230] J.E. Penner-Hahn, X-ray Absorption Spectroscopy, The University of Michigan, 2003.

[231] M. Eckert, P. Knipping, W.H. Bragg, W.L. Bragg, Max von Laue and the discovery of X-ray diffraction

in 1912, Ann. Phys. 5 (2012) A83–A85.

[232] W. Wubet, Green Synthesis of CuO Nanoparticles for the Application of Dye Sensitized Solar Cell, World Journal of Pharmaceutical Research. 9 (2019) 29-51.

[233] A. Paar, X-Ray diffraction (XRD), Https://wiki.anton-Paar.com/en/x-Ray-Diffraction-Xrd/.

[234] B.J. Inkson, Scanning electron microscopy (SEM) and transmission electron microscopy (TEM) for materials characterization, Materials Characterization Using Nondestructive Evaluation (NDE) Methods, (2016) 17-43.

[235] S. Reyntjens, R. Puers, A review of focused ion beam applications in microsystem technology, J. Micromech. Microeng. 11 (2001) 287-300.

[236] M. Prestigiacomo, L. Roussel, A. Houel, P. Sudraud, F. Bedu, D. Tonneau, V. Safarov, H. Dallaporta, Studies of structures elaborated by focused ion beam induced deposition, Microelectronic Engineering. 76 (2004) 175–181.

[237] J. Abed, Characterization and Modification of Solar Energy Water Splitting Material for Storable Fuel Generation, 2017.

[238] F. Wu, Planar Defects in Metallic Thin Film Heterostructures, 2014.

[239] https://www.wikiwand.com/en/Transmission_electron_microscopy#/Optics.

[240] S. Kumar, C. Neelakandhan, In situ TEM studies on the graphitization and growth of nanocrystalline graphene from polymers, 2019.

[241] C. Kübel, in-situ electron microscopy lecture, 2020.

[242] H.G. Brown, J. Ciston, Atomic Resolution Imaging of Light Elements in a Crystalline Environment using Dynamic Hollow-Cone Illumination Transmission Electron Microscopy, Microscopy and Microanalysis. 26 (2020) 623–629.

[243] W. Wang, Quantitative 3D Structure Studies of Supported Catalysts at the Nanoscale, 2019.

[244] P.D. Nellist, S.J. Pennycook, The Principles and Interpretation of Annular Dark-Field Z-Contrast Imaging, Advances in imaging and electron physics. 113 (2008) 147–203.

[245] S.S. Division, O. Ridge, O. Ridge, Z-contrast stem for materials science, Ultramicroscopy. 30 (1989) 58–69.

[246] 4D STEM, Https://www.gatan.com/techniques/4d-Stem.

[247] C. Ophus, Four-Dimensional Scanning Transmission Electron Microscopy (4D-STEM): From Scanning Nanodiffraction to Ptychography and Beyond, Microscopy and Microanalysis. 25 (2019) 563–582.

[248] JEOL, coma-free axis, Https://www.jeol.co.jp/en/words/emterms/search_result.html?keyword=coma-free%20axis.

[249] S. Uhlemann, M. Haider, Residual wave aberrations in the first spherical aberration corrected transmission electron microscope, Ultramicroscopy. 72 (1998) 109-119.

[250] P. Hartel, M. Linck, F. Kahl, H. Müller, M. Haider, On Proper Phase Contrast Imaging in Aberration

Corrected TEM, Microsc. Microanal. 20 (2014) 768–769.

[251] D. Wang, High-resolution transmission electron microscopy and spherical aberration correction lecture, 2019.

[252] N.J. Zaluzec, Innovative Instrumentation for Analysis of Nanoparticles : The π Steradian Detector, Microscopy Today. (2014) 56–59.

[253] FEI, ChemiSTEM Technology: A revolution in EDX analytics.

[254] E. Wilkins, Lecture 4 - Spectroscopy, https://slideplayer.com/slide/5668584/.

[255] No Title, Https://eels.info/how/getting-Started/collection-Angle-Considerations.

[256] S.C.C. T. MALIS, R.F. EGERTON, EELS Log-Ratio Technique for Specimen-Thickness Measurement in the TEM, Hournal of electron microscopy technique. 8 (1988) 193–200.

[257] M. Gorgoil, D.R.T. Zahn, Density of occupied and unoccupied states monitored during metal deposition onto phthalocyanine layers, J. Phys. IV France. 132 (2006) 337–340.

[258] T. Manoubl, M. Tencl, C. Colliex, Quantification of white lines in electron energy loss spectroscopy (EELS), Ultramieroscop. 28 (1989) 49–55.

[259] T. Egami, S.J.L. Billinge, Underneath the Bragg peaks structural analysis of complex materials, Kidlington, 2003.

[260] R.B. Neder, T.Proffen:, Diffuse scattering and defect structure simulations: a cook book using the program DISCUS. 2008.

[261] Xiaoke Mu, TEM study of the structural evolution of ionic solids from amorphous to polycrystalline phases in the case of alkaline earth difluoride systems Experimental exploration of energy landscape, 2013.

[262] X. Mu, S. Neelamraju, W. Sigle, C.T. Koch, P.A. Van Aken, Evolution of order in amorphous-to-crystalline phase transformation of MgF_2 research papers, J. Appl. Cryst. 46 (2012) 1105–1116.

[263] X. Hua, R. Robert, L. Du, K.M. Wiaderek, M. Leskes, K.W. Chapman, P.J. Chupas, C.P. Grey, Comprehensive Study of the CuF_2 Conversion Reaction Mechanism in a Lithium Ion Battery, J. Phys. Chem. C. 118 (2014) 15169–15184.

[264] D.J.H. COCKAYNE, D.R. MCKENZIE, Electron Diffraction Analysis of Polycrystailine and Amorphous Thin Films, Acta Cryst. A44 (1988) 870–878.

[265] X. Mu, D. Wang, T. Feng, C. Kübel, Radial distribution function imaging by STEM diffraction: Phase mapping and analysis of heterogeneous nanostructured glasses, Ultramicroscopy. 168 (2016) 1–6.

[266] X. Mu, L. Chen, R. Mikut, H. Hahn, C. Kübel, Unveiling local atomic bonding and packing of amorphous nanophases via independent component analysis facilitated pair distribution function, Acta Materialia. 212 (2021) 116932.

[267] C.M. Rost, E. Sachet, T. Borman, A. Moballegh, E.C. Dickey, D. Hou, J.L. Jones, S. Curtarolo, J. Maria, Entropy-stabilized oxides, Nature Communications. 6 (2015) 8485.

[268] A. Sarkar, R. Djenadic, N.J. Usharani, K.P. Sanghvi, V.S.K. Chakravadhanula, A.S. Gandhi, H. Hahn,

S.S. Bhattacharya, Nanocrystalline multicomponent entropy stabilised transition metal oxides, Journal of the European Ceramic Society. 37 (2017) 747–754.

[269] D. Berardan, A.K. Meena, S. Franger, C. Herrero, N. Dragoe, Controlled Jahn-Teller distortion in (MgCoNiCuZn)O-based high entropy oxides, Journal of Alloys and Compounds. 704 (2017) 693–700.

[270] G. Anand, A.P. Wynn, C.M. Handley, C.L. Freeman, Phase stability and distortion in high-entropy oxides, Acta Materialia. 146 (2018) 119–125.

[271] H.S.C.O. Neill, Thermodynamics of Co_3O_4: a Possible Electron Spin Unpairing Transition in Co^{3+}, Phys Chem Minerals. 12 (1985) 149–154.

[272] N.A. Mayer, D.M. Cupid, R. Adam, A. Reif, D. Rafaja, H.J. Seifert, Standard enthalpy of reaction for the reduction of Co_3O_4 to CoO, Thermochimica Acta. 652 (2017) 109–118.

[273] D.Narducci, F.Negroni, C.M.Mari, High temperature standard gibbs free energy determinations for Co-O systems by e.m.f. measurements. A statistical approach to evaluate the reliability of the current methods, Materials Chemistry and Physics. 12 (1985) 377–388.

[274] J. Lis, R. Pampuch, The role of surface diffusion in the sintering of micropowers, J. Phys. Colloques. 47 (1986) C1-219-C1-223.

[275] H. Ji, A. Urban, D.A. Kitchaev, D. Kwon, N. Artrith, C. Ophus, W. Huang, Z. Cai, T. Shi, J.C. Kim, H. Kim, G. Ceder, Hidden structural and chemical order controls lithium transport in cation-disordered oxides for rechargeable batteries, Nature Communications. 10 (2019) 592.

[276] C. Kim, J.W. Kim, H. Kim, D.H. Kim, C. Choi, Y.S. Jung, J. Park, Graphene Oxide Assisted Synthesis of Self-assembled Zinc Oxide for Lithium-Ion Battery Anode, Chem. Mater. 28 (2016) 8498–8503.

[277] C.J. Pelliccione, J.E. Soc, C.J. Pelliccione, Y. Ding, E. V Timofeeva, C.U. Segre, In Situ XAFS Study of the Capacity Fading Mechanisms in ZnO Anodes for Lithium-Ion Batteries, Journal of The Electrochemical Society. 162 (2015) A1935–A1939.

[278] T. Eisenmann, A. Birrozzi, A. Mullaliu, G. Giuli, A. Trapananti, S. Passerini, D. Bresser, Effect of Applying a Carbon Coating on the Crystal Structure and De-/Lithiation Mechanism of Mn-Doped ZnO Lithium-Ion Anodes, Journal of The Electrochemical Society. 168 (2021) 30503.

[279] J. Deng, K. Dong, P. Yang, Y. Peng, G. Ju, J. Hu, G.M. Chow, J. Chen, Large lattice mismatch effects on the epitaxial growth and magnetic properties of FePt films, Journal of Magnetism and Magnetic Materials. 446 (2017) 125–134.

[280] T. Zheleva, K. Jagannadham, J. Narayan, Epitaxial growth in large-lattice-mismatch systems, J. Appl. Phys. 75 (1994) 860–871.

[281] S.M. Bhaway, Y. Chen, Y. Guo, P. Tangvijitsakul, M.D. Soucek, M. Cakmak, Y. Zhu, B.D. Vogt, Hierarchical Electrospun and Cooperatively Assembled Nanoporous Ni/NiO/MnO_x/Carbon Nanofiber Composites for Lithium Ion Battery Anodes, ACS Appl. Mater. Interfaces. 8 (2016) 19484–19493.

[282] A.R.C. Bredar, A.L. Chown, A.R. Burton, B.H. Farnum, Electrochemical Impedance Spectroscopy of

Metal Oxide Electrodes for Energy Applications, ACS Appl. Energy Mater. 3 (2020) 66–98.

[283] X. Li, J. Liu, X. Meng, Y. Tang, M. Norouzi, J. Yang, Significant impact on cathode performance of lithium-ion batteries by precisely controlled metal oxide nanocoatings via atomic layer deposition, Journal of Power Sources. 247 (2014) 57–69.

[284] L.P. Teo, M.H. Buraidah, A.K. Arof, Study on Li ion diffusion in Li_2SnO_3 anode material by CV and EIS techniques, Molecular Crystals and Liquid Crystals. 694 (2020) 117–130.

[285] F. Nobili, S. Dsoke, F. Croce, R. Marassi, An ac impedance spectroscopic study of Mg-doped $LiCoO_2$ at different temperatures : electronic and ionic transport properties, Electrochimica Acta. 50 (2005) 2307–2313.

[286] Z. Zhao, S. Dsoke, P. Helmut, S.Z. Zhao, S. Dsoke, J.M.C. A, Elucidating the energy storage mechanism of ZnMn2O4 as promising anode for Li-ion batteries, J. Mater. Chem. A. 6 (2018) 19381.

[287] X. Hua, R. Robert, L. Du, K.M. Wiaderek, M. Leskes, K.W. Chapman, P.J. Chupas, C.P. Grey, Comprehensive Study of the CuF2 Conversion Reaction Mechanism in a Lithium Ion Battery, J. Phys. Chem. C. 118 (2014) 15169−15184.

[288] D. Juliusz, A. St, M. Danielewski, K. Swierczek, Mixed ionic-electronic transport in the high-entropy (Co, Cu, Mg, Ni, Zn)$_{1-x}$Li$_x$O oxides, Acta Materialia. 208 (2021) 116735.

[289] X.H. Huang, R.Q. Guo, J.B. Wu, P. Zhang, Mesoporous ZnO nanosheets for lithium ion batteries, Materials Letters. 122 (2014) 82–85.

[290] M. Bianchini, E. Gonzalo, N. Drewett, N. Ortiz Vitoriano, J.-M. Lopez del Amo, F.J. Bonilla, B. Acebedo, T. Rojo, Layered P2-O3 sodium-ion cathodes derived from earth abundant elements, J. Mater. Chem. A. 6 (2018) 3552–3559.

[291] J. Park, J. Kim, J. Park, T. Nam, K. Kim, J. Ahn, G. Wang, H. Ahn, Discharge mechanism of MoS_2 for sodium ion battery : Electrochemical measurements and characterization, Electrochimica Acta. 92 (2013) 427–432.

[292] W. Ren, H. Zhang, C. Guan, C. Cheng, Ultrathin MoS_2 Nanosheets@ Metal Organic Framework-Derived N-Doped Carbon Nanowall Arrays as Sodium Ion Battery Anode with Superior Cycling Life and Rate Capability, Adv. Funct. Mater. 27 (2017) 1702116.

[293] S. Hao, R. Yu, Z. Wang, L. Chen, Reversible conversion of MoS_2 upon sodium extraction, Nano Energy. 41 (2017) 217–224.

[294] X. Wang, X. Shen, Z. Wang, R. Yu, L. Chen, Atomic-Scale Clarification of Structural Transition of MoS_2 upon Sodium Intercalation, ACS Nano. (2014) 11394–11400.

[295] J.B. Parise, E.M. Mccarron, J.A. Goldstone, Produced from a Novel Freeze Drying Route, J SOLID STATE CHEM. 3 (1991) 193–201.

[296] H. Wang, H. Jiang, Y. Hu, P. Saha, Q. Cheng, C. Li, Interface-engineered MoS_2/C nanosheet heterostructure arrays for ultra-stable sodium-ion batteries, Chemical Engineering Science. 174 (2017) 104–111.

[297] W. Ren, H. Zhang, C. Guan, C. Cheng, Ultrathin MoS_2 Nanosheets @ Metal Organic Framework-Derived N-Doped Carbon Nanowall Arrays as Sodium Ion Battery Anode with Superior Cycling Life and Rate Capability, Adv. Funct. Mater. 27 (2017) 1702116.

[298] H. Zhu, F. Zhang, J. Li, Y. Tang, Penne-Like MoS_2/Carbon Nanocomposite as Anode for Sodium-Ion-Based Dual-Ion Battery, Small. 14 (2018) 1703951.

[299] B. Chen, E. Liu, T. Cao, F. He, C. Shi, C. He, L. Ma, Nano Energy Controllable graphene incorporation and defect engineering in MoS2 -TiO2 based composites : Towards high-performance lithium-ion batteries anode materials, Nano Energy. 33 (2017) 247–256.

[300] Q. Pan, Q. Zhang, F. Zheng, Y. Liu, Y. Li, X. Ou, X. Xiong, C. Yang, M. Liu, Construction of MoS2/C Hierarchical Tubular Heterostructures for High-Performance Sodium Ion Batteries, ACS Nano. 12 (2018) 12578–12586.

[301] D. Zhou, R.G. Spruit, M. Pen, H.P. Garza, Q. Xu, B. V Denssolutions, Correlative In-situ Gas and Heating TEM : Integrating Calorimetry and Mass Spectroscopy, Microsc. Microanal. 26 (2020) 3044–3046.

[302] N. Zink, H.A. Therese, J. Pansiot, A. Yella, F. Banhart, W. Tremel, In Situ Heating TEM Study of Onion-like WS_2 and MoS_2 Nanostructures Obtained via MOCVD, Chem. Mater. 20 (2008) 65–71.

[303] W. Li, L. Chen, D. Liu, J. Liu, L. An, Ultra-low temperature reactive flash sintering synthesis of high-enthalpy, Materials Letters. 304 (2021) 130679.

Curriculum Vitae

Personal Information:

Name: Kai Wang

Date of Birth: April 15, 1991

Place of Birth: Hengshui, Hebei, China

Nationality: P.R. China

Education:

- *Doctoral studies* in Materials Science 11.2017- 06.2022

  Joint Research Laboratory for Nanomaterials, Technical University of Darmstadt and Karlsruhe Institute of Technology, Karlsruhe, Germany

  Title of Ph.D. thesis: "Understanding fundamental migration processes during battery cycling and material synthesis using advanced transmission electron microscopy methods" supervised by Prof. Christian Kübel

- *Master of Engineering* in Chemical Engineering

  09.2014- 06.2017

  Department of Chemical Engineering, Sichuan University, Chengdu, China

  03.2015- 03.2017

  Joint training in College of Energy, Xiamen University, Xiamen, China

  Title of Master's thesis: "Synthesis and research of layer oxide cathode materials in sodium ion battery" supervised by Prof. Benhe Zhong

- *Bachelor of Engineering* in Chemical Engineering and Technology

  09.2010- 06.2014

  Department of Chemical and Pharmaceutical Engineering, Hebei University of Science and Technology, Shijiazhuang, China

List of publications (during PhD)

[1] L. Lin, **K. Wang**, A. Sarkar, C. Njel, G. Karkera, Q. Wang, R. Azmi, M. Fichtner, H. Hahn, S. Schweidler, B. Breitung, High-Entropy Sulfides as Electrode Materials for Li-Ion Batteries, Adv. Energy Mater. 2103090 (2022). https://doi.org/10.1002/aenm.202103090

[2] F. Strauss, J. Lin, M. Duffiet, **K. Wang**, T. Zinkevich, A. Hansen, S. Indris, T. Brezesinski, High-Entropy Polyanionic Lithium Superionic Conductors, ACS Materials Lett. 4 (2022), 418–423. https://doi.org/10.1021/acsmaterialslett.1c00817

[3] **K. Wang**, W. Hua, Z. Li, Q. Wang, C. Kübel, X. Mu, New Insight of De-/sodiation Mechanism of MoS_2: Sodium Insertion in Amorphous Mo-S Clusters, ACS Appl. Mater. Interfaces. 2021. https://doi.org/10.1021/acsami.1c07743

[4] D. Stenzel, I. Issac, **K. Wang**, R. Azmi, R. Singh, J. Jeong, S. Najib, S.S. Bhattacharya, H. Hahn, T. Brezesinski, S. Schweidler, B. Breitung, High Entropy and Low Symmetry: Triclinic High-Entropy Molybdates, Inorg. Chem. 60 (2021) 115–123. https://doi.org/10.1021/acs.inorgchem.0c02501.

[5] P.A. Sukkurji, Y. Cui, S. Lee, **K. Wang**, R. Azmi, A. Sarkar, S. Indris, Subramshu, Bhattacharya, R. Kruk, H. Hahn, Q. Wang, M. Botros, B. Breitung, Mechanochemical synthesis of novel rutile-type high entropy fluorides for electrocatalysis, J. Mater. Chem. A. 9 (2021) 8998–9009. DOI: 10.1039/D0TA10209A.

[6] W. Hua, S. Wang, **K. Wang**, A. Missyul, Q. Fu, M. Susana, D. Darma, H. Li, V. Baran, L. Liu, C. Kübel, J.R. Binder, M. Knapp, H. Ehrenberg, S. Indris, Li+/Na+ Ion Exchange in Layered Na2/3(Ni0.25Mn0.75)O2: A Simple and Fast Way to Synthesize O3 / O2-Type Layered Oxides, Chem. Mater. 3 (2021). (**Equal contribution**) https://doi.org/10.1021/acs.chemmater.1c00962.

[7] Y. Ma, Y. Ma, S.L. Dreyer, Q. Wang, **K. Wang**, D. Goonetilleke, A. Omar, D. Mikhailova, H. Hahn, B. Breitung, T. Brezesinski, High-Entropy Metal – Organic Frameworks for Highly Reversible Sodium Storage, Adv. Mater. 2101342 (2021) 2101342. https://doi.org/10.1002/adma.202101342.

[8] **K. Wang**, Z. Wu, G. Melinte, Z. Yang, A. Sarkar, W. Hua, X. Mu, Z. Yin, J. Li, X. Guo, B. Zhong, C. Kübel, Preparation of intergrown P/O-type biphasic layered oxides as high-performance cathodes for sodium ion batteries, J. Mater. Chem. A. (2021). DOI: 10.1039/D1TA00627D.

[9] J. Wang, D. Stenzel, R. Azmi, S. Najib, **K. Wang**, J. Jeong, A. Sarkar, Q. Wang, P.A. Sukkurji, T. Bergfeldt, M. Botros, J. Maibach, H. Hahn, T. Brezesinski, B. Breitung, Spinel to Rock-Salt Transformation in High Entropy Oxides with Li Incorporation, Electrochem. 1 (2020) 60–74. https://doi.org/10.3390/electrochem1010007.

[10] W. Hua, **K. Wang**, M. Knapp, B. Schwarz, S. Wang, H. Liu, J. Lai, M. Mu, A. Scho, A. Missyul, D.F. Sanchez, X. Guo, J.R. Binder, J. Xiong, S. Indris, H. Ehrenberg, Chemical and Structural Evolution during the Synthesis of Layered Li(Ni,Co,Mn)O_2 Oxides, Chem. Mater. (2020) 4984−4997. https://doi.org/10.1021/acs.chemmater.9b05279.

[11] J. Wang, Y. Cui, Q. Wang, **K. Wang**, X. Huang, D. Stenzel, A. Sarkar, R. Azmi, T. Bergfeldt, S.S. Bhattacharya, R. Kruk, H. Hahn, S. Schweidler, T. Brezesinski, B. Breitung, Lithium containing layered high entropy oxide structures, Scientific Reports. 10 (2020) 1–13. https://doi.org/10.1038/s41598-020-75134-1.

[12] L. Lin, **K. Wang**, R. Azmi, J. Wang, A. Sarkar, M. Botros, S. Najib, Y. Cui, D. Stenzel, P.A. Sukkurji, Q. Wang, H. Hahn, S. Schweidler, B. Breitung, Mechanochemical synthesis : route to novel rock-salt-structured high-entropy oxides and oxyfluorides, J Mater Sci. 55 (2020) 16879–16889. https://doi.org/10.1007/s10853-020-05183-4.

[13] Y. Zhang, S. Zhang, J. Li, **K. Wang**, Y. Zhang, Q. Liu, R. Xie, Y. Pei, L. Huang, S. Sun, Improvement of electrochemical properties of P2-type Na2/3Mn2/3Ni1/3O2 sodium ion battery cathode material by water-soluble binders, Electrochimica Acta. 298 (2019) 496–504. https://doi.org/10.1016/j.electacta.2018.12.089.

[14] Z. Yin, X. Peng, J. Li, C. Shen, Y. Deng, Z. Wu, T. Zhang, Q. Zhang, Y. Mo, **K. Wang**, L. Huang, H. Zheng, S. Sun, Revealing of the Activation Pathway and Cathode Electrolyte Cathode by in Situ Electrochemical Quartz Crystal Microbalance, ACS Appl. Mater. Interfaces. 3 (2019) 16214−16222. https://doi.org/10.1021/acsami.9b02236.

[15] Z. Huang, J. Li, **K. Wang**, W. Ren, Y. Lu, L. Deng, L. Huang, S. Sun, Synthesis of LiFe0.4Mn0.4Co0.2PO4/C cathode material of lithium ion battery with enhanced electrochemical performance, Journal of Alloys and Compounds. 782 (2019) 413–420. https://doi.org/10.1016/j.jallcom.2018.12.169.

[16] Z. Li, S. Liu, B.P. Vinayan, Z. Zhao-karger, **K. Wang**, R.J. Behm, C. Kübel, R. Klingeler, Hetero-layered MoS2 /C composites enabling ultrafast and durable Na storage, Energy Storage Materials. 21 (2019) 115–123. https://doi.org/10.1016/j.ensm.2019.05.042.

[17] Z. Li, A. Ottmann, Q. Sun, A.K. Kast, **K. Wang**, T. Zhang, H.-P. Meyer, C. Backes, C. Kubel, R.R. Schroder, J. Xiang, Y. Vaynzof, R. Klingelerac, Hierarchical MoS2–carbon porous nanorods towards atomic interfacial engineering for high- performance lithium storage, J. Mater. Chem. A., 7 (2019) 7553–7564. DOI: 10.1039/C8TA12293H.

[18] Z. Gao, S. Zhang, Z. Huang, Y. Lu, W. Wang, **K. Wang**, J. Li, Y. Zhou, Protection of Li metal anode by surface-coating of PVDF thin film to enhance the cycling performance of Li batteries, Chinese Chemical Letters. 30 (2019) 525–528. https://doi.org/10.1016/j.cclet.2018.05.016.

[19] X. Yang, S. Wang, D. Han, **K. Wang**, A. Tayal, V. Baran, A. Missyul, Q. Fu, J. Song, H. Ehrenberg, S. Indris, W. Hua, Structural Origin of Suppressed Voltage Decay in Single-Crystalline Li-Rich Layered $Li[Li_{0.2}Ni_{0.2}Mn_{0.6}]O_2$ Cathodes, Small. 18 (2022) 2201522. https://doi.org/10.1002/smll.202201522

[20] Y. Cui, P. Sukkurjia, **K. Wang**, R. Azmi, A. Nunn, H. Hahn, B. Breitung, Y. Ting, P. Kowalski, P. Kaghazchi, Q. Wang, S. Schweidler, M. Botros, High entropy fluorides as conversion cathodes with tailorable electrochemical performance, Journal of Energy Chemistry. 72 (2022) 342-351. https://doi.org/10.1016/j.jechem.2022.05.032

Acknowledgements

At the end of this thesis, I would like express gratitude to a lot of persons and organizations. Without their generous encouragement and support, I have no chance to be here writing my PhD thesis.

Firstly, I thank my supervisor Prof. Christian Kübel, who gave me the chance of doing PhD four years ago. From the proposal of my PhD work to my PhD thesis, he gave me countless support, guidance and encouragement. His optimistic and friendly attitude towards life has created a pleasant and comfortable research environment for me during my PhD period. His rigorous and positive attitude towards scientific research would benefit me during all my life. I learnt a lot from him, not only scientific knowledge. I would also like to express my sincere thanks to my daily superiors, Dr. Melinte Georgian and Dr. Xiaoke Mu. Dr. Melinte Georgian is friendly and diligent, who help me a lot on my experiments and guided this thesis. Dr. Xiaoke Mu has always been enthusiastic about scientific research and has always been full of ideas. The works in this thesis were done under his constructive comments and guidance.

My thanks also extend to Dr. Di Wang, Dr. Torsten Scherer, Dr. Sabine Schlabach, Dr. D. Vinga Szabo, Dr. Yushu Tang, Xiaohui Huang, Mantha, Lakshmi Sravani, Yuting Dai, Ou Jin, Sangjun Kang, Ziming Ding, and all other members of Kübel group for their help in the work and my daily life.

I also thank all kind collaborators in Dr. Zhirong Zhao-Karger group, Dr. Ben Breitung Group and Prof. Dr. Helmut Ehrenberg Group for their contribution and discussion about my PhD work. It was a real pleasure to work with them.

I thank my motherland, China. Her strong economic strength, good social atmosphere and right direction have provided me with a good security for life and education. China Scholarship Council (CSC) gave me the financial support, which gave me the chance to have a rich experience of studying abroad. I sincerely thank Germany, a powerful, inclusive, democratic country. The four years' German life is one of the most memorable memories of my life.

Last but not the least, I would like to thank my parents, who gave me the life and unconditional love. I thank my wife, Can Su. You are the best thing that ever happened to me. I married with love. I thank my grandparents. I miss you. Although you already left me 13 years, I have dreamed about you many nights. When I was in trouble, I would imagine how you would encourage me. When I had some achievement, I would share it with you in mind, which just like I ran to you with a certificate in my hand when I was a kid. So even if you are gone, you are still my most thankful persons.